Optimised DC Microgrid for Future Aircraft Platforms

Mohamed Mohamed (BSc, MSc)

Thesis submitted to the University of Nottingham for the degree of Doctor of Philosophy

February 2022

Abstract

The aircraft industry's continued push towards the concept of a More Electric Aircraft (MEA), and All Electric Aircraft (AEA) to optimize its performance, decrease operating and maintenance costs, increase dispatch reliability, and reduce gas emissions. Particularly, the MEA concept aims to use electric power for all non-propulsive systems. Currently, the electrification trend is accelerating as aircraft Original Equipment Manufacturers (OEMs) engage with their suppliers to build new systems and install new power-dense electrically intensive architectures. This will lead to a significant challenge in the design of aircraft Electric Power systems (EPSs). The engineering community is currently researching various power system topologies.

Among these topologies, single DC bus EPS architecture is considered one of the promising candidates for future MEA/AEA due to its simplicity. In this topology, the electrical power is provided from engine-driven generators to the single DC bus through Active Rectifiers (ARs).

In this thesis, the potential solutions at the device and system levels for optimization of a single DC bus-based, multiple-source multiple-load power system with battery integration are investigated in terms of Energy Management (EM) and system losses minimization. The optimization of the single DC bus is achieved in this study by considering the following proposed control approaches:

1. An innovative multi-function battery controller is presented and the Back Tracing (BT) algorithm for a seamless transition between controllers is used. The battery controller performs different functions i.e. providing DC power, maintaining DC bus voltage, controlling battery voltage and battery current for charging and discharging process purposes.

2. A control scheme for Permanent Magnet Machine (PMM) based aircraft Starter/Generator (S/G) operated in Flux Weakening (FW) mode is presented. The proposed scheme helps the previous approach adopted for the Variable Voltage Bus (VVB) concept for an aircraft EPS to cover a wide speed range in motoring and generation modes. The control plants are derived specifically to design the controllers for the S/G control scheme. Moreover, a detailed small-signal analysis is performed on the derived plant while considering the aircraft operating speed and load range.

3. Droop control has been widely used as a load-sharing method among paralleled power sources due to its inherent modularity, reliability, and ease of implementation. In this thesis, a streamlined design approach for optimal droop gains is presented, to achieve minimum power losses for an MEA DC microgrid while relying only on knowledge of the local converter power losses model. Additionally, a simplified, but sufficiently accurate, converter losses model is proposed to help in the optimal droop gains design.

4. A new approach is presented here for optimal droop gain design in a DC microgrid, using an Artificial Neural Network (ANN) to achieve multiple-objectives, such as minimum system losses, improved voltage regulation, and current sharing of power converters. The inputs of the ANN are the normalized power system losses, DC bus voltage regulation, and current sharing while the outputs are optimal droop gains.

5. Due to the increase of electrical loads onboard an MEA, the EPS is becoming more and more complex. Therefore, there is a need to develop a control strategy to manage the overall energy flow and ensure the operation of safety-critical loads under different operating scenarios considering system losses minimization (maximum efficiency), exploiting the thermal capability of generators, using variable load priorities, and battery charging and discharging schedules. This thesis presents an EM strategy based on an optimal droop gain approach to minimize the total system losses for MEA applications taking into account the aforementioned optimized objectives. The Finite State Machine (FSM) structure has been chosen to implement the control strategy to realize the EPS reconfiguration operation.

Throughout the thesis, the technical results and time-domain simulations are supported by Matlab/Simulink based models and validated by experimental work on small-scaled rigs.

Claims and Novelty

In this thesis:

1. The control design process for an enhanced FW control method for the S/G system is introduced. The designed controllers (PI-based) can ensure stable operation of the S/G system throughout the speed and load ranges.

2. A novel battery control scheme is proposed with the strategy to cover the concept of four functionalities: battery current, DC power, DC bus voltage, and battery voltage control. A detailed analysis of the proposed approach, control challenges, and the corresponding solutions is presented.

3. A streamlined optimal droop gain design method for DC microgrid to minimize total system losses including power converters and transmission lines losses is proposed. The optimal droop gain is obtained for different load types. Additionally, a simplified, but sufficiently accurate, converter losses model is proposed to help in the design process.

4. A new approach is presented for multi-objective optimal droop gain design in a DC microgrid, using an ANN to achieve minimum system losses, improved voltage regulation, and the current sharing of power converters.

5. An energy management strategy is proposed, to ensure that the critical loads are supplied under different circumstances e.g. emergency scenario. The optimal droop gain approach is used as a power-sharing method between sources to minimize the total system losses for MEA during flight. The EM strategy takes into account the system losses minimization (maximum efficiency), exploiting the thermal capability

of generators, using variable load priorities and battery charging and discharging schedules.

Acknowledgements

Firstly, I am grateful to be funded by the Egyptian Government ministry of higher education (cultural affairs and missions sector) and the British Council through Newton-Mosharafa program throughout my Ph.D. studies.

I would like to express my gratitude to my supervisors Prof. Serhiy Bozhko, Dr. Mohamed Rashed, Dr. Jason Atkin, and Dr. Seang Yeoh for their guidance and technical support. Furthermore, I would like to thank Prof. Serhiy Bozhko for his mentorship and availability during the whole project period. I would like to thank Dr. Mohamed Rashed and Dr. Seang Yeoh for his help to explore the laboratory and the useful discussions and all other members of the ATC Laboratory, Dr. Quanxue Guan and Mr. Xiaoyu Lang.

Also, thanks to Dr. Christian Klumpner for reviewing my annual reports and giving me valuable suggestions on my topic. Moreover, special thanks are given to Prof. Martin Foster and Dr. Christian Klumpner for sparing their time to be my examiners.

A million thanks to my friends and colleague, especially to Dr. Reda Felfel, Dr. Fathy Aboshady, Mr. Habibu Hussaini, Mr. Ahmed Hebala, Mr. Ahmed Diab, and Mr. Mustafa Ahmed. Over the years, I have learned many things from them, and hopefully they too from me.

I would like to express my heartfelt appreciation to my mum, the memory of my dad, sisters, brothers, my father in law, and my mother in law for their love. Last but not least, I would like to thank my wife Samar for her love, continuous support and encouragement.

Special mentions to Dr. Bob (Dr. Ponggorn Kulsangcharoen), Dr. Sharmila Sumsurooah for their technical and emotional support. My Ph.D. experience has been enhanced by getting to work and know them.

There is also my appreciation to Dr. Mohsen Khalaf for convincing me to pursue my Ph.D.

Moses said: Who are the most knowledgeable of your servants? Allah said: A scholar who is unsatisfied with his knowledge and adds the knowledge of people to his own.

Contents

1 Introduction **1**

1.1 Background 1

1.1.1 Overview of Existing Aircraft Power Systems 2

1.1.2 The More Electric Aircraft 3

1.2 Challenges of moving Towards the MEA 6

1.2.1 Power Electronics 6

1.2.2 Electrical Machines 7

1.2.3 Power Systems 8

1.3 Challenges of Single Bus EPS Topology 9

1.3.1 Increased Diversity of Onboard Sources and Loads 10

1.3.2 Voltage Control 11

1.3.3 Load Sharing 11

1.3.4 System Losses Minimization 11

1.3.5 System Stability 12

1.3.6 Integration of energy storage system 12

1.3.7 Fault Current Protection 12

1.4 Project aims and Objectives 13

1.4.1 Aims 13

1.4.2 Objectives 13

1.5 Thesis Outline 14

2 Electric Power System in the MEA **18**

2.1 Introduction 18

2.2 Power Generation 20

2.2.1 DC Generation 20
2.2.2 Electric Machines 21
2.2.3 Constant Frequency (CF) System 24
2.2.4 Variable Speed Constant Frequency (VSCF) System 26
2.2.5 Variable Speed Variable Frequency (VSVF) System 27
2.2.6 Electric Starter/Generators 28
2.2.7 Energy Storage Systems 31
2.3 Power Distribution and Conversion 32
2.3.1 Power Distribution in Conventional Aircraft 33
2.3.2 Power Distribution in MEA 34
2.3.3 Power Converters for Onboard Microgrids 39
2.4 Utilisation System (Aircraft Electric Loads) 44
2.5 The Load Sharing Methods Used in DC Microgrids 46
2.5.1 Centralised Control Approach 47
2.5.2 Distributed Control Approach 49
2.5.3 Decentralised Control Approach 50
2.6 Energy Management Strategies in Aircraft 54
2.6.1 Implementation of EPS Logic Control 54
2.6.2 Typical Implementation of Energy Management 56
2.7 Single DC Bus-based Multiple−Sources Multiple-Loads EPS Topology and Challenges 56
2.8 Conclusion on Chapter 2 59

3 Single Bus EPS topology with Integrated Batteries 60
3.1 Introduction 60
3.2 The EPS Under Study Description 61
3.2.1 Operation Scenarios 63
3.3 Load Analysis of Aircraft EPS (case study, flying Crane Aircraft) 64
3.4 Sizing of the Major sub-systems 65
3.4.1 Sizing of The Main Generators 66
3.4.2 Sizing of the Auxiliary Power Unit 67

3.4.3 Sizing of the Batteries 67
3.5 Conclusions on Chapter 3 71

4 Enhanced Starting Control Scheme for PMM−based Starter/Generator System 72

4.1 Introduction 73
4.2 Electric Power System Analysis 74
4.3 S/G System Capabilities and Limitations 76
4.4 Analysis of Variable Voltage Bus Method 78
4.4.1 Limitations of VVB Method 80
4.5 Proposed Control Scheme 82
4.5.1 Small Signal Analysis 83
4.6 Design of Proposed Controllers 84
4.6.1 Design of Current Controller for Starter Mode 84
4.6.2 Speed Controller Design 87
4.7 Controller Design using the VVB Method 87
4.8 Simulation Results 88
4.9 Experimental Validation 96
4.9.1 Results for VVB method 96
4.9.2 Results for Starting Mode using Proposed Method 97
4.9.3 Results for Generating Mode using VVB Method 106
4.10 Conclusion on Chapter 4 109

5 Analysis and design of Multi-function Battery controller 110

5.1 Introduction 111
5.2 Battery Model 114
5.2.1 Parameter Extraction 117
5.3 Battery Power System 117
5.4 Proposed Battery Controller Design 120
5.4.1 Control Scheme 120
5.4.2 Energy Management Strategy 122
5.4.3 Controller Design 123

5.5 Simulation results . . . 128
5.6 Conclusion on Chapter 5 . . . 131

6 Onboard Microgrid Droop Control to Minimize Total Losses 132
6.1 Introduction . . . 132
6.2 Modelling and Analysis of Single DC Bus EPS with i Paralleled Converters 135
6.3 Converter Power losses model . . . 137
6.4 Proposed Method for Analytical Based Optimal Droop Gains Selection . . 140
6.4.1 Optimal Droop Gains for Constant Current Load . . . 141
6.4.2 Optimal Droop Gains for Constant Resistive Load . . . 143
6.4.3 Optimal Droop Gains for Constant Power Load . . . 146
6.4.4 Optimal Droop Gains for Mixed Loads . . . 148
6.5 Validation of The Optimal Droop Gains Design Method . . . 149
6.5.1 Case 1: Different Converter Ratings and Different Efficiencies . . . 151
6.5.2 Case 2: Identical Converter Ratings and Different Efficiencies . . . 152
6.6 Experimental Results . . . 154
6.7 Conclusions on Chapter 6 . . . 160

7 Multi-Objective Droop Gain Design based-on Artificial Neural Network 161
7.1 Introduction . . . 161
7.2 Proposed ANN-based Droop gain Design Approach . . . 166
7.2.1 Procedure for Data Generation . . . 168
7.3 Structure and Training of the ANN . . . 169
7.4 Application and Validation of the Proposed Design Approach . . . 171
7.5 Conclusion . . . 178

8 Energy Management for onboard EPS with Batteries Integration 179
8.1 Introduction . . . 179
8.2 Proposed Energy Management Strategy . . . 181
8.2.1 **Normal scenario** . . . 183
8.2.2 **Both Power Generation Channels Fail and APU is Started Scenario** . . . 185

8.2.3 **One Power Generation Channel Fails and APU Fails Scenario** 187
8.2.4 **One Power Generation Channel Fails and APU is running Scenario** . . . 190
8.2.5 **Both Main Power Generation Channels Fail and APU Fails or not started Scenario (Emergency)** . . . 191
8.2.6 **State Transition** . . . 193
8.3 Simulation Results . . . 195
8.3.1 Normal Scenario . . . 196
8.3.2 One Power Generation Channel Fails and APU is Running/Fails case 199
8.3.3 Both Power Generation Channels Fail and APU is Running/Fails case . . . 203
8.4 Conclusion on Chapter 8 . . . 207

9 Conclusion and Future Work **208**
9.1 Conclusion of this Research . . . 208
9.2 Future Work . . . 212

10 Appendices **214**

A Inverse dqTransformation Convention **215**

B Linearisation approach **216**
B.1 Battery Current controller . . . 216
B.2 Battery Voltage controller . . . 216
B.3 DC Bus Voltage controller . . . 217
B.4 q-axis Current Controller (W_{cq}) . . . 217
B.5 Optimal Droop Gains for Constant Power Load Case . . . 217

C Experimental setup **218**
C.1 Experimental setup for S/G system . . . 218
C.1.1 AC Drive System (PMM Side) . . . 219
C.1.2 AC Drive System (IM Side) . . . 222
C.2 Experimental setup for optimal droop gains design . . . 225

D Simulation Models **228**

E Publication List **242**

E.1 Conference Papers 242

E.2 Journal Papers 243

E.3 Journal Papers under Review 243

List of Figures

1.1 Power sources distribution in conventional aircraft [3] 2
1.2 Power sources distribution of MEA [3] 4
1.3 Single Bus EPS architecture 10
1.4 Simplified single DC bus EPS with the thesis chapters 17

2.1 Evolution of electrical system for aircraft [5] 19
2.2 DC voltage regulator [5] 21
2.3 Comparison of IM, PM, and SR machines at different power levels designed for a rated speed in the neighbourhood of 10,000 rpm [25] 22
2.4 Cross section of a typical SRM (left), IM (middle), and PMM (right) [27] . 22
2.5 Constant frequency integrated drive generator system. 25
2.6 VSCF system using a DC link. 26
2.7 VSCF system using a AC/AC direct frequency converter 26
2.8 A variable frequency generation system (with AC distribution) 27
2.9 A variable frequency generation system (with DC distribution) 28
2.10 General starting sequence of a turbo-jet engine [35] 29
2.11 Torque-speed characteristic of the starter/generator [1] 30
2.12 Electric starter/generator system [35] 30
2.13 Comparison between the power distribution of conventional aircraft and the MEA [7] 33
2.14 Conventional B767 aircraft power distribution system [43] 34
2.15 Power distribution system in a modern aircraft B787 [5] 34
2.16 A380 AC electrical power architecture [5] 35
2.17 A380 DC electrical power architecture [5] 36

2.18 The MOET large aircraft electrical power system [52] 37
2.19 Power electronics converter classification tree [53] 39
2.20 Structure of the two-level voltage source inverter [55] 40
2.21 Grid-connection of a three-phase 3L-NPC VSI with an L-type filter [57] . . 41
2.22 Eighteen-pulse rectifier transformer system [58] 41
2.23 A common three-phase to three-phase direct matrix converter configuration [62] 42
2.24 Schematic diagram of indirect matrix converter [63] 43
2.25 Onboard motor applications and their functions [5] 45
2.26 Operating principles of centralized control in DC EPS [69] 47
2.27 Hierarchical control of DC MGs 48
2.28 Operating principles of distributed control in DC EPS [69] 49
2.29 Operating principles of decentralised control in DC EPS [69] 51
2.30 Operation modes and basic principle of the DBS approach. (a) Utility dominating mode. (b) Storage dominating mode. (c) Generation dominating mode. (d) Basic principle of the DBS approach [69] 51
2.31 Single Bus EPS architecture 57

3.1 Single Bus Power System architecture [53] 62
3.2 Layout of power distribution system 63
3.3 820 Lithium-ion battery system connected in series/parallel 69

4.1 S/G system based on PMM feed by AFE topology 75
4.2 Voltage and current limit circles @ $|V_{max}|$=50V, left: Normal circles and right: Zoom in of circles 77
4.3 (a) WIPS integration in current MEA EPS architectures. (b) Proposed integration [100] 78
4.4 Variable Voltage Bus control strategy of PMM [100] 79
4.5 Time response of VVB control scheme in the starter mode: a) Speed, b) *dq* currents, c) Voltage magnitude, and d) *dq* voltages 81
4.6 The overall proposed system control block diagram 83

4.7 Pole zero movement for starter mode: (a) speed increment at 760, 800, and 900 rpm at no load (b) load increment at 25, 50 and 100 % of rated torque at 900 rpm 85
4.8 Frequency response of closed-loop plant at speed 760rpm and 25% loading for starter mode 86
4.9 Time response for start up mode from standstill to 900 rpm using the proposed method: a) Speed, b) *dq* currents, c) Voltage magnitude, and d) *dq* voltage references sent to PWM modulator 88
4.10 Simulation results of starter mode with speed change from 600 to 900 rpm, using the proposed method: a) Speed, b) *dq* currents, c) Voltage magnitude, and c) Modulation index 90
4.11 Simulation results of starter mode with speed change from 600 to 900 rpm using the proposed method: a) *dq* voltages references sent to PWM modulator, b) DC current, c) DC bus voltage, d) AC currents 91
4.12 Simulation results of starter mode in FW with load change from 2 to 3 N.m at 800 rpm: a) Speed, b) *dq* currents, c) Voltage magnitude, and d) Modulation index 92
4.13 Simulation results of starter mode in FW with load change from 2 to 3 N.m at 800 rpm: a) *dq* voltages references sent to PWM modulator, b) DC current, c) DC bus voltage, and d) AC currents 93
4.14 Simulation results of generation mode in FW with i_q^*=-2 A at 1000 rpm: a) Speed, b) *dq* currents, c) Voltage magnitude, and d) Modulation index . 94
4.15 Simulation results of generation mode in FW with i_q^*=-2 A at 1000 rpm: a) *dq* voltages references sent to PWM modulator, b) DC current, c) DC bus voltage, and d) AC currents 95
4.16 Layout of the experimental rig 97
4.17 Experimental results of speed changes from 600 to 800 rpm using VVB method: a) Speed, b) *dq* currents, c) Voltage magnitude, and d) *dq* voltages references sent to PWM modulator. 98

4.18 Experimental results of start-up mode using proposed method from standstill to 900 rpm for the test bench AC drive system: a) Speed, b) Electromagnetic torque c) dq currents, d) Voltage magnitude, and e) dq voltages references sent to PWM modulator. 99
4.19 Experimental results of speed changes from 600 to 900 rpm using the proposed method: a) Speed, b) dq currents, c) Voltage magnitude, and d) Modulation index 100
4.20 Experimental results of speed change from 600 to 900 rpm using the proposed method: a) dq voltages references sent to PWM modulator, b) DC current, c) DC bus voltage, d) AC currents 101
4.21 Experimental results of speed changes from 800 to 900 rpm using the proposed method: a) Speed, b) dq currents, c) Voltage magnitude, and d) Modulation index 102
4.22 Experimental results of speed changes from 800 to 900 rpm using the proposed method: a) dq voltages references sent to PWM modulator, b) DC current, c) DC bus voltage, d) AC currents 103
4.23 Experimental results of i_q^* changes from 2 to 3 A at 800 rpm using proposed method: a) Speed, b) dq currents, c) Voltage magnitude, and d) Modulation index 104
4.24 Experimental results of i_q^* changes from 2 to 3 A at 800 rpm using the proposed method: a) dq voltages references sent to PWM modulator, b) DC current, c) DC bus voltage, d) AC currents 105
4.25 Experimental results of steady state values for generating mode at speed 1000 rpm: a) Speed, b) dq currents, c) Voltage magnitude, and d) Modulation index 106
4.26 Experimental results of steady state values for generating mode at speed 1000 rpm: a) dq voltages references sent to PWM modulator, b) DC current, c) DC bus voltage, d) AC currents 107

5.1 Charging and discharging processes of Li-ion battery [111] 111
5.2 A Li-ion battery model (Includes the additional polarization term) [127] . . 115

5.3 Discharge characteristics of A123's Nano phosphate lithium iron phosphate cell using parameters extraction 115
5.4 Electric circuit of bidirectional DC-DC converter interfacing the battery to the aircraft DC bus 118
5.5 Change of inductor i_L current with respect to duty cycle D 120
5.6 Proposed battery controller with their associated control plants 121
5.7 Energy management strategy 123
5.8 Poles/zeros map of the linearized plant (5.21) 124
5.9 Poles/zeros map of the linearized plant (5.22) 125
5.10 Step response of inner and outer control loops 127
5.11 Frequency response of inner and outer control loops 127
5.12 Time response: (a) Generator status, (b) Battery controller switch signal, (c) Battery SOC 128
5.13 Time response: (a) Battery current, (b) Zoom in of battery current, (c) Battery voltage, and (d) Zoom in of battery voltage 129
5.14 Time response: (a) DC voltage, (b) Zoom in of DC voltage, (c) Dc power, and (d) Zoom in of DC power 130

6.1 DC microgrid power system of the system under study 135
6.2 Equivalent circuit of i parallel converter-based DC microgrid of the system under study 136
6.3 Converter efficiency curves with different split ratios 139
6.4 Optimal droop gains for constant current load system at I_L=650 A, a) optimal droop gains, b) Total system losses, c) DC bus voltage, and d) Zoom in of (a) 143
6.5 Optimal droop gains for resistive load system at R_L=0.5Ω a) Optimal droop gains, b) Total system losses, c) DC bus voltage, and d) Zoom-in of (a) . . 146
6.6 Optimized droop gains for constant power load (150 kW) using two converter system a) Optimal droop gains, b) Total system losses, c) DC bus voltage, and d) Zoom in of (a) 148
6.7 Voltage mode droop-controlled converters scheme [136] 150

6.8 Variation of system losses, DC bus voltage, and converters output currents with load current for case (1), (a) system losses, (b) DC bus voltage regulation and (c) Current sharing ratio 152
6.9 Variation of system losses, DC bus voltage, and converters output currents with load current for case (2). (a) System losses, (b) DC bus voltage regulation, and (c) Current sharing ratio 153
6.10 Experimental setup 154
6.11 Experimental results with 40 Ω CIL using the conventional design approach 156
6.12 Experimental results with 40 Ω CIL using the proposed design approach . 157
6.13 Experimental results with 40 Ω CIL and CPL with conventional design approach 158
6.14 Experimental results with 40 Ω CIL and CPL with proposed design approach 159

7.1 The trad off between different optimisation objectives 162
7.2 Schematic diagram of a Biological neuron 163
7.3 Schematic diagram of the perceptron 164
7.4 Supervised learning of ANN [154] 164
7.5 Unsupervised learning of ANN [154] 165
7.6 Reinforcement learning of ANN [154] 166
7.7 Flowchart for the design of the droop gain using ANN method 167
7.8 Structure of the three-layer FFNN which serves as a surrogate model of the MEA EPS model shown in Fig. 6.1 170
7.9 Variation of droop gains with load current for test 1 172
7.10 Variation of sources currents with load current change using proposed method for test 1 172
7.11 Variation of sources currents with load current change using conventional method [80] 173
7.12 Variation of current sharing with load current for test 1 173
7.13 Variation of system losses with load current for test 1 174
7.14 Variation of DC bus voltage with load current for test 1 174
7.15 Variation of droop gains with load current for test 2 175

7.16 Variation of sources currents with load current change using proposed method for test 2 . . . 175
7.17 Variation of current sharing with load current for test 2 . . . 176
7.18 Variation of system losses with load current for test 2 . . . 176
7.19 Variation of DC bus voltage with load current for test 2 . . . 177

8.1 Single Bus EPS architecture . . . 180
8.2 Example of reactive system . . . 182
8.3 ST1 illustration on simplified EPS . . . 185
8.4 ST2 illustration on simplified EPS . . . 185
8.5 ST3 illustration on simplified EPS . . . 186
8.6 ST4 illustration on simplified EPS . . . 187
8.7 ST5 illustration on simplified EPS . . . 187
8.8 ST6 illustration on simplified EPS . . . 188
8.9 ST7 illustration on simplified EPS . . . 189
8.10 ST8 illustration on simplified EPS . . . 189
8.11 ST9 illustration on simplified EPS . . . 190
8.12 ST10 illustration on simplified EPS . . . 190
8.13 ST11 illustration on simplified EPS . . . 191
8.14 ST12 illustration on simplified EPS . . . 192
8.15 Power distribution state diagram . . . 192
8.16 Simulation results under normal flight scenario . . . 197
8.17 Switching states, reference battery voltage, APU signal and overload signal under normal flight scenario . . . 198
8.18 Total system energy losses under normal scenario . . . 199
8.19 Simulation results under one of power generation channel failure scenario . 200
8.20 Switching states, reference battery voltage, APU signal and overload signal under one of power generation channels failure scenario . . . 201
8.21 Total system energy losses under one of power generation channel failure scenario . . . 202
8.22 Simulation results under both of power generation channel failure scenario 204

8.23 Switching states, reference battery voltage, APU signal and overload signal under both of power generation channels failure scenario 205
8.24 Total system energy losses under both of power generation channel failure scenario 206

C.1 Layout diagram for the experimental rig of S/G system. 219
C.2 Parker ME series PMM. 220
C.3 SEMIKUBE power stack. (a) Prototype. (b) Schematic. (c) IGBT modules prototype. (d) IGBT modules schematic. 221
C.4 The interface board. 222
C.5 Control platform. 222
C.6 Sensor board. (a) Voltage sensor. (b) Current sensor 223
C.7 VASCAT induction machine 223
C.8 Mitsubishi AC drive with protection circuit 224
C.9 Layout diagram for the experimental rig of parallel operation of two sources 225
C.10 Control platform 226
C.11 Programmable AC source 227
C.12 Electronic load 227

D.1 Battery multifunction controller consisting of battery pack, bidirectional DC-DC converter, DC bus, battery controller and energy management. . . 228
D.2 Battery controller. 229
D.3 Energy management. 230
D.4 S/G power system consisting of PMM, AFE, DC bus,Transmission line and DC grid (for generation mode only). 230
D.5 Controller. 231
D.6 PWM genration. 231
D.7 Optimal droop gain design using ANN. 232
D.8 Controller for AFE converter. 232
D.9 Overall EM strategy Simulink model. 233
D.10 EM strategy. 233
D.11 Energy load management centres. 234

D.12 System losses calculation. 235
D.13 Onboard loads. 236

List of Tables

1.1 Power generation capability in the existing aircrafts [6] 5

2.1 Summary of trade-off comparison between different machines as S/G [35]. . 25
2.2 Main features of batteries (based on [50]) 32
2.3 External and Internal lighting systems on aircraft [5] 46
2.4 Comparison among different control approaches 53

3.1 Flying Crane aircraft data 65
3.2 A123's Nano phosphate lithium iron phosphate (LiFePO4) cell datasheet [99] 69

5.1 System under study parameters value 126
5.2 Desired specification of controllers and corresponding gains value 126

6.1 Technical Data for ABB String Inverter [149] 138
6.2 Converters Data and Optimal Droop Gains Values 144
6.3 Electric Power System Parameters 150
6.4 Conventional and Optimal Droop Gains Values 151
6.5 Conventional and Optimal Droop Gains Values for Experimental Tests . . 155
6.6 Measurements with 40 Ω Resistive Loads 155

7.1 Converters Data and Optimal Droop Gains Values 168

8.1 All possible states combinations 184
8.2 Conditions for states transition for the different scenarios 194

8.3 Status of generators, batteries SoC and overloading time during different scenarios 195
8.4 System switches and variables settings 195
8.5 Converters, transmission line data, and optimal droop gains values 196
8.6 Time and numbers of flight phases 196

C.1 Experimental rig PMM parameters 220
C.2 Induction machine parameters 224
C.3 Parameters of the lap prototype 226

Nomenclature

ΔV_{max}	Maximum allowable voltage degradation (V)
η_{cablei}	Effeciency of i^{th} cable (H)
η	Battery efficiency (%)
η_n	Nominal converter efficiency (%)
$\int idt$	Actual battery charge (Ah)
λ	Lagrange multiplier
ω_b	Base speed of the machine (rad/sec)
ω_e	Electrical speed of the machine (rad/sec)
ω_m	Mechanical speed of the machine (rad/sec)
ω_m^*	Reference mechanical speed of the machine (rad/sec)
ϕ_m	Machine flux (Wb)
θ_m	Mechanical angle (^{o})
A	Exponential zone amplitude (V)
B	Exponential zone time constant inverse $(\text{Ah})^{-1}$
C_B	Total capacity of all the batteries (Ah)
C_b	Battery capacitor (F)
C_{dcb}	DC bus capacitor (F)
d_1	Duty cycle of switch Q_1
E_o	Battery constant voltage (V)
E_{min}	Minimum energy required by the battery (Wh)
g	Constraints functions
i	Battery current (A)
i^*	Filtered battery current (A)
I_c	Converter output DC current (A)

i_d^*	d-axis refernce current (A)
I_L	Load current (A)
i_q^*	q-axis refrence current (A)
I_r	Machine rated current (A)
I_s	Stator current vector magnitude (A)
I_{ci}	Output current of i^{th} converter (A)
$i_{d,q}$	PMM stator currents (A)
i_{dc}	DC side current (A)
i_{dc}^*	Reference DC side current (A)
I_{smax}	Maximal phase current of PMM (A)
K	Polarisation voltage (V/Ah)
k_{id}	d-axis integral gain
k_{iq}	q-axis integral gain
k_{pd}	d-axis proportional gain
k_{pq}	q-axis proportional gain
L	Inductance of the converter inductor (H)
$L_1 - L_5$	Line inductance (H)
$L_{d,q}$	PMM stator inductances in dq frame (H)
p	Number of pair poles
P_B	Total load requirement from the battery to be supplied (kW)
P_n	Nominal output power (W)
P_{losses}	Converter losses (W)
P_{noload}	Converter no load losses (W)
Q	Maximum battery capacity (Ah)
Q_{exp}	End of exponential zone battery capacity (Ah)
Q_{nom}	End of nominal zone battery capacity (Ah)
R_b	Internal resistance of battery (Ω)
R_L	Equivalent resistance of inductor (Ω)
R_l	Load resistance (Ω)
R_s	Stator resistance (Ω)
R_{ci}	Transmission line resistance of i^{th} converter (Ω)

R_{di-opt}	Optimal droop gain of i^{th} converter (Ω)
R_{di}	Virtual resistance of i^{th} converter (Ω)
R_{dt}	The total global droop gain (Ω)
R_{eq}	Sum of battery and inductor resistances (Ω)
R_{es}	Equivalent series resistance (Ω)
S_r	Split ratio (%)
SOC_{max}	Maximum state of charge (%)
SOC_{min}	Minimum state of charge (%)
t	Time in minutes
$t_1 - t_5$	Time constant of converter (sec)
V_B	Terminal battery voltage (V)
V_b	Battery capacitor voltage (V)
V_c	Stator voltage vector magnitude (V)
v_d^*	d-axis refernce voltage (V)
V_o	No load system voltage
v_q^*	q-axis refrence voltage (V)
V_{cmax}	Inverter maximum phase voltage limit at the fundamental frequency (V)
$v_{d,q}$	PMM stator voltages (V)
V_{dcb}	Battery DC bus voltage (V)
V_{DCi}^{ref}	reference output voltage of i^{th}converter (V)
V_{dcr}	Rated DC bus voltage (V)
V_{dc}	S/G DC bus voltage (V)
v_{desti}	Estimated d-axis voltage (V)
V_{exp}	End of Exponential zone battery voltage (Ah)
V_g	DC grid voltage (V)
V_{nom}	End of nominal battery zone voltage (V)
V_{oi}	No-load output voltage of i^{th} converter (V)
W_b	Battery voltage controller
W_c	Battery current controller
W_p	Battery power controller
W_v	Battery DC bus voltage controller

W_{cd}	d-axis current controller
W_{cq}	q-axis current controller
W_{dc}	DC bus current controller
${V_{dcb}}^*$	Reference voltage of converter (V)

Abbreviations

ADRC	Active disturbance rejection control
AFE	Active front end
AEA	All electric aircraft
AC	Alternating current
AI	Artificial intelligence
ANN	Artificial neural network
ATRU	Automatic transformer rectifier unit
APU	Auxiliary power unit
BT	Back tracing
BCRU	Battery charge regulator unit
BBCU	Buck-boost converter unit
BTB	Bus-tie breaker
VLIPS	C language integrated production system
CC	Constant current
CCL	Constant current load
CCCV	Constant current-constant voltage
CF	Constant frequency
CIL	Constant impedance load
CPL	Constant power load
CSD	Constant speed drive

CV	Constant-voltage
DoD	Depth of discharge
DCL	Digital communication link
DSP	Digital signal processor
DC	Direct current
DPS	Distributed power system
ELM	Electric load management
ELMC	Electric load management centres
EPS	Electric power system
EHA	Electro-hydraulic actuator
EMF	Electromagnetic force
EMI	Electromagnetic interference
EMA	Electro-mechanical actuators
EM	Energy management
EMC	Energy management centre
ESS	Energy storage system
ECS	Environment control system
ESR	Equivalent series resistance
EEPDC	Essential electrical power distribution centre
ETOPS	Extended range twin-engine operations performance standards
FFNN	Feed Forward Neural Network
FPGA	Field programmable gate array
FSM	Finite state machine
FW	Flux weakening
GaN	Gallium nitride
GCU	Generator control unit

HP	High pressure
HPL	High priority load
HVA	High voltage AC
HVDC	High voltage DC
IM	Induction machine
IGBT	insulated-gate bipolar transistor
IDG	Integrated drive generator
LRU	Line replaceable unit
LTL	Linear temporal logic
Li-ion	Lithium ion
LC	Local controller
LP	Low pressure
LPL	Low priority load
MPL	Medium priority load
MINLP	Mixed-integer non-linear programming
MIQP	Mixed-integer quadratic problem
MEA	More electric aircraft
MOET	More Open Electrical Technology
MSCC	Multi-stage constant current
NPC	Neutral point clamped
Ni-cd	Nickel cadmium
OEM	Original equipment manufacturer
OCP	Overcurrent protection
OPP	Overpower protection
OTP	Overtemperature protection
OVP	Overvoltage protection

PMM	Permanent magnet machine
PC	Power Converter
PLC	Power line communication
PLS	Power line signalling
PEPDC	Primary electrical power distribution centre
RAT	Ram air turbine
RU	Rectifier unit
RHP	Right half plane
RMS	Root mean square
SiC	Silicon carbide
ACR-VAC	Single current regulator and voltage angle control
SVPWM	Space vector pulse width modulation
S/G	Starter/generator
SoC	State of charge
SMPMSM	Surface mounted permanent magnet synchronous machine
SRM	Switched reluctance machines
TLR	Transmission line resistance
VRLA	Valve regulated lead acid
VF	Variable frequency
VSCF	Variable speed constant frequency
VSVF	Variable speed variable frequency
VVB	Variable voltage bus
VWB	Variable wild bus
WBG	Wide band gape
WIPS	Wing ice protection system

Chapter 1

Introduction

1.1 Background

In recent years, aircraft have been widely accepted as a convenient way of travel, allowing long-distance, high-speed travel, and in some cases, becoming a fuel-efficient mode of transportation. Global aviation traffic is growing at a phenomenal rate to cope with the increase of passengers and cargo demand. By 2030, it is estimated that there will be approximately 27,000 new aircraft in the air [1]. This is an industry that is vital to today's international society. It connects different cultures and achieves strong annual economic growth worth US$452 billion globally [1]. Nevertheless, this growth leads to environmental and climate impacts beyond the questions of how to manage fuel consumption and emissions. In comparison to other types of travel, aircraft are relatively noisy. The future aerospace industry needs to provide more flights, operate more efficiently, and increase the respect for the environment in which it develops, whilst remaining competitive. One of the main threats facing the aerospace industry is that if future emissions are not reduced, the industry may be subject to severe penalties, which will drive up ticket prices and reduce the competitiveness in comparison to other types of transport such as railways, etc. Due to threats to the quality of life and even the survival of future generations, improved energy efficiency, lower CO2 and NOx emissions, and low audible noise produced by aircraft have become key issues that need to be addressed.

Based on this background, there is a need to develop a more fuel-efficient and sustainable aircraft. One of the most promising solutions to tackle these challenges is

moving to More Electric Aircraft (MEA) and All Electric Aircraft (AEA) concepts. The MEA concept aims to replace traditional pneumatic, mechanical, hydraulic power sources, and loads with electrical ones. By adopting the MEA concept, the efficiency and dispatch reliability are increased as well as decreasing the operating and maintenance costs of aircraft due to elimination of the maintenance-intensive bleed system [2].

1.1.1 Overview of Existing Aircraft Power Systems

In order to compare conventional aircraft and MEAs, it makes sense to first introduce the conventional aircraft systems. Commonly, in a conventional aircraft, there are two types of energy sources primary and secondary. The primary source is the aircraft engines while the secondary sources are electrical, hydraulic, pneumatic, and mechanical systems powered by the primary sources. Fig. 1.1 shows the distribution of conventional aircraft power sources consisting of pneumatic, hydraulic, mechanical, and electrical sources. Pneumatic power is used to supply the Environment Control System (ECS) and supply hot air to the Wings Ice Protection System (WIPS). WIPS has two modes of operation: Anti-icing and De-icing. Anti-icing mode is a preventative mode and is activated before

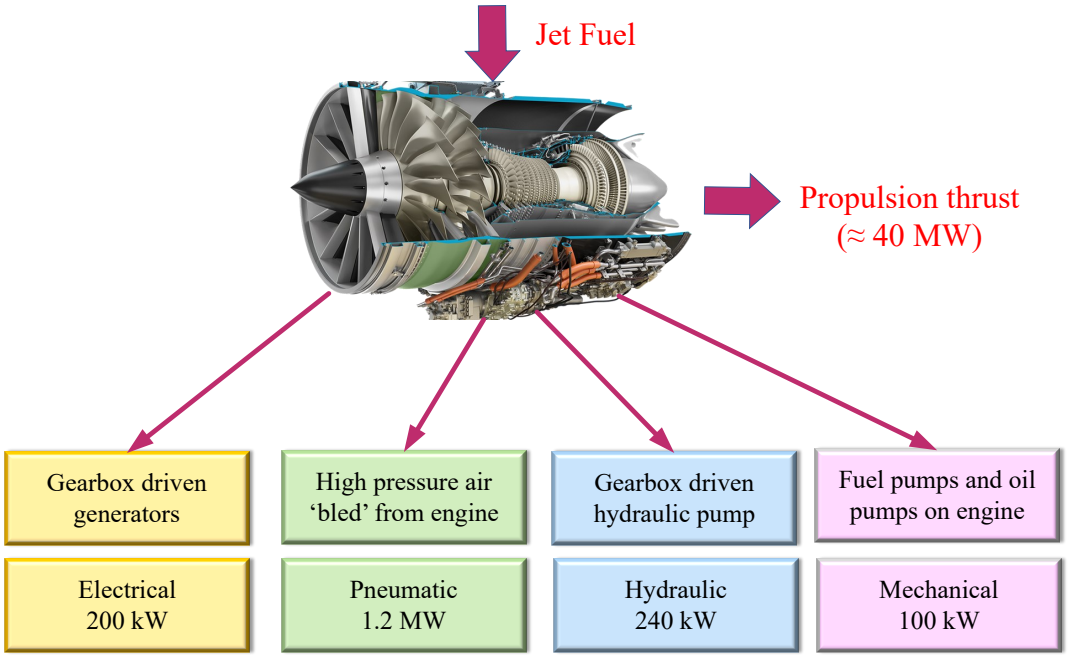

Fig. 1.1: Power sources distribution in conventional aircraft [3]

the flight enters icing conditions, while the de-icing mode is a reactive mode and is used after ice has been accumulated. Pneumatic power suffers from low efficiency and a difficulty in detecting leaks [4].

Hydraulic power is required for primary and secondary flight control and for the landing gear (deployment, reaction, and braking). It is transferred from the central hydraulic pump to the actuation systems. The hydraulic systems are very robust and have a very high power density. However, rigid infrastructure and the possibility of dangerous and corrosive liquids leakage are the main disadvantages [1].

Mechanical power is transferred from the engines to central hydraulic pumps, to local pumps for engine equipment and other mechanically driven subsystems, and the main electrical generator through the gearbox. The drawbacks of the mechanical system are the use of a heavy gearbox and its associated maintenance cost [1].

Electrical power in the aircraft is generated by the gearbox-driven generators and distributed throughout the aircraft for use by avionics, cabin electronics, utility actuators, lighting, and galleys. The electrical power represents a small amount/value among all power sources in conventional aircraft as shown in Fig. 1.1.

Compared with the shortcomings of pneumatic, hydraulic, and mechanical power, the electrical power system has many outstanding advantages such as high efficiency, low maintenance, good controllability, and advanced diagnostics. Because of the advantages mentioned above, the use of more electrical power has become an unavoidable trend. The concept of a "MEA" which aims to increase the penetration rate of electrical power in aircraft systems was proposed and has become the main trend in modern aerospace engineering. However, MEA is heavier in general with the technologies we have today and higher electrical power demand challenges the cooling and dynamic control of power generations and conversions.

1.1.2 The More Electric Aircraft

A key aspect of the MEA concept is that the non-propulsive power such as mechanical, hydraulic, and pneumatic can be replaced by electrical equivalents. Fig. 1.2 illustrates the concept of the MEA where many devices, such as electric pumps, electric heaters, electrically driven air compressors, etc, are driven by electricity. Consequently, the

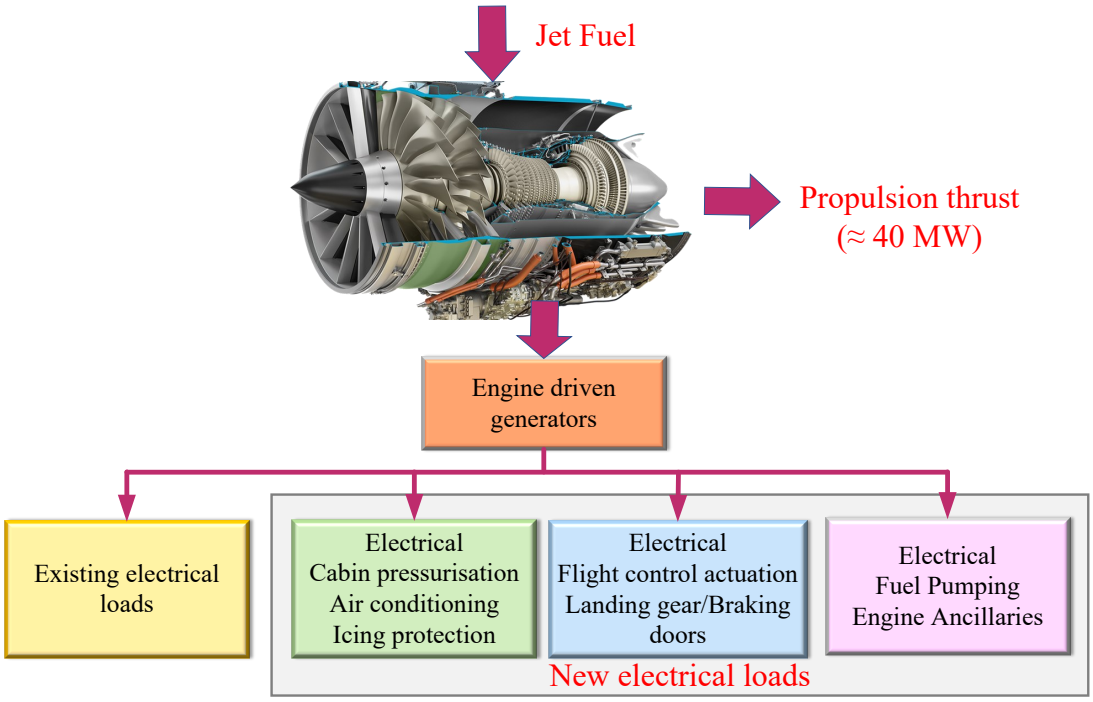

Fig. 1.2: Power sources distribution of MEA [3]

pneumatic system and the mechanical system in conventional aircraft can be replaced by electrical power systems. Beyond the above, conventional hydraulic actuators could be modified to become Electro-Hydraulic Actuators (EHA), which involves using electric power as the main power to drive hydraulics and remove the pipes and weight associated to the hydraulic power distribution system. In the future, hydraulics could be eliminated through the use of Electro-Mechanical Actuators (EMA) [5].

The advantages of MEA over conventional aircraft can be summarized as follows [1]:

1. Elimination of expensive hydraulic and pneumatic systems which are difficult to maintain, and prone to leak. Hence, the weight, cost, and complexity of the system are reduced and reliability and efficiency are improved.

2. One of the core ideas of the MEA is to integrate multiple aircraft functions into one system such as the electrical S/G. The S/G can also be used for aircraft aero-engine starting, which eliminates the need for engine tower shaft and gears, power take-off shaft, accessory gearboxes, and reduces the engine starting power, especially in cold conditions as the engine needs to be preheated to protect it from damage.

3. Using a fan shaft generator as an emergency power source instead of the conventional

inefficient single-shot Ram Air Turbine (RAT) as it is expensive to develop, install and maintain. This in turn enhances the system's reliability and robustness against engine contingency.

In summary, the aerospace industry can be revolutionized by the adoption of MEA. Better maintainability and system reliability can be achieved through significant improvements in terms of weight, cost, and fuel consumption. Nevertheless, the MEA presents several challenges to the aircraft's electrical system, where the amount of onboard power is increased significantly with the electrical loads increasing and the management of that power is required. Table 1.1 lists the onboard electric power generation for the existing aircraft.

Table 1.1: Power generation capability in the existing aircrafts [6]

Aircraft	First year of service	(Approx.) Passenger capacity	Main generators power (excluding APU)
Convair B-36	1949	(Military)	4x30 kVA
Boeing B-52H	1955	(Military)	4x60 kVA
Boeing 707	1958	219	4x30 kVA
Boeing 727	1964	189	3x38 kVA
Vickers VC10	1964	151	4x40 kVA
Boeing 737NG	1968	210	2x90 kVA
Airbus A320	1987	220	2x90 kVA
Boeing 747-800	1988	660	4x90 kVA
Boeing 767-300ER	1988	258	2x90 kVA
Airbus 340	1991	375	4x90 kVA
Airbus A330	1992	335	2x115 kVA
Boeing 777	1994	396	2x120 kVA
Boeing 717	1999	100	2x40 kVA
Boeing 767-400ER	2000	256	2x120 kVA
Airbus A380	2005	853	4x150 kVA
Boeing B787	2011	336	4x250 kVA

Clearly, the capacity of power generation has been increased over the years, for example,

it is over 600 kVA for MEA Airbus A380 and it reached 1 MVA for MEA Boeing B787 (MEA).

1.2 Challenges of moving Towards the MEA

The MEA applications aim to reduce overall weight, maintenance costs, fuel consumption, environmental impact while requiring improved reliability and high power density [7]. Weight is considered one of the main challenges. Many studies have shown that MEA can significantly reduce fuel consumption, but with the technology we have today, MEA technologies are usually heavier. This is because the power density of the power electronics box is low when the weight of the Electromagnetic Interference (EMI) filters represents $25-40\%$. However, continuous improvements in power electronics and related cooling and control will continue to reduce the weight of these electrical components.
Another challenge with MEA is that due to replacing pneumatic and/or hydraulic power with electrical power, the demand for electric power is much higher than the conventional systems. Significantly higher power demands pose challenges for cooling and the dynamic control of power generation and conversion.

From a power system perspective, the new power electronics, new cooling, new control, and new system-level designs pose challenges to the safety, robustness, reliability, stability, and certification of the new MEA. Therefore, this adds enormous challenges to the technology, cost, resource, and schedule risks to MEA development and investment.
This means that all areas of electrical engineering are facing challenges, including power electronics (power equipment, converters), electric machines (electric drives and machine design), and power systems (power system topologies and power management).

1.2.1 Power Electronics

Wide Band Gap (WBG) semiconductor devices, such as Silicon Carbide (SiC) or Gallium nitride (GaN), have become part of the solution to address the weight, volume, and losses reduction issues due to their capability to operate at high temperature (250^{o}C), low losses, and high switching frequency capabilities [8]. WBG devices can be switched faster while the switching energy loss remains low, which means an improvement of

converter efficiency. In addition, it allows a higher switching frequency operation. This leads to smaller and lighter passive elements,i.e. inductors and capacitors, which increases the power density of the conversion unit. The high-temperature capability has the benefit, as it reduces the thermal management requirements of the system. For example, this can lead to the use of a smaller size heat sink or facilitate the use of a high temperature coolant cycle, which already exists in the system, such as combining motor and drive cooling circuits. SiC is particularly attractive in terms of thermal conduction and technological maturity, and GaN will become a low-cost device in the future with comparable performance to existing silicon devices. Compared to classical silicon switching devices, conduction and switching losses are also reduced [9].

The challenges are to keep these converters running and maintain the high performance of power converters (including drivers and sensors) at higher temperatures and reliable fashion. In recent years, a lot of research has been conducted to improve the reliability of power converters. This includes fault-tolerant converters, real-time fault detection, and dynamic reconfiguration of power electronic converters besides the reliability of power switches and drivers. Certainly, all of these techniques will have an impact on the MEA's development of next-generation power converters.

1.2.2 Electrical Machines

Electrical machines are considered one of the key components of the MEA EPS. There are many physical and operational differences between electrical machines which are used in industry and aviation [10]. The most notable difference is the voltage level. In industry, a 230/400 VAC system at 50 or 60 Hz is used. In aviation, 115/200 VAC at 400 Hz or 230/400 V AC at a variable frequency (360 to 900 Hz) and 28 VDC or $\pm$270 VDC is usually used. The selection of the electrical machine depends not only on its size and power but also on its weight. Therefore, the desired characteristics of electrical machines in MEA are high speed, high power density, and high torque density. Higher-speed machines or machines with a higher number of poles are possible by utilizing high switching WBG devices. Integrating high-speed machines offers new opportunities to improve the power density of the entire drive system. To achieve high power density (minimum weight) drive system, the following measures can be included:

- New electric machine topologies
- Machine design by utilizing advanced materials
- Advanced control and manufacturing
- Thermal management

Correspondingly, to improve the torque density of the machine the following ways can be considered:

- Outer rotor configuration
- Unequal wound and unwound tooth width
- High pole number
- Halback magnet arrangement
- High grade soft magnetic material
- Open slot design

Additionally, the operational conditions of machines have to be considered because aircraft machines operate at a very wide range of temperatures and air pressures, hence a sufficient cooling has to be ensured.

1.2.3 Power Systems

The MEA poses more demands on the aircraft electrical power system in terms of power generation and reliability, fault tolerance, power management, and stability of the DC and AC power systems [7]. These require innovations in power generation, distribution, processing, and management systems. At the same time, this trend has increased the challenges of aircraft EPS design [4]. Many architectural models are currently the subject of engineering studies [11]. With a growing number of power electronic loads, an MEA with a classical AC network includes a high number of AC–DC rectifier stages (Automatic Transformer Rectifier Unit (ATRU)). A High Voltage DC (HVDC) network with an optimized association consisting of a generator, an Active

Rectifier Unit (ARU), a filter, and a generator control unit would be the best system solution for mass reduction as it provides the lightest weight, smallest size, highest operational temperature, best safety, lowest cost, best performance, best power switching and overload capabilities [11]. The HVDC network would facilitate direct generator–load coupling without using transformer with possible regenerative load acceptance [12]. The evolution of power generation, distribution, and the utilization system will be overviewed in detail in Chapter 2. HVDC power distribution systems are used in a variety of applications, hence, different architectures have been proposed, for instance, single bus, multibus, and ring bus configurations. Fig. 1.3 shows the single bus EPS architecture which is considered one of the promising candidates for future MEA. Twin engine-driven generators provide the electrical power to the single DC bus through Active Front End (AFE) converters. This architecture will be discussed in detail in Chapter 3.

To achieve high power quality, good dynamic performance, appropriate power-sharing among sources, and stability in the existence of non-linear loads for single bus topologies , relevant technologies such as power electronic converters including WBG and new types of machines which include increased fault tolerance will need to be developed.

1.3 Challenges of Single Bus EPS Topology

Parallel energy sources are used to increase the power system redundancy[13]. However, a single bus HVDC EPS architecture poses challenges for the power system designer which are as follows:

1. Increased diversity of onboard loads and sources
2. DC bus voltage control
3. Load sharing among parallel sources
4. System losses minimization
5. System stability
6. Integration of energy storage systems
7. Fault Current Protection

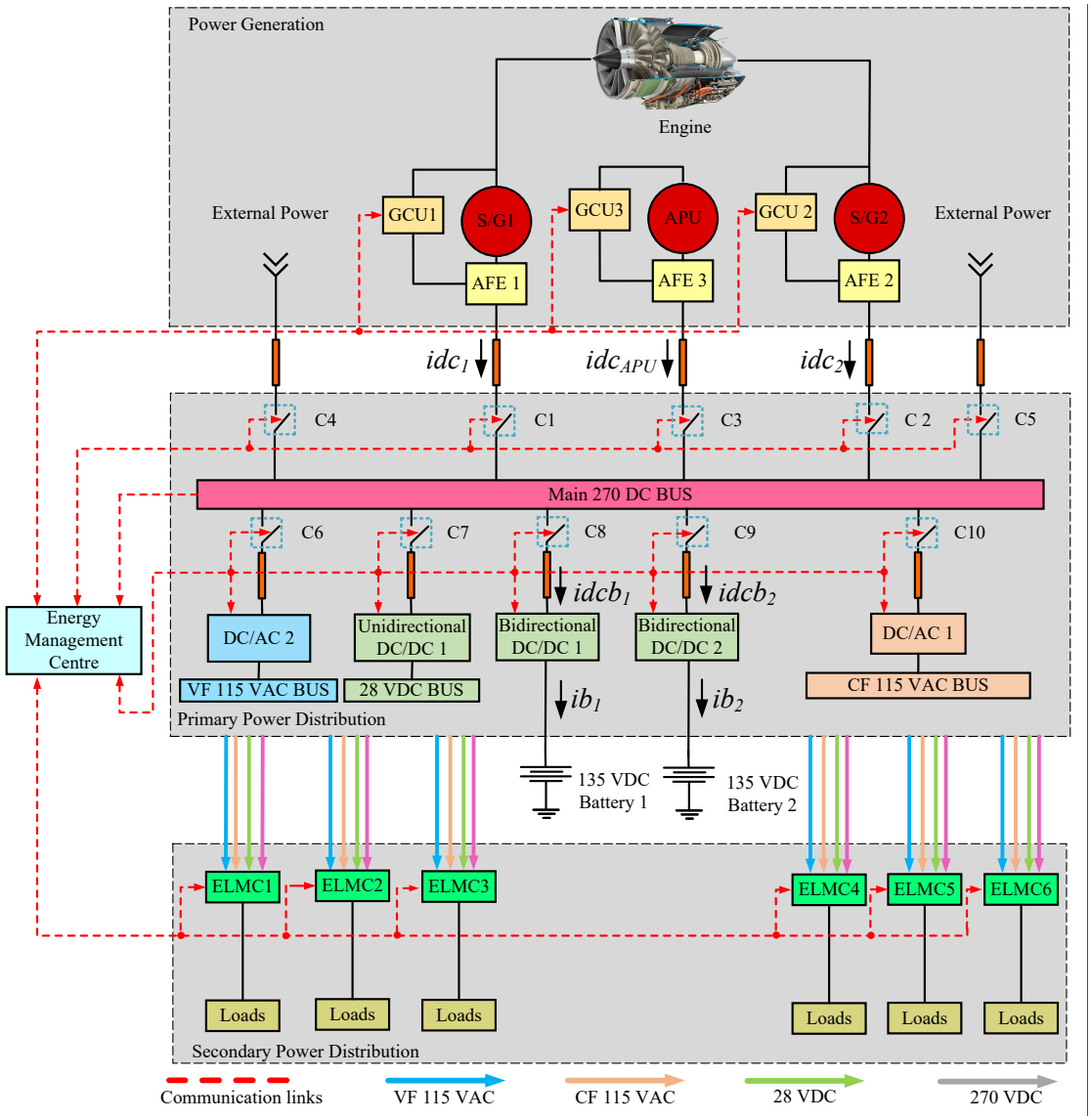

Fig. 1.3: Single Bus EPS architecture

1.3.1 Increased Diversity of Onboard Sources and Loads

Due to the substantial increases in the numbers and diversity of onboard sources and loads of an MEA EPS, the EPS is becoming more and more complex. This means there is a need to optimize and manage the aircraft's EPS to increase the system efficiency. The optimization of EPS can be either done at the preliminary design stages or via control optimization to make the best use of the connected devices.

1.3.2 Voltage Control

For systems based on a single power source, only one power source is controlling the bus voltage. While in the case of multiple power sources and multiple converters working in parallel, at least one converter is responsible for regulating the DC bus voltage, and all other converters will operate in active power control mode. Ideally, after shutting down one or more converters, the remaining converters should share the resulting power mismatch in an appropriate proportion. Therefore, it is beneficial for all converters to operate in the DC link voltage control mode rather than trying to strictly follow their respective active power references. However, the set value of the DC bus voltage reference in all converters may conflict, unless they are correctly modified according to the reference value and actual value of the active power and DC bus voltage.

As a result, most parallel power supplies must be involved in controlling the DC bus voltage, which means that coordinated voltage control is required between all power sources.

1.3.3 Load Sharing

Parallel energy sources are expected to share the load power demand according to the rated power ratio. In this type of multi-source and multi-load energy system, it is important to carry out proper load-sharing according to the capacity of the power source. The details about the load-sharing methods will be discussed in Chapter 2.

1.3.4 System Losses Minimization

To improve energy efficiency, the operation loss including the distribution loss and converter loss should be minimized [14], [15]. Distribution losses depend on the voltage level, the load power, and the length of the cables. The loss of the power electronic converter depends on the number of active converters, the converter topology, the number of active and passive components in the converter, and the duration of power processing [16]. It should be noted that for different power sources and different cables there is a trade-off between achieving equal load-sharing and minimum system losses. Therefore, system losses minimization is a very important challenge to increase the efficiency of

single bus topology and needs to be addressed along with better load-sharing and voltage control.

1.3.5 System Stability

In MEA applications, the electrical loads can be divided into three categories: Constant Current Load (CCL), Constant Impedance Load (CIL), and Constant Power Load (CPL) [17]. CCL draws a fixed current from the source with wide variations in source voltage. For CIL the current intake is proportional linearly to the terminal voltage. Classic heaters can be considered a good example of constant impedance load, with a tendency to be resistive load only. In the case of CPL, the current is adjusted inversely-proportionally with the input voltage to maintain the power delivered to the load constant. A typical example of CPL is a controlled motor drive system [18].

CPLs can lead to undesired destabilization effects, oscillations, and possibly instability due to their negative incremental impedance characteristics. This instability effect not only poses a great threat to the stability of the system but also hinders the optimization of the system, such as reducing the size and weight. Consequently, the instability caused by a CPL is a great challenge for MEA EPS.

1.3.6 Integration of energy storage system

The batteries have several functions in the aircraft e.g. start the APU, boost the low voltage generation by the generators (e.g. to maintain the single DC bus voltage within the steady-state voltage range set by MIL-STD-704F [19]), or meet the emergency load requirement. The integration of the battery system to a single bus DC power distribution network will require bidirectional power flow capability as the battery will be charged and discharged over a period of time. To meet and fulfil the above challenges and the requirements, a multifunction control algorithm can be adopted.

1.3.7 Fault Current Protection

Aside from safety, there is a critical need to quickly identify and locate electrical faults as part of the MEA's development [20]. Fault management devices, which are

especially important for aircraft safety, are one of the most important requirements for MEA technology [21]. A combination of faults can always lead to system failure; hence, the potential faults must be handled or controlled in order to establish a system with predictable and reliable characteristics, which can be enhanced by regular maintenance service [20]. Faults are typically caused by component failures, such as faulty devices and sensor failures, which can distort readings or result in missing sampling. Faults can also be caused by broken or poor connections, weak communication, hardware, or software problems. The design schemes of protection methods in electric system circuits of MEAs is a challenging issue. DC circuit breakers, for example, are more complicated to design and implement than AC circuit breakers since there is no natural zero current that can cut off the current [22].

1.4 Project aims and Objectives

1.4.1 Aims

Following an overview of the potential opportunities and challenges for the possible application of the single bus EPS architecture in the future MEA, this research aims to develop new knowledge regarding optimization of single bus multiple sources topologies by proposing and investigating solutions at the low and high levels of the system. The low-level system measures includes an enhanced S/G control system, proposed multifunction battery controller, and system losses minimization using optimal droop gains design, while high level measures involves a supervision strategy to manage the overall system.

1.4.2 Objectives

The specific objectives that are addressed in this thesis are as follows:

1. Investigation of an enhanced control scheme for the S/G system to cover the entire speed range covering both motoring and generation modes. As the key element towards this objective, the control plant should be investigated and a mathematical model suitable for advanced control design should be developed.

2. Propose a multifunction battery controller with seamless transition between the controllers for future MEA platforms. The battery controller performs different functions, e.g. providing DC power, maintaining DC bus voltage, controlling battery voltage and battery current for charging and discharging process purposes.

3. Review the existing load-sharing methods for DC bus systems and develop a new streamlined load-sharing approach among the multiple parallel sources in the single bus electric power system, to minimize total system losses including power converters and transmission lines losses.

4. Development of a new approach for load-sharing in a single DC bus, using an ANN to achieve multiple optimized objectives, e.g. minimum system losses, improved voltage regulation, and current sharing of power converters.

5. Investigation of a control strategy to manage the overall energy flow and ensure operation of safety-critical loads under different operating scenarios, considering system losses minimization (maximum efficiency), exploiting the thermal capability of generators, using variable load priority and battery charging and discharging schedules.

6. Development of simulation models in support of the aim. These include the plant, the control scheme, and representative loads models at different levels (architectural, functional, and behavioural) for the aforementioned objectives.

7. Construction of scaled prototype test rigs to enable experimental validation for the achieved analytical design results.

1.5 Thesis Outline

Chapter 2 reviews the MEA EPSs, discussing the electrical S/G system and possible electrical machine candidates. The integration of energy storage systems with single DC bus architecture and the aviation requirements for any battery intended for use as a power source onboard aircraft. The paralleling of generation channels supplying the same DC bus is introduced and possible load sharing methods are overviewed. Finally,

the EM strategies goals, implementation of logic control, and typical implementation of EM in today's aircraft are presented.

Chapter 3 deals with the analysis of a single DC bus-based system with battery integration. A detailed description of the system under study and the load analysis of the Flying Crane aircraft EPS which was used as a case study in this research for EM strategy purposes, are presented. All loads are divided into different categories based on their functions, for example, Low Priority Loads (LPLs), Medium Priority Loads (MPLs), and critical/High Priority Loads (HPLs). This load analysis is crucial for the EPS components' sizing. The EPS components include main power generation channels, APU, and batteries system.

Chapter 4 introduces an enhanced control scheme of PMM-based aircraft S/G operated in FW mode covering a wide speed range for motoring mode aligned with the Variable Voltage Bus (VVB) control approach. The S/G system capabilities and limitations are identified beforehand in order to aid with the control design process. Following this, the analysis of the VVB control method is performed and the associated issues are discussed. The linear equations of the entire proposed system are derived for the motoring and generating modes to aid with the design of the controller using linear design methods. The worst-case scenario for starter mode is considered for the design of the FW controller. Following the controller design, time-domain simulations and experiments across the whole starter and generator modes operation are performed to confirm the achieved control performance.

Chapter 5 presents a detailed analysis and design of the multi-function battery controller which is used for the charging/discharging process with seamless transition between controllers. Subsequently, for simulation purposes, a model of the lithium-ion battery and its extraction of related model parameters was proposed. The proposed controller integrates different controllers such as the inductance current of the batteries controller, battery voltage controller, output power controller, and battery DC bus voltage controller. The design specifications required by the controllers are outlined and verified. In addition, due to the complexity of the process of charging and discharging, a robust EM strategy is proposed as well. Finally, the controllers are simulated with different operating scenarios in order to validate the achieved control performance.

Chapter 6 focuses on the optimal droop gains design method to achieve minimum system losses (maximum system efficiency) in DC bus-based multiple-sources multiple-load MG, considering transmission line losses and converters losses for the common types of loads; CIL, CCL, and CPL. The converter losses model is presented to help with the derivation of the optimal droop gain. The optimal droop gains are analytically derived for the three different types of loads. The effectiveness of the optimal droop gains design method is verified in Matlab/Simulink environment and evaluated experimentally using a laboratory DC microgrid test rig.

Chapter 7 considers a new method to optimize the droop-gain design in a single DC bus multi-source multi-load microgrid, using ANN to minimize system losses, improve voltage regulation, and the current-sharing of power converters. The data generation process for artificial neural network training purposes is discussed. In addition, the structure and training of artificial neural networks is introduced. Finally, the proposed ANN-based droop gain design method will be tested in simulation, to confirm the performance.

Chapter 8 discusses the intelligent EM strategy based on the optimal droop gain approach which is introduced in chapter 6 to minimize the total system losses for single DC bus multiple-sources multiple loads EPS. The EM strategy aims to ensure the HPLs are supplied during all operating scenarios. In addition, the hypothesis of the proposed EM strategy was put forward and then all potential operational flight scenarios were discussed. The conditions of state transitions and the status of system components, switches, and variable settings are investigated. The Finite-state Machine (FSM) structure has been chosen to implement the control strategy to perform the EPS reconfiguration operation. The proposed EM strategy is implemented and simulated using Matlab/Simulink showing how it can manage the EPS under different operating conditions and reduce the system losses.

Chapter 9 concludes the thesis with the overall work and main outcomes. Possible future research work is also proposed in this Chapter. A list of publications that resulted from the research is also given.

Fig. 1.4 depicts the simplified diagram of the single DC bus presented in Fig. 1.1 and the link to the thesis chapters.

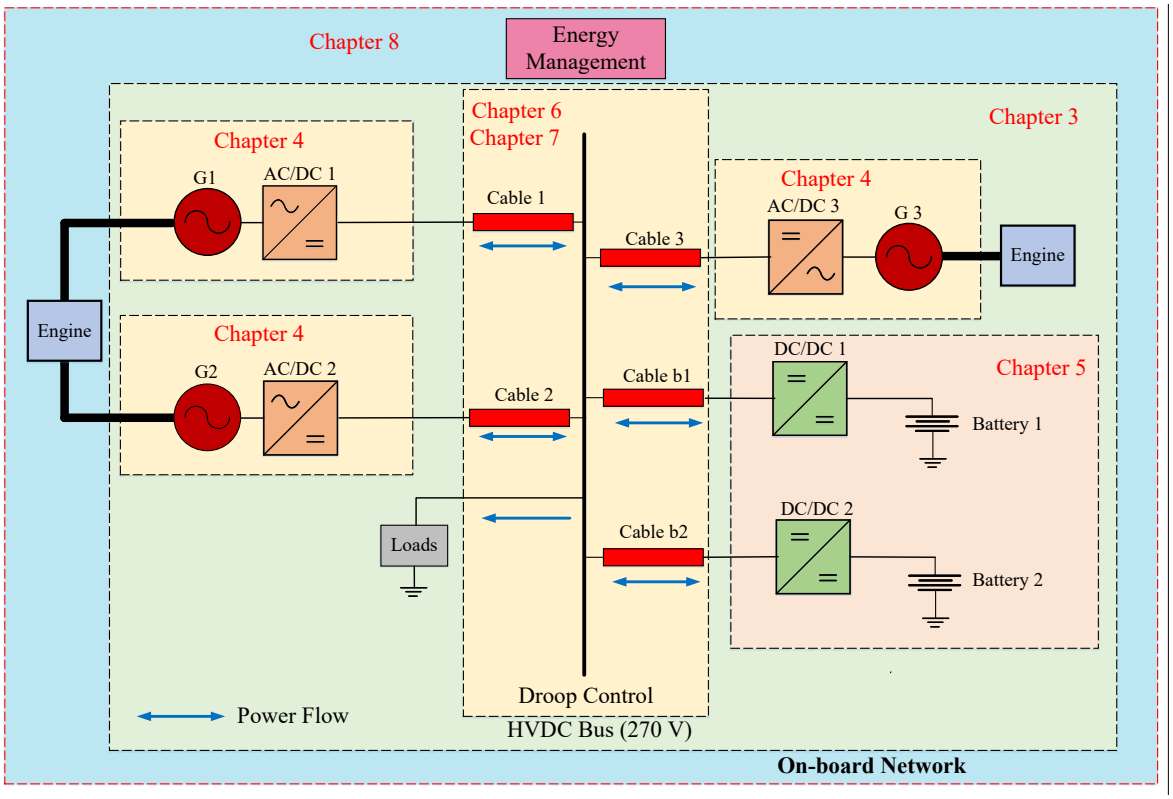

Fig. 1.4: Simplified single DC bus EPS with the thesis chapters

Chapter 2

Electric Power System in the MEA

This chapter provides a literature review in MEA electrical power systems. The content is divided into three main sections: power generation, distribution and conversion, and utilization. It also reviews the DC microgrid load-sharing methods, as well as introducing the EM strategy, the logic control implementation, and the typical EM realization.

2.1 Introduction

As aircraft have become more reliant on electrically powered services, electrical systems have progressed significantly over the years. The twin 28 VDC system was a typical electrical power system in the 1940s and 1950s. This technology was widely employed on twin-engine aircraft, where each engine was driving a 28 VDC generator that could share the load with its neighbour if necessary. There were also one or two batteries installed, as well as an inverter to deliver 115 VAC to the flight instruments [5]. The introduction of the V-bombers changed everything due to significantly higher power requirements; one of them, the Vickers Valiant incorporated an electrically actuated landing gear. Each engine was equipped with four 115 VAC generators, one per engine. These generators were paralleled to provide the benefits of no-break power, which increased the amount of control and protection circuitry. The V-bombers were equipped with four 73kVA AC generators to power heavy loads such as radar and electronic warfare jammer devices. Since then, electrical systems have progressed in the way depicted in Fig. 2.1. Powerful

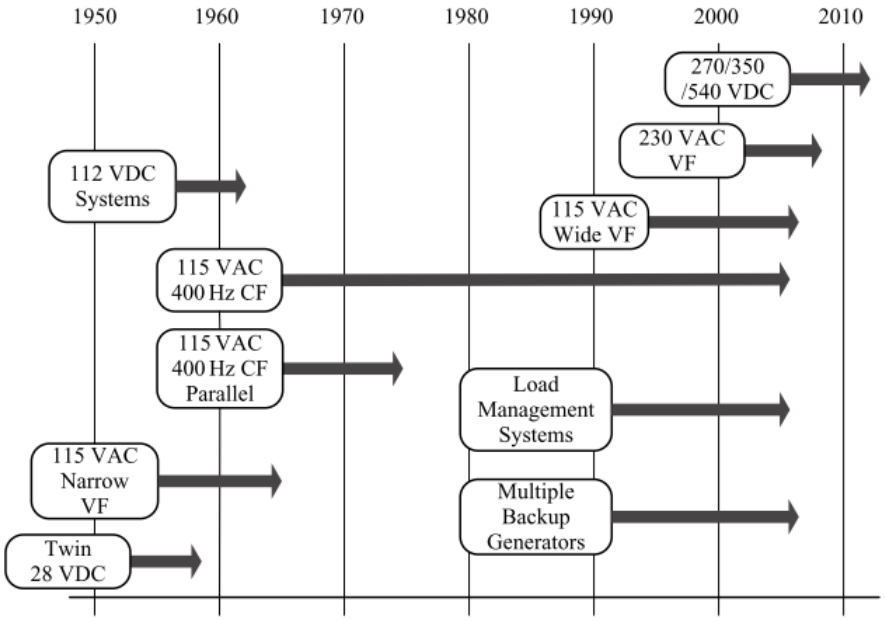

Fig. 2.1: Evolution of electrical system for aircraft [5]

new AC electrical systems prepared the way for the introduction of electrically powered flying controls. Flight control actuators powered by the aircraft AC electrical system, rather than centralized aircraft hydraulic systems, were used on the Avro Vulcan B2 and Handley Page Victor V-Bombers, as well as the Vickers VC10 transport aircraft from the mid 1956s to the mid 1965s [5]. High-power AC generation systems was first used in fighter aircraft McDonnell Douglas F-4 Phantom [5]. A Constant Speed Drive (CSD), was applied to create a Constant Frequency (CF) 115 VAC at 400Hz while cancelling the aircraft engine speed variation over approximately a 2:1 speed range (full power speed: flight idle speed). These are intricate hydro-mechanical devices that are, by their nature, unreliable and inefficient. As a result, the introduction of CF AC generating systems was not without its drawbacks (reliability problems), especially on fighter planes where engine throttle settings are often adjusted throughout the mission.

Variable Speed Constant Frequency (VSCF) systems have become a realistic option in recent decades due to advancements in high-power solid-state switching technology and advances in the control electronics. The unreliable CSD part was replaced by the VSCF technology, which transformed Variable Frequency (VF) or frequency wild power from the AC generator to 400 Hz constant frequency 115 VAC power via a solid-state VSCF

converter. VSCF systems became increasingly common: the F-18 fighter utilizes one, and some versions of the Boeing 737-500 did as well, though not with great success [5]. A VSCF system has also been used for backup AC power generation aboard the Boeing 777. The US Air Force and the US Navy were putting much effort into developing 270 VDC systems. High-capacity generators generate 270 VDC, which is converted to 115 VAC 400 Hz or 28 VDC as needed to power specific equipment and loads. Both F-22 and F-35 Lockheed Martin aircraft use this strategy. It is claimed that this is more efficient than traditional power generation methods and that the amount of power conversion required is minimized, resulting in weight reductions. These advancements are linked to the concept of a "MEA," which aims to assign more aircraft power system operations to electrical means rather than hydraulic or high-pressure bleed air, as is now the case. As a result, future fighter aircraft will need to generate much higher levels of electrical power than they do now [5].

2.2 Power Generation

2.2.1 DC Generation

Initially, electric power was primarily used on aircraft for communication and ignition systems. In fact, the power rating of the first DC generators was usually less than 500W, and voltage levels of 6 and 12V DC were typically used [6]. The installation of lighting, signaling and heating systems has increased the demand for electrical energy. Therefore, the generators' ratings had to be increased to 1 kW (value kept until the beginning of World War II) and the voltage level was standardised to 28Vdc. After World War II, the trend of aircraft power generation moved to AC power generation systems. However, they continued to develop and use DC generators. A customized DC S/G for the Republic F-84 Thunder jet was built in the early 1950s. This starter generator was able to run continuously at 7500 rpm while supplying 400 A of load current at 28V DC. Today, many small modern airplanes continue to use DC generators for the main and the backup power generation systems. Examples of civil aircraft using 28V DC S/G are: 1) ATR600; 2) Dornier 328; 3) Gulfstream G280; and 4) Falcon 2000. Various military aircraft that use

28 Vdc to start generators include: 1) Alpha jets; 2) C295; 3) CN235 and 4) IJT36 [6].

DC generators in aircraft are typically shunt-wound, with the high resistance field coils connected in parallel with the armature as shown in Fig. 2.2. In order to keep the terminal voltage constant while the aircraft engine speed and generator loads vary, a voltage regulator is used to modify the field current. The voltage regulation must comply with the standard used to specify aircraft power generation systems, such as MIL-STD704F [19].

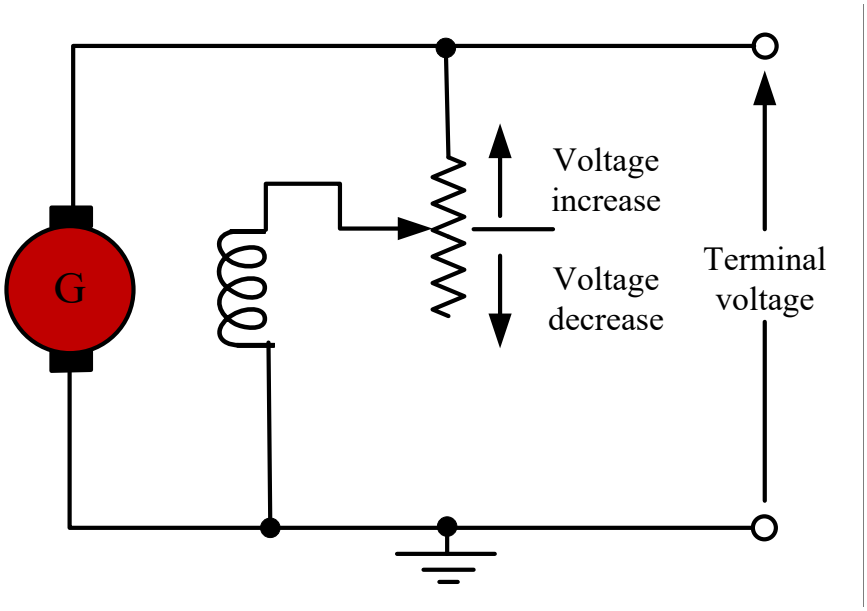

Fig. 2.2: DC voltage regulator [5]

However, 28V DC systems are limited to around 400 amps or 12 kW per channel maximum due to the following reasons [5]:

- The current cannot exceed 400A, otherwise, the size (weight) of conductors and switchgear to carry the necessary current becomes prohibitive
- If the current or power levels exceeded the limits, the brush wear of the brushed DC generator will become excessive, resulting in early failure and high maintenance costs

2.2.2 Electric Machines

In the last few decades, a lot of research has been done on the electrical machine technology used in MEA. In [23], different electrical machine topologies for electric aircraft

propulsion are compared. Considering the trade-off of power electronics, fault response equipment, and gearbox components, the permanent magnet machine was found to have an outstanding power density as shown in Fig. 2.3 [24], [25]. Moreover, when considering additional drive and fault response components, PMM still maintains the low weight advantage. As aerospace applications place particularly stringent requirements on the power density, reliability, and availability of the electrical machine, these three types of electric machine are used in aircraft: Induction Machines (IM), PMM, and Switched Reluctance Machines (SRM) [26]. Fig. 2.4 shows the cross-section of the three electrical machine types.

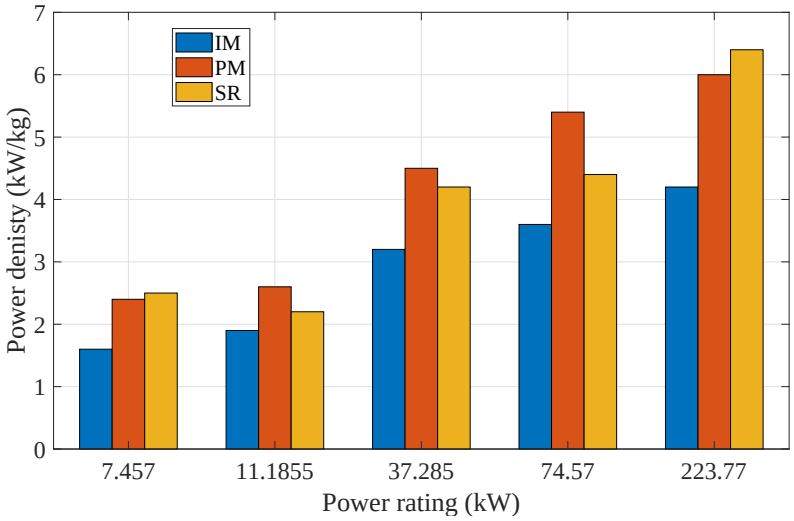

Fig. 2.3: Comparison of IM, PM, and SR machines at different power levels designed for a rated speed in the neighbourhood of 10,000 rpm [25]

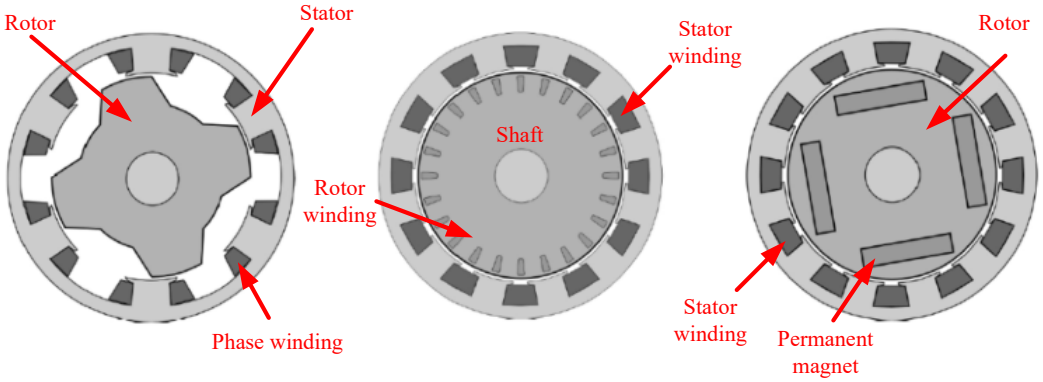

Fig. 2.4: Cross section of a typical SRM (left), IM (middle), and PMM (right) [27]

2.2.2.1 The Switched Reluctance Machine (SRM)

For aircraft applications, high power density, wide speed range, wide operating temperature range, low volume, high reliability, and easy control are all required. SRM matches most of these requirements. The SRM S/G system is regarded as a top candidate technology for meeting the requirements and constraints of embedded power generation in aircraft applications. SRM has been used and investigated as an S/G in [28], [29]. However, due to its nature, the three-phase output voltages are not sinusoidal, which means that the harmonic content is high, which may influence the power quality of the main bus. In addition, SRM generates a high torque ripple, which has an adhering effect on mechanical gearboxes and engines. Then filters are needed to ensure that the power quality meets aircraft standards, which will affect the overall weight of the aircraft [30]. Therefore, the use of SRM in aerospace applications is still limited.

2.2.2.2 The Induction Machine (IM)

Due to simplicity, fault-tolerant capability, operation at high temperatures, and robust characteristics, the IM is one of the most commonly used electrical machines in the industry. It is also inexpensive to produce because it has been a well-established technology for many years. Generally, there are two types of IM: wound and squirrel cage IM. The latter is widely used in industries because of its reliability and low cost of construction. The rotor core is made of steel with laminations from aluminium or copper bars casted in the slots. The magnetic field is carried through the rotor conductors by the core. Fig. 2.4 depicts the cross-section of the IM. An S/G operation with resonant converter fed IM is presented in [31]. DC motors is used to mimic the aircraft engine and the experimental results show the feasibility of IM operation as an S/G [32]. IM suffers from a low power density and mechanical constraints when operating at high speeds. When the rotational speed increases, the rotor cage begins to expand, which may cause conflict with the stator component [33]. A careful design of the rotor will allow for IM to operate at high speed. Induction generators have not been employed in aircraft power generation, despite their use in automotive electric propulsion. The usage of an IM as an embedded S/G for aircraft applications has to be further studied with active rectifier and

field orientation control.

2.2.2.3 The Permanent Magnet Machine (PMM)

PMM is the choice for many recent applications due to its high power density, high torque, relative ease of field weakening operation, high efficiency, and existing self-excitation from using magnets [1]. The magnets are usually attached to the rotor of the machine and installed either on the surface or are interior mounted, as shown in Fig. 2.4. Before using PMM for aerospace applications, several key drawbacks need to be addressed. For example, cooling systems are required to ensure the magnets are within the safe operating temperature range. The inability to deactivate the magnetic field is also a safety concern to be considered [34]. Moreover, the cost and the availability of rare-earth material used in a permanent magnet is considered as a challenge for this topology. In addition, the PMMs are not inherently fault tolerant, since the flux generated by a permanent magnet can not be disengaged electrically.

Briefly, the key advantages of each of the three machine types detailed above when utilized as S/G can be summarised as follows:

- SRM for its robustness.
- IM for its mature technology and low cost of construction.
- PMM for its power density and high performance.

Table 2.1 shows the pros and cons of the different machines when utilized as S/G.

2.2.3 Constant Frequency (CF) System

In this topology, the generator shaft is mechanically coupled through a variable-ratio transmission gearbox referred to as a CSD as schematically illustrated in Fig. 2.5. The CSD converts the variable-speed input to a constant speed output, which is used to drive the generator. Since the 1960s, CF generation systems that use CSD and generate 115/200 V at 400 Hz have been widely used in aircraft. There was a trend in the 1970s to integrate generators and CSD stages into one unit to reduce weight and improve reliability [36]. Therefore, the integration into a common housing improves the reliability of the entire

Table 2.1: Summary of trade-off comparison between different machines as S/G [35].

Machine	Merits	Demerits
IM	• Robust • High power factor • Reliable • Field weakening	• Significant rotor losses • Limited fault tolerance
SR	• Inherently safe • Reliable	• High mass • High losses from torque ripples
PMM	• Low overall mass • High performance • High power density	• Fault detection • Limited fault tolerance • Knowledge of rotor position

system level [37]. By designing a common oil system for generator cooling and CSD lubrication, weight and size are greatly reduced and this compact unit is called Integrated Drive Generator (IDG) [38]. Due to their efficiency and power density improvement (1.5 kVA/kg), IDG systems have been very popular for more than 20 years [6]. A number of conventional civilian aircraft such as Airbus A320, A330, A340, Boeing B747, B757, B767, and B777 implemented IDG systems [39]. However, due to the complexity of this hydro-mechanical drive system, the purchase and maintenance costs of the system may be high [40].

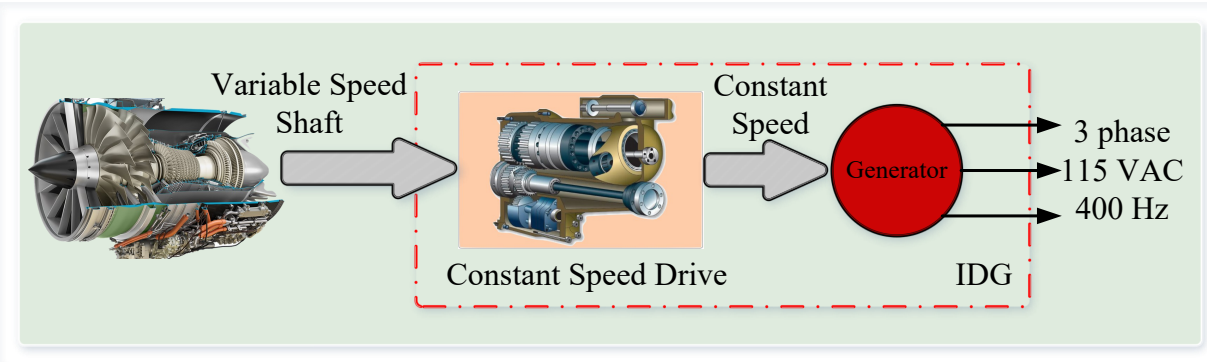

Fig. 2.5: Constant frequency integrated drive generator system.

2.2.4 Variable Speed Constant Frequency (VSCF) System

The CSD used in the AC CF system requires maintenance and significantly increases the weight and size of the system. For these reasons, a new approach was introduced in the 1980s to connect a generator directly to the engine shaft to generate constant frequency power [41]. The generator output has a variable frequency related to the speed of the turbine. Therefore, there are two approaches in order to provide CF voltage. The first method is to use a rectifier and inverter to implement a DC link between the AC generator and the AC load [42]. Fig. 2.6 shows the architecture of the VSCF converter system with a DC link. The VSCF with a DC-link has been used in the B777 (backup) and MD-90. The second approach for generating the CF voltage includes an AC/AC converter (for example, a cycloconverter or a matrix converter), which is connected between the generator and the AC load. The block diagram of the VSCF system with AC/AC converter is shown in Fig. 2.7. The architecture of a VSCF with a cycloconverter is mainly used on military aircraft such as F18 fighter jets and F117A stealth attack aircraft [5].

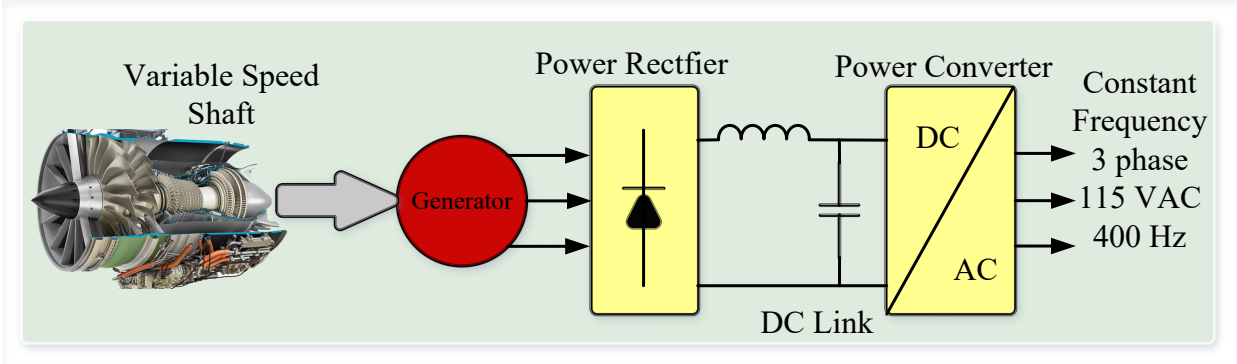

Fig. 2.6: VSCF system using a DC link.

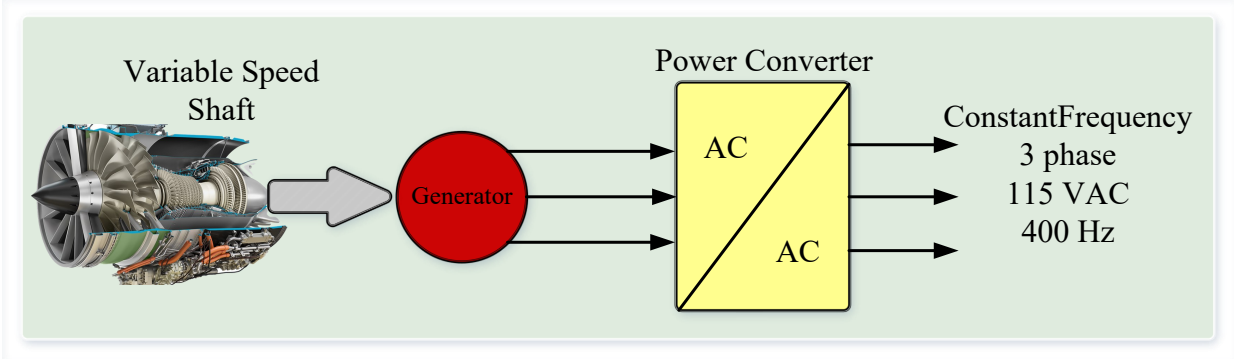

Fig. 2.7: VSCF system using a AC/AC direct frequency converter

For this type of power generation system (VSCF), no gearbox is needed between the engine shaft and the generator. However, the disadvantage is that the Power Converter (PC) must handle all the generated power and represents a single point of failure. So the PC needs to be designed for the full rated power and has a high-reliability requirements. In such a system, the power electronic converter will become a reliability bottleneck.

2.2.5 Variable Speed Variable Frequency (VSVF) System

Fig. 2.8 shows the variable frequency generation with AC distribution where the loads can be adapted to run at a variable frequency and the generator can be connected directly to the engine shaft. The generator provides fixed voltage at a variable frequency output and the frequency is related to the speed of the engine shaft, generally in the range of 360 to 900 Hz. The main advantage of the VSVF topology is the direct connection between the generator output and the EPS, which results in a simple and potentially very reliable configuration. The disadvantage is that almost all aircraft loads will require power electronic converters for control because some onboard loads cannot use the variable-frequency supply directly. The VSVF architecture has been utilized in new aircraft for example, Boeing 787, Airbus A380, and A350 [43]. While the voltage is regulated at either 115 (A380) or 230 VAC (B787) and the output frequency typically varies between 320 and 900Hz [44]. In contrast, variable frequency generation with an HVDC distribution structure is shown in Fig. 2.9, where the generated electrical power is rectified to the DC bus for further distribution, which has an HVDC bus bar (270 V or 540 V). The benefits of such a topology can be summarised as follows [11]:

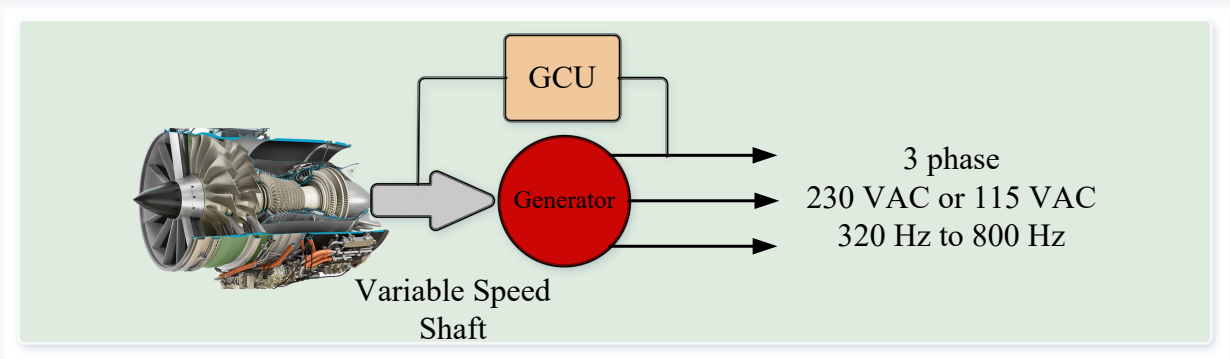

Fig. 2.8: A variable frequency generation system (with AC distribution)

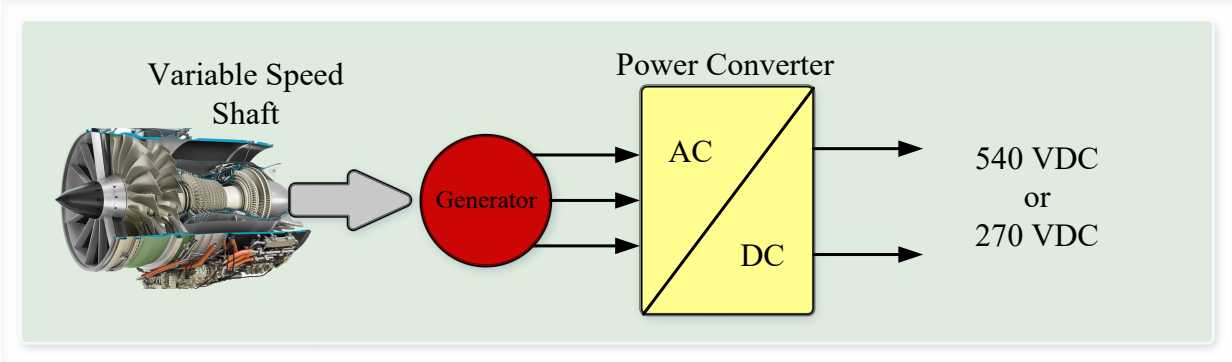

Fig. 2.9: A variable frequency generation system (with DC distribution)

- Only two conductors are required in HVDC distribution, whereas three conductors are required in AC distributions and this leads to a reduction in transmission line losses [11].
- Due to the reduction of the skin effect in HVDC, the power losses and the dielectric losses in the power cables can be decreased [11].
- In comparison to AC inductors, the HVDC system provides less corona effect [11].
- Reactive power compensation equipment is not required and this leads to a significant reduction in the capacity of wires and devices.

2.2.6 Electric Starter/Generators

One of the MEA's core ideas is the integration of multiple aircraft functions into a single system for reduced mass, which would result in fuel savings and improved efficiency. The S/G structure is one of the key changes brought by the MEA concept [35]. The process of starting a large aircraft engine requires the assistance of a starter to provide smooth acceleration. Air starter motors are typically used to rotate the starter turbine which drives the engine and are supplied from a ground cart or APU. A start-up sequence of an aircraft engine is shown in Fig. 2.10 and the steps are listed below:

- When the ignition switch is turned on, the starter motor performs its function to start driving the engine.
- The air starts to flow into the engine with help from the compressors.

- As the speed reaches about 10% of the engine maximum speed, fuel is injected into the combustion chamber.
- The air and fuel mixture is ignited to aid the engine to reach self-sustaining speed.
- Once a self-sustaining speed is reached, the starter circuit is disabled. The engine continues to accelerate by itself until the idle speed is reached.

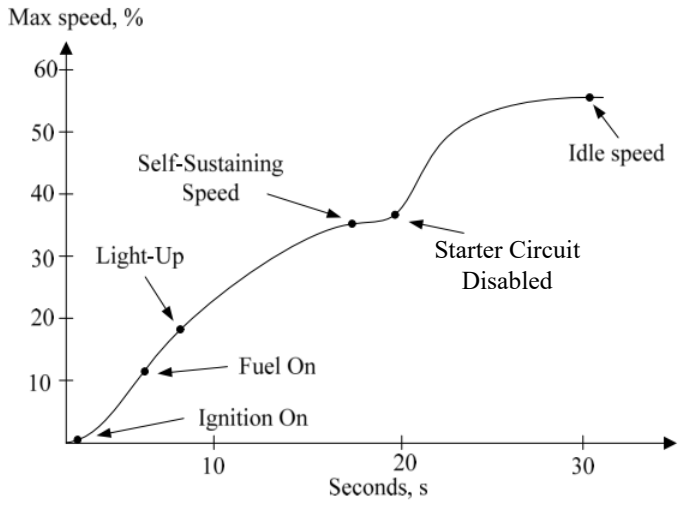

Fig. 2.10: General starting sequence of a turbo-jet engine [35]

The starter should be designed according to the engine torque-speed characteristics and these vary depending on the environmental temperature. Therefore, the starter should be able to overcome the torque requirements for these temperature ranges. The aircraft S/G torque-speed characteristics are shown in Fig. 2.11, and can be divided into three regions. In the first region, from standstill to ω_b, the machine works as a motor with constant torque, where the maximum torque of the machine is delivered. The second region, which extends from ω_b to ω_{min}, the machine supplies constant power for engine acceleration until the engine becomes self-sustaining at ω_{min}. When the engine reaches the self-sustaining speed, the generator operation is considered to be initiated. In the generation mode, the machine is required to provide maximum constant power to the maximum speed ω_{max}. If the same electrical machine can perform the starting function and generating power, it will have a significant advantage in reducing weight and volume.

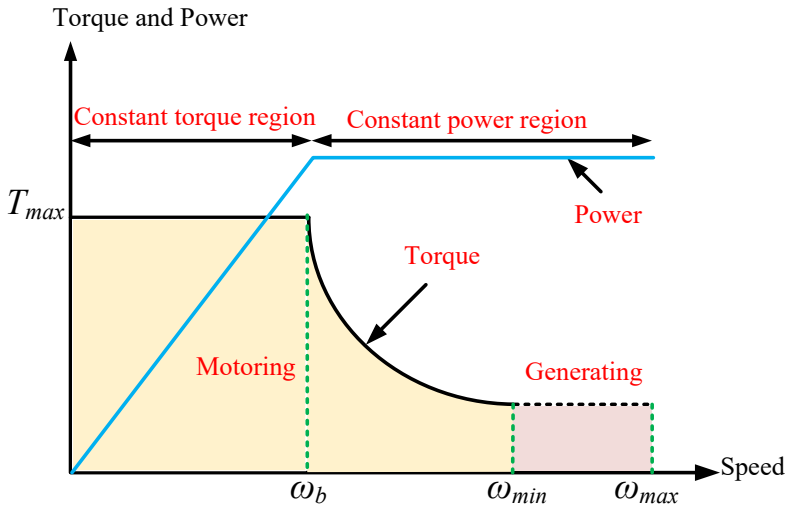

Fig. 2.11: Torque-speed characteristic of the starter/generator [1]

Fig. 2.12 shows the architecture of the electric S/G system and the corresponding power flows. In addition, each operating mode is briefly described. The PC is used to replace the accessory gearbox and interface between the electric machine and the aircraft main DC bus. By controlling the PC, the power can be directed to flow into or out of the machine, and the starter or generator role can be determined. In start-up mode, the electric machine accelerates the aircraft engine and receives the electric power from the supply bus, the APU or the ground power supply. Therefore, in this mode, the objective of the control system is to regulate the machine speed to its reference value. After the starting operation is completed and the engine becomes self-sustaining,

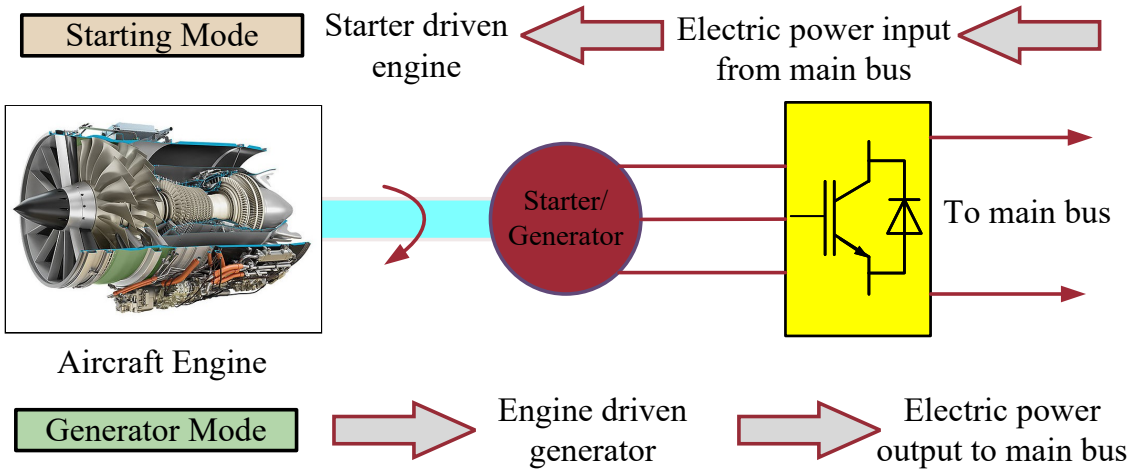

Fig. 2.12: Electric starter/generator system [35]

the process is reversed and the engine acts as a source of mechanical power which is converted into electrical power to supply onboard loads employing machine and converter.

2.2.7 Energy Storage Systems

The battery system is an essential component for both MEA and AEA concepts. Batteries used for MEA/AEA applications should cope with different functions such as delivering the power required by loads during dynamic and steady-state operation, assisting the internal engine S/G system, maintaining the DC Bus voltage within its allowed operating limit, and hybrid electric taxing systems, etc [45], [46]. The most important function is ensuring the emergency power, considering safety requirements. For instance, the Federal Aviation Administration requires that the battery guarantees to be able to supply emergency loads for at least 30 minutes [47].

The aviation requirements for any battery intended for use as a power source for equipment installed onboard aircraft must be safe over any operating condition, ideally having a high energy density, being lightweight, reliable, requiring minimal maintenance, and being able to operate safely over a wide operating temperature range. The main battery technologies considered for aerospace are Valve Regulated Lead Acid (VRLA), Nickel-Cadmium (Ni-Cd), and Lithium-ion (Li-ion) [48]. The VRLA batteries have been developed to address the issues of traditional lead-acid batteries, but still suffer from low energy density and specific energy. However, they have the lowest cost and they can deal with high currents [48]. Due to their high capacity and longer life cycles compared to other available technologies and high charging rates, Ni-Cd batteries were the most used in aircraft in the late 80s. Nevertheless, Ni-Cd batteries suffer from memory effects, high self-discharge, and toxicity of cadmium, which limit their usage [49]. Li-ion batteries have some key advantages which guarantee much better performance, i.e. have high energy density and specific energy, no memory effect, low self-discharge, and low maintenance. However, they still require complex and costly protection and cell voltage monitoring circuits. Li-ion batteries have been recently used by both B 787 and A 350 [49], [50]. Table 2.2 summarizes the key features of different battery types.

Table 2.2: Main features of batteries (based on [50])

Feature	Unit	VLRA	Ni-Cd	Li-ion
Specific energy	Wh/kg	40	65	135
Energy density	Wh/L	70	105	200
Specific power	W/kg	450	1000	2000
Life cycle	n.	250	1500	3000
Self discharge	%/month	15-20	4-6	2-3
Memory effect	-	No	Yes	No

2.3 Power Distribution and Conversion

The power distribution systems of the majority of civil aircraft are hybrid AC/DC topologies. For example, a 115V/400Hz AC supply is used for large loads such as galleys, whereas a 28V DC supply is used for flight control, avionics, and battery-powered vital services [51]. In the traditional aircraft model, all of the electrical power is generated remotely, by the main generators driven by the engines and the APU-driven generators located in the aft area as shown in Fig. 2.13. The power distribution on conventional aircraft is of the centralized type where the generated electrical power is routed to the front for protection and control. The MEA offers the flexibility to generate and distribute electrical power efficiently near to its consumption. This leads to a reduction in losses due to short distances between generation and consumption, hence, the efficiency of the power distribution system is improved. Due to the reduction in the power rating of the main conductors, a weight and volume saving may be realized. These weight savings and rating reductions, can result in both improved fuel efficiency for the aircraft and a lower total cost as the lower-rated devices may be provided at a reduced price. Moreover, the distributed power system configuration realizes maintenance cost savings. Fig. 2.13 illustrates the power distribution of Boeing 787 as an example of MEA [7].

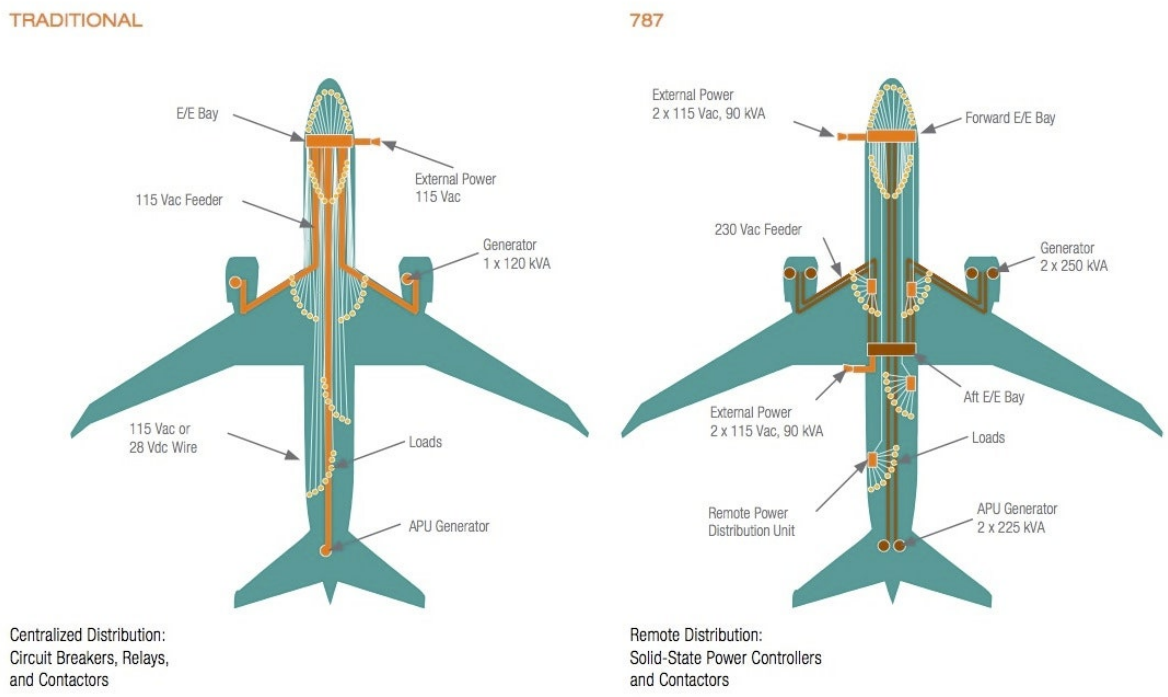

Fig. 2.13: Comparison between the power distribution of conventional aircraft and the MEA [7]

2.3.1 Power Distribution in Conventional Aircraft

The EPS in conventional aircraft often consists of two or more engine-driven generators to provide AC power to the loads. In some civil aircraft configurations, the engine-driven generators are connected to the high voltage distribution buses [43]. Each generator is responsible for feeding a certain number of buses. The main generators' busbars are connected together via Bus-Tie Breaker (BTB). In the case of failure of one generator, it is isolated automatically from its respective busbar, and all loads connected to this busbar are supplied by the operative generator. When both generators fail, the Low Priority Loads (LPLs) can no longer be supplied. However, the essential/High Priority Loads (HPLs) will automatically be supplied by the batteries until the aircraft lands safely. In Fig. 2.14, the synchronous generator provides AC voltage at CF to the AC loads in the aircraft EPS. In order to supply the DC loads, AC/DC rectifiers are used to convert the AC voltage to multi-level DC voltages at the secondary buses [43].

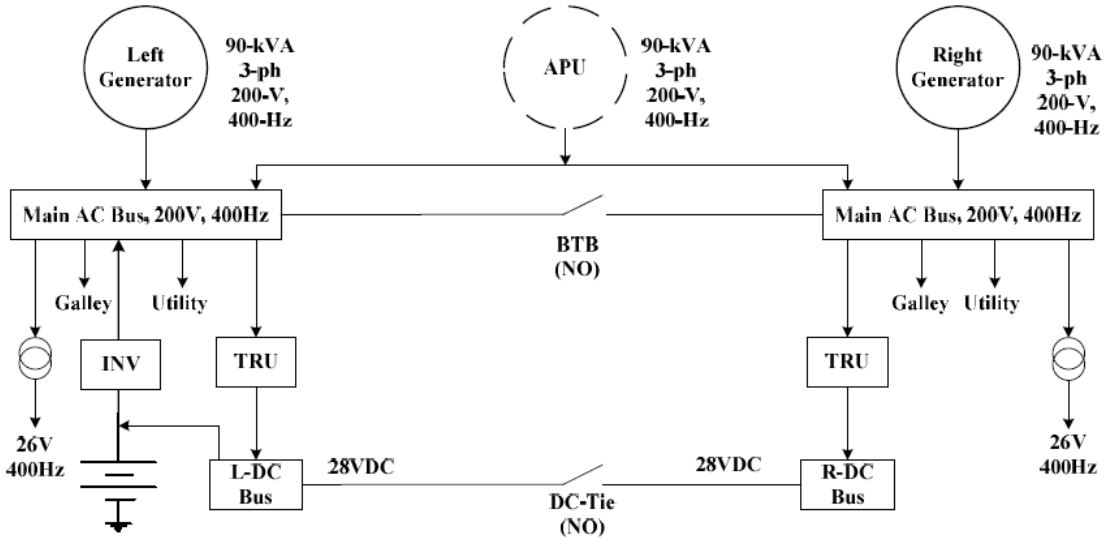

Fig. 2.14: Conventional B767 aircraft power distribution system [43]

2.3.2 Power Distribution in MEA

For modern MEA, a new type of power distribution system is employed, for example the PDS of a Boeing B787 is shown in Fig. 2.15. The key feature of the B787

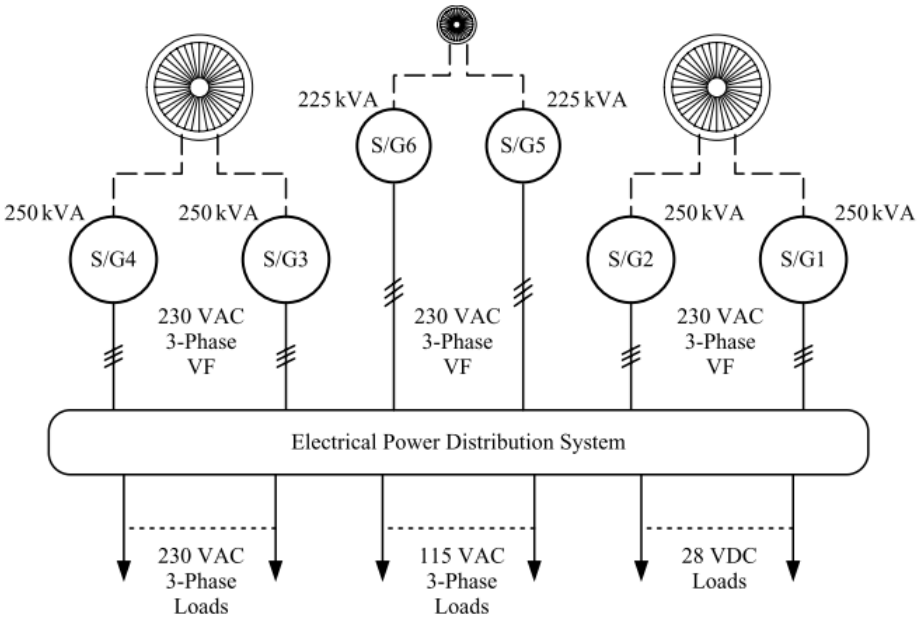

Fig. 2.15: Power distribution system in a modern aircraft B787 [5]

is the adoption of three-phase 230 VAC variable frequency (ranging from 360Hz to 800Hz) electric power compared with the conventional three-phase 115 VAC arrangement normally used. The increase in the voltage leads to a reduction in feeder losses and wiring in the electrical distribution system [5]. The B787 has the following key characteristics:

- 2x250 kVA S/G per engine and this results in 500 kVA of generated power per channel.
- 2x225 kVA APU S/G are utilized.

In comparison to the B787, the key characteristics of the A380 electrical power distribution systems are as follows [5]:

- 4x150 kVA variable frequency generators
- 2x120 kVA constant frequency APU generators at 400 Hz
- 4x external power connections for ground power at 400 Hz
- 1x70 kVA ram air turbine for emergency use

The AC power system architecture is shown in Fig. 2.16 where the two APU generators are driven by their corresponding APUs. Each main generator provides power to its associated AC bus and is controlled by the Generator Control Unit (GCU). It should be

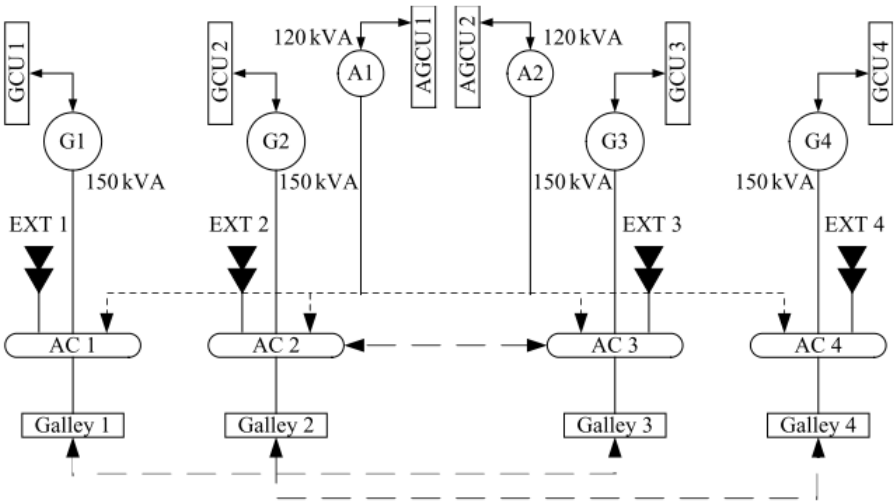

Fig. 2.16: A380 AC electrical power architecture [5]

noted that parallel operation at primary AC buses is not allowed since the frequency of the output power is variable, therefore can be different.
The key characteristics of the A380 DC power conversion and energy storage system are outlined below:

- 3x300A, 28V Battery Charge Regulator Units BCRU; these are regulated TRUs
- 1x300A TRU
- 3 x 50 Ah Batteries
- 1xstatic Inverter

The DC system of A380 provides a no-break power capability as shown in Fig. 2.17. Consequently, permitting key aircraft systems to operate without power interruption during changes in system configuration. Using DC paralleling techniques makes it easier

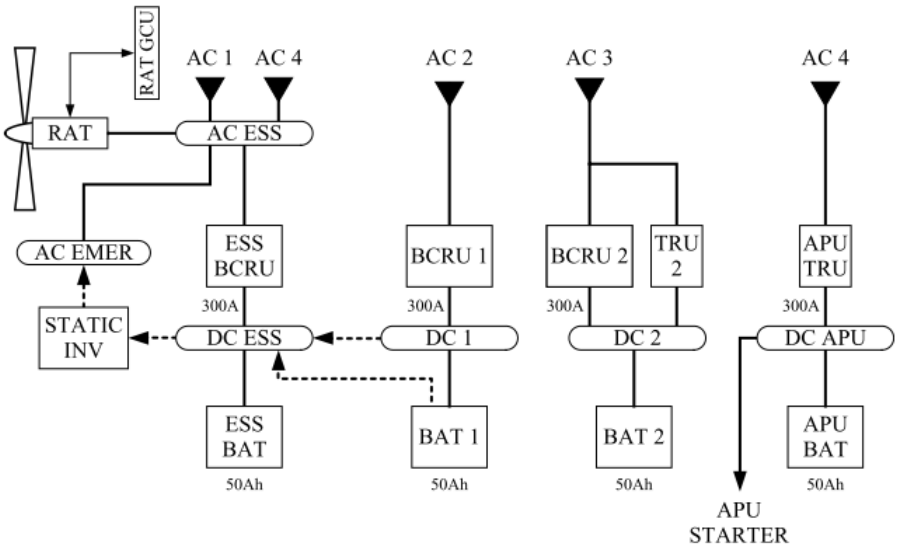

Fig. 2.17: A380 DC electrical power architecture [5]

to provide no-break power for crucial components i.e. control computers [5].

Another example for MEA is More Open Electrical Technology (MOET) aircraft platform. It is based on an A380 power system and was the subject of studies within the MOET project [52]. The top-level line diagram of this power system design is shown in Fig. 2.18. The power system is divided into three sections: generation, distribution and

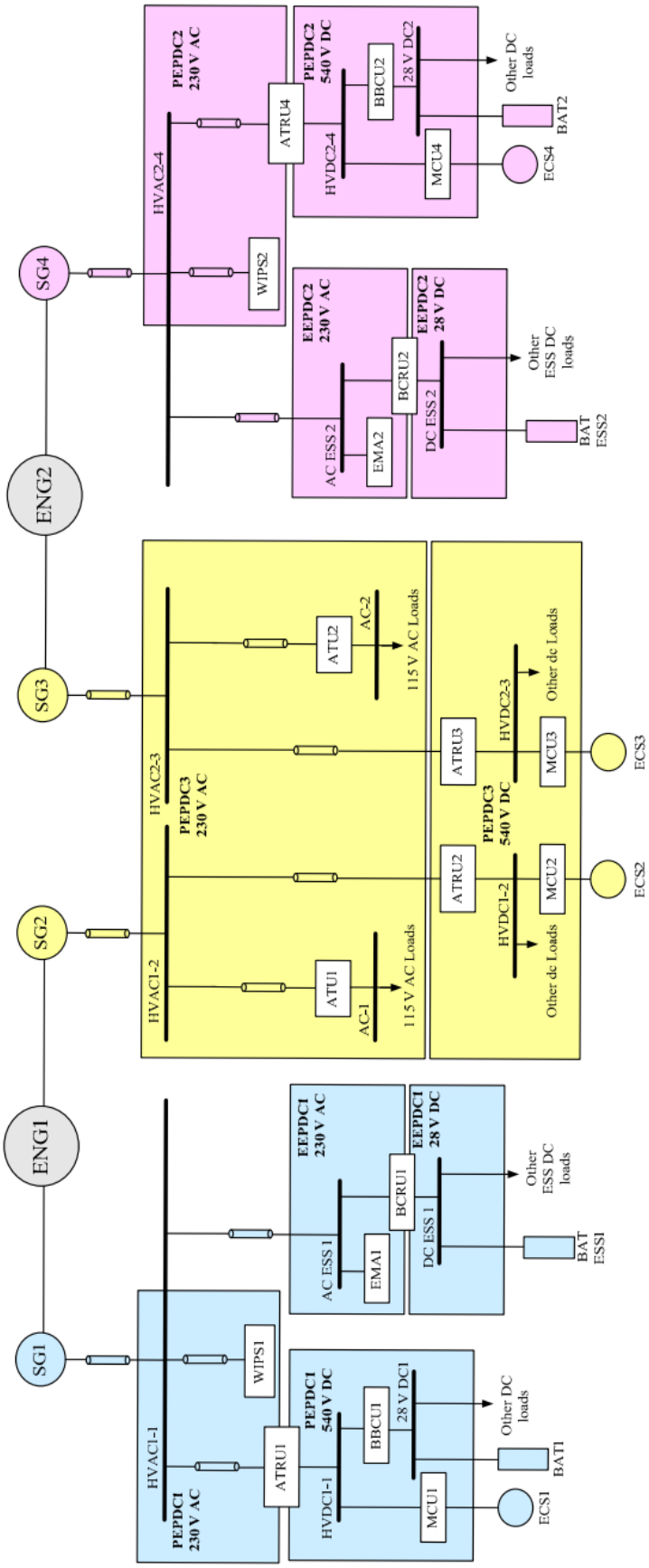

Fig. 2.18: The MOET large aircraft electrical power system [52]

conversion, and onboard electrical loads. Two gas turbine engines (ENG1/ENG2) provide the primary power for this system. Each aircraft engine drives two starter/generators (S/G1-S/G4) per channel. The GCU regulates the voltage at each generator's terminal to ensure that it maintains at 230V RMS. The power system is the VF (360-900Hz) because the generator is directly controlled by the aircraft engine, following current industry trends away from constant frequency 400Hz power. In this power system, electrical power is distributed in AC form via four High Voltage AC (HVAC) distribution buses (HVAC1-1, HVAC1-2, HVAC2-3, and HVAC2-4). It's worth noting that no HAVC bus is ever powered by more than one generator.

There are two types of centres of the power distribution. The Primary Electrical Power Distribution Centre (PEPDC) is one, while the Essential Electrical Power Distribution Centre (EEPDC) is the other. The primary electrical loads, such as the WIPS, the ECS, backup batteries, and other AC or DC demands, are supplied by the PEPDC. The EEPDC is responsible for supplying the critical electrical loads that ensure flight control in emergencies. This means that the electrical power supply will be maintained in the event of an emergency, ensuring that vital electrical loads are not disrupted. Due to the necessity of certain critical electrical loads for managing flight control, the electrical power supply to loads within the PEPDC can be discontinued if an emergency arises during the flight process.

The PEPDC1 is a multiple-bus power electrical system that includes a 230V AC bus (HVAC1-1), a 540V DC bus (HVDC1-1) and a 28V DC bus, as shown in Fig. 2.18. The power on the 540V DC bus is produced by converting AC power to DC power via the ATRU1. To feed a 28V DC bus, the Buck-Boost Converter Unit (BBCU) is connected to the 540V DC bus. the PEPDC2 has a power system architecture that is identical to the PEPDC1. The ATRU2 and the ATRU3 in the PEPDC3 convert the 230V AC bus power (HVAC1-2, HVAC2-3) to 540V DC bus for the (HVDC1-2, HVDC2-3 buses). The HVAC1-2 and HVAC2-3 feed the 115V AC bus (AC1, AC2) for supporting legacy loads through the (ATU1, ATU2). A 230V AC essential bus (AC ESS1) and a 28V DC essential bus (DC ESS1) are fed by a battery charge rectifier unit for the EEPDC1 (BCRU1). The AC-fed EMA is represented by the EMA1 and is fed by the AC essential bus. The architecture of the EEPDC2 is identical to that of the EEPDC1. The MOET aircraft

power system is symmetrical in terms of the arrangement of the onboard electrical loads, as can be observed from Fig. 2.18. Half of the electrical aircraft power system is made up of the S/G1, S/G2, PEPDC1, EEPDC1, and half of the PEPDC3. S/G1 provides power to PEPDC1, EEPDC1, and WIPS1 during normal operation. The PEPDC2, EEPDC2, and WIPS2 are all fed via S/G4. The electrical loads for the PEPDC3 are the ECS2, ECS3, and additional 115V AC loads, which are supplied by S/G2 and S/G3. During normal operation, four batteries (BAT1, BAT ESS1, BAT2, and BAT ESS2) are charged.

2.3.3 Power Converters for Onboard Microgrids

The inherently hybrid AC and DC characteristics of the electric power distribution system of MEA imply power electronics conversion stages [53]. Many PC topologies have been proposed and investigated, this section will go over the most investigated ones for the MEA microgrids. A PC classification tree is depicted in Fig. 2.19, where the main families of DC/AC, AC/DC, AC/AC and DC/DC converters are listed and they are described in the following subsections.

2.3.3.1 AC Power Converter Technologies

AC PCs are used in a range of applications in aircraft, namely:

- Inverters – DC/AC
- Rectifiers – AC/DC
- Direct – AC/AC

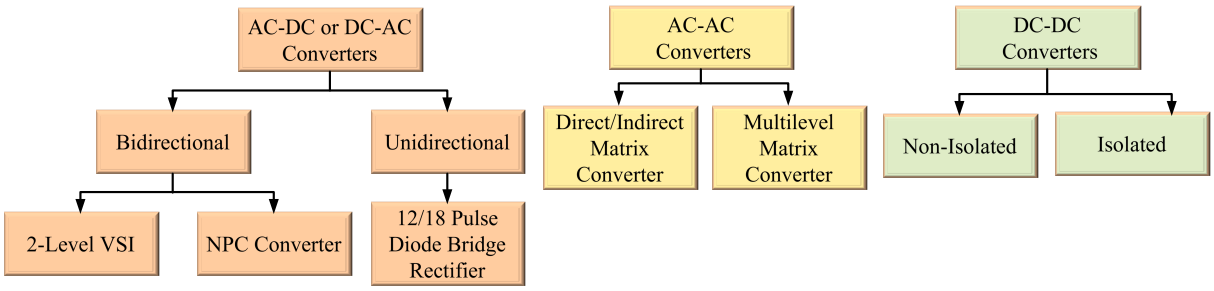

Fig. 2.19: Power electronics converter classification tree [53]

There is a variety of topologies and technologies available within these classifications. Some of the PC options will be discussed in this section for use on existing and future aircraft platforms.

One of the most common uses for power electronics aboard an MEA is the DC/AC PC [54]. The control of AC loads such as electrical machines from a DC bus or supply requires the use of these DC/AC PC. Fig. 2.20 shows the standard 3 phase voltage source inverter configuration that is dominant in many applications. Because this topology

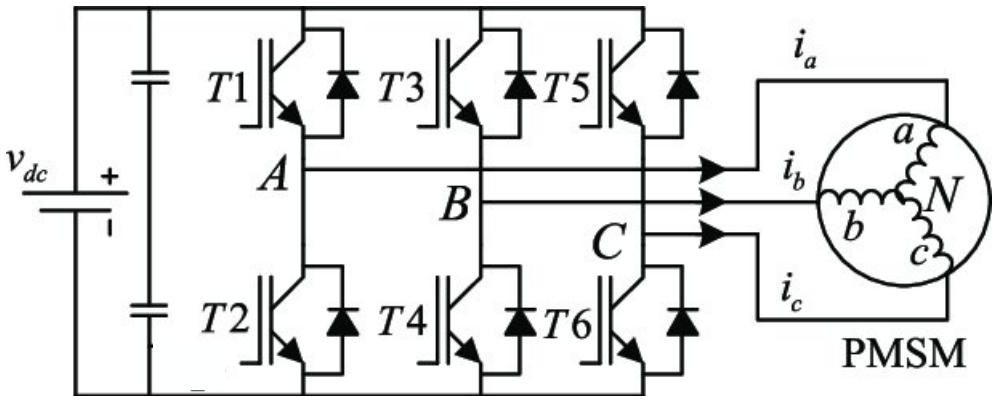

Fig. 2.20: Structure of the two-level voltage source inverter [55]

is utilized in a vast majority of industrial motor drives, there is a great amount of knowledge and experience in using, modulating, and controlling this converter topology and associated loads. When high-frequency fundamental AC waveforms are required in high-speed electrical machine applications, the three-level Neutral Point Clamped (NPC) PC topology is considered [56] as shown in Fig. 2.21. The multilevel nature of the output waveform from the NPC means that for the same device switching loss, a far better output waveform quality is possible at the cost of additional semiconductor switching devices.
Connecting an AC generator to power a DC electrical system, as well as a front end PCs for back-to-back AC/AC power converters, require AC to DC power conversion. Traditionally, diode-based passive rectifiers have dominated these applications. Whilst the six pulse diode bridge has the essential functionality, power quality concerns due to low order frequency current harmonics, make 12 and 18 pulse diode bridge rectifiers the better choice in all but the lowest power applications. Fig. 2.22 shows the 18 pulses diode rectifier topology. The inclusion of extra diodes and a phase-shifting transformer allows

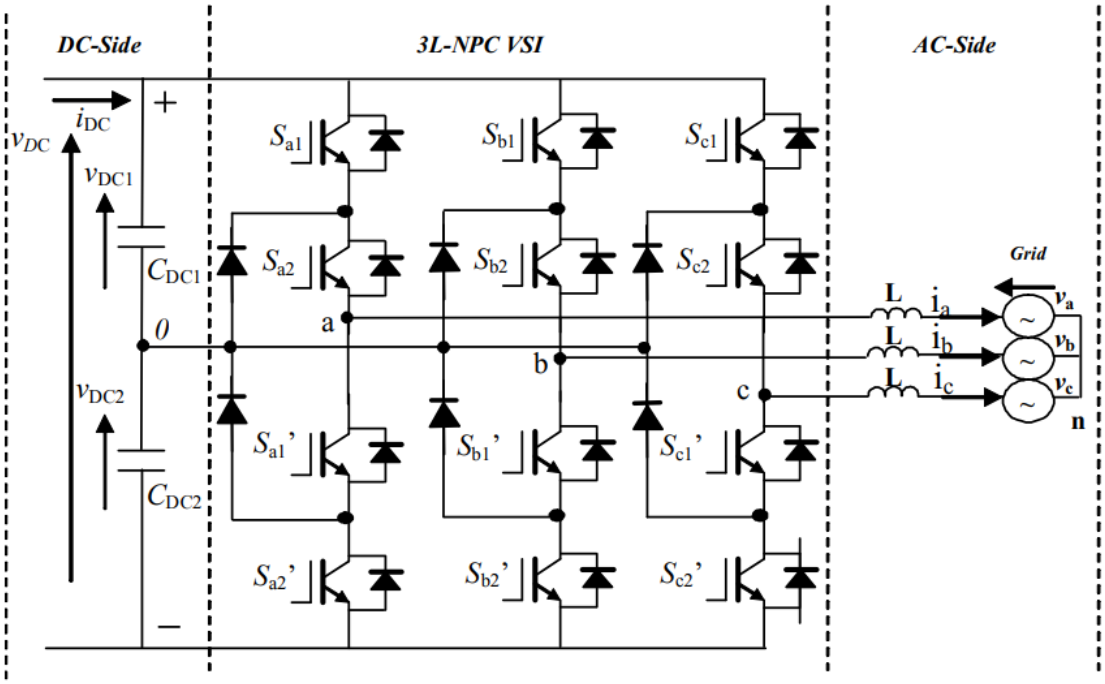

Fig. 2.21: Grid-connection of a three-phase 3L-NPC VSI with an L-type filter [57]

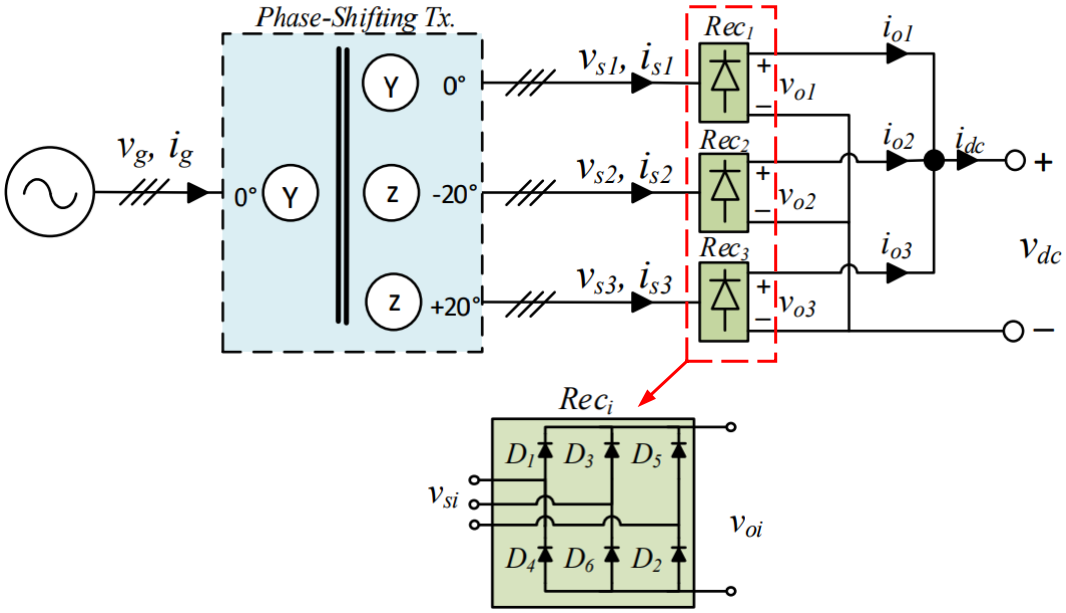

Fig. 2.22: Eighteen-pulse rectifier transformer system [58]

some of the low order frequency harmonics in the AC current waveforms to be avoided, and this is the solution assumed in many aircraft's power quality standards [54]. The diode bridge and transformer-based solutions are considered to be reliable and effective,

but with only unidirectional power flow possible, they will always require a braking circuit, even if power quality requirements allow for electrical energy regeneration.
Active PCs in an AC/DC configuration are an alternative to diode bridge-based rectifiers. It is possible to obtain good quality AC current waveforms with just high order switching frequency components in the AC current waveforms by ensuring that there is sufficient inductance on the AC side of the converter [56]. If better power quality is desired, an NPC converter can be used in the same way as fo the DC/AC PCs [59].

A single-stage converter can convert the electrical power and control the load current in motor drive applications on an aircraft with an AC power system. When compared to the back-to-back connection of an AC/DC and a DC/AC PC [60], this can be a very favourable method for minimizing the converter's weight and volume. In this case, the Matrix Converter is the leading PC technology to consider for future applications [61]. For a 3-phase AC/AC PC, the Direct Matrix Converter uses nine bi-directional switches to ensure that each output phase can be linked to any input phase as shown in Fig. 2.23.

There are also a variety of Indirect Matrix Converter topologies [52] that provide different efficiency and some device count reduction, but the latter may come at the

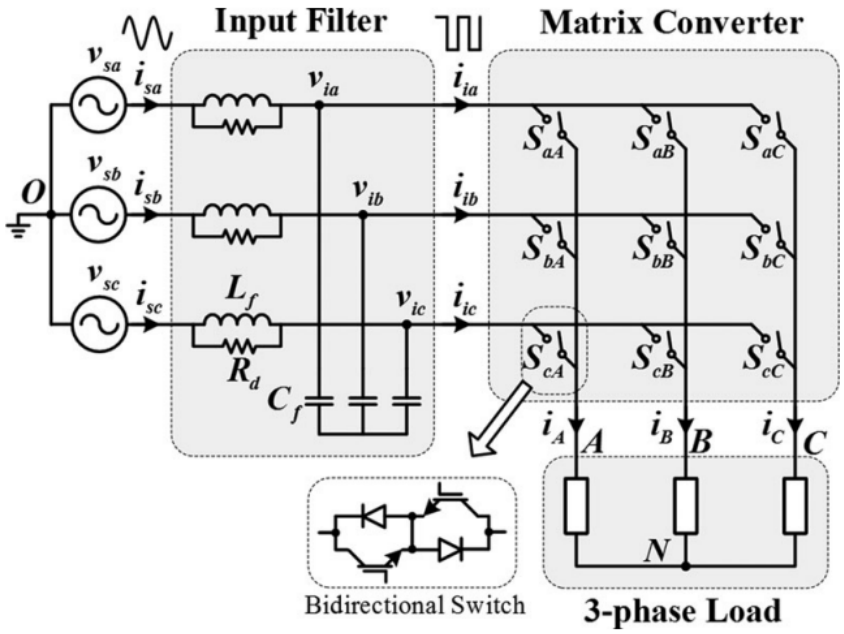

Fig. 2.23: A common three-phase to three-phase direct matrix converter configuration [62]

expense of a smaller operating envelope as depicted in Fig. 2.24 [53]. In case regeneration

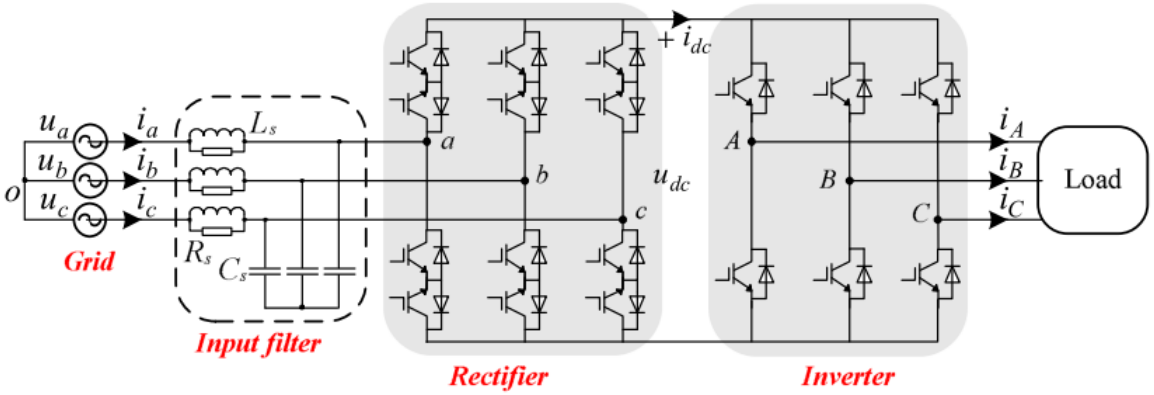

Fig. 2.24: Schematic diagram of indirect matrix converter [63]

of electrical energy back to the grid is not allowed, an additional braking circuit is essential, which is a slightly more sophisticated solution than traditional back-to-back topologies [64]. This AC/AC converter topology has the benefit of minimizing the amount of stored energy within the converter, hence reducing the weight and volume of the passive components. Instead of having large DC link storage elements, Matrix Converters require an input filter to meet power quality standards, which is often based on a basic LC single-stage filter. While the number of semiconductor devices increases, these devices are often less stressed, resulting in similar overall reliability [65]. Multi-level Matrix Converters exist, but they are complicated topologies that have not been explored so extensively for aerospace applications. In terms of waveform quality benefits for a specific semiconductor device switching frequency, these topologies are similar to the NPC converter [53].

2.3.3.2 DC/DC Power Converter Technologies

DC/DC power conversion is needed in the MEA framework to:

- Step down the voltage level to feed the low-voltage avionics.
- Regulate the power flow among different interconnected DC buses.
- Interface with the electrochemical energy storage.

DC/DC converters are generally categorized into two categories, namely isolated and non-isolated converters. Isolated converters contain galvanic isolation as it utilizes a transformer that isolates the input from the output converter sides [66]. It can operate in a wide range of input voltages and generate a stable output voltage. Isolated converters have some significant transformer related issues, such as leakage inductance, core saturation, thermal effect, high voltage spikes across the switches, and bigger size which also makes it costly compared to non-isolated converters [66]. Non-isolated topologies do not have galvanic isolation between the input and output side, so the input side directly affect the output side of the converters. Their component count is lower in comparison to the isolated converter topology, however,they have some issues that need to be addressed, such as high duty cycle ratio of PWM, poor voltage gain, and additional circuitry for optimum operations. Both categories of converter topologies have their share of advantages and disadvantages [67]. The selection is based on application requirements. Due to a huge number of topologies for DC/DC converter, both isolated and non-isolated, it is outside the scope of this thesis to review them all, and only the previous comparison is considered.

2.4 Utilisation System (Aircraft Electric Loads)

Once the electrical power is generated and distributed throughout the aircraft, it can be used by electrical loads/services to perform a range of functions, for examples [5]:

1. Thermal management systems: WIPS and ECS
2. Motors and actuation
3. Lighting services
4. Subsystems controllers and Avionics systems

On an aircraft, the electrical power required by the thermal management systems can be substantial. The largest amount of onboard power is used to supply the anti-icing or de-icing systems, which can consume hundreds of kW. Another essential electrical heating service is windscreen heating. The heating element and the controlling thermostat are both built into the windscreen. The temperature of the element is maintained at a

predetermined level by a dedicated controller, ensuring that the windscreen is demisted at all times. An ECS's role is to ensure the passenger's physiological comfort while also ensuring that the crew has adequate working conditions. All equipment, including electrical equipment and materials, must be kept cool. To accomplish these goals, the ECS must be designed to control temperature, pressurise relevant compartments, provide adequate ventilation and fresh air to passengers, keep cabin humidity below acceptable ranges, and eliminate contaminants [68].

The typical applications of motors on onboard aircraft can be summarized as shown in Fig. 2.25 [5]: Lighting systems are an integral part of an aircraft's electrical system. Modern aircraft spend a significant amount of time flying at night or in low-visibility

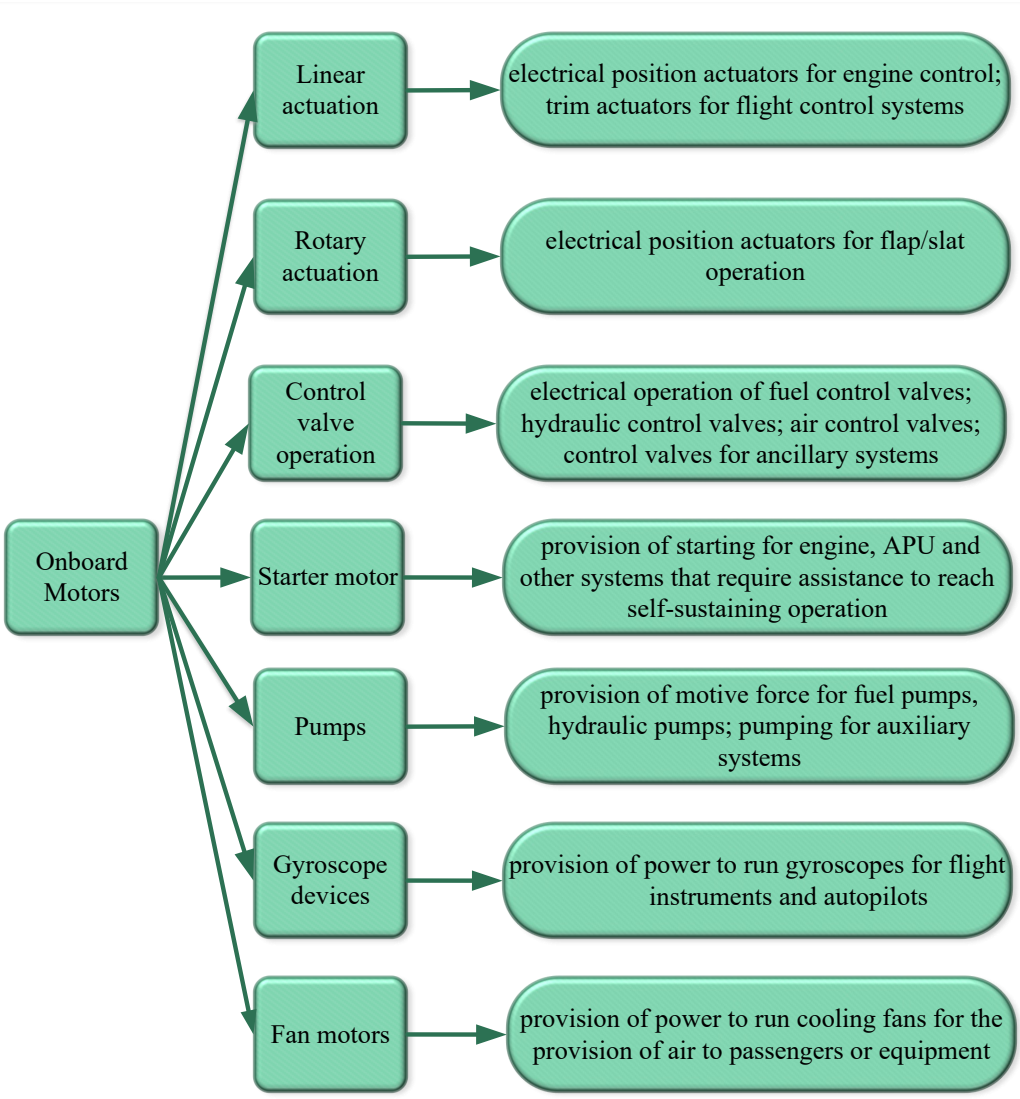

Fig. 2.25: Onboard motor applications and their functions [5]

circumstances. The provision of proper lighting is critical for the aircraft's safe operation. The lighting systems can be classified into external and internal lighting systems as shown in Table 2.3. The sophistication of the aircraft subsystems has increased as aircraft have

Table 2.3: External and Internal lighting systems on aircraft [5]

External Lighting Systems	Internal Lighting Systems
• Navigation light	• Cockpit/flight deck lighting
• Landing/taxi lights	• Passenger cabin general and personal lighting
• Emergency evacuation light	• Emergency/evacuation lighting
• Inspection lights(wing/engine anti-ice)	• Passenger information lighting
• Searchlights (for search and rescue)	• Bay lighting (cargo or equipment bays for servicing)

become more complex. Many controllers have been used to perform certain system control functions. For many years, aircraft avionics systems, communication, embracing display, and navigation operations, have been packaged into Line Replaceable Units (LRUs), which allow for quick replacement in the event of a fault occurrence. Because of increased complexity and functionality, as well as the need for rapid replacement in the event of a failure, many aircraft subsystem controllers are now packaged into similar LRUs and these LRUs can be supplied with DC or AC depending on their functions and modes of operation.

2.5 The Load Sharing Methods Used in DC Microgrids

As noted earlier, DC EPS based on multiple generators can be viewed as an islanded DC MG. Therefore, the power-sharing methods similar to those in the DC MG can be applied in the EPS of the aircraft under study. Depending on the means of communication between the interface converters, the coordinated control can be realized either by using centralized, decentralized, or distributed control [69].

2.5.1 Centralised Control Approach

Centralized control can be achieved in DC MGs by using a central controller and a digital communication network to connect it with sources and loads as shown in Fig. 2.26. For small-scale DC MGs, a master/slave approach is used to control it, and each

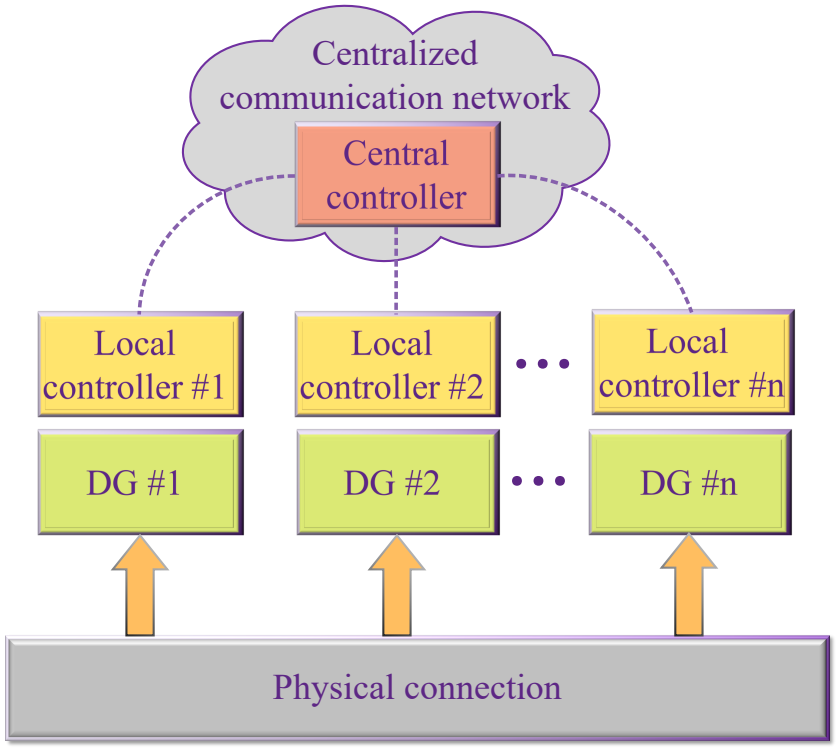

Fig. 2.26: Operating principles of centralized control in DC EPS [69]

unit can be directly controlled by the central controller that employs a high-bandwidth communication [70], [71]. A master-slave control can be realized by designating one module as a "master" and the remaining modules as "slaves". Typically, the "master" module is the one with the largest capacity, or which is the most reliable. The master module regulates the load voltage and generates current references for the other "slave" modules [72]. On the other hand, hierarchical control [71] is generally preferred for larger scale DC MGs because it introduces a degree of independence between multiple control levels. Moreover, it is more reliable since it continues to function even if centralized control fails. Local converter control and Digital Communication Link (DCL)-based coordinated control, which are decoupled by at least an order of magnitude in control bandwidth, are used together to achieve hierarchical control [73]. The coordinated functions may involve

secondary/tertiary DC voltage regulation, power flow control, and various grid-interactive control objectives, such as unit commitment and changing operational modes, or global optimization aimed at maximizing efficiency, minimizing operating cost, etc as shown in Fig. 2.27.

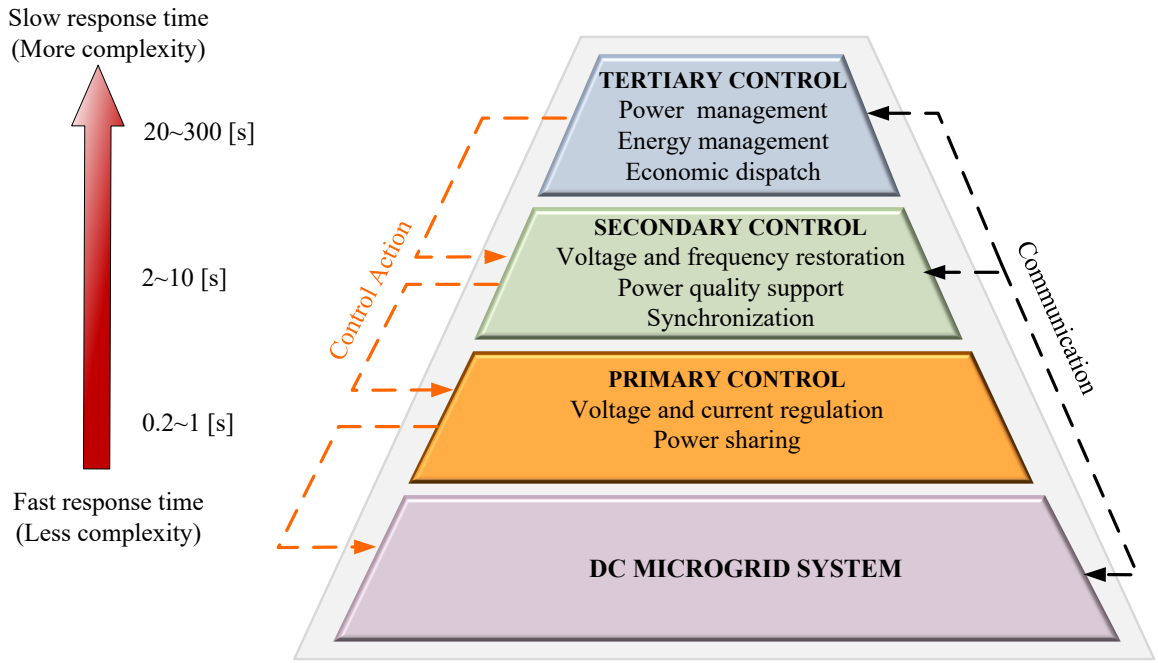

Fig. 2.27: Hierarchical control of DC MGs

Reference [74] proposes a centralized supervision control method for achieving the adaptive functioning of a DC MG-based data center. The control scheme has eight operation modes and the features of 23 transitions between them have been investigated. A hierarchical control scheme for the reliable and cost-effective operation of stand-alone DC MGs is presented [75]. With a different State of Charge (SoC) of onboard batteries, the DC bus regulation and prioritizations for batteries charging or discharging are investigated. Meanwhile, load shedding is investigated for harsh operating situations.
Since all essential data may be collected and processed in a single controller, centralized control provides the ideal foundation for the use of sophisticated control features. However, the main drawback of this strategy is that it has a single point of failure. The commands from/to the control will not be transmitted if the central controller or any other important communication connection fails, and the associated control objectives will most likely not be realized [69].

2.5.2 Distributed Control Approach

As illustrated in Fig. 2.28, distributed control refers to a control principle in which there is no central control unit and Local Controllers (LC)s only connect through specific DCLs. The key benefit of this method is that it allows the system to function normally even if some communication links fail, as long as the communication network stays linked. As a result, distributed control is protected from a single point of failure. This technique can achieve functions that are similar to centralized control [69]. However,

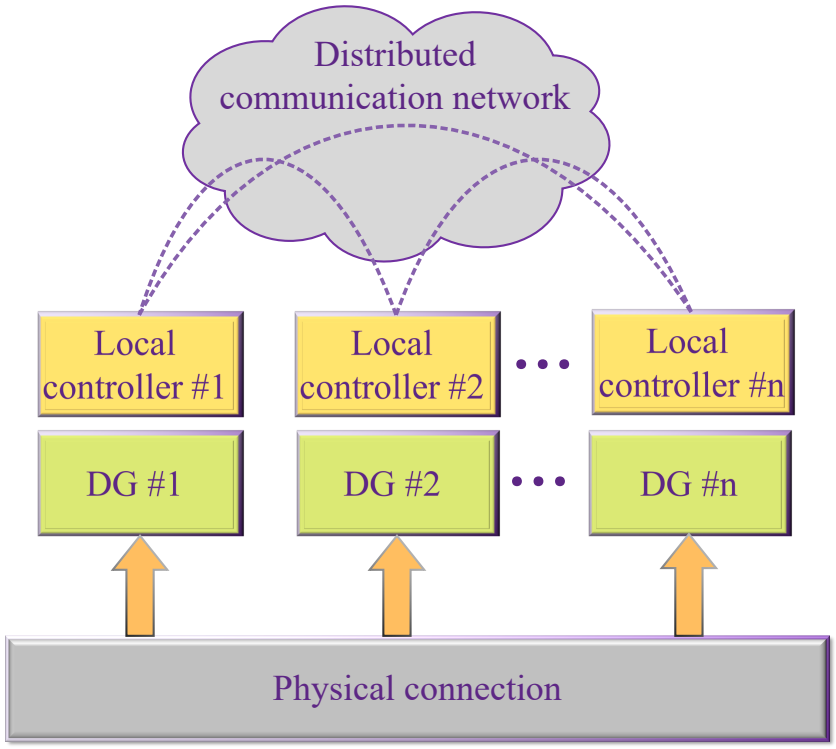

Fig. 2.28: Operating principles of distributed control in DC EPS [69]

the information transmitted over DCLs must first be adequately processed in order to allow these features. The information transmitted between LCs can only contain locally available variables. To be more specific, if the two units aren't connected by a DCL, they don't have direct access to each other's data, and their ability to observe the system is limited. A consensus algorithm can be employed to overcome this problem and to bring an LC's degree of awareness closer to that of a central controller. A consensus algorithm is a simple protocol implemented within each LC that continuously adds up all algebraic differences of some variable(s) of interest present in a specific LC and those present

in LCs adjacent to it [76], [77]. For LC $\#i$, this definition can also be expressed as follows:

$$\dot{x_i}(t) = \sum_{j \in N_i} [x_i(t) - x_j(t)] + b_i(t) \tag{2.1}$$

where $x_i(t)$ and $x_j(t)$ are the values of variables of interest in LC$\#i$ and LC$\#j$, respectively. Here, j is iterated through the whole set of neighbours of LC$\#i$ which is represented by N_i. While $b_i(t)$ is an optional input bias of the LC, which can be used to declare it as a virtual leader.

Consensus techniques have been used recently in a variety of MG applications [78], [79]. Some of these are discussed below. In [80] the average DC voltage and average DC current obtained by the low-bandwidth communication-based consensus approach are controlled by two additional PI controllers. As a result, the objectives of restoring DC voltage and improving output current sharing accuracy can be met simultaneously. It should be emphasized that only static averaging was utilized in this application because it was expected that all units could communicate with one another. In [78], a noise-resilient DC voltage observer is built using the nearby DG's knowledge to correct the local voltage set points, using a dynamic consensus process. A current regulator is also used to compare the local current to that of the neighbours, so that the current sharing error is removed.

2.5.3 Decentralised Control Approach

Decentralized coordinating techniques use local measurement to implement local regulation as shown in Fig. 2.29 and this can be achieved exclusively by LCs. Because there are no communication links between the sources or a centralized controller, each parallel module can operate independently, relying on local measurements and controllers. Thus, the system reliability and modularity are increased [73]. The most common decentralized methods that can coordinate the performance of multiple converters in DC MGs are the Distributed Power System (DPS), the adaptive adjustment of droop coefficients, and the Power Line Signaling (PLS) [69].

For DC MGs, DPS is the most widely used decentralized coordination method [69].

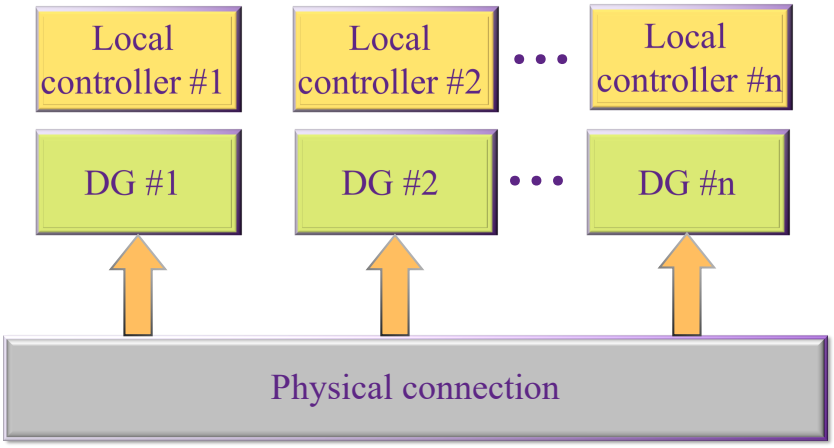

Fig. 2.29: Operating principles of decentralised control in DC EPS [69]

By imposing and identifying variations in the common DC bus voltage, the DPS method allows for coordinated operation of different units in DC MGs [81], [82] The DPS principle is illustrated in Fig. 2.30, where three operating modes are constructed, each of which incorporates a different combination of Photovoltaic (PV), ESS, and AC grid interfacing converter operating states. Depending on their internal operating mode, units are represented as current sources/sinks or by Thevenin equivalent circuits, as shown in Fig. 2.30. The Thevenin circuit truly shows that a certain unit is in droop control mode. After that, the voltage source becomes a voltage reference, and the series impedance becomes a virtual impedance. Different preset DC bus voltage values trigger transitions between different modes. To summarise up the previous discussion, DPS relies solely on

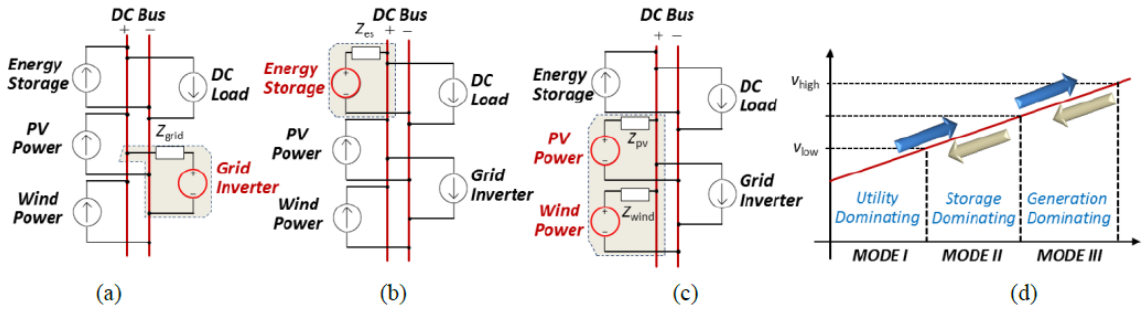

Fig. 2.30: Operation modes and basic principle of the DBS approach. (a) Utility dominating mode. (b) Storage dominating mode. (c) Generation dominating mode. (d) Basic principle of the DBS approach [69]

local data and does not require any additional components other than interface converters. As a result, it is simple to construct. The most important consideration here is choosing adequate voltage levels for identifying distinct operation modes (as indicated in Fig. 2.30 (d)). The DC bus voltage fluctuations will exceed the permissible range if the difference between adjacent voltage levels is too large. Nonetheless, the difference between the voltage levels should also not be too small, as the sensor inaccuracy and DC bus voltage ripples could make reliable detection of proper operating modes impossible [69].

Another decentralized method for coordinated control that can be used is PLS. Sinusoidal signals of a certain frequency are injected into the DC bus via amplifiers, allowing each device to communicate and receive data about its status, performance, history, and internal operational mode. Despite the fact that PLS uses digital communication, it is classified as decentralized in this case because the power network is the only means of communication. This mode of communication is also known as Power Line Communication (PLC) in the power systems literature [83]. PLS is more difficult to deploy compared to other decentralized approaches like DPS and adaptive droop. Furthermore, it is typically used solely to switch operating modes or shut down corrupted system components, and it is not ideal for power-sharing. Sinusoidal signals are only periodically injected into the system, as opposed to permanent voltage deviation in the common DC bus, which is inherent in DPS and adaptive droop systems. As a result, when compared to other methods, the quality of the voltage waveform can be considered to have improved to some degree [69].

Droop control has been widely accepted as a decentralized control method since there is no reliance on communication links. The desired power or current sharing conditions can be obtained by implementing specific droop characteristics. Droop control is usually accomplished by adding a virtual resistance to an existing system. Similarly to the AC system, the droop concept has already been successfully used in DC systems. The difference is that "reactive power" is not applicable and only active power is transferred. The amount of active power transferred in the DC network can be determined by the voltage. The most common DC system droop types are P-V and I-V characteristics. The relation between power or current and voltage can be given as follows:

$$V_{DCi}^{ref} = V_{oi} - P_{ci}K_{di} \tag{2.2}$$

$$V_{DCi}^{ref} = V_{oi} - I_{ci}R_{di} \tag{2.3}$$

where V_{DCi}^{ref} is the output of the droop controller, i.e., the reference value of DC output voltage of the converter number i; V_{oi} is the rated value of DC voltage; K_{di} and R_{di} are the droop coefficients in power- and current-based droop controllers; and P_{ci} and I_{ci} are the output power and current of the converter number i, respectively.

Conventional droop control does not consider the change of operating modes, so it needs to change the droop coefficients adaptively. It's typically used to balance SoC over multiple energy storage systems to prevent overcharging or over-discharging [69]. In [84]–[86], a dynamic SoC balancing approach is obtained by modifying the droop coefficients in both charging and discharging operations depending on SoC. Various functions have been developed to manage the SoC convergence speed as well as the system's stability attributes at the same time. The main drawback of the adaptive droop coefficients method is the potential instability caused by incorrectly designed droop characteristics. Thus, a trade-off always exists between allowable voltage deviation and the stability of the system, i.e. higher voltage deviation is associated with higher phase margin.

In summary, Droop control, as a type of decentralized control system, can accomplish optimal-power sharing between parallel sources using local variable information. Droop control is a good candidate for dealing with the power-sharing issue in DC systems due to its increased modularity and reliability. Table 2.4 summarizes the key features of each power-sharing control approach.

Table 2.4: Comparison among different control approaches

	Centralised control	Distributed control	Decentralised control
Communication medium	DCL	DCL	Power line
Centralised controller	Yes	No	No
Modularity	Low	High	High
Reliability	Low	Medium	High
Single point of failure	Yes	No	No
Advantages	Proper coordination and leadership	Improved Immunity to single point of failure	Local measurement and regulation
Disadvantages	Single point of failure	Complex interaction network	Lack of global information

2.6 Energy Management Strategies in Aircraft

The goal of an EM strategy is to ensure the stability and quality of the EPS network by managing the power flow while respecting nominal operating points and avoiding unfavourable conditions of usage i.e. high cycling rates for batteries or high dynamics power demands for generators [87]. Moreover, during the development of EPS EM strategies, the safe operation of the EPS is another critical factor to consider. By designing the right EM strategy the system weight is minimized hence, the overall efficiency is improved. Further, a properly designed management strategy provides the potential for the aircraft to operate at it is maximum performance under fault conditions. To achieve these aims the controller can be given the task of reconfiguring the system by switching on or off a number of circuit breakers based on the reconfiguration strategy [88]. The reconfiguration approach is utilized to find the correct power path for each load to be fed by using switches while considering the optimization of the system in terms of power flow and avoiding unsafe configurations [89], [90]. The EPS is managed by the control system in order to maintain an uninterruptible power supply for loads. However, rules must be defined to avoid unsafe conditions such as creating parallel power paths between two sources, or discharging of the batteries beyond a pre-set limit. The most common methods for the implementation of an EPS control strategy will be discussed in the following section.

2.6.1 Implementation of EPS Logic Control

The controller which performs the EM strategy can be implemented using different methods. For instance, a Knowledge-based method, Linear Temporal Logic (LTL) method, or finite state machine method [91]. A knowledge-based method was developed by NASA's Johnson Space Centre from 1985 to 1996 and is implemented in the C Language Integrated Production System (CLIPS) programming language. CLIPS is a rule-based programming language useful for creating expert systems and other programs where a heuristic solution is easier to implement and maintain compared to an algorithmic solution. CLIPS can be installed and used, on a wide range of platforms and has been

available as public domain software since 1996[92]. The Knowledge-based approach is based on the implementation of the business rules and mandatory rules in a single framework. For example, the business rules aim to produce reconfiguration solutions and mandatory rules are responsible for checking the validity of the proposed solutions. The fundamental structure of a rule consists of two key parts: a condition part (IF) and action part (THEN). When all the conditions of the rule are satisfied, the rule can be applied and all the actions are performed [89]. The advantages of this approach include the capacity to activate rules when the conditions are satisfied, and a priority level can be specified for each rule. If multiple rules can be applied at the same time, the highest priority rule would be activated at first.

Linear temporal logic is an extension of propositional logic that integrates notions of temporal ordering to judge the correctness over a sequence of states [93]. The use of temporal logics has been observed in various applications to formally define and verify behavioural properties, including embedded systems, robotics, and controls. Using LTL to control the EPS has the merit that the EPS can be seen as a reactive system (system reacts to dynamic changes in the environment). Where the states depend on the inputs, outputs, and execution of the system.

A Finite State Machine (FSM) is a way of formalizing the logic of a controller, where the controller is considered to be in one of a set number of states, and will transition to other states (or the same state) during its operation, potentially setting some outputs as a consequence of the state it is in or the transitions it performs. When LTL is used to specify a controller, a 'controller synthesis' step is usually performed, whereby an FSM is automatically generated from the LTL formulation. However, it is still much more common to generate an FSM manually and has for many years been considered a suitable tool for the control logic design of EPS management, as well as being applied to model problems in many other areas, including mathematics and artificial intelligence. FSM is a computation model that can be used to simulate sequential logic and can be implemented with hardware or software. In FSM, it is possible to model the behavior of the system as a set of states and transitions between states, which are known as reactive systems [94]. The advantages of using FSM for controller design are that it is easy to use and visualize, and formulations already exist for many powerful and fast algorithms [88].

2.6.2 Typical Implementation of Energy Management

In today's aircraft, Electric Load Management (ELM) based on fixed priorities of loads is often implemented [95]. The loads can be shed and reconnected depending on their importance during the flight. There is often a fixed, predefined priority for each controllable load and the HPLs will be shed later. The power of the generators and the loads are measured to determine the number of loads to be shed. Often a set of similar priority loads are connected to one switch so that they can be shed all at once. In the case of many loads with the same priority, the ELM uses an additional criteria to determine which loads are shed and which are not. One solution is to shed the large loads first, this keeps as many low power loads as possible connected. Another solution is to find a set of loads which consume as much as possible of generator capacity and this is called the "Knapsack Problem".

The advantages of ELM strategy are a simple basic implementation, just defining the priorities for each load and thresholds at which shedding and reconnection take place, and that proven and mature algorithms are available for it, since it has been applied for decades. Regarding the disadvantages, ELM is limited to switchable loads in most cases and cannot deal sufficiently with continuously controllable loads [95]. The priorities of loads may not be fixed during flight, as these can depend on the flight phase and other conditions, but this is not considered by the typical ELM. Further, ELM is not capable of optimizing the system efficiency or reducing the size and weight of EPS.

2.7 Single DC Bus-based Multiple−Sources Multiple-Loads EPS Topology and Challenges

Following the review of MEA power generation, distribution, utilization system, power-sharing methods, and energy management strategies, this section highlights the single-bus EPS architecture [1] with multiple generators and battery integration feeding the same bus. By utilization of this EPS topology on an aircraft, the power system redundancy is improved i.e. the parallel generation system can provide no-break power in the case the generator fails. Fig. 2.31 illustrates the single-bus EPS architecture considered

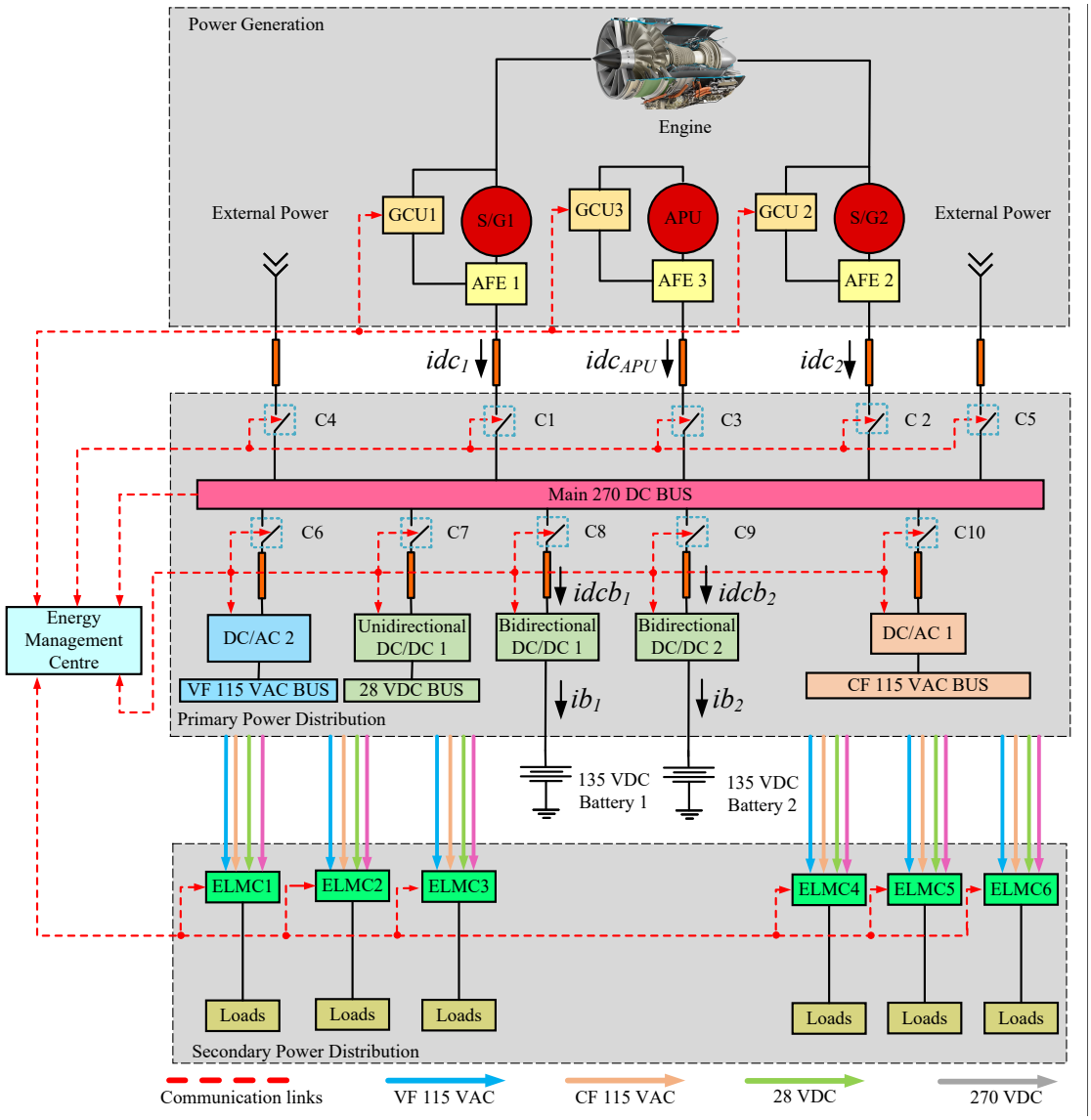

Fig. 2.31: Single Bus EPS architecture

in this study, where the two S/G (PMM) are driven directly by the High Pressure (HP) and Low Pressure (LP) engine shafts. This arrangement ensures that the power extracted from the engine is exploited efficiently as, conventionally, generators are coupled only to the HP shaft because the HP shaft features a relatively high and constant speed and this leads to minimizing the weight and size of the coupled HP generator [96]. However, they can operate at variable speeds. The electrical terminals of generators are connected to the main DC bus normally 270 VDC via AFEs. As mentioned in Section 1.3 Chapter 1, the challenges for a single bus are proper power management and coordinated control of the multiple sources and loads, system losses minimization, integration of energy storage, and

finally, energy management strategies to ensure that the vital loads are supplied under different flight scenarios. The potential solutions for the aforementioned challenges will be proposed in this thesis.

2.8 Conclusion on Chapter 2

Through this chapter, the evolution of aircraft electrical power systems, including power generation, distribution and conversion, utilization, and energy management were discussed. The different electric power generation options were reviewed and emphasized. The candidates of power generating system, electric machines for the S/G, and battery storage system have been presented and compared. Moreover, this chapter reviewed the control strategies of the DC power system and power-sharing methods among the parallel generation sources. Based on the dependency on the communication link, centralized control, distributed control, and decentralized control are presented and discussed. It may be concluded that distributed control can reach information awareness that is comparable to centralized control. As a result, objectives like output current sharing, voltage regulation, global efficiency improvement, SoC balancing, and others can be achieved.

Distributed control has more useful features than decentralized control, e.g. protecting against a single point of failure, as shown in Table 2.4. The complexity of analytical performance analysis, i.e., the assessment of convergence speed and stability margins, is its main drawback, particularly in non-ideal environments with communication time delays and measurement errors.

In addition, this chapter provided an overview of the energy management strategies in aircraft, the various methods of logic control implementation, and the typical implementation of energy management in today's aircraft. Overall, this chapter described the challenges of the power system under investigation and presented the state-of-the-art research on the power system topology and power management. Finally, based on the detailed review of the MEA EPS, the single DC bus topology with multiple sources and battery integration is chosen in this study due to its simplicity and improved redundancy. In this thesis, the potential solutions for the challenges of this topology i.e. battery integration, system losses minimization, load sharing, and energy management of the increased diversity of onboard loads and sources will be investigated in the next chapters.

Chapter 3

Single Bus EPS topology with Integrated Batteries

This chapter provides the pros and cons of utilizing the HVDC system in MEA based on the single bus topology as illustrated by Fig. 3.1. The Flying crane aircraft [97] has been selected for EPS load analysis and used to determine the capacity of all system components. Based on this, the sizing of core EPS components including the main generators, APU, and batteries has been conducted according to the load analysis. These calculations will be required to validate the smart energy management strategy that will be introduced in Chapter 8.

3.1 Introduction

As the demand for electric power in modern aircraft rises dramatically, low maintenance and a high EPS reliability are required for the design of advanced aircraft platforms. The 270 HVDC EPS concept is considered as the optimal option due to its relative safety, simplicity, flexibility, and unique ability of DC systems to supply uninterrupted power to electrical loads [98]. In addition to the advantages already outlined above, the following advantages of HVDC system can be added [97]:

1. High efficiency improvement, as some components associated with the AC system are not needed in DC, such as Constant Speed Drive (CSD) and power converter

which are utilised in VSCF generating system, so the power losses in the DC system occur in fewer places: the generator and its corresponding AC/DC converter.

2. DC systems transmission are typically lighter, as conductor mass is reduced compared to other types of power (no reactive power ampacity) and only two conductors are required.

3. 270V DC or higher voltage for power distribution can be obtained directly from full-wave rectification of three phases AC 115V generators by employing, for example, traditional TRU.

4. High reliability compared to the CSD/VSCF AC generating system, due to the simple architecture of DC systems.

5. Power continuity is the unique feature of a DC power system as it is easy to connect multiple sources in parallel. Therefore, it is easier to provide uninterrupted power to the DC bus and the loads.

6. Some types of onboard equipment (e.g. radar) require 270 VDC to operate. These equipment have an integrated rectifier units that convert 115VAC to 270 VDC. Consequently, it is possible to reduce the weight of such equipment by supplying it directly from the 270 VDC bus and removing the embedded rectifier unit. Although the DC system technology is expected to be further developed, in comparison with the AC system the main disadvantage of the DC system is the higher risk of arcing and increased risk of partial discharge when operating at higher altitudes and low pressure.

3.2 The EPS Under Study Description

This section gives an overview of single DC bus multiple-sources multiple-loads EPS with battery system integration as shown in Fig. 3.1. This power distribution topology can be conditionally divided into three stages, namely power generation, primary power distribution, and secondary power distribution. At the power generation level there are two main generators driven by the engines and one APU, all interfaced with a 270 V single

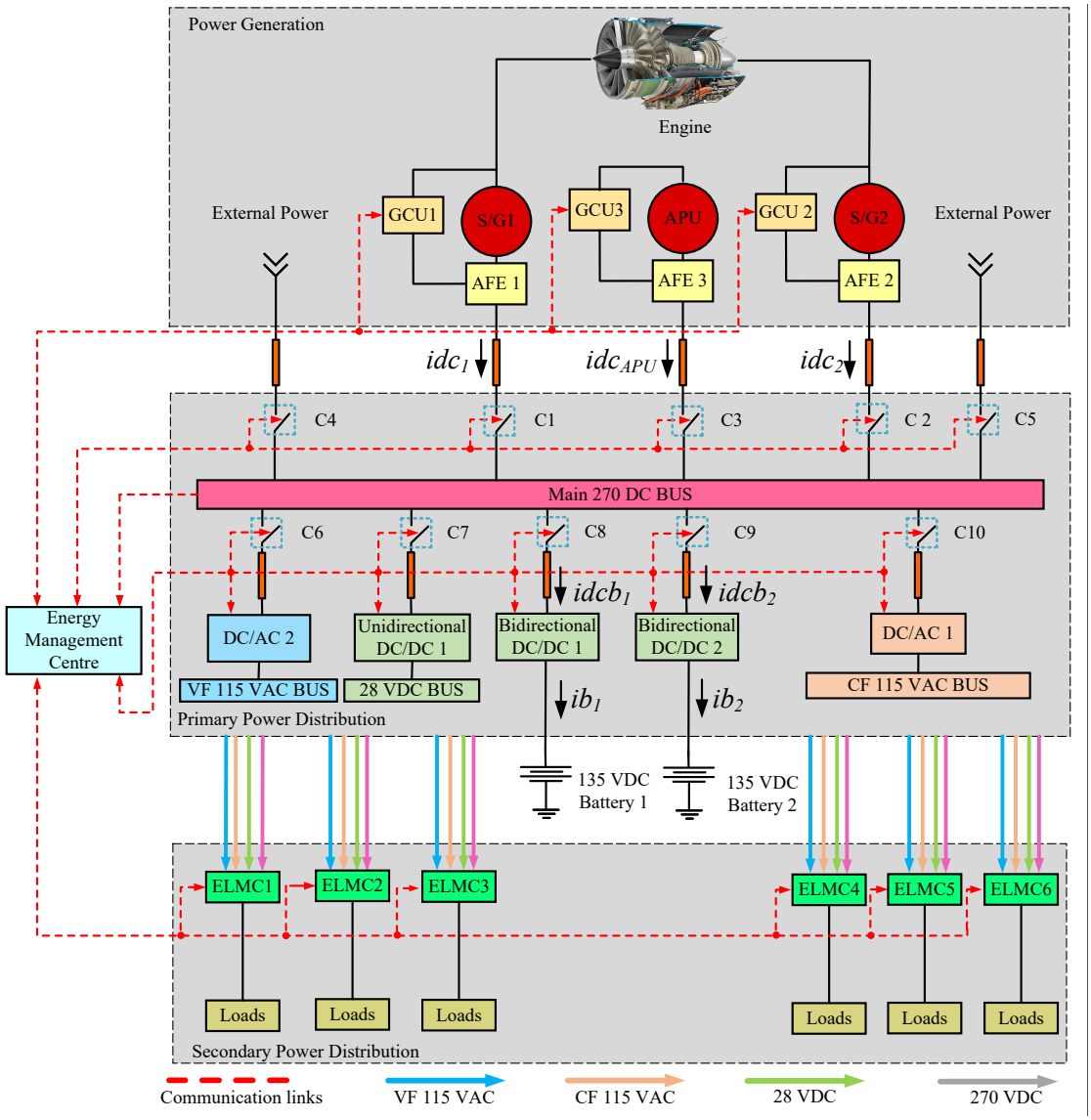

Fig. 3.1: Single Bus Power System architecture [53]

DC bus through AFE converters. The APU is used as a backup power source during the flight when necessary (e.g. during generator failures) and provides power to the required loads during ground operations, which makes the aircraft electrically self-sufficient on the ground.

The GCU controls the operation of the generator circuit breaker, as well as other functions, e.g. voltage regulation, over-voltage and other protections, and managing parallel generator operation. There are four different voltage buses at the primary power distribution stage to supply different load types, namely: VF 115/ VAC, CF 115 VAC/400 Hz, and 28 VDC, besides 270 VDC. The conversion to different operating voltages to

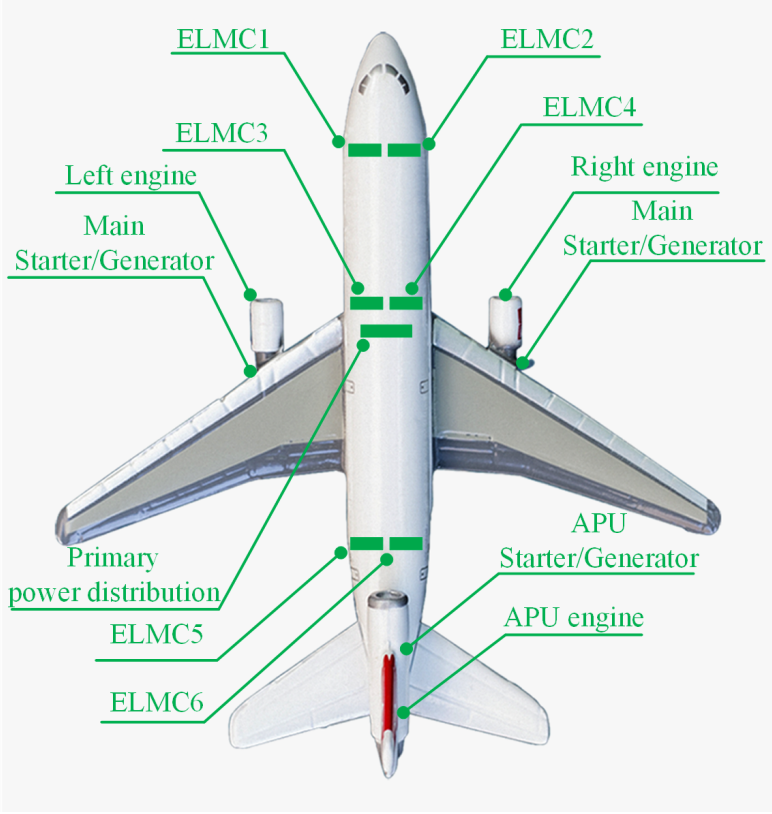

Fig. 3.2: Layout of power distribution system

drive all of the onboard loads is performed using power converters. The secondary power distribution system includes six Electric Load Management Centres (ELMC) to deliver and manage power to the loads, as shown in Fig. 3.2. During emergency situations, the EPS relies on receiving power from two Li-ion batteries. These batteries are used to provide emergency power for the high priority loads when faults occur in flight, and for starting the APU. HV power is recommended to reduce the size/weight of conductors and the power losses of the distribution system. In order to realize safe and reliable flight missions and improve the energy efficiency of MEA, the EM strategy is applied (covered in Chapter 8). The EM strategy utilizes the optimal droop gain approach that will be presented in Chapter 6 as a load-sharing method between different sources to minimize the total system losses under different flight scenarios.

3.2.1 Operation Scenarios

The possible EPS operations include five possible scenarios, namely:

- normal operation, when all equipment is operating;
- one of the power generation channels fails, APU started,
- one of the power generation channels fails, and APU fails to start.
- both of the main power generation channels fail, APU successfully started,
- Both power generation channels fail, APU failed to start(emergency),

All these scenarios will be covered in details in Chapter 8.

3.3 Load Analysis of Aircraft EPS (case study, flying Crane Aircraft)

The first step of EPS design is to understand the electric load requirement as the EPS aims to provide electric power to all of the onboard loads. Moreover, load analysis is important to determine the required generating capacity and the required number of main power sources. It is recommended that the majority of loads should be of the same voltage type as the primary source. In this study the available report on load analysis for the Flying Crane aircraft have been used [97]. The Flying Crane is a medium to short-haul aircraft with 130 seats which is mainly aimed at the domestic air transport market. It is also considered to be a competitor of the current aircraft in the B737 and A320 series [97]. The load analysis must include continuous analysis, 5-minute analysis, and 5-second analysis. Due to confidentiality issues, the detailed load information could not be obtained, therefore, the 5-second analysis could not be included in this study. All of these loads are divided into different categories based on their functions as follows:

- Low Priority Loads (LPL): these are not related to flight safety and can be shed in case of power generation shortage.
- Medium Priority Loads (MPL): these loads are required to operate aircraft safely and they are divided into 4 equal separate parts. Some of them can be shed in case of deficiency of generated power, for example when only one generator is operating.

- High Priority Loads (HPL): these are critical for flight safety, hence must operate under any circumstances during the flight, even in the harshest emergency situations.

Table 3.1 shows the load analysis results for the Flying Crane aircraft including continuous and intermittent or 5-minute loads. It should be noted that the Environmental Control System (ECS) power requirement takes nearly half of the total power required, and ECS is powered by 270 VDC.

Table 3.1: Flying Crane aircraft data

Load category	Ground	Take-off	Climb	Cruise	Descending	Loiter	Landing	Unit
Low priority (C)	8.25	7.4	39.68	50.3	39.68	7.4	40.53	kW
Low priority (C+T)	10.25	7.4	39.68	50.3	39.68	7.4	53.83	kW
Medium priority (C)	281.2	327.73	328.53	291.82	328.53	315.8	315.73	kW
Medium priority (C+T)	291.2	343.53	328.53	304.53	338.53	315.8	346.93	kW
High priority (C)	4	3	3	3	3	3	3	kW
Total (C)	293.5	338.13	371.21	345.12	371.21	326.2	359.26	kW
Total (C+T)	305.5	353.93	371.21	357.83	381.21	326.2	403.75	kW
Duration	t_1	t_2	t_3	t_4	t_5	t_6	t_7	Minutes
C= Continuous T= Intermittent								

3.4 Sizing of the Major sub-systems

The size of the components here refers to determining the capacity of all generators and power conversion devices. The sizing procedure is based on the load requirement analysis as well as on the following criteria [97]:

1. The maximum load requirement and the operating cycle can be determined. For example in [97], 33% to 50% additional power of maximum loads requirements P_{load}^{max} should be considered when sizing the generator to allow for some safety margin. It is assumed a unity power factor in this study.

2. In order to size the generator properly, the overload requirement needs to be considered and it is assumed here to be 10% of rated capacity (P_{NG}) for 5 minutes.

3. In addition, if the generator provides engine starting functionality, i.e. works as S/G, the power requirement for engine starting must be considered. If the power in starting mode exceeds the maximum load power requested in generation mode, then the power generating capability should be chosen based on the power in starting mode.

4. In terms of the power conversion equipment, the capabilities of these equipment are according to the load analysis. Normally, the safety margin is set to 33% to 59% of the maximum generator power [98].

5. On civil aircraft, the capacity of the APU generator is equal to the capacity of the main generator.

6. The battery should be capable of providing different functions, e.g. starting the APU, powering the HPLs under emergency conditions (normally for 30 minutes [98]), and supplying part/two parts of MPLs for 5 minutes.

According to the above sizing criteria, the detailed sizing procedures will be presented in the following subsections.

3.4.1 Sizing of The Main Generators

Under normal circumstances, all of the loads are powered by the 2 generators available in the aircraft. Therefore, the nominal generating capacity is determined by the total power demand of all of the continuous loads. According to the sizing criteria in step 1, an additional 33% capacity should be considered. The following equation is used to determine the size of each of the main generators:

$$P_{NG} = \frac{P_{load}^{max}}{2} * 1.33 \tag{3.1}$$

where P_{NG} is the rated of each of the main generators and P_{load}^{max} is the maximum power requirement of all continuous loads onboard.

According to the load analysis discussed previously, the maximum continuous power demand happens during the climb and descending phases. Therefore, P_{load}^{max}=371.21 kW and P_{NG}= 247 kW, hence the generator rated capacity is selected to be 250 kW. It should

be noted that the associated power converters are rated of the same power levels as the generators.

3.4.2 Sizing of the Auxiliary Power Unit

The function of the APU generator is to replace either (or both) main generators if they fail during flight. Therefore, the reliability of the power supply is affected by the capacity of the APU generator. The APU is usually rated to the same power as the main generator. At present, most aircraft developers adopt this approach. For example, the main power in a Boeing 777 is provided by two generators of 120 kVA each, and the APU capacity is 120 kVA as well [5].

3.4.3 Sizing of the Batteries

As aforementioned in Section 2.2.7, the function of a battery for aircraft is to power the HPLs in flight, start the APU and supply MPL when a power shortage has occurred. The emergency here refers to the failure of all other power generation sources. In such an emergency situation from the aircraft's point of view, the only remaining alternative for the pilot is to perform a emergency landing. Consequently, only the HPLs need to be powered in this scenario. The minimum duration for emergency power supply required is of at least 5 minutes according to the airworthiness regulation CCAR25 1351 [97]. In this case study, it is assumed that the battery should supply critical loads for 30 minutes. The starting time required for the APU engine is assumed here to be 45 seconds and to start the APU, 10 kW of power is required. As a matter of safety and following the recommendations in [45], the starting time is taken for the worst-case scenario (three attempts to be made for starting and 1 minute cooling period), the starting time is taken as 5 minutes in total and this is assumed to be on the safe side. The capacity of the battery and the minimum energy required are calculated as follow:

$$C_B = \frac{P_B}{V_B} \times \frac{t}{60} \tag{3.2}$$

$$E_{min} = P_B \times \frac{t}{60} \tag{3.3}$$

where

- C_B is the battery capacity (Ah)
- P_B is the load power (W)
- V_B is the battery terminal voltage (V)
- t is the time (minutes)
- E_{min} is the minimum energy required (Wh)

The nominal battery voltage is chosen here to be 135 V so that duty cycle at zero current will be 0.5, which allows for an equal range of duty cycle variation for buck/boost modes.

- The starting process requires 10 kW for 5 minutes, the minimum battery capacity is 6.2 Ah, and the minimum energy required is 834 Wh.
- The emergency loads require a power of 4.5 kW with 25% extra for 30 minutes, hence the minimum battery capacity is 18.5 Ah, and the minimum required energy is 2.5 kWh.
- The power required from the battery pack is set equal to 75 kW for five minutes. The corresponding minimum battery capacity is calculated, and it is equal to 46.296 Ah while the minimum required energy is 6.250 kWh.

According to these calculations, the maximum power required from the battery is 75 kW, and this should be guaranteed for 5 minutes. The maximum discharging current of the battery cell shown in Table 3.2 is 50 A (at 20C), hence, if assumed all battery cells are connected in series only, the voltage of the battery stack required to deliver 75 kW at 50 A would be as follows:

$$V = \frac{P}{I} = \frac{75000}{50} = 1500V \tag{3.4}$$

It is convenient to split the load current into several parallel connected branches instead of using only one string, and to reduce the voltage. In this study case the voltage of each branch is chosen to be 135V, therefore the number of branches is 1500/135=12, but this number could not satisfy the minimum energy required (6.250 kWh) so that it is chosen to have 20 branches in parallel, as shown in Fig. 3.3. The total maximum current that can

Table 3.2: A123's Nano phosphate lithium iron phosphate (LiFePO4) cell datasheet [99]

Parameter	Value
Nominal voltage	3.3 V
Nominal capacity	2.5 Ah
Weight	0.076 kg
Maximum charging current continuous	20 A
Maximum discharge current continuous	50 A
Cut off voltage	2.487 V
Fully charged voltage	3.85 V
Watt hour	8.25 Wh
Operating temperature range	-40^o to 60^o

be supplied to the load is 20×50=1000 A at 135V. The number of cells for each branch is approximately is (135/3.3)= 41 cells, then the total number of cells is 41×20=820 cells. The energy stored in one battery pack is 820×8.25=6.765 kWh, and this results in a total gross weight of 62.32 kg, if the considered Li-ion cells are used. It should be noted that this gross weight is only for the battery cells and does not include the busbars, cooling, and packaging. The fully and cut off voltages of the stack are 158 V and 102 respectively, while

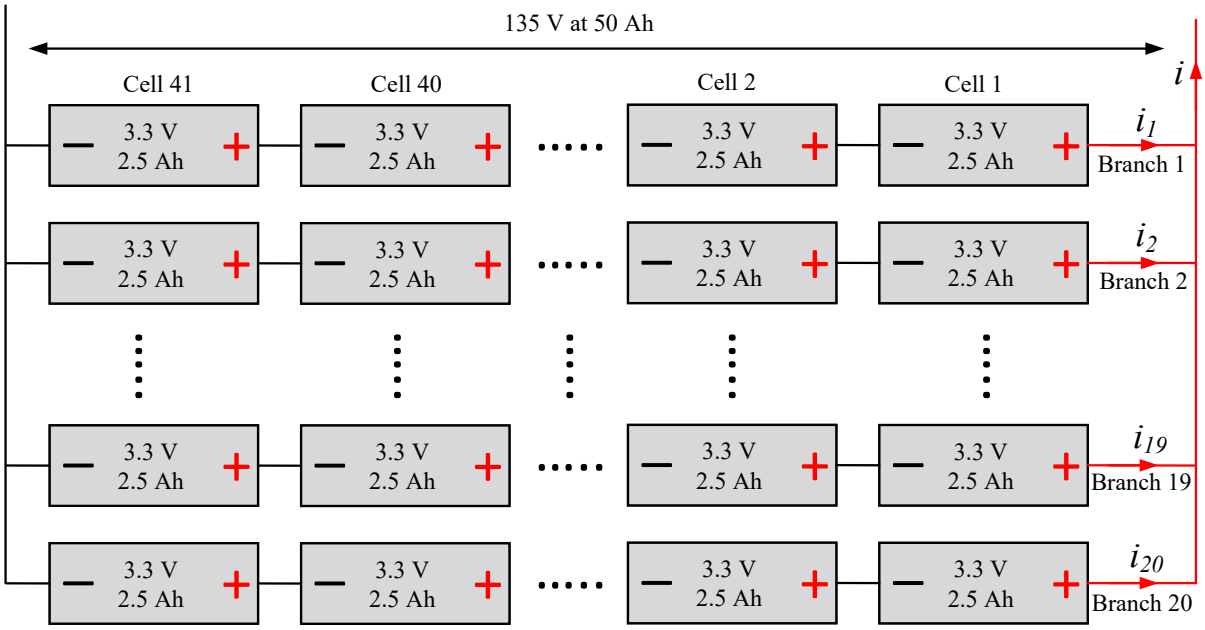

Fig. 3.3: 820 Lithium-ion battery system connected in series/parallel

the maximum charging current is 400 A. This battery pack will be capable of delivering 6765 W for 1 hour, 13.530 kW (6765×(60/30)) for 30 min or 81.18 kW (6765×(60/5)) for 5 min. Assuming the battery system is initially fully charged, after APU starting, the SOC using (3.5) reduces to 82% and Depth of Discharge DoD using (3.6) is 13%, which are acceptable levels after the APU start, as there might be some transient loads which need to be powered up by the battery immediately after the starting of APU.

$$SOC = SOC_{initial} - \frac{1}{Q}\int_0^t i(t)dt \tag{3.5}$$

$$DOD = 1 - SOC \tag{3.6}$$

The maximum state of charge SOC_{max} when fully charged is chosen here to be 95% (6.426 Wh) and the minimum state of charge SOC_{min} can be found according to the minimum energy required to supply the vital loads for 30 minutes. It should be noted that the batteries in the emergency case will discharge until zero SOC, if necessary. This energy is 2.5 kWh, which is equivalent to 37% of the total energy of one battery pack. Therefore, the required minimum SoC of each battery pack is 20%, and 30/% is selected to allow for some margin.

3.5 Conclusions on Chapter 3

This chapter discusses the advantages and disadvantages of using an HVDC system for MEA and provides an overview of the selected single bus-based topology. The power distribution system is arranged in 3 stages, including power generation, primary power distribution, and secondary power distribution. In addition, the function of each component is defined. In order to ensure that the required power is delivered to all onboard loads, a load analysis is performed to size the generators, APU, and batteries and define their rating. All of the loads are classified into three categories according to their functions: LPL, MPL, and HPL.

The sizing of the main components of the system under study EPS is necessary for implementing a suitable energy management strategy design which will be introduced in Chapter 8. Moreover, the battery sizing is required for its proposed controller design, which will be covered in Chapter 5.

Chapter 4

Enhanced Starting Control Scheme for PMM−based Starter/Generator System

The S/G scheme is one of the MEA solutions that significantly improves the electrical power generation system. In generation mode, the Variable Voltage Bus (VVB) or Voltage Wild Bus (VWB) concept is adopted in this chapter to supply increased load demand within the powertrain capabilities, machine thermal limits, and power converter maximum current [100]. This control concept is not investigated for starting mode therefore, this Chapter deals with the investigation of the VVB concept in motoring/generating modes and the improvement of S/G control to align it with the VVB EPS concept. In contrast to previous publications, the proposed control scheme uses a single current regulator to adjust the q-axis reference voltage, and the d- axis voltage is calculated considering the maximum available voltage from the converter. By integrating the proposed starter control scheme with the VVB control scheme, the S/G system can be used in a wide speed range, which allows for full utilization of the available voltage supplied by the PMM. Further, the S/G system capabilities and limitations are identified beforehand in order to address these in the control design process. The linearized model of the overall system is derived for motoring mode to assist in the controllers' design. The speed and current controllers shall be properly designed to achieve good overall performance. The analytical design results and the system performance are confirmed by time-domain simulation and

experimentation, and are compared against the traditional approach.

4.1 Introduction

Newly developed systems for MEA aim to integrate different functions in order to optimise weight and volume at the aircraft level. For example, starter-generator systems to integrate functions of the engine starting with electrical power generation when the engine is running. In MEA these functions can be accomplished by an integrated electric S/G system [101]. Previously, engine starting was performed in different ways, e.g. using the power of air, hydraulics, and pneumatic energy. With an adequate power converter, electrical machine, and control scheme, the drive system can operate as S/G. The general control aspects of S/G operation could be determined as follows:

- In starter mode, speed or torque control is essential to drive the engine accelerating it to a self-sustained speed
- In generator mode, control of the DC link bus power is the primary objective and the speed is defined by the engine.

The use of the electrical S/G system has advantages in terms of high instantly available power/torque and better efficiency over a wide speed range [59].

Due to high torque, high efficiency, fast dynamic response and high power density, the PMM is one of the potential solutions to be adopted in future S/G systems [102]–[104]. The S/G system is operating in a wide speed range and this may lead the power converter to be subjected to very high machine back-emf at high speeds. Consequently, a flux weakening algorithm should be considered to ensure that the back-emf is within the converter limits [100] .

Several flux weakening methods are presented in the literature e.g. analytical methods[103], Single Current Regulator and Voltage Angle Control (SCR-VAC) methods[105][106], torque and flux control methods[107], and non-linear control methods[108][109]. Analytical methods utilize the PMM equations to generate the required d- and q-axis currents for constant torque and constant power regions. Although these methods have simple control implementation, they are sensitive towards parameter

variations. In SCR-VAC, the output of the current controller is the reference voltages. The SCR-VAC provides robustness towards parameter variations but is unable to operate at no load condition in the FW zone. The torque and flux control method uses a look-up table to calculate the reference currents, which reduces the online computational time but requires a high amount of memory for practical implementations. In addition, this method is sensitive towards parameter variations. The non-linear control is used to replace speed and current controllers used in a conventional cascade structure. The controller parameters and system parameters are tuned online, the non-linear control techniques simplify the controller structure and are robust against parameter variation. However, the computational complexity is much higher compared to other control algorithms. In [100] at high speeds, flux weakening is employed when needed to maintain converter controllability. The d-axis current controller works over a limited range. The reference d-axis current is kept equal to zero ($i_d^* = 0$), which allows the d-axis current to change naturally and ensures the voltage is always within the limit, hence the possibility to operate at max modulation index at all times. The control plants are derived for controller design purposes in generating mode only, the starter mode is not investigated.

Therefore, both starter and generation modes for this method proposed in [100] are investigated in this Chapter, followed by consideration of proposed enhanced technique. A comparison between the two control schemes is done and verified by time-domain simulation and experiments.

4.2 Electric Power System Analysis

In order to prepare for the control plant derivation, the equations for the machine, converter, and DC link are presented. For consistency of analysis, all of the power system equations are expressed in the *dq* frame. Fig. 4.1 shows the topology of a PMM-based S/G system controlled by an AFE converter. The electrical equations of the PMM in rotational reference *dq* frame (using Park transformation) can be written as [100]:

$$v_d = R_s i_d + L_d \frac{di_d}{dt} - L_q \omega_e i_q \tag{4.1}$$

$$v_q = R_s i_q + L_q \frac{di_q}{dt} + (L_d i_d + \psi_m)\omega_e \tag{4.2}$$

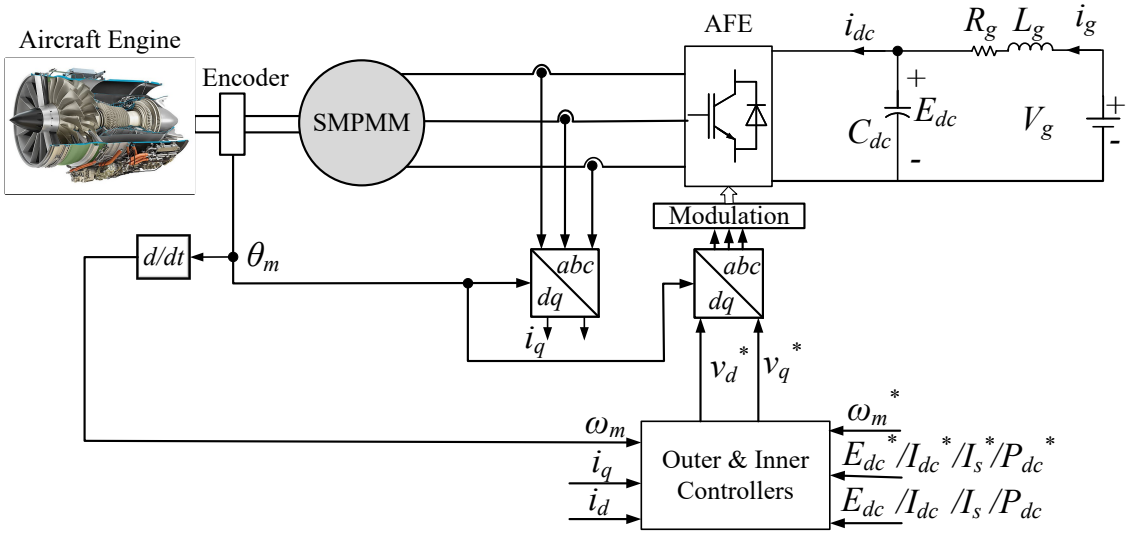

Fig. 4.1: S/G system based on PMM feed by AFE topology

where,

- $v_{d,q}$ and $i_{d,q}$ are the PMM stator voltages and currents
- R_s is the stator resistance
- ω_e is the electrical speed of the machine
- $L_{d,q}$ are PMM stator inductances in dq frame
- ψ_m is the machine flux produced by PMM
- C_{dc} is the DC bus capacitance
- E_{dc}, i_{dc} are the DC link capacitor voltage and the DC bus current
- i_g is the grid current
- V_{dc} is the DC grid voltage

The average model equation of a 2-level power converter can be represented by a complex power equation in the dq frame as [100]:

$$E_{dc} i_{dc} = \frac{3}{2}(v_d i_d + v_q i_q) \tag{4.3}$$

In this study, positive i_{dc} direction is defined when power is supplied to the machine while negative direction is when power flow is towards the DC link bus. The DC link voltage (voltage across the output capacitor C_{dc}) can be defined as:

$$C_{dc}\frac{E_{dc}}{dt} = i_g - i_{dc} \tag{4.4}$$

The DC grid is represented by an equivalent constant DC source behind constant impedance, hence the relation between the DC link capacitor voltage and DC grid voltage is given as:

$$E_{dc} + L_g\frac{di_g}{dt} + i_g R_g = V_g \tag{4.5}$$

The operating conditions of the S/G system are considered in the next section in preparation to the design process.

4.3 S/G System Capabilities and Limitations

The S/G system capabilities are identified in order to support the control design process. The control performance in the design of the S/G system is limited by two factors:

1. The maximum current limit defined by the machine rated current I_r and converter device rated current I_{conv}.

2. The inverter maximum phase voltage limit, V_{cmax}, is limited by the over modulation limit and can be defined by the DC link voltage, v_{dc} and the type of a modulation scheme.

The maximum current of the machine can be given as:

$$I_{smax} = I_s \geq \sqrt{i_q^2 + i_d^2} \tag{4.6}$$

The machine voltage magnitude is governed by:

$$\mid V_c \mid = \sqrt{v_q^2 + v_d^2} \tag{4.7}$$

When operating at high speeds, the machine back-emf is typically very high and FW control is a method to ensure that is within V_{cmax}. Using Space Vector Pulse Width

Modulation (SVPWM), V_{cmax} and the DC link capacitor voltage are linked as follows [100]:

$$V_{cmax} = \frac{V_{dcr}}{\sqrt{3}} \tag{4.8}$$

The voltage and current limits can be considered by neglecting stator resistance, because it is usually very small in a high efficiency machine, giving the transient terms:

$$v_d = -L_q \omega_e i_q \tag{4.9}$$

$$v_q = (L_d i_d + \psi_m)\omega_e \tag{4.10}$$

The voltage limit equation is derived using (4.7) and (4.9) to (4.10) as:

$$\left(\frac{V_{cmax}^2}{L_s^2 \omega_e^2}\right) = \left(i_d + \frac{\psi_m}{L_s}\right)^2 + \left(i_q + \frac{R_s \psi_m}{L_s^2 \omega_e}\right)^2 \tag{4.11}$$

where $L_d = L_q = L_s$ for a Surface Mounted Permanent Magnet Synchronous Machine (SMPMSM). Equation (4.11) shows the voltage limit follows a circle trajectory and can be plotted in the i_d-i_q plane as shown in Fig. 4.2. The radius and the center of the voltage circle are $\frac{V_{cmax}}{L_s \omega_e}$ and $\left(-\frac{\psi_m}{L_s}, -\frac{R_s \psi_m}{L_s^2 \omega_e}\right)$, respectively. It should be noted that, from Fig. 4.2, when speed increases the radius decreases. The blue circle represents the current limit while the others are the voltage limits at different operating speeds. The blue circle intersects the voltage limit circle at point (A') when i_q is maximum and i_d is zero to represent the base speed ω_b. If the speed has to be further increased moving towards

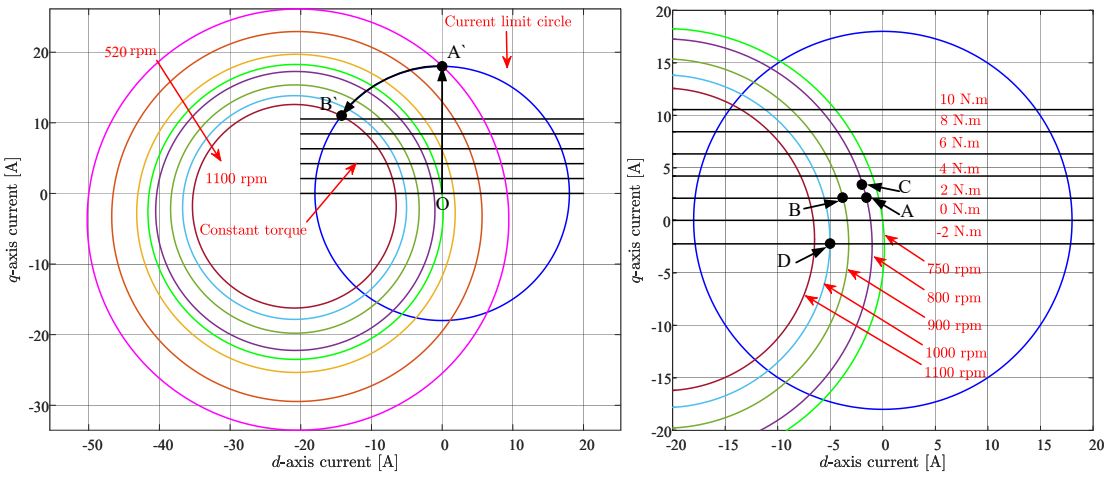

Fig. 4.2: Voltage and current limit circles @ $|V_{max}|$=50V, left: Normal circles and right: Zoom in of circles

point (B'), FW may be applied, and this is considered the lower speed value for activating FW ω_b. Using the voltage limit equation (4.11), this value was found to be 520 rpm for the PMM used in this study; the parameters are given in Appendix C, Table C.1. The speed above which FW should always be on is defined by the circle touching the origin (o) and it was found to be 750 rpm, as the ω_b.

4.4 Analysis of Variable Voltage Bus Method

The DC bus voltage has a natural opportunity to increase its output, by narrowing the region of FW operation with the current limit of the power converter and torque capabilities of the power train, only if the voltage level is not restricted. This can be accomplished via a separate bus for the WIPS, as shown in Fig. 4.3. When the WIPS requires a high amount of power, such as for anti-icing, voltage levels "above the rated" can be set, and this is referred to as a VVB or VWB bus concept. This arrangement reduces the need for local WIPS power converters, which could result in a weight reduction in the overall aircraft [100]. The disadvantages of this concept are the semiconductor losses assuming the same current operation levels are high, and the

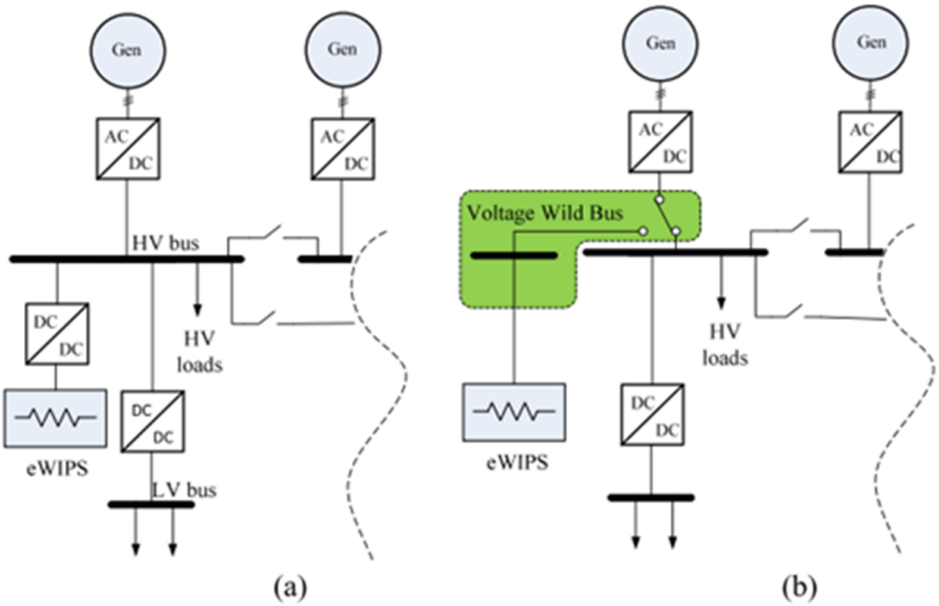

Fig. 4.3: (a) WIPS integration in current MEA EPS architectures. (b) Proposed integration [100]

need for appropriate circuit protection devices. Hence, the converter, the cooling system, and circuit protection devices may have to be over-rated to compensate for the losses. Moreover, the voltage variation should be within the maximum limits of the electrical machine as partial discharges may occur [100]. In future MEA, the VVB concept [100] can be exploit to increase the output power within powertrain capabilities, machine thermal limits, and power converter maximum current. It can be implemented using innovative sources actively controlled by power electronics to supply increased load demands under certain conditions. The structure of the VVB control method is shown in Fig. 4.4 [100]. The reference current i_q^* is selected as the output of one of the outer controllers according to the required operation: current limit controller, DC voltage controller, and DC power controller. The current limit controller is used to maintain th stator current within the designated limits. The DC voltage controller is used to keep E_{dc} constant when connected to the normal bus, and the DC power controller is used to deliver extra power to demanding loads under specific operating conditions, such as de-icing flying surfaces with WIPS.

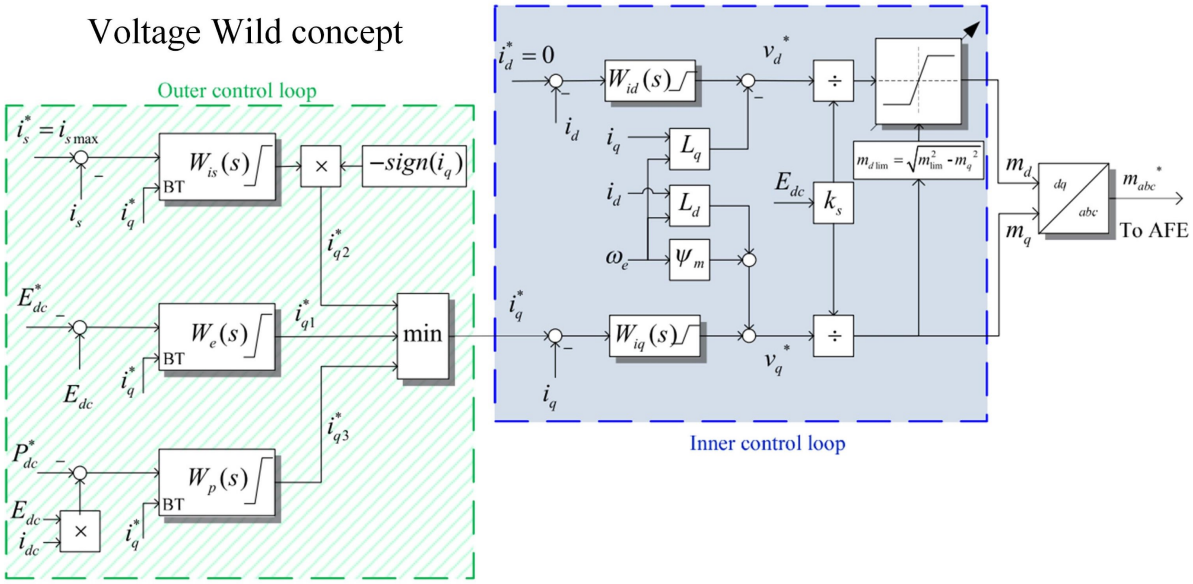

Fig. 4.4: Variable Voltage Bus control strategy of PMM [100]

4.4.1 Limitations of VVB Method

In generating mode, i_q is negative and the speed is assumed constant. By increasing i_q^* from zero to the rated value, the q-axis PI current controller W_{cq} increases its output in the negative direction to let i_q follow the reference current. Consequently, the reference q-axis voltage v_q^* decreases according to (4.12). Simultaneously, the output of the d-axis current controller W_{cd} is zero due to the limitation, but i_d is changed naturally in negative value to decrease the effect of the back emf ($\psi_m \omega_e$). Therefore, the reference voltage in the d-axis is increased in positive value as in (4.13), but still the magnitude of v_q^* and v_d^* within the limitation:

$$v_q^* = (i_q^* - i_q)\left(\frac{k_{iq} + k_{pq}s}{s}\right) + L_d i_d \omega_e + \omega_e \psi_m \tag{4.12}$$

$$v_d^* = (i_d^* - i_d)\left(\frac{k_{id} + k_{pd}s}{s}\right) - L_q i_q \omega_e \tag{4.13}$$

In starter mode, i_q is positive and the speed is assumed constant to consider FW mode. By increasing i_q^* from zero to the rated value, the controller W_{cq} increases its output in the positive direction to let i_q track the reference current to accelerate the PMM. Hence, the reference q-axis voltage v_q^* is increased according to (4.12). In the same time, i_d increases its positive value to let the output of the d-axis current controller to become positive, to decrease v_d^*, to maintain the voltage magnitude within the limits, but due to the limits it stalls at zero value. As follows from above, positive i_d values lead to further v_q^* increases causing the maximum value of voltage limit to be hit and making the system non-operational. At speeds below the base speed, the VVB method can operate in starter mode, but in limited torque mode when the back emf is smaller than the maximum value, this allows a margin for v_d^* to increase. Fig. 4.5 depicts the simulation results of testing the limitation of the VVB method in starting mode when a step speed reference from 600rpm to 800rpm, with $i_q^* = 2$A and $i_d^* = 0$A is applied using the control scheme shown in Fig. 4.4 and the machine parameters shown in Table C.1. At reference speed 600rpm, the controller W_{cq} output is positive in order for i_q to match the reference current and v_q^* is still below the maximum limit (50V). When the reference speed steps to 800rpm, i_d starts to increase in the positive direction so that v_d^* decreases but this led to an increase in v_q^*, hence v_q^* hits the maximum voltage limitation at $t \approx 1.35$s and the system reaches

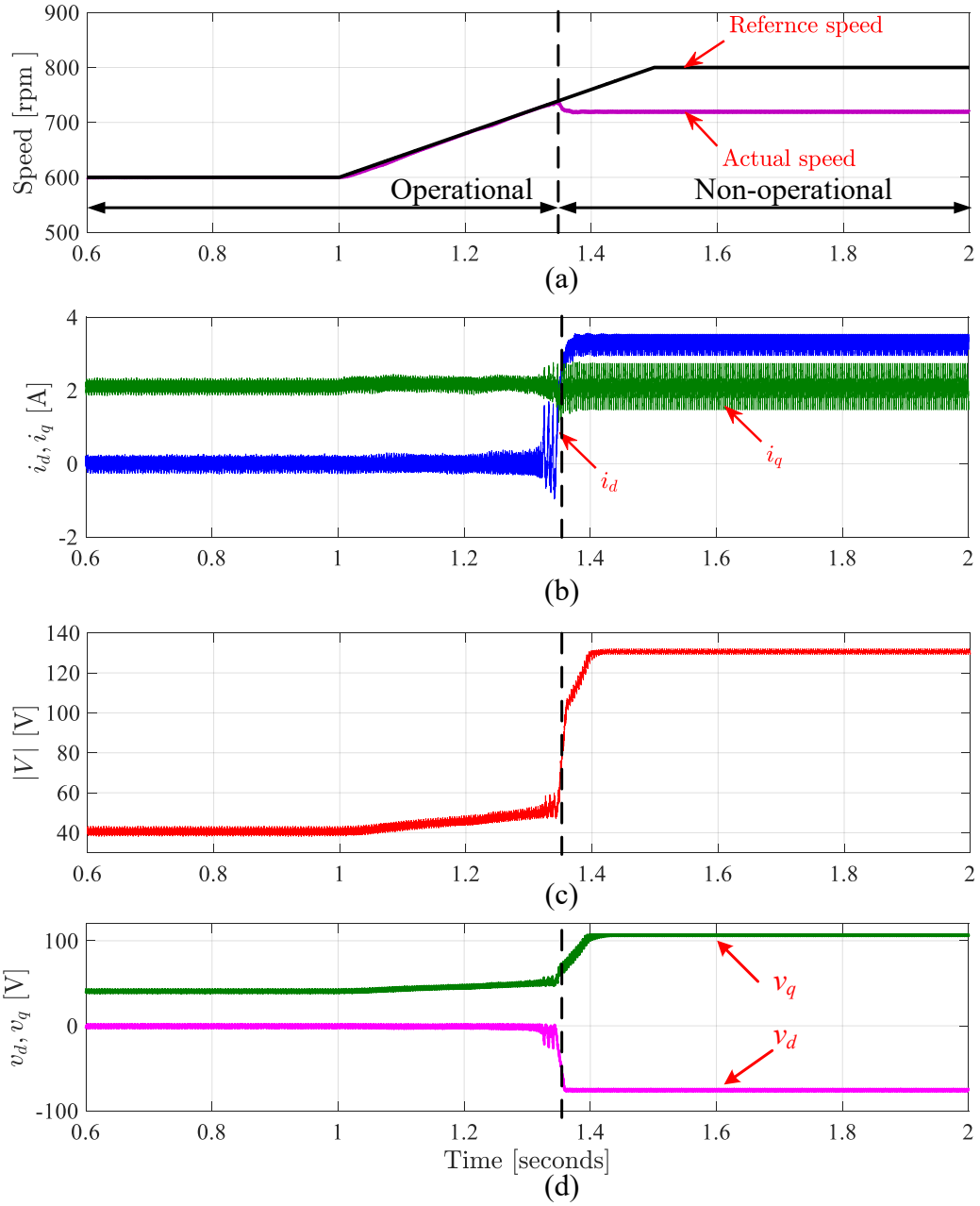

Fig. 4.5: Time response of VVB control scheme in the starter mode: a) Speed, b) *dq* currents, c) Voltage magnitude, and d) *dq* voltages

its operational limit and lose its controllability.

Based on the previous analysis, this Chapter offers a solution for the VVB control scheme enhancing it to be operational as S/G in a wide speed range. The proposed solution is considered in the next section.

4.5 Proposed Control Scheme

Based on the analysis in the previous section, it can be concluded that the VVB method can not work at high speeds (FW) in starting mode. Therefore, this section proposes a solution to overcome this issue. The proposed control scheme uses a single current controller to generate the quadrature axis voltage component reference and the direct axis component is calculated from the available maximum voltage. The proposed control scheme will be integrated with the VVB control scheme to enable the S/G system to operate in a wide speed range at full utilization of DC bus voltage. The proposed PMM-based S/G system control is shown in Fig. 4.6. The starter controller consists of low speed range and high speed range controllers. The low speed range controller (mode 1) accelerates the machine up to the base speed and it can be seen from Fig. 4.6 that, the controller is very simple as the machine normally operates at high speed. The reference q-axis voltage is calculated from the back emf and the d-axis reference voltage is obtained from the term $\omega_e L q i_q$, by ignoring the stator resistance. The high speed range controller (mode 2) is used for operating speed above the base speed, until the self-sustaining speed of the engine is reached. After the engine reaches the self-sustaining speed the switch moves to mode 3 to apply the generating controller VVB concept. A BT algorithm is applied to switch between controllers in a seamless way [100]. This algorithm takes into account the output v_q^* and maintains each controller integrator state to be of similar values. In the high speed range controller, a single current controller which controls the active power through the controller, W_{cq}, for the starter mode operated in FW is used, as shown in Fig. 4.6. Contrary to the traditional approach, here in starter mode, reversing the sign of the error signal of the q-current control loop leads to a reduction of v_q^* and increase of v_d^* as the current reference increases. The output of W_{cq} controller is the reference voltage v_q^*, and the reference voltage in the d-axis v_d^* can be calculated from (4.14).

$$v_d = -\sqrt{V_{cmax}^2 - v_q^2} \tag{4.14}$$

It can be seen from (4.1), (4.2) and (4.14) that, the system is non-linear and a linearisation is required for the controller design, which will be discussed in the next section.

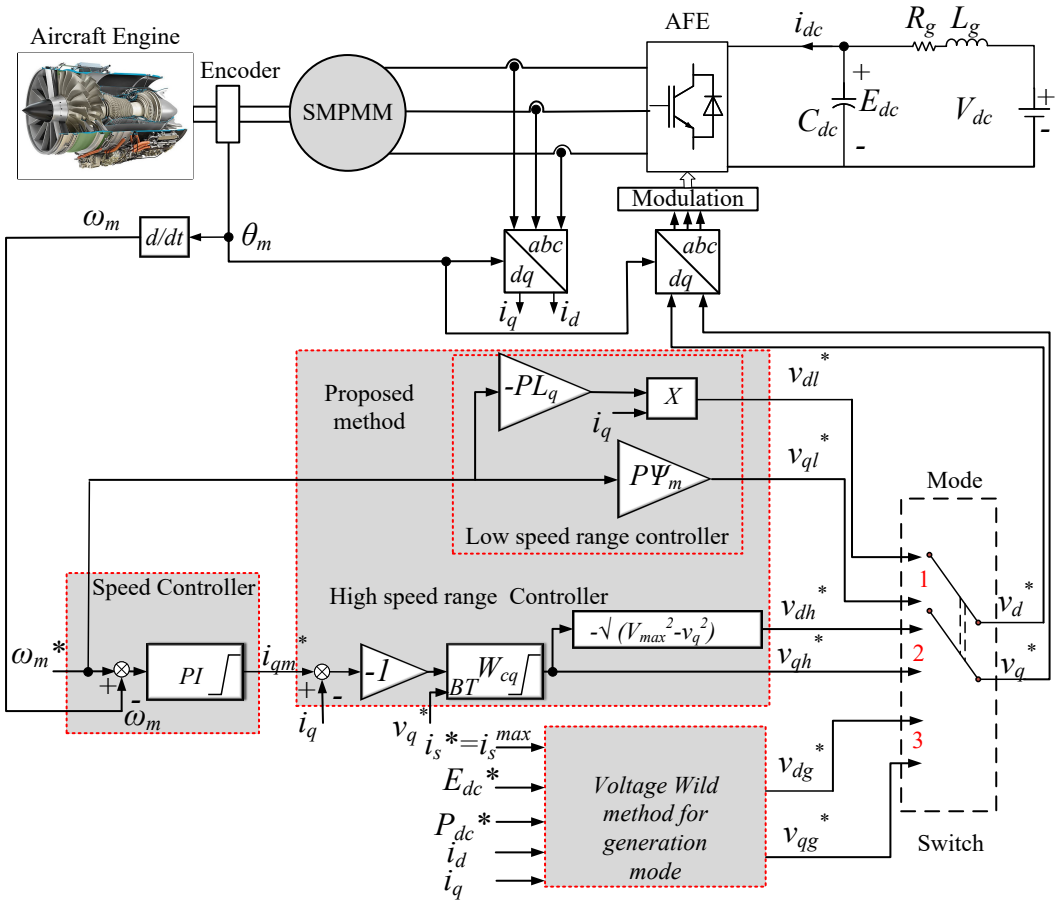

Fig. 4.6: The overall proposed system control block diagram

4.5.1 Small Signal Analysis

The linearised plants are derived in this section to support the controller design. The analysis is performed in the small signal domain which leads to linear plants. The non-linear equations (4.1) to (4.5) and (4.14) are linearised using Taylor's approximation around a given operating point. Afterword, applying the Laplace transform results in:

$$\Delta v_d = (R_s + L_d s)\Delta i_d - \omega_{eo} L_q \Delta i_q \tag{4.15}$$

$$\Delta v_q = (R_s + L_q s)\Delta i_q + \omega_{eo} L_q \Delta i_q \tag{4.16}$$

$$\Delta v_d = \frac{-v_{qo}}{v_{do}} \Delta v_q \tag{4.17}$$

It is assumed that ω_e is constant, as the speed changes are small compared to others dynamics. It is required to derive the transfer function between Δi_q and Δv_q , and from

(4.15) Δi_d can be found as:

$$\Delta i_d = \frac{\Delta v_d + \omega_{eo} L_q \Delta i_q}{R_s + L_d s} \tag{4.18}$$

Substituting (4.17) and (4.18) in (4.16) the open loop transfer function $G_{pq}(s)$ can be given by (4.19):

$$G_{pq}(s) = \frac{\Delta i_q}{\Delta v_q} = \frac{L_d s + \left(R_s + \frac{v_{qo}}{v_{do}} \omega_{eo} L_d\right)}{L_q L_d s^2 + \left(R_s L_d + R_s L_q\right) s + \left(R_s^2 + \omega_{eo}^2 L_d L_q\right)} \tag{4.19}$$

Any variable with the "o" subscript denotes its initial operating point value. The closed-loop transfer function for i_q is:

$$\frac{\Delta i_q}{\Delta i_q^*} = \frac{a_0 s^2 + a_1 s + a_2}{b_0 s^3 + b_1 s^2 + b_3} \tag{4.20}$$

where the coefficients are given in Appendix C.1.

4.6 Design of Proposed Controllers

In this section, the S/G system is designed to meet the following technical specifications to comply with the experimental rig capabilities and limitations, which will be used to verify the proposed control scheme; the machine speed is up to 800 rpm in starter mode and in generating mode the speed is 900 to 1100 rpm.

4.6.1 Design of Current Controller for Starter Mode

In this section, the transfer function in (4.19) shall be analysed under different operating conditions i.e. different speeds and loads for starter mode, then the design of the current controller, W_{cq}, for the high speed range for the worst-case scenario is presented. In starter mode, the open loop transfer function $G_{pq}(s)$ has Right Half Plane (RHP) zero and can be given as in (4.21). This zero location depends on the initial operating point as follows.

$$Z = \frac{-R_s}{L_d} - \frac{v_q^o \omega_{eo}}{v_d^o} \tag{4.21}$$

The RHP zero restricts the achievement of high dynamic performance and makes the control design a challenging task due to the additional phase lag and the normally limited

achievable closed loop bandwidth. The second order plant (4.19) has been analysed with different operating points at various speeds and loads. The load demands investigated were set at 100 %, 50%, and 25% of rated value, to cover the effect of load torque on the S/G system. The root locus of the transfer function in (4.19), with speed change at no load to ensure that the transfer functions were purely influenced by speed, can be seen in Fig. 4.7 (a). As the speed increases, the RHP zero moves towards the origin. Fig. 4.7 (b) shows the root locus for different loads at 900 rpm: the RHP zero position changed, moving towards the origin as the load impact increases. All other poles and zeros did not change due to the load variations. As can be seen from these figures, the worst-case scenarios is at the lowest speed (760rpm) and smallest load (25%), and the

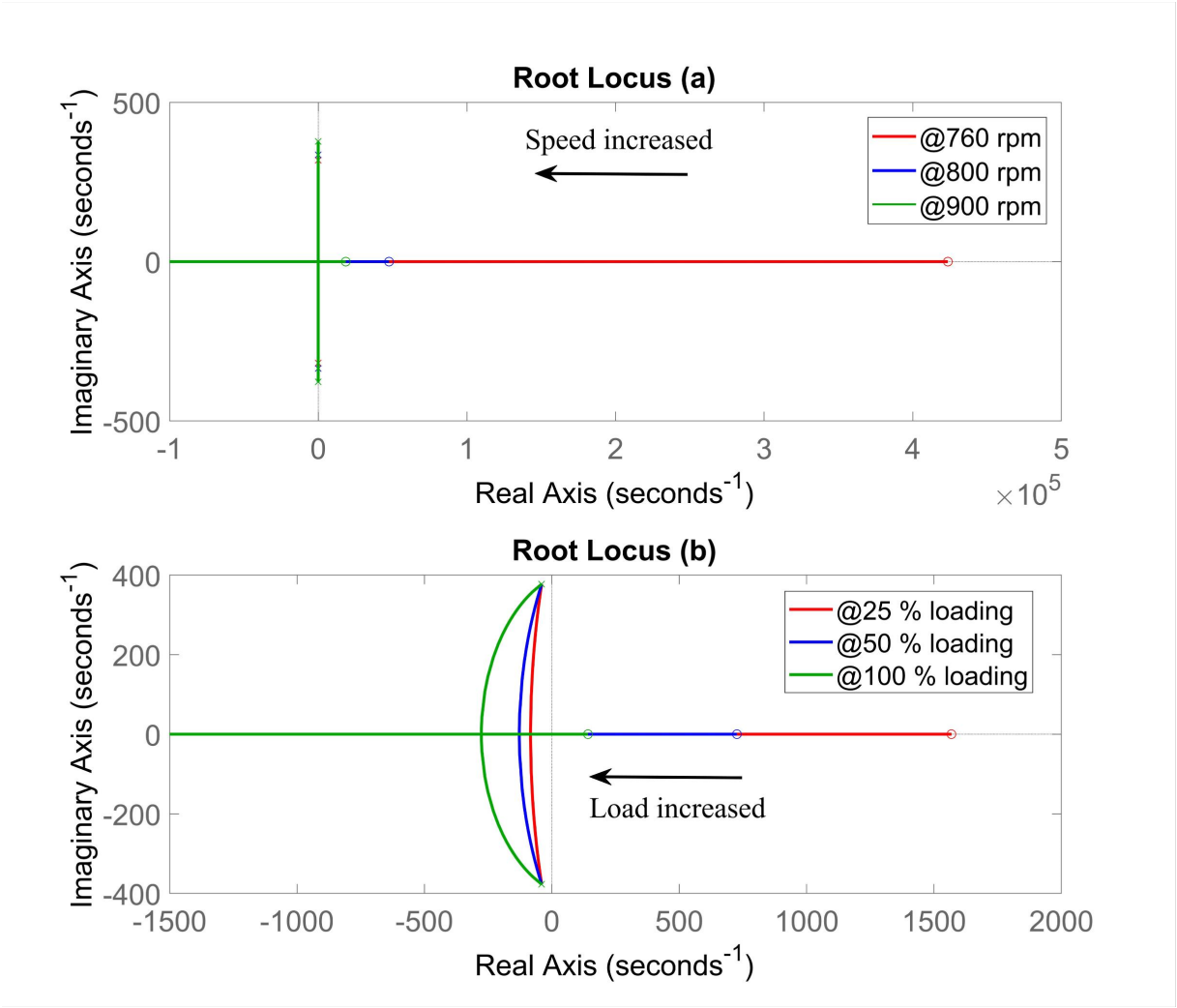

Fig. 4.7: Pole zero movement for starter mode: (a) speed increment at 760, 800, and 900 rpm at no load (b) load increment at 25, 50 and 100 % of rated torque at 900 rpm

current controller will be designed based on this operating point. The initial operating point is chosen as ω_{eo}=318.3 rad/sec, T_L=3.4 Nm (25% Loading). The steady-state equilibrium values are v_d^o=-8.835V, v_q^o=49.21V, i_d^o=-0.91A, i_q^o=3.59A, V_{dc}^o=98.88V and i_{dc}^o=2.8 A. The linearized transfer function $G_{pq}(s)$ is given as:

$$G_{pq}(s) = \frac{\Delta i_q}{\Delta v_q} = \frac{0.0075s - 13}{5.625e{-}05s^2 + 0.0045s + 5.791} \tag{4.22}$$

The controller W_{cq} is designed based on the following desired control specifications of (10 to 200Hz) bandwidth and 0.7 damping factor. The resulting design parameters of the PI controller are $k_{pq} = 0$ and $k_{iq} = 30$. Fig. 4.8 shows the frequency response of the closed loop system. It is clearly seen that the maximum achievable bandwidth is 13 Hz due the existence of RHP zero. The active disturbance rejection control (ADRC),

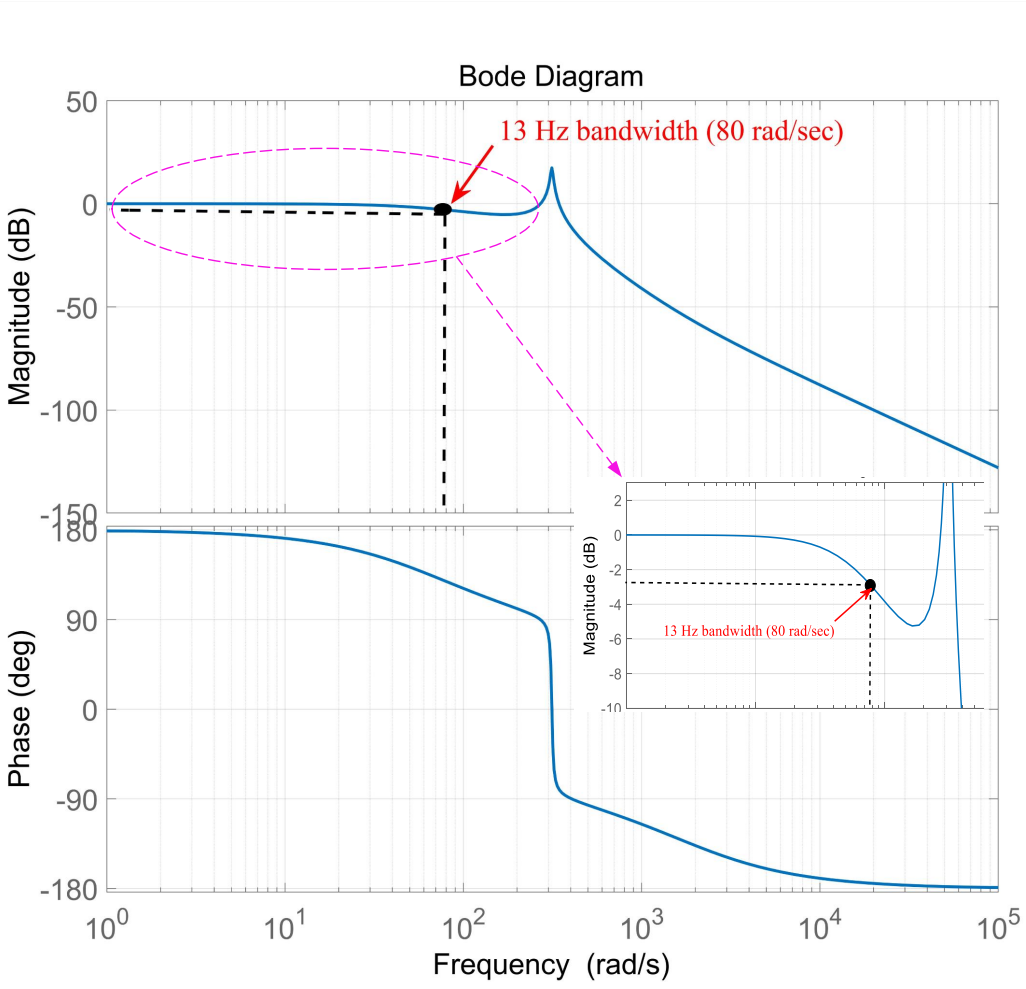

Fig. 4.8: Frequency response of closed-loop plant at speed 760rpm and 25% loading for starter mode

originating from the disturbance rejection paradigm (DRP), provides a potential solution for non-minimum phase systems [110].

4.6.2 Speed Controller Design

The control plant for the speed loop requires the electromechanical torque equation along with the i_q current loop. The assumptions for speed controller design are: the bandwidth of the speed controller is much slower than the i_q loop; there is no reluctance torque since ($L_d = L_q$); and no disturbance was introduced during the control design. The equation for the speed control plant can then be derived as (4.23), as in [35]:

$$\frac{\Delta\omega_r}{\Delta i_q^*} = \frac{1.5p\psi_m}{Js} \tag{4.23}$$

The bandwidth of the speed controller is chosen to be at least 10 times slower the current loop bandwidth, to ensure good control performance for both loops [35]. The bandwidth of 1 Hz was chosen and 0.7 damping ratio, therefore, the PI controller gains were calculated to be k_{ps}=0.92 and k_{is}=83.

4.7 Controller Design using the VVB Method

The controller design of the VVB control scheme presented in Fig. 4.4 is introduced for the validation of the overall S/G system performance. The selection of control bandwidth for the currents is preferred to be as high as possible in order to achieve good performance for the outer loop controllers. For the system in this study, the current controllers are designed to have 1 kHz bandwidth and 0.7 damping ratio similar to the internal loop specifications of the proposed FW control method [100]. The resulting PI parameters are k_{pd}= 38.7, k_{pq}=52.5, k_{id}= 7803, k_{iq} =7796. For the DC link current controller, the desired specifications are similar to the proposed method which are the bandwidth of 100 Hz and 0.7 damping ratio, the corresponding controller parameters are k_{pdc}=0 and k_{idc}=162.

4.8 Simulation Results

The dynamic performance of the proposed control scheme has been studied using simulations in the MATLAB /Simulink enviroment and models developed and reported in Appendix D. Fig. 4.9 shows the start up mode of AC drive system with the designed

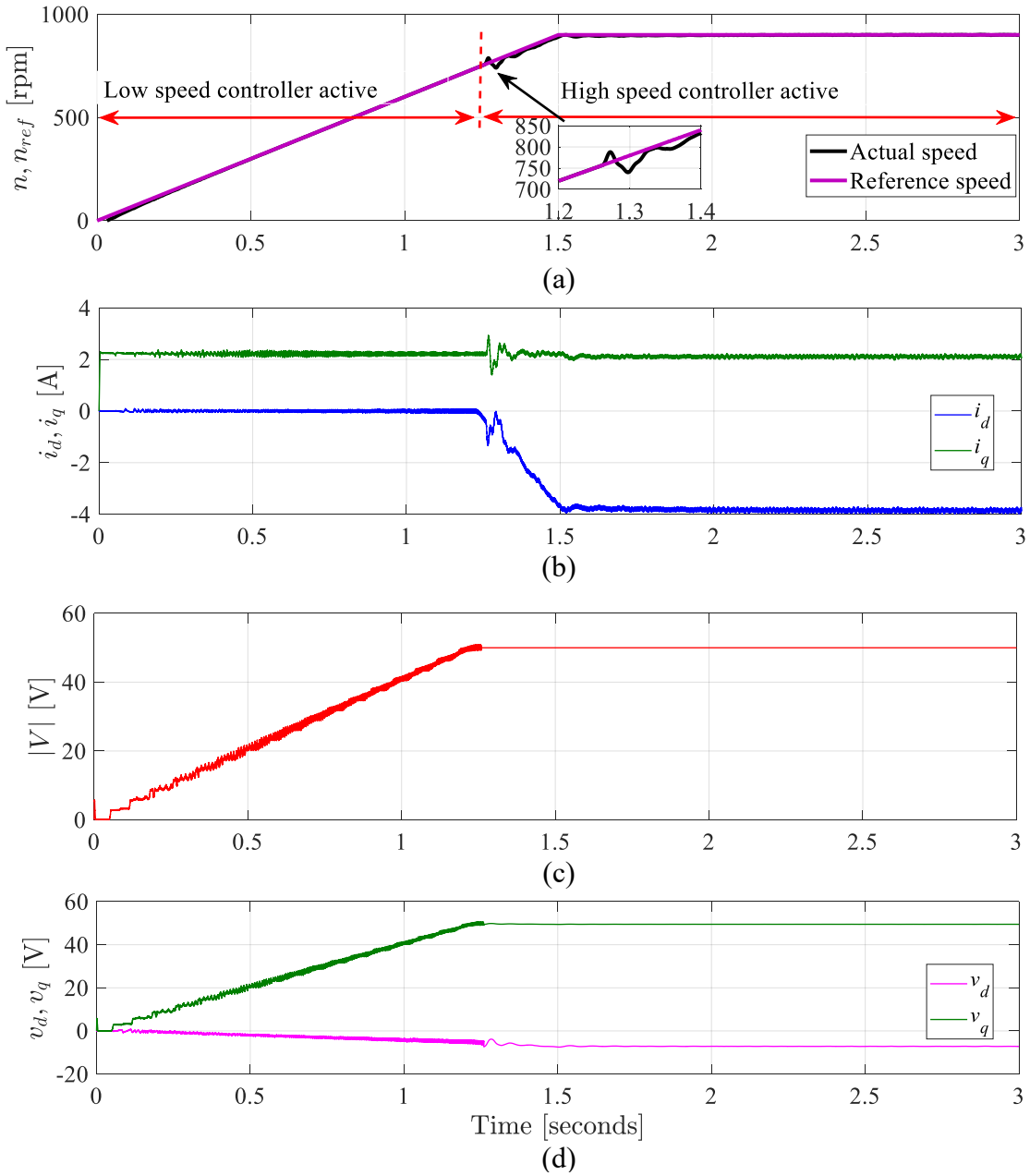

Fig. 4.9: Time response for start up mode from standstill to 900 rpm using the proposed method: a) Speed, b) dq currents, c) Voltage magnitude, and d) dq voltage references sent to PWM modulator

controllers to accelerate a load of 2 N.m (25% rated torque) from 0 rpm to 900 rpm. At t=0s, the mode selector switch is turned to mode 1 and the low speed range controller is activated, so the reference voltage v_{qm}^* is generated from the back emf in response to the load. Once this voltage hits the limit (50V) at the base speed, the switch moves to mode 2 to activate the high speed range controller (at $t \approx 1.25$s), and the machine works in FW mode. It can be seen from the speed response that the transition between the two controllers is seamless, without any issues. Fig. 4.10 and Fig. 4.11 show the responses to the step change of the speed reference from 600 rpm to 900 rpm (operating point B as shown in Fig. 4.2) at 2 N.m load. The controller W_{cq} decreases its output for i_q to track the reference. As is clearly seen from these figures, when the rotor accelerates, the output of the speed controller increases, so n follows n_{ref}. The transition between low and high speed range controllers happens at $t \approx 1.3$s. As the motor load doesn't change, the reference current, i_q^* drops to the previous value and the generated motor torque returns to its previous value (2 N.m). The current i_d changes naturally in the negative direction for FW to maintain the machine voltage under limitation.

Fig. 4.12 and Fig. 4.13 show the step responses to the load change from 2 to 3 N.m at 2s at speed 800 rpm (from operating point A to C as shown in Fig. 4.2). Here, i_q increases to match the load torque demand and i_d increases in the negative direction to provide FW. The rotor speed settles at its reference value, as shown in Fig. 4.12.

The generation mode using VVB concept is tested through Matlab/Simulink. Fig. 4.14 and Fig. 4.15 report the steady-state results when i_q^* is set -2A at 1000 rpm (operating point D as shown in Fig. 4.2). In order to push the power from the generator to the DC bus, the DC local bus voltage (100.8) must be higher than the main DC bus voltage (set to 100V) as shown in Fig. 4.15.

The results confirm that the proposed control method can effectively achieve a wide operational speed range in both starter and generation modes, and achieve better of DC bus voltage, as the system always operates at the maximum voltage.

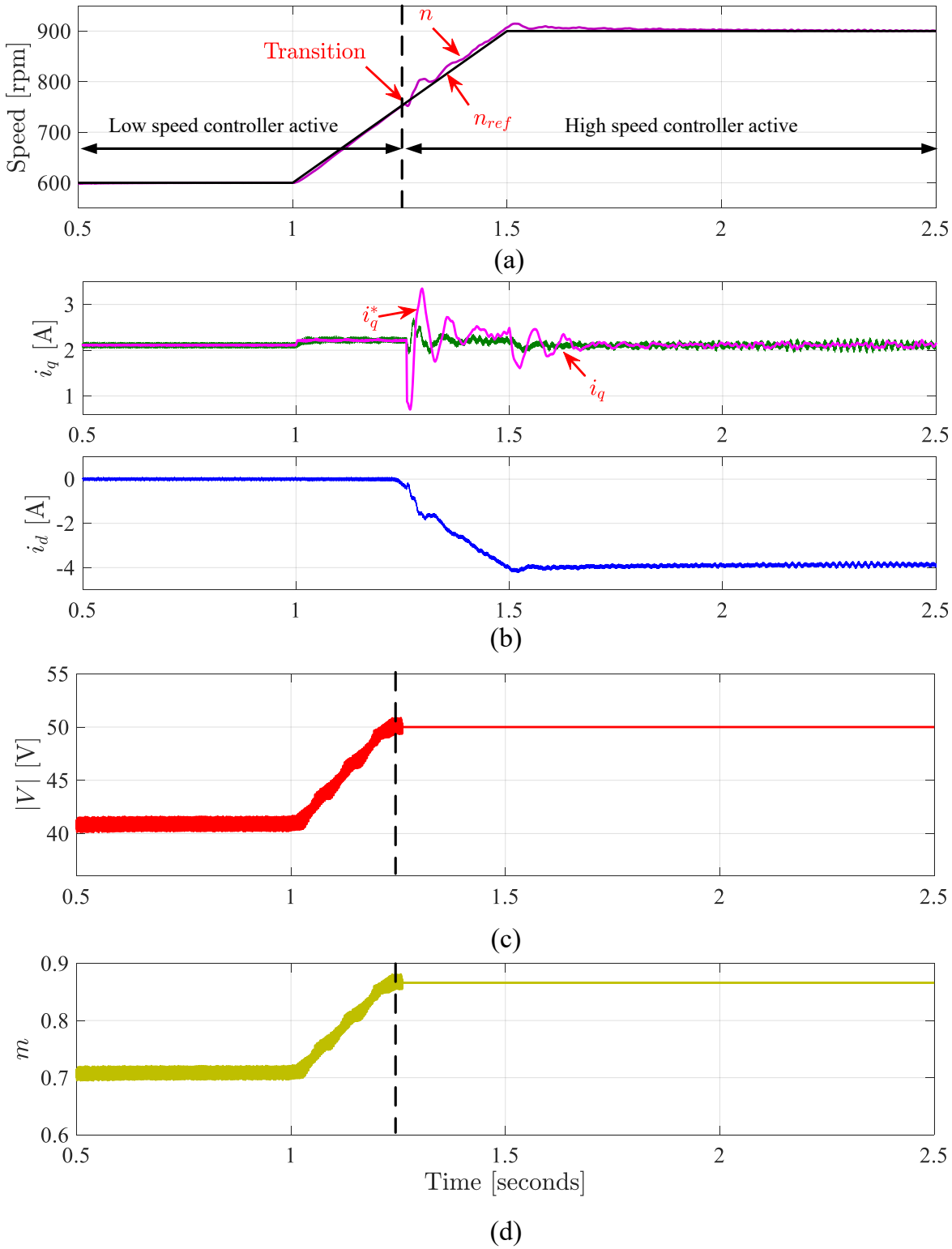

Fig. 4.10: Simulation results of starter mode with speed change from 600 to 900 rpm, using the proposed method: a) Speed, b) *dq* currents, c) Voltage magnitude, and c) Modulation index

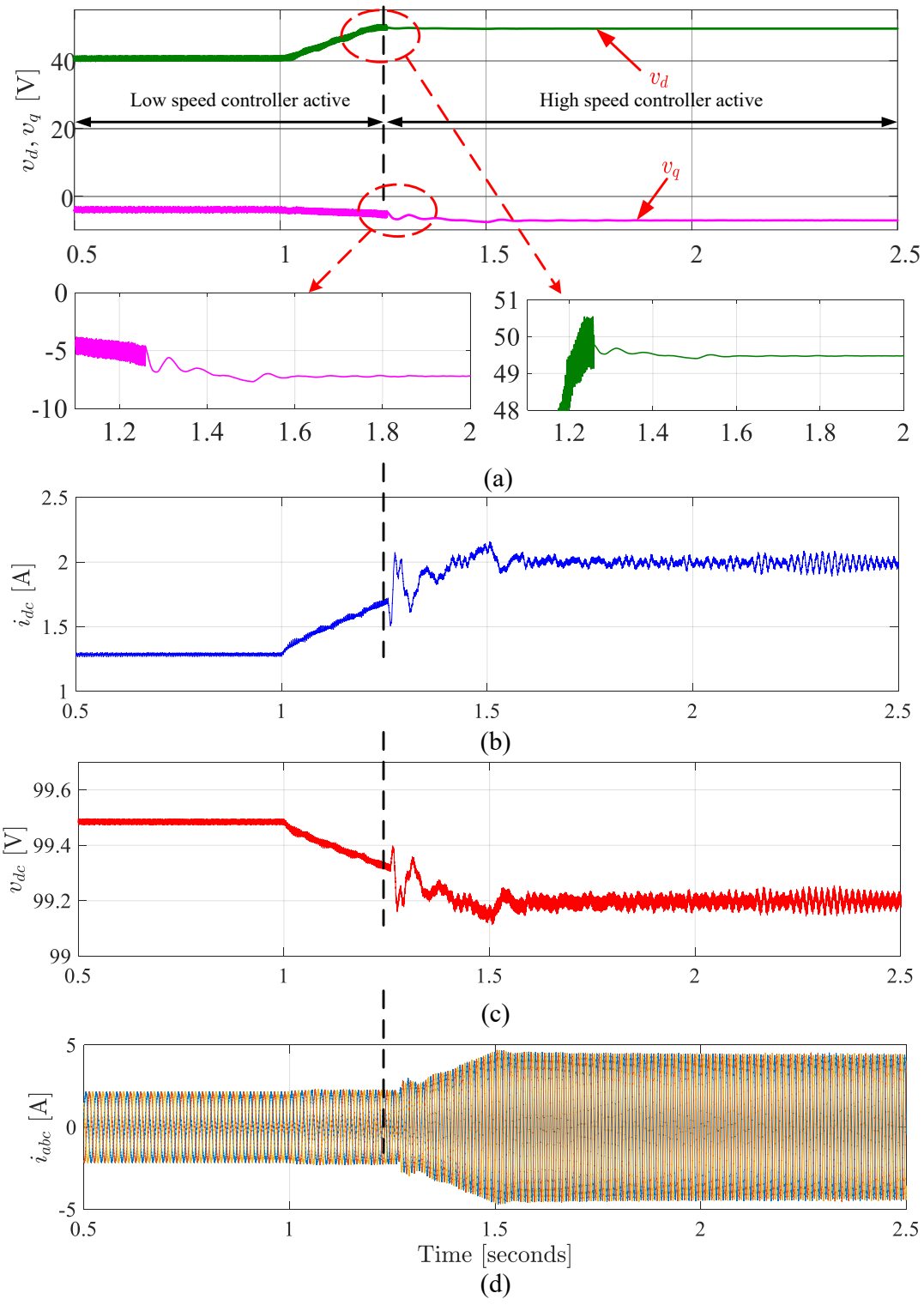

Fig. 4.11: Simulation results of starter mode with speed change from 600 to 900 rpm using the proposed method: a) *dq* voltages references sent to PWM modulator, b) DC current, c) DC bus voltage, d) AC currents

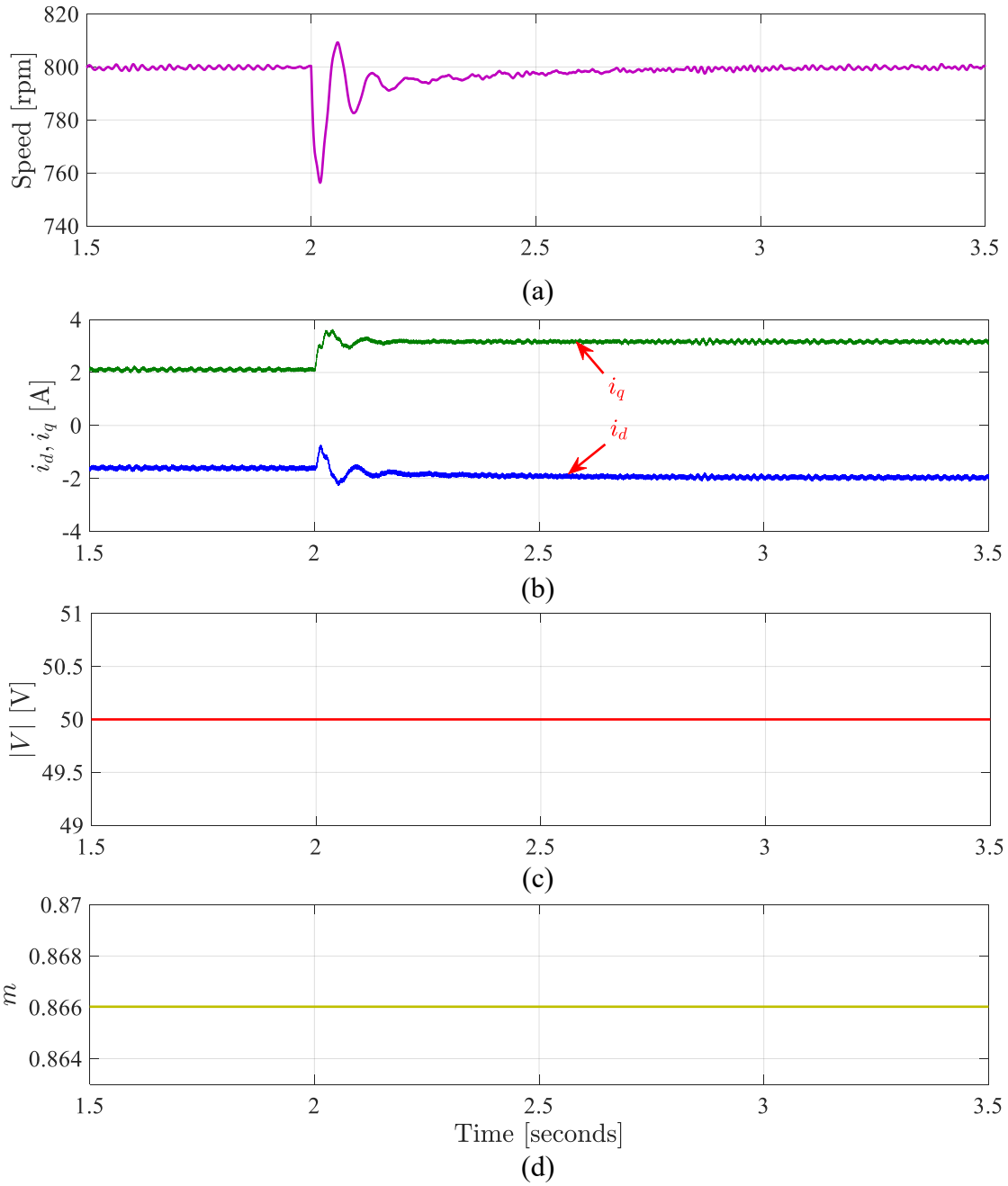

Fig. 4.12: Simulation results of starter mode in FW with load change from 2 to 3 N.m at 800 rpm: a) Speed, b) dq currents, c) Voltage magnitude, and d) Modulation index

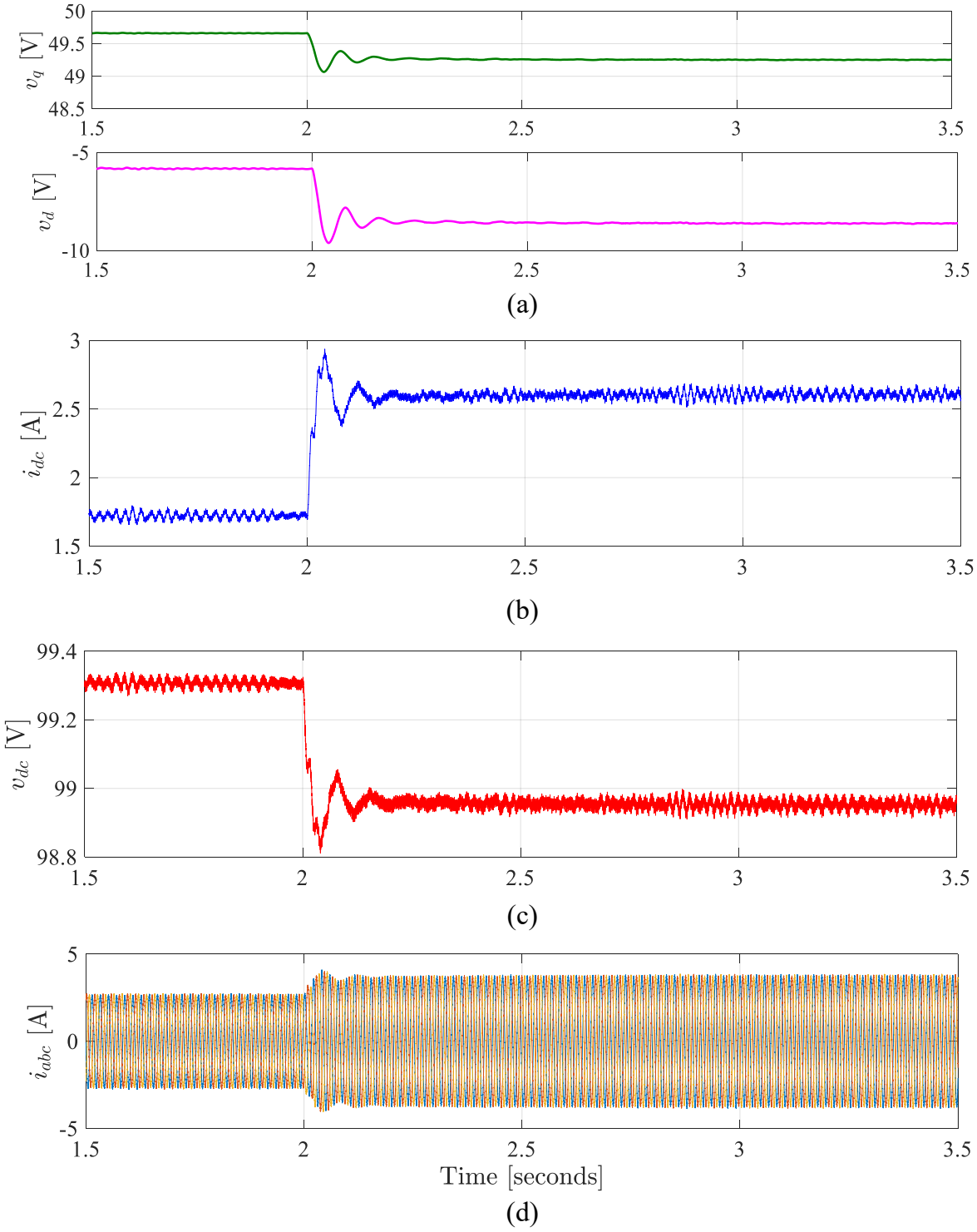

Fig. 4.13: Simulation results of starter mode in FW with load change from 2 to 3 N.m at 800 rpm: a) *dq* voltages references sent to PWM modulator, b) DC current, c) DC bus voltage, and d) AC currents

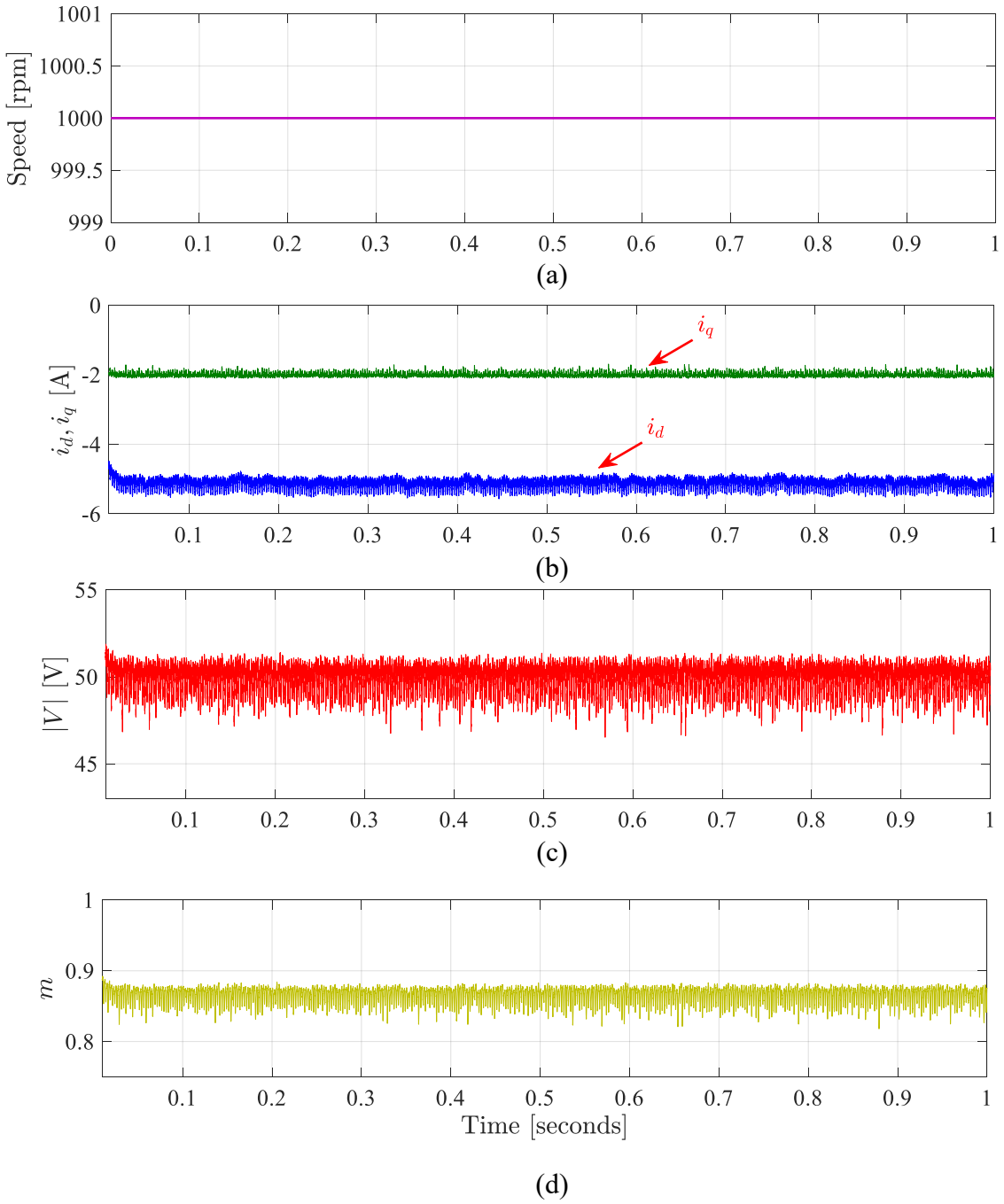

Fig. 4.14: Simulation results of generation mode in FW with i_q^*=-2 A at 1000 rpm: a) Speed, b) *dq* currents, c) Voltage magnitude, and d) Modulation index

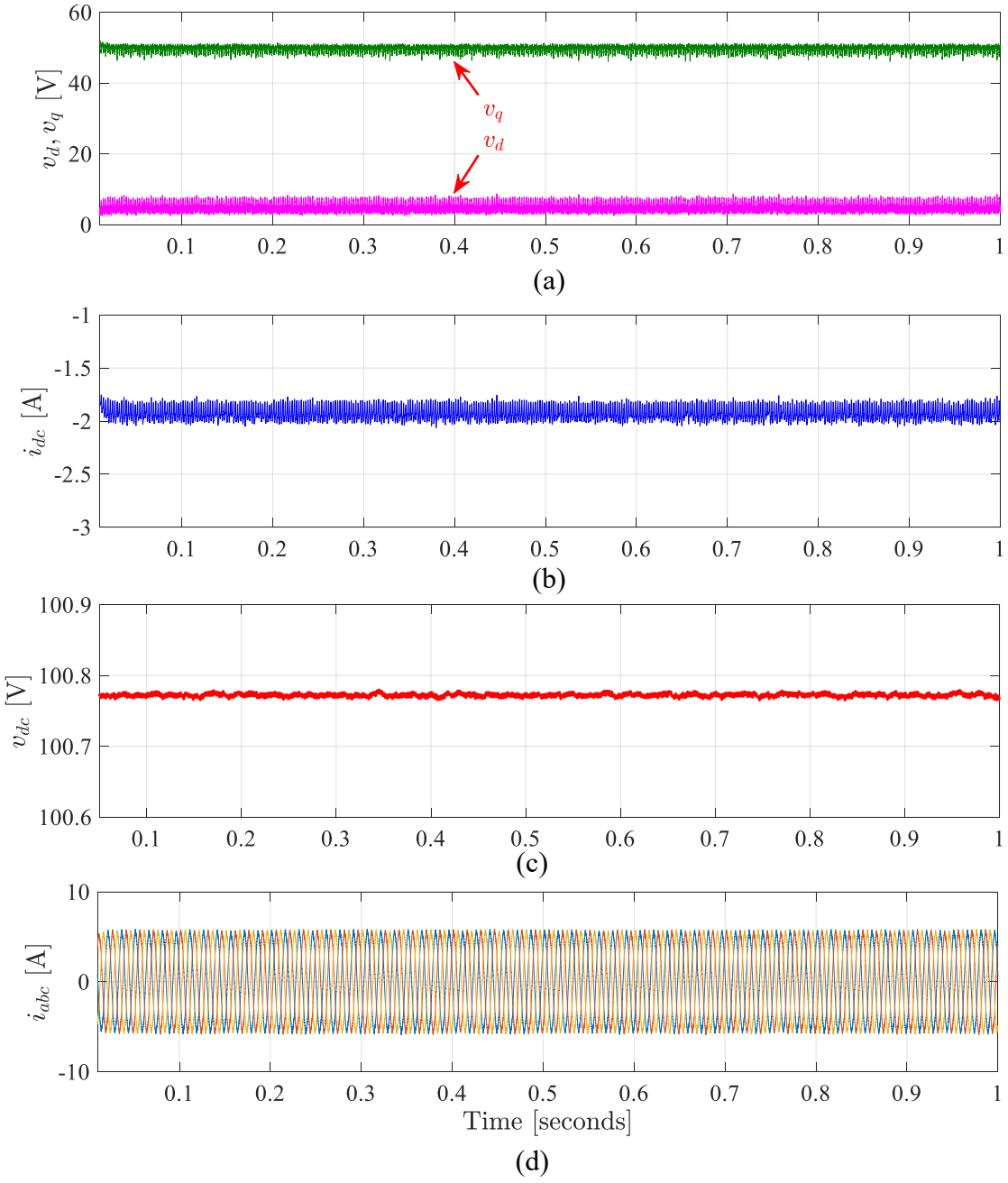

Fig. 4.15: Simulation results of generation mode in FW with i_q^*=-2 A at 1000 rpm: a) dq voltages references sent to PWM modulator, b) DC current, c) DC bus voltage, and d) AC currents

4.9 Experimental Validation

The experimental setup has been used to verify the proposed control S/G scheme in both motoring and generating modes and under different operating scenarios, namely:

- Starting process from standstill to above FW speed
- Torque load change within FW region
- Operation mode switching between different controllers (low and high-speed controllers)
- Speed change in FW mode
- Generation mode for VVB method

Fig. 4.16 shows the experimental test rig developed to verify key analytical findings of this study. The PMM with the two-level AFE and corresponding control equipment are considered to form an AC drive system to emulate the S/G system. The other subsystem consists of an induction machine and its drive, hence forms an AC drive system to mimic the aircraft engine. Both of these subsystems are controlled independently from each other. The operating points used are similar to those tested in the simulation analysis. The DC bus voltage is set to 100VDC and the maximum voltage V_{max} is set to 50 V to enable FW at an early stage. It should be noted that the IM (prime mover) operates in speed control mode while the PMM operates in constant torque/speed mode.

4.9.1 Results for VVB method

Fig. 4.17 shows the results for the VVB method in motoring mode when the reference speed is stepping from 600 rpm to 800 rpm. Based on the voltage and current circle limitation shown in Fig. 4.2, the FW is expected to start at a speed 750 rpm, since the voltage reaches its maximum value V_{max}. at this speed. It can be clearly seen that the system is non-operational after this speed, as the v_q hits the maximum limits, and this issue will be addressed by the proposed method.

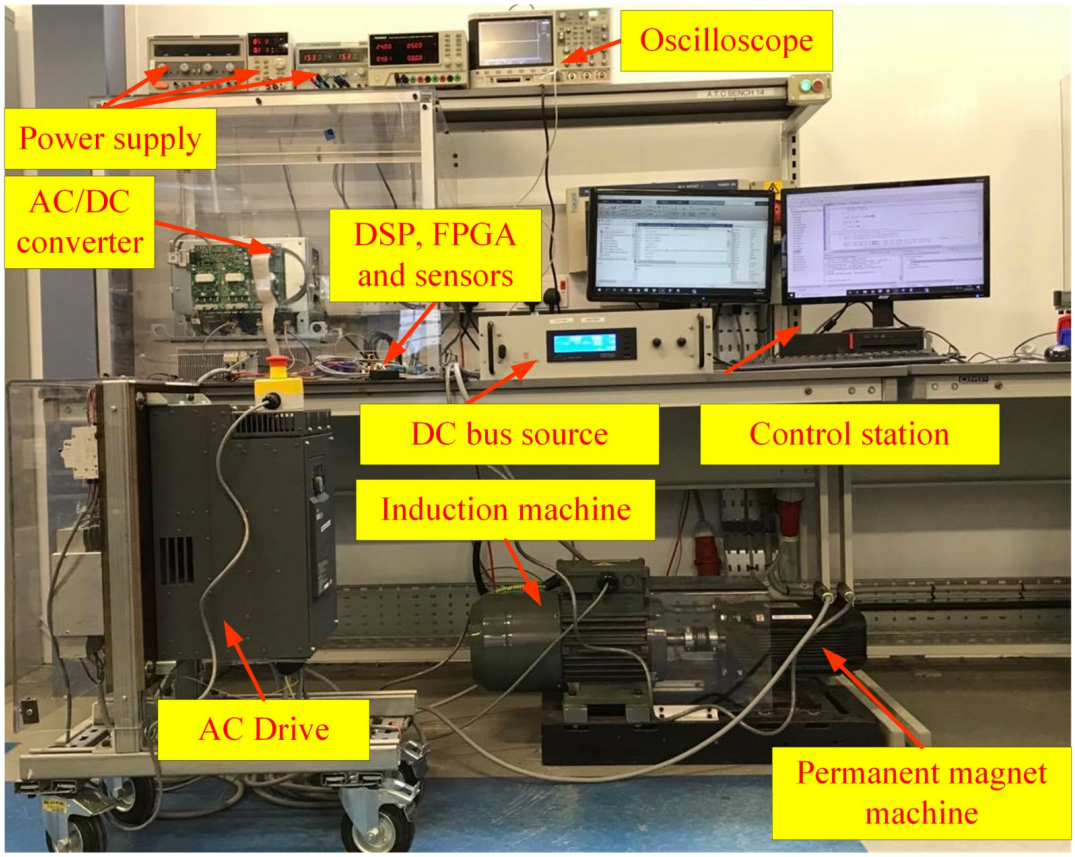

Fig. 4.16: Layout of the experimental rig

4.9.2 Results for Starting Mode using Proposed Method

Fig. 4.18 shows the key results from the proposed PMM drive system in start up mode with the designed controllers. At t=0.90s, the PMM drive starts from standstill condition and accelerates to 900 rpm, following the ramp reference speed. As the speed increases, $|V|$ also increases but it is limited to 50 V ($|V_{max}|$). A negative i_d is required from t=3.15s, as the result of entry FW, in order to regulate $|V|$. At this time, the transition from a lower speed controller to a high speed controller occurs. It can be seen that v_q decreases to allow v_d to increase and all of the variables are in a steady-state when the speed reaches the speed reference at 5s. It can be clearly seen that the transition between the two controllers is very smooth without any overshoot in speed response.

Fig. 4.19 and Fig. 4.20 present results when the proposed method is applied. At t=0, the reference speed is set to 600 rpm by the IM drive, i_q^* is set to 2 A, and the PMM is running under VVB. As the reference speed increases to 900 rpm, the voltage magnitude

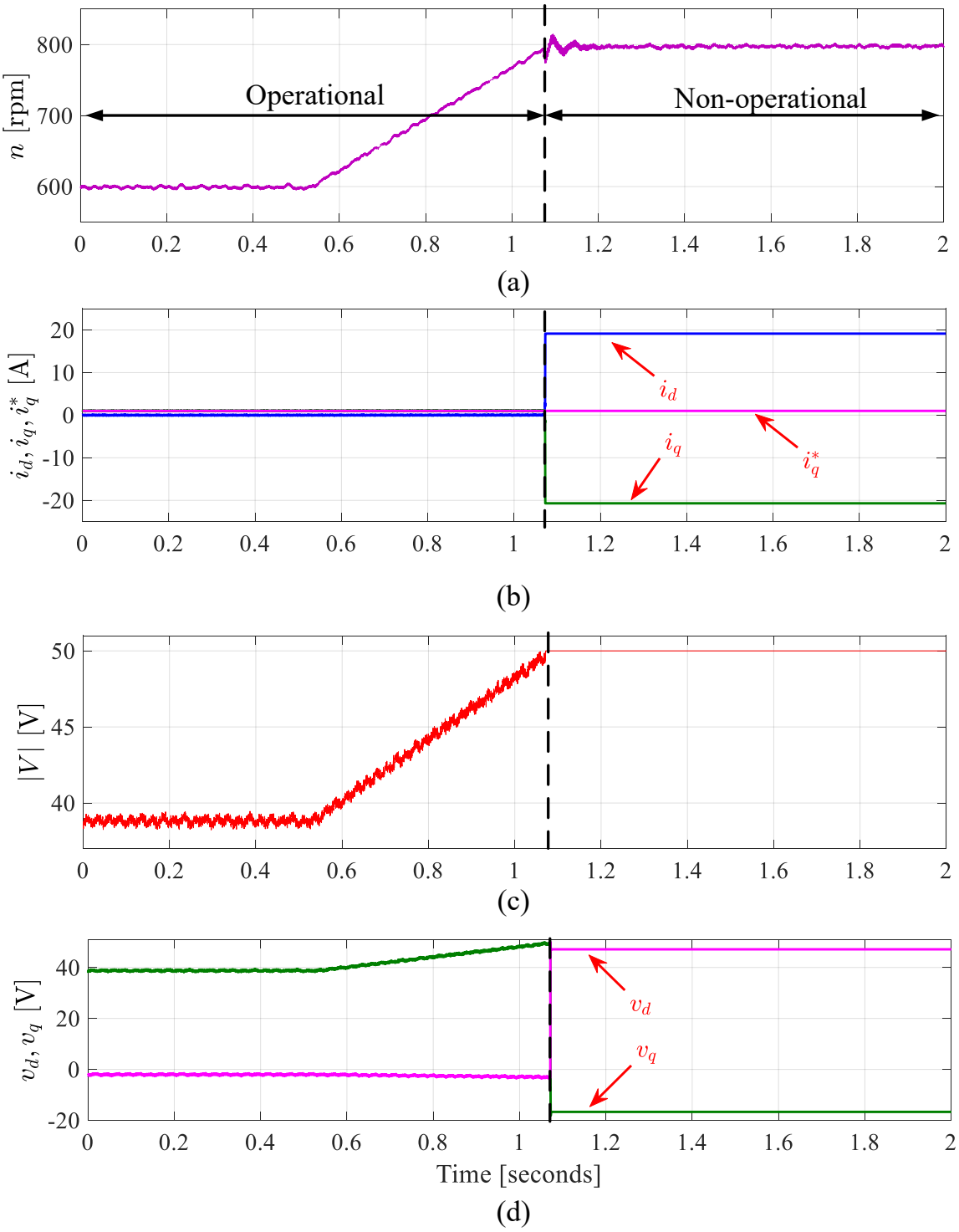

Fig. 4.17: Experimental results of speed changes from 600 to 800 rpm using VVB method: a) Speed, b) *dq* currents, c) Voltage magnitude, and d) *dq* voltages references sent to PWM modulator.

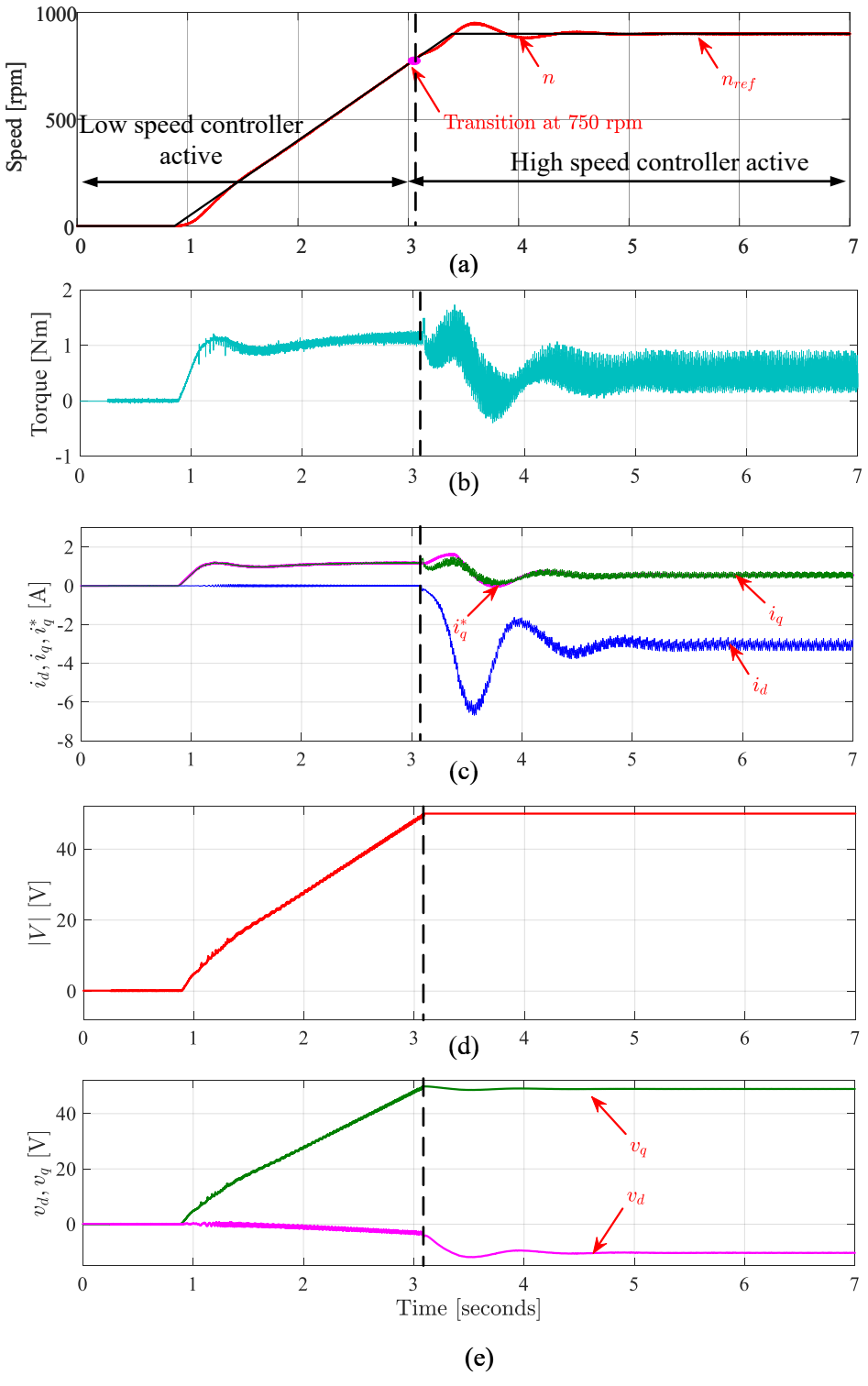

Fig. 4.18: Experimental results of start-up mode using proposed method from standstill to 900 rpm for the test bench AC drive system: a) Speed, b) Electromagnetic torque c) dq currents, d) Voltage magnitude, and e) dq voltages references sent to PWM modulator.

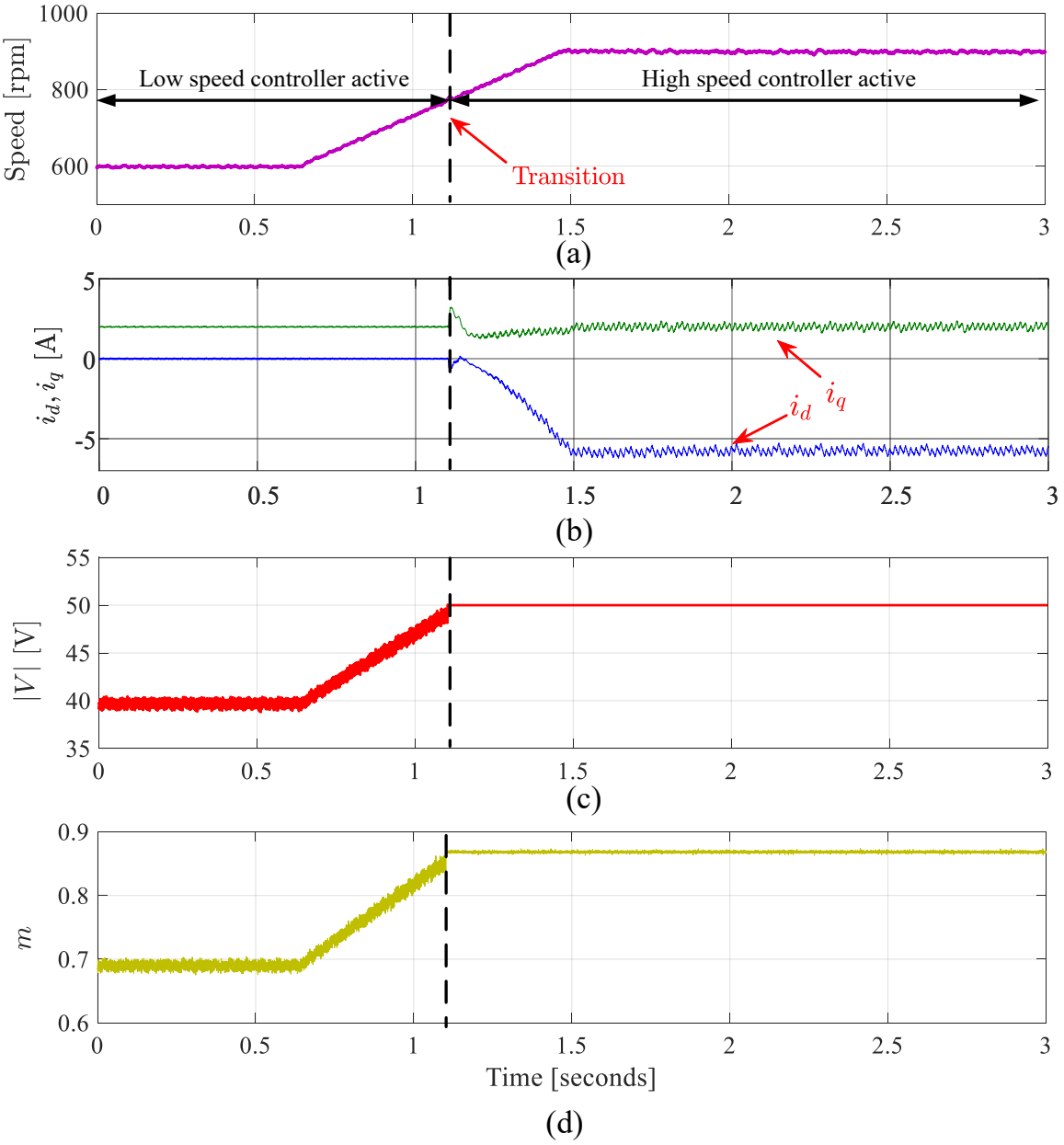

Fig. 4.19: Experimental results of speed changes from 600 to 900 rpm using the proposed method: a) Speed, b) dq currents, c) Voltage magnitude, and d) Modulation index

increases until the limit (50 V) is reached, and the FW is activated at $t \approx 1.1$ s. At this point, the condition for the transition from VVB to the proposed control is met, hence the transition takes place around a speed of 750 rpm. In the proposed method, the voltage controller reduces v_q to allow v_d to increase, as shown in Fig. 4.20. In addition, i_q sets the positive value for motoring mode, the current will generate a torque, trying to accelerate

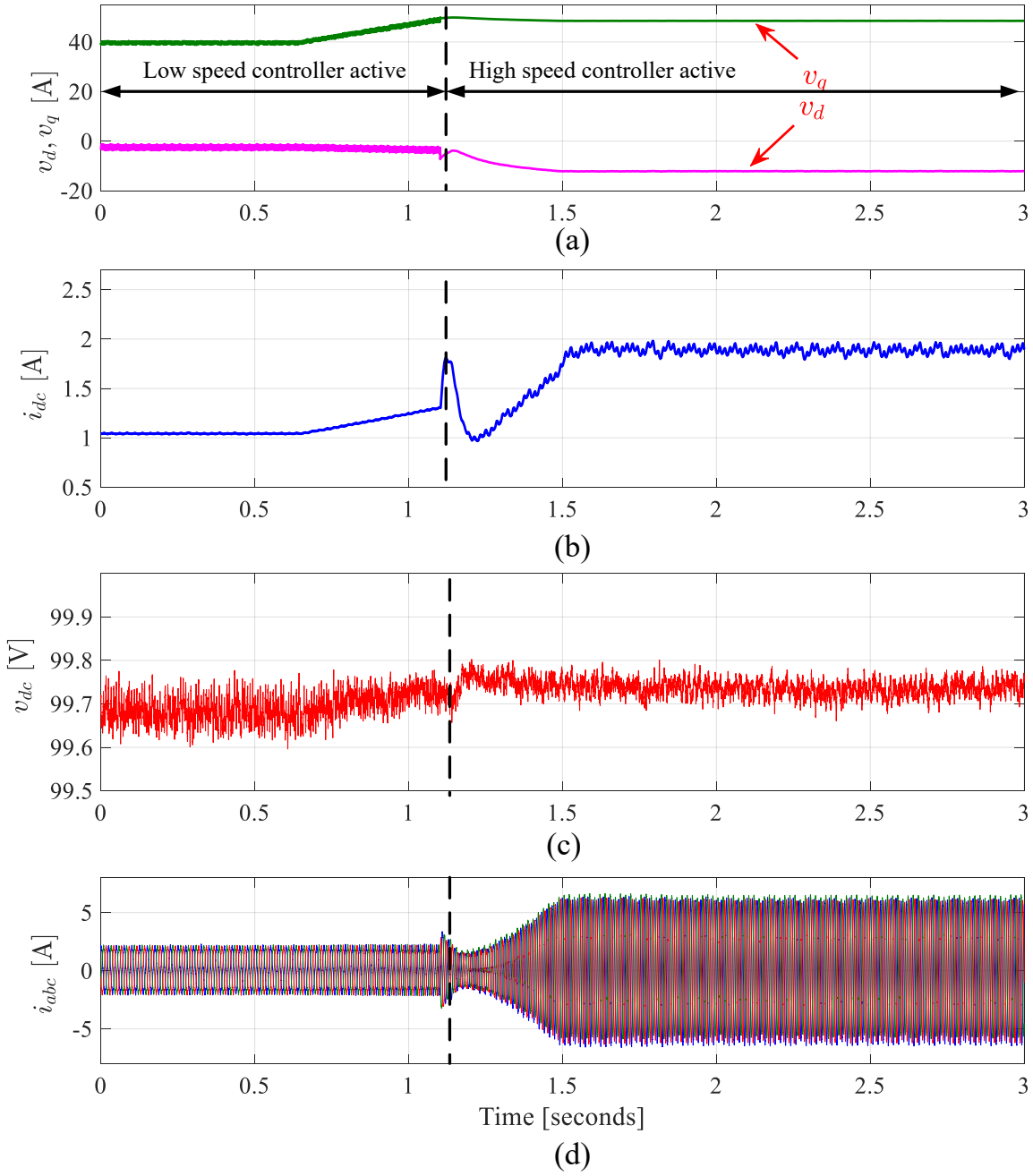

Fig. 4.20: Experimental results of speed change from 600 to 900 rpm using the proposed method: a) *dq* voltages references sent to PWM modulator, b) DC current, c) DC bus voltage, d) AC currents

the IM in the same direction, but the IM drive fixes the rotating speed, and this will be seen from the PMM side as a mechanical load. Through the transition, i_q tries to follow the reference current, but due to the ramp speed reference used and low current

loop bandwidth, i_q drops. The results shown in Fig. 4.19 and Fig. 4.20 demonstrate the smooth transition between the controllers as a result of changing operation modes. To validate the suggested approach in the deep FW region, the reference speed is modified from 800rpm to 900rpm and the reference current, i_q^*, is set to 2A in this test. The results

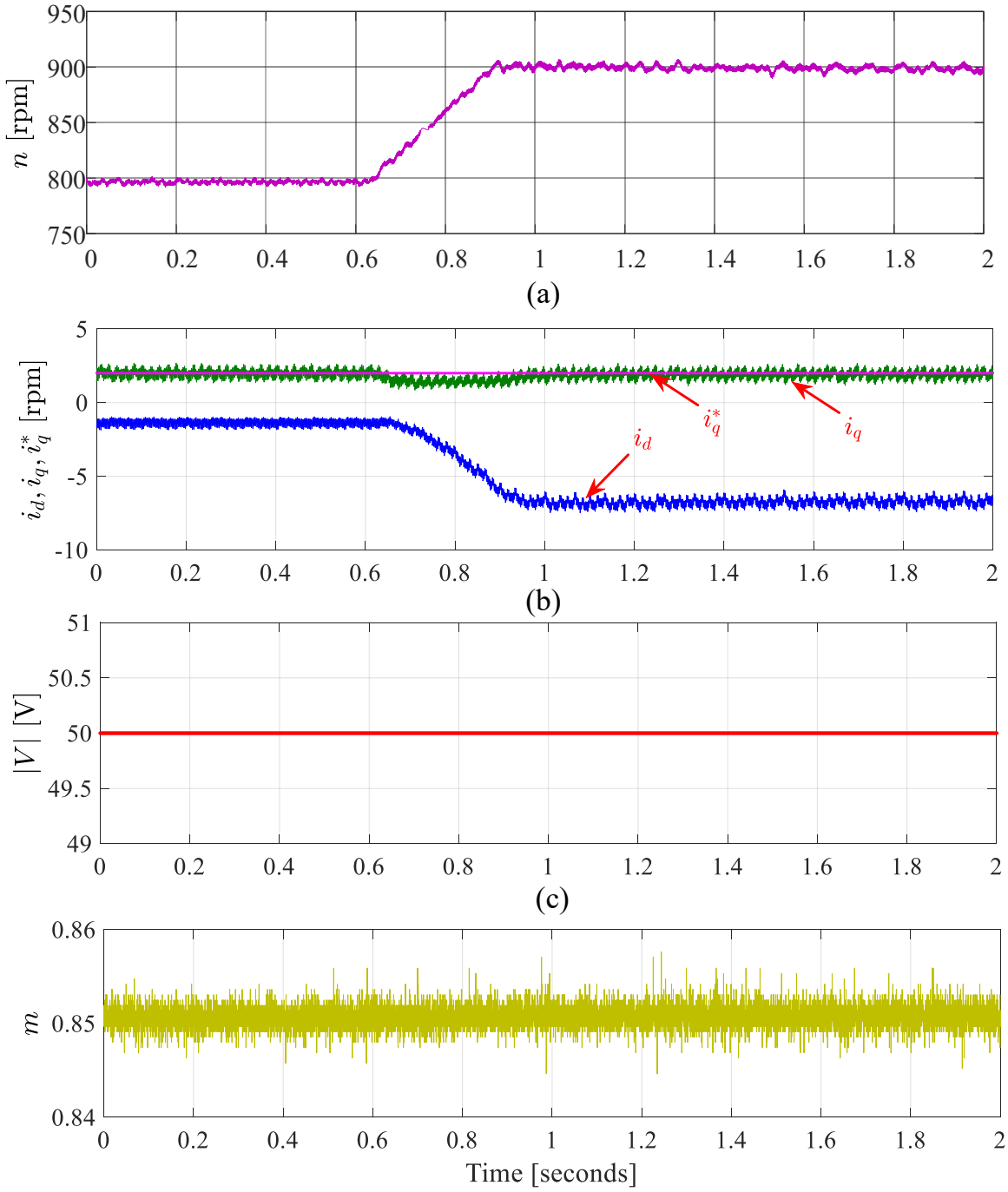

Fig. 4.21: Experimental results of speed changes from 800 to 900 rpm using the proposed method: a) Speed, b) dq currents, c) Voltage magnitude, and d) Modulation index

are shown in Fig. 4.21 and Fig. 4.22. It can be seen that increasing the speed causes the

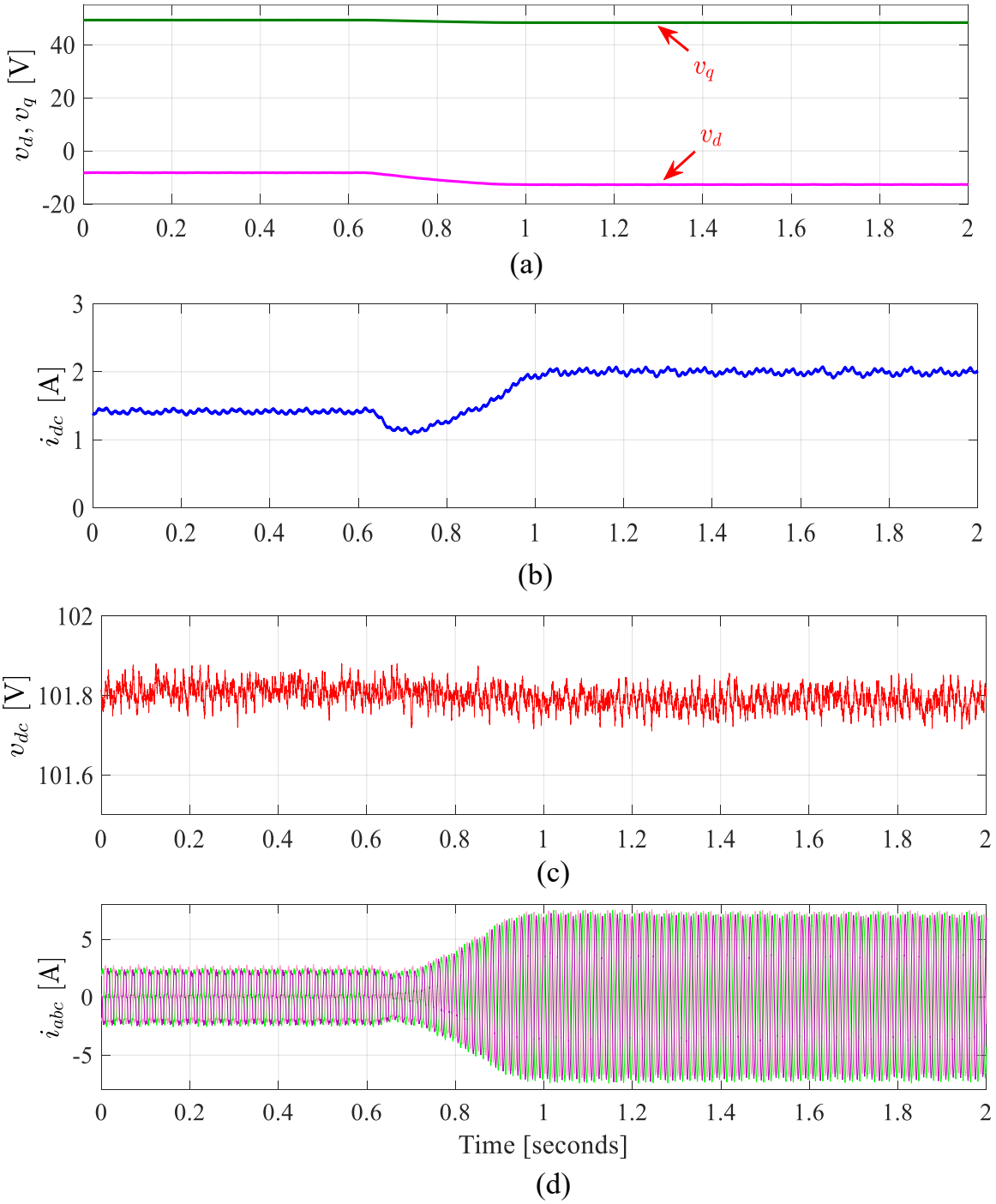

Fig. 4.22: Experimental results of speed changes from 800 to 900 rpm using the proposed method: a) *dq* voltages references sent to PWM modulator, b) DC current, c) DC bus voltage, d) AC currents

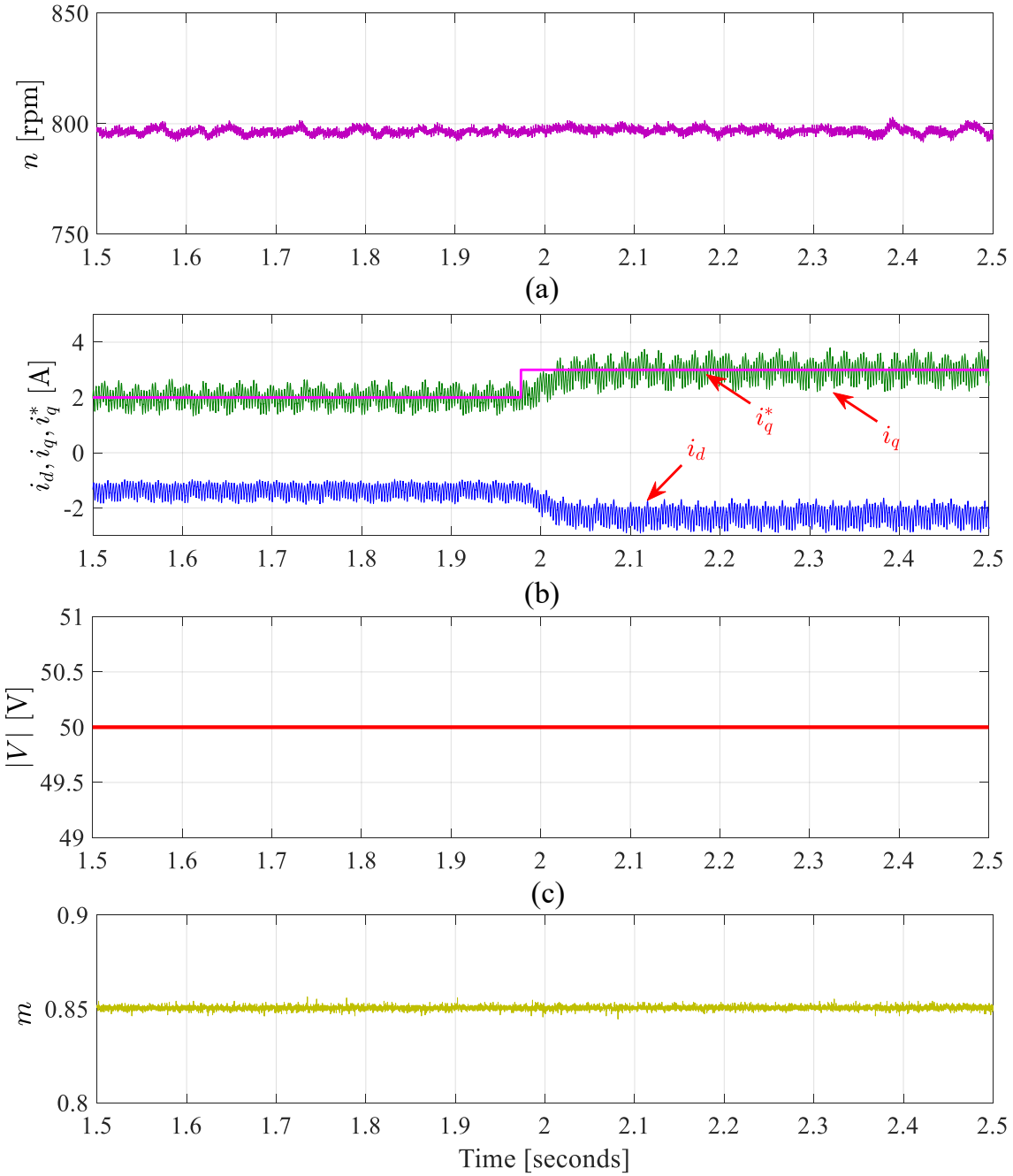

Fig. 4.23: Experimental results of i_q^* changes from 2 to 3 A at 800 rpm using proposed method: a) Speed, b) dq currents, c) Voltage magnitude, and d) Modulation index

controller to lower v_q, allowing v_d to increase. In results shown in Fig. 4.21, the d-axis current is raised in a negative direction to prevent the increase in the back emf.

In Fig. 4.23 a step change in i_q from 2A to 3A at $t \approx 1.97$s is utilized to validate the feasibility of the suggested approach for the generalized load condition during the FW

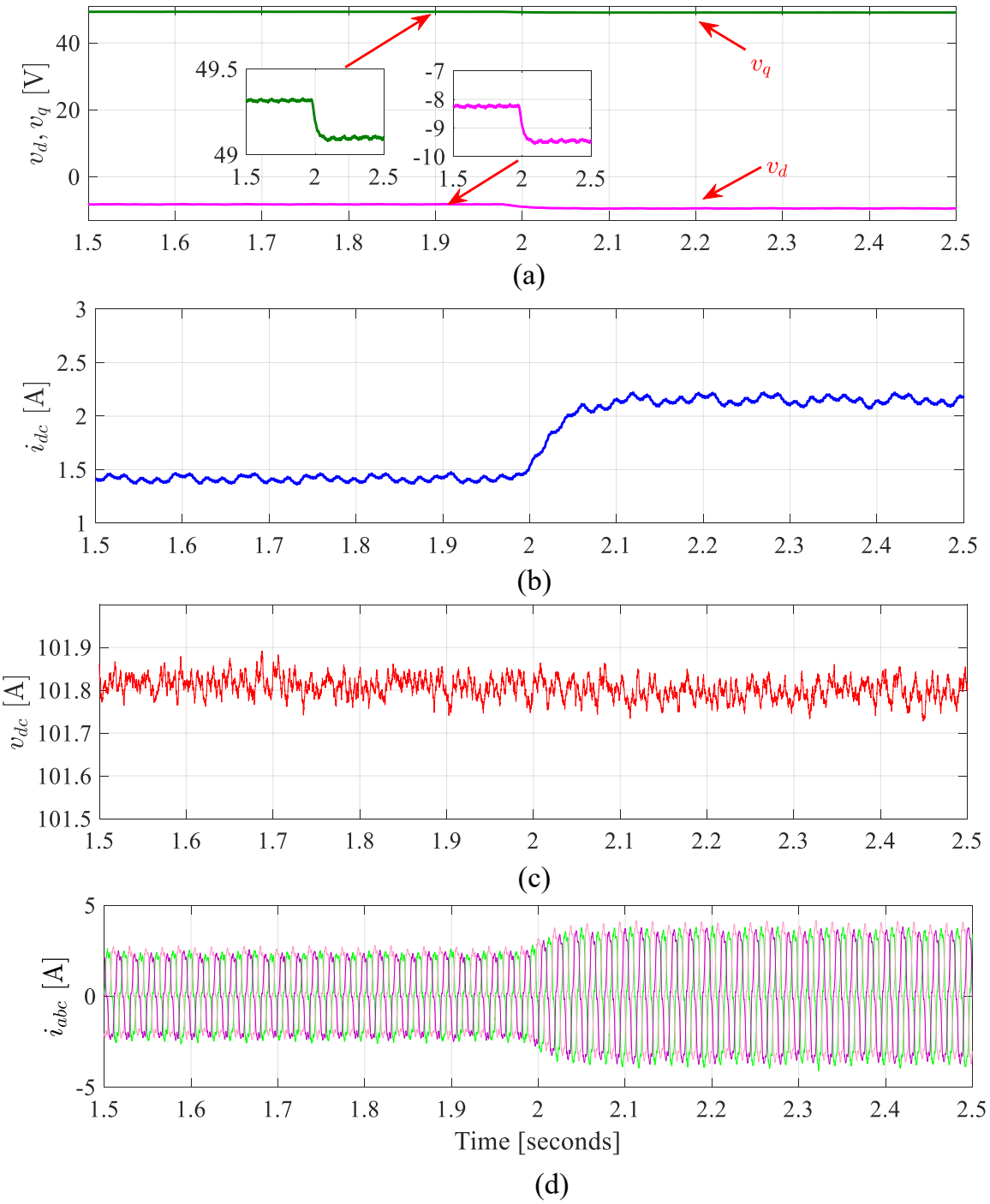

Fig. 4.24: Experimental results of i_q^* changes from 2 to 3 A at 800 rpm using the proposed method: a) dq voltages references sent to PWM modulator, b) DC current, c) DC bus voltage, d) AC currents

region. Fig. 4.23 and Fig. 4.24 show that i_q follows its reference i_q^*, and i_d increases in magnitude as the operating point moves from A to C as shown in Fig. 4.2. Due to the presence of RHP zero in the control plant, the time response appears to be slow.

4.9.3 Results for Generating Mode using VVB Method

In order to perform tests in generator mode, the operating speed was set to 1000 rpm by the IM drive. Fig. 4.25 and Fig. 4.26 show the steady-state results for generating

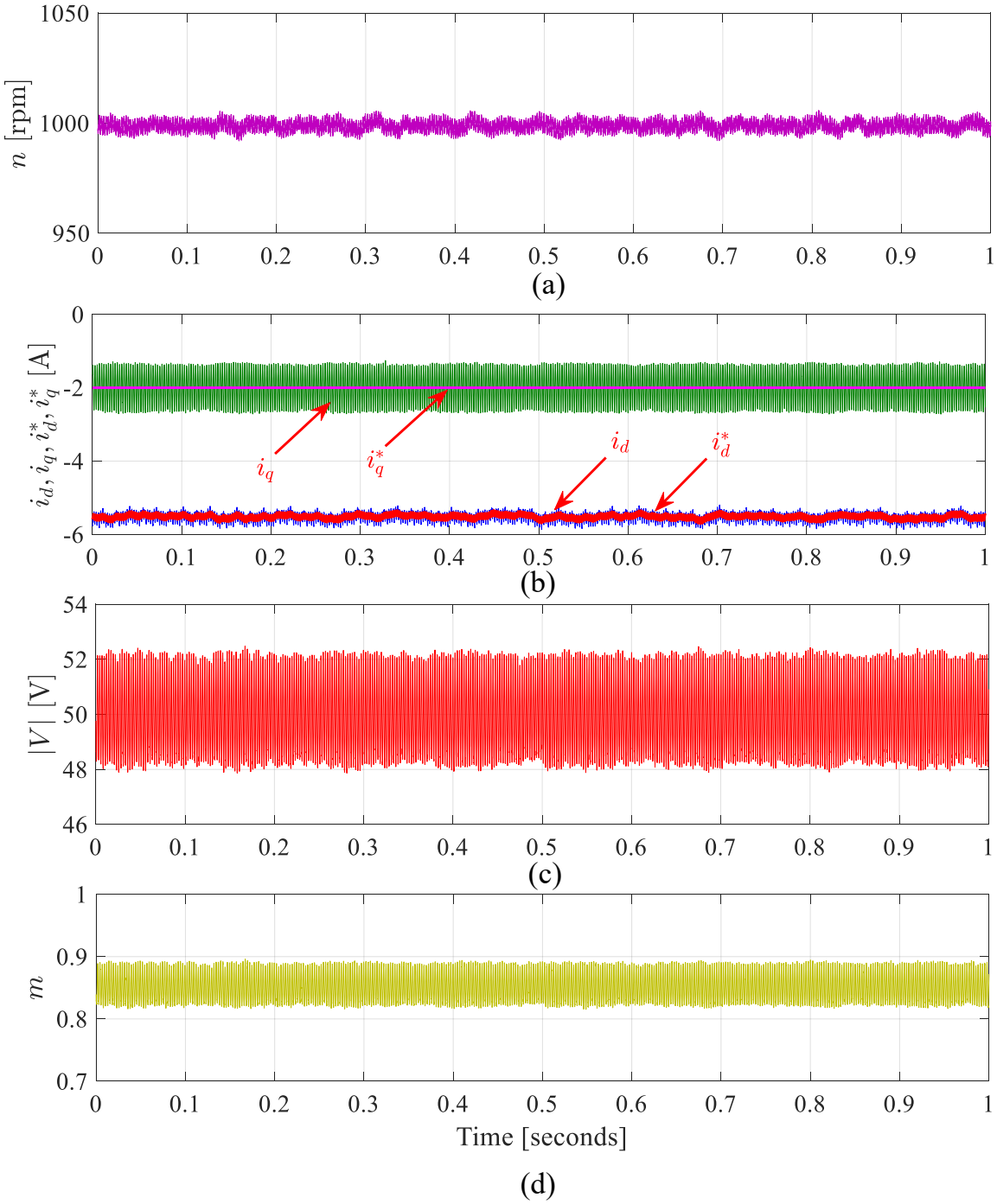

Fig. 4.25: Experimental results of steady state values for generating mode at speed 1000 rpm: a) Speed, b) *dq* currents, c) Voltage magnitude, and d) Modulation index

mode using the VVB method, and controller parameters calculated in Section 4.7, when i_q^* equals -2 A. It can be seen that the DC bus voltage increases above the setting value (100 V) to 101.6 to supply the power from PMM to the DC supply. Furthermore, the

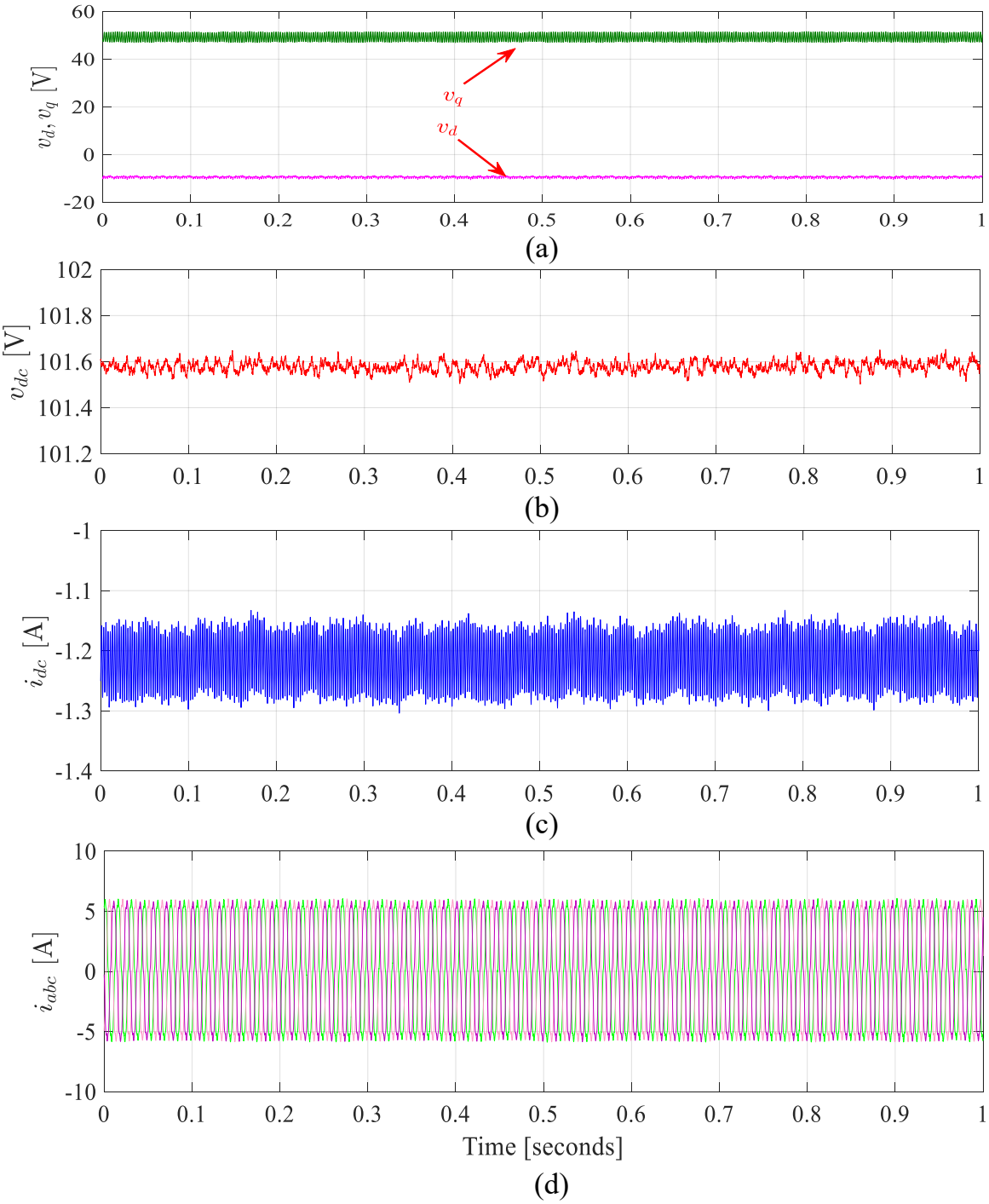

Fig. 4.26: Experimental results of steady state values for generating mode at speed 1000 rpm: a) *dq* voltages references sent to PWM modulator, b) DC current, c) DC bus voltage, d) AC currents

experimental results match those obtained from simulation. The experimental results reported and discussed in this Section have clearly demonstrated that the proposed method is capable of operating the S/G system in a wide range of speeds and loads, in both motoring and generating modes compare to the VVB method.

4.10 Conclusion on Chapter 4

This chapter proposed a simple control scheme for starting mode, which aligns with the VVB control approach for the S/G system to enable it to work in a wide speed range. A detailed analysis of the control strategy for the S/G system, which is part of the EPS in this study, is presented. After detailed analysis for motoring mode, considering different scenarios (e.g. load changes at a constant speed and speed changes at constant torque), it was found that the control plant for starter mode includes a RHP zero, which restricts the achievable high performance. The RHP zero moves towards the origin as the load and speed increase. A solution to address this issue is proposed, and its dynamic performance is tested and validated using both MATLAB/Simulink simulations and experimentally. The simulation and experimental results confirm that the proposed control scheme is capable of working in a wide range of speeds for both starter and generator modes. Moreover, the proposed control scheme allows the full utilization of DC bus voltage and improves aircraft efficiency as it allows to the S/G system to work in wide speed range. The proposed S/G system would be integrated with the single DC bus EPS to start the engine and provide power to onboard aircraft loads.

Chapter 5

Analysis and design of Multi-function Battery controller

The integration of the battery system with the single DC bus MEA EPS architecture is important when the battery can be responsible for different objectives, such as: bringing the aircraft online before the engines have been started; supporting/assisting ground operations such as refuelling; powering the brake system when the aircraft is being towed; starting the APU; and providing backup power for critical systems during the flight in the event of a total power failure. Therefore, a multi-function battery controller design is needed to facilitate the integration of the battery with the MEA EPS to fulfill its objectives. This Chapter will deal with a detailed analysis and design of the multi-function battery controller for the charging/discharging process with seamless transition between controllers. Firstly, the construction and the operation of the Li-ion battery, the different charging/discharging techniques of the battery, and their pros and cons are discussed. Then, the model of the Li-ion battery and its associated parameters are presented for simulation purposes. The proposed controller, which integrates different controllers such as battery current controller, battery voltage controller, output power controller, and battery DC bus voltage controller, and its integration with the electric power system are investigated. The desired design specifications of the controllers are outlined and verified. Due to the complexity of the process of charging and discharging a robust Energy Management (EM) strategy is proposed as well.

5.1 Introduction

Lithium-ion batteries have key advantages which enable them to be used in aircraft, as discussed in Chapter 2. A Li-ion battery is composed of 1) the anode and the cathode electrodes; 2) a separator between the two electrodes that prevents electrons passing through; and 3) an electrolyte that fills the remaining space of the battery. The anode and cathode are capable of storing lithium ions. Energy is stored and released as lithium ions travel between these electrodes through the electrolyte. Fig. 5.1 illustrates the battery and its charging and discharging processes. Inside a Li-ion battery, oxidation-reduction reactions take place.

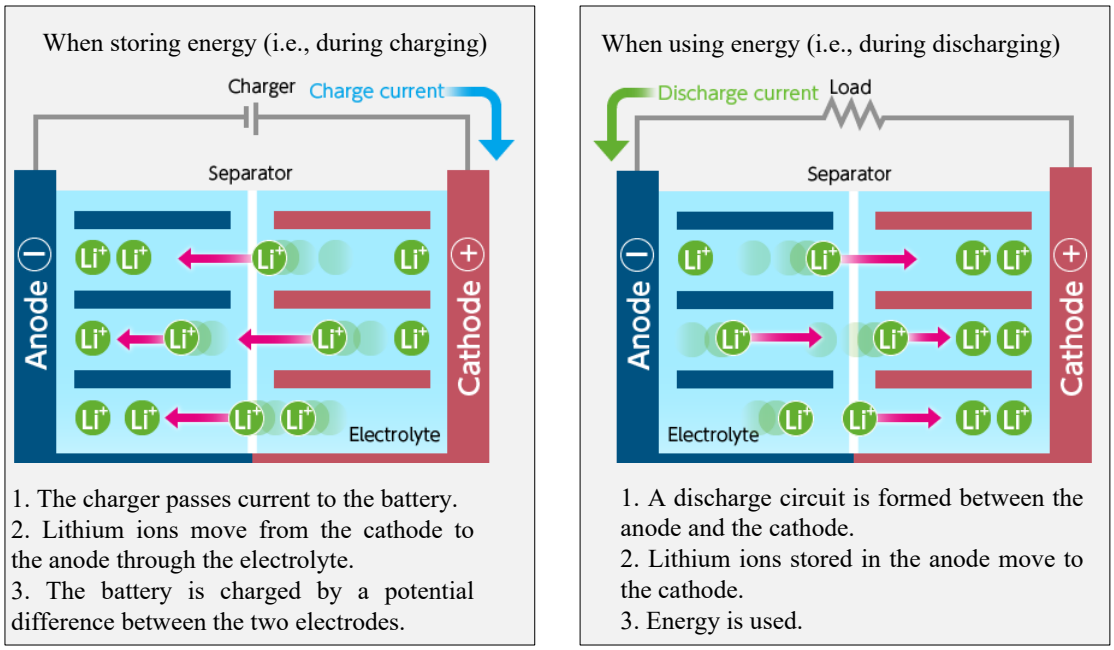

Fig. 5.1: Charging and discharging processes of Li-ion battery [111]

Reduction takes place at the cathode. There, cobalt oxide combines with lithium ions to form lithium-cobalt oxide ($LiCoO_2$). The half-reaction is:

$$CoO_2 + Li^+ + e^- \rightarrow LiCoO_2 \tag{5.1}$$

Oxidation takes place at the anode. There, the graphite intercalation compound LiC_6

forms graphite (C_6) and lithium ions. The half-reaction is:

$$LiC_6 \rightarrow C_6 + Li^+ + e^- \tag{5.2}$$

Here is the full reaction (left to right = discharging, right to left = charging):

$$LiC_6 + CoC_2 \leftrightarrows C_6 + LiCoO_2 \tag{5.3}$$

When the battery terminal voltage drops below the cut-off voltage (or the State of Charge (SOC) becomes lower than the predefined limit), the discharging process must be stopped to avoid irreversible degradation of electrode material. The degradation process of the battery speeds up dramatically as a result of any incorrect operations, such as over-discharging, over-charging, or improper charging. The Li-ion battery has stable performance but less cycle life at high-temperature conditions, while charging below freezing is not possible, [112]. By proper estimation of battery State of Charge (SoC) and temperature, correct approaches can be effectively designed to charge the battery from its initial state to a target SoC value. Moreover, proper charging approaches can also protect batteries from overheating, prolong the service life and improve capacity utilization.

The charging techniques can be divided into traditional and advanced techniques. The traditional techniques can be mainly classified as Constant Current (CC) charging, Constant-Voltage (CV) charging, Constant Current-Constant Voltage (CC-CV) charging, and Multi-stage Constant Current (MCC) charging [113], [114]. The CC approach adopts a small current rate to charge the battery over the whole charging process and the charging is stopped when the predefined charging time or voltage is reached. This charging approach was first introduced to charge Ni-Cd batteries [115], and is also widely used for Li-ion batteries [116]. The CC charging approach is easy to implement, however the selection of a suitable charging current rate that is capable of equilibrating battery charging speed and capacity utilization is a challenge. For example, a large current rate improves the charging speed, but the battery aging process will be accelerated. On the other hand, with a small current rate, high capacity utilization is achieved, but the battery charging speed slows down.

The CV charging concept adopts a predefined constant voltage to charge batteries. The advantage of using CV charging is to avoid over-voltage and irreversible side reactions

which may occur in the charging process, so as to prolong battery cycle life. When the CV charging is applied, the charging current gradually declines due to the low acceptance with progressing recharge. The main issue of the CV charging approach is the selection of an appropriate value for the constant voltage which will obtain a good trade-off among the charging speed, electrolyte decomposition, and capacity utilization [117]. CC charging and CV charging can be integrated to produce a hybrid charging approach named CC-CV. The idea behind this approach is that the battery is first charged by a predefined constant current in the CC stage whilst the battery voltage increases to the maximum safe threshold. Then, the battery enters into the CV stage with a predefined constant voltage and the charging current will be decreasing naturally. When the terminal value of the decreasing charging current, or a predefined capacity, is reached, the CV stage stops. The advantages of the standard CC-CV charging approach are its ease of implementation and the high capacity utilization that can be achieved. However, the challenging issue is to set the appropriate constant current rate at the CC stage and constant voltage value at the CV stage to improve the overall charging performance and guarantee the operation safety of the battery [118]. The switching between battery current and voltage controllers can be done depending on the battery terminal voltage or used within a cascade control system arrangement [119].

Another popular approach is MCC charging. The main difference between MCC charging and CC-CV charging is that in MCC charging, the multi-stage series of charging currents are injected into the battery during the total charging process. The charging speed for the standard MCC approach is usually a bit slower than in CC-CV with the same initial current. Moreover, it is difficult to balance objectives such as charging speed, capacity utilization, and battery lifetime using MCC charging [120]. In order to further improve charging performance, such as avoiding over-voltage, enhancing capacity utilization, and achieving fast charging, some hybrid charging approaches have been developed, including CC-CV and MCC. The issue for using these hybrid approaches is to find the proper current and voltage values to effectively balance conflicting objectives such as charging speed, energy loss, temperature variation, and battery lifetime. Different optimization techniques have been investigated to solve this problem, as in [121]–[123].

The CC-CV method is adopted in this work for the charging/ discharging process.

The CC-CV method can be implemented using separate current and voltage controllers or using a cascaded control system arrangement. In the latter approach, the current controller is the inner loop as it needs to be faster and the battery voltage controller is the outer loop as it can be slower [119]. By adopting cascaded control, the design and verification of each control loop can be performed separately and the battery current can be limited by controlling the saturating level of the battery voltage controller. Furthermore, the switching between current and voltage control is straightforward and this increases the control system modularity [124].

Due to the increase of the electrification level of civil aircraft, load variations, and intermittent operation, it may lead to transient phenomena and voltage disturbances that impact the DC voltage of the distribution network buses [125]. Therefore, there is a need to mitigate the voltage transient phenomena and keep the DC bus voltage within the limits. This can be achieved by the utilization of a battery pack along with a bidirectional DC/DC converter. The controller can be implemented by using a cascaded controller system where the outer loop controls the DC bus voltage and the inner loop controls the battery current [126].

5.2 Battery Model

A battery model is needed, to estimate its voltage in terms of current and SOC. The modified Shepherd model has been employed to represent the voltage dynamics of the Li-ion cell as shown in Fig. 5.2 [127]–[129]. Fig. 5.3 (a) shows the typical discharge curve of the Li-ion battery which can be divided into three parts.

- The first part represents the exponential potential drop of the cell during initial discharge.
- The second part represents the amount of charge that can be extracted from the cell before reaching the nominal voltage of the cell.
- The last part represents the total discharge of the cell when the voltage of the cell drops rapidly to the cut-off voltage.

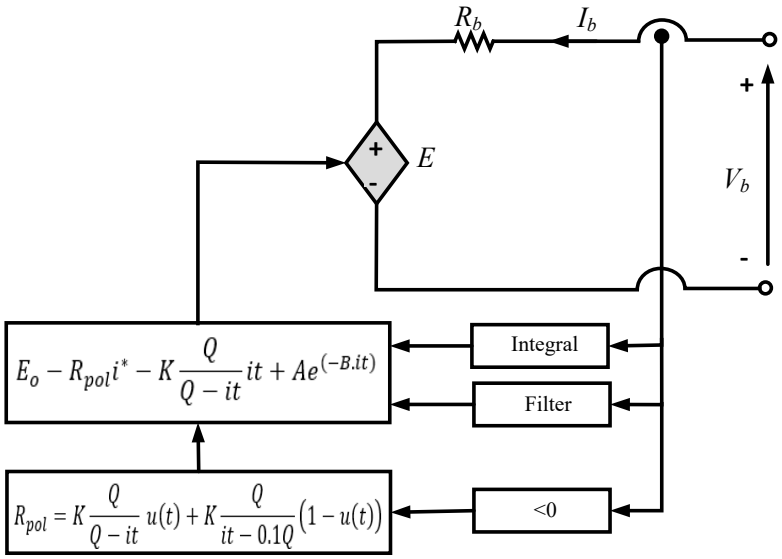

Fig. 5.2: A Li-ion battery model (Includes the additional polarization term) [127]

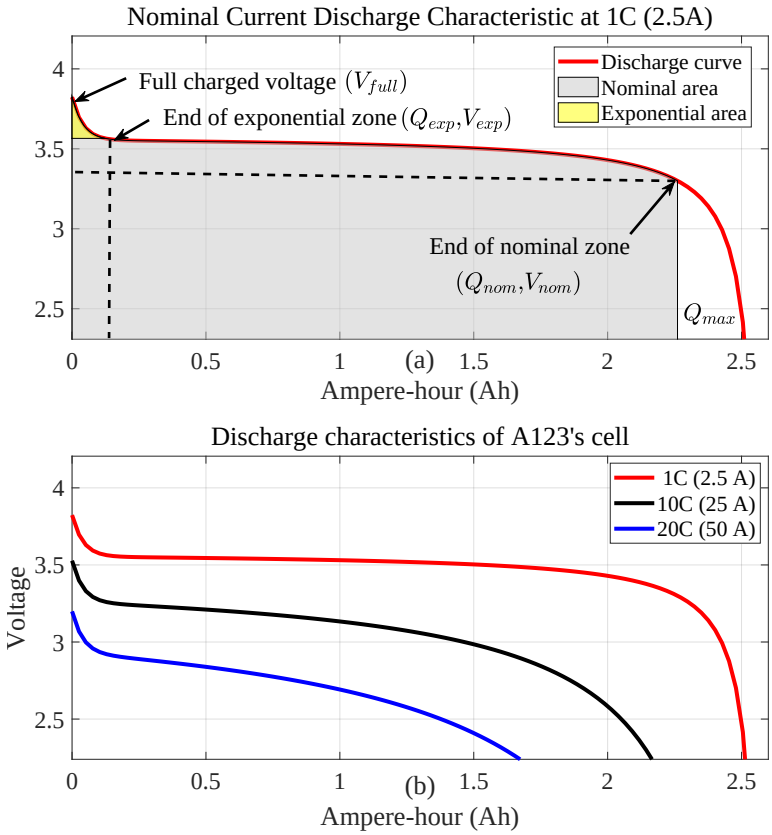

Fig. 5.3: Discharge characteristics of A123's Nano phosphate lithium iron phosphate cell using parameters extraction

The modified Shepherd equation for charging and discharging (Li ion) is given by (5.4) and (5.5) respectively [130]. It is assumed that the internal resistance of the cell is constant during the charging and discharging cycle and does not change with the *it*-rates. The temperature effect on the battery model behaviour is neglected and the model parameters for discharging and charging are identical.

For charging ($i^* < 0$):

$$V_b = E_o - K\frac{Q_{max}}{\int idt - 0.1Q_{max}}.i^* - K\left(\frac{Q_{max}}{Q_{max} - \int idt}\right)\int idt + A\ e^{(-B.\int idt)} - i.R_b \quad (5.4)$$

For discharging ($i^* > 0$):

$$V_b = E_o - K\frac{Q_{max}}{Q_{max} - \int idt}.i^* - K\left(\frac{Q_{max}}{Q_{max} - \int idt}\right)\int idt + A\ e^{(-B.\int idt)} - i.R_b \quad (5.5)$$

where $K\frac{Q_{max}}{Q_{max}-\int idt}it$ is a polarization voltage and $K\frac{Q_{max}}{it-0.1\int idt}$ polarization resistance, and

- V_b is the terminal battery voltage (V)
- E_0 is battery constant voltage (V)
- K is polarisation voltage (V/Ah)
- it is battery capacity (Ah)
- Q_{max} is maximum battery capacity (Ah)
- i^* is filtered battery current (A)
- A is exponential zone amplitude (V)
- B is exponential zone time constant inverse $(\text{Ah})^{-1}$
- i is battery current (A)
- R_b is the internal resistance of the battery (Ω)

The coefficients in (5.4) and (5.5) can be determined in the next section.

5.2.1 Parameter Extraction

The internal resistance can be calculated as [127]:

$$R_b = V_{nom}\frac{1-\eta}{0.2Q_{nom}} \tag{5.6}$$

The three necessary points used to extract the model parameters are:

- The fully charged point (0, V_{full})
- The end of the exponential zone (Q_{exp}, V_{exp})
- The end of the nominal zone (Q_{nom}, V_{nom}).

The voltage of the cell at a fully charged state is defined as:

$$V_{full} = E_o - i.R + A \tag{5.7}$$

The voltage at the exponential section is defined as:

$$V_{exp} = E_o - K\frac{Q}{Q-Q_{exp}}(i+Q_{exp}) + A\ e^{(-B*Q_{exp})} - i.R \tag{5.8}$$

The nominal zone voltage is given by:

$$V_{nom} = E_o - K\frac{Q}{Q-Q_{nom}}(i+Q_{nom}) + A\ e^{(-B*Q_{nom})} - i.R \tag{5.9}$$

Therefore, the parameters E_o, $K$and A can be found by solving 5.7-5.9. By using the parameters of the LiFePO4 battery shown in Table 3.2 [99], the extracted coefficients can be obtained as E_o=3.587 V, K=0.007152 (V/Ah) and A= 0.26963 V. Fig. 5.3 (b) shows the discharging curves of the A123 cell at 1C, 10C, 20C using the values of the extracted coefficients and it is clear that the curves are well aligned.

5.3 Battery Power System

Based on the literature review in Section 2.3.3.2 , the non-isolated bidirectional DC/DC converter is chosen to interface the battery to the DC bus due to having less weight and lower cost. The bidirectional DC/DC converter is assumed to be working in continuous conduction mode, and the switches are considered ideal for simplicity as shown

in Fig. 5.4. The equivalent resistance of the inductor, R_L is included in the model and the DC microgrid is represented by an equivalent inductor L_g, resistor R_g and a constant DC voltage source V_g. It is assumed that the battery model is simplified to a constant voltage E_b and an equivalent internal resistance R_b derived around a particular operational point. The converter non-linear model is linearized using using Taylor approximation around a given operating point and expressed in state space form as:

$$\Delta \dot{X} = AX + BU \tag{5.10}$$

$$Y = CX + D \tag{5.11}$$

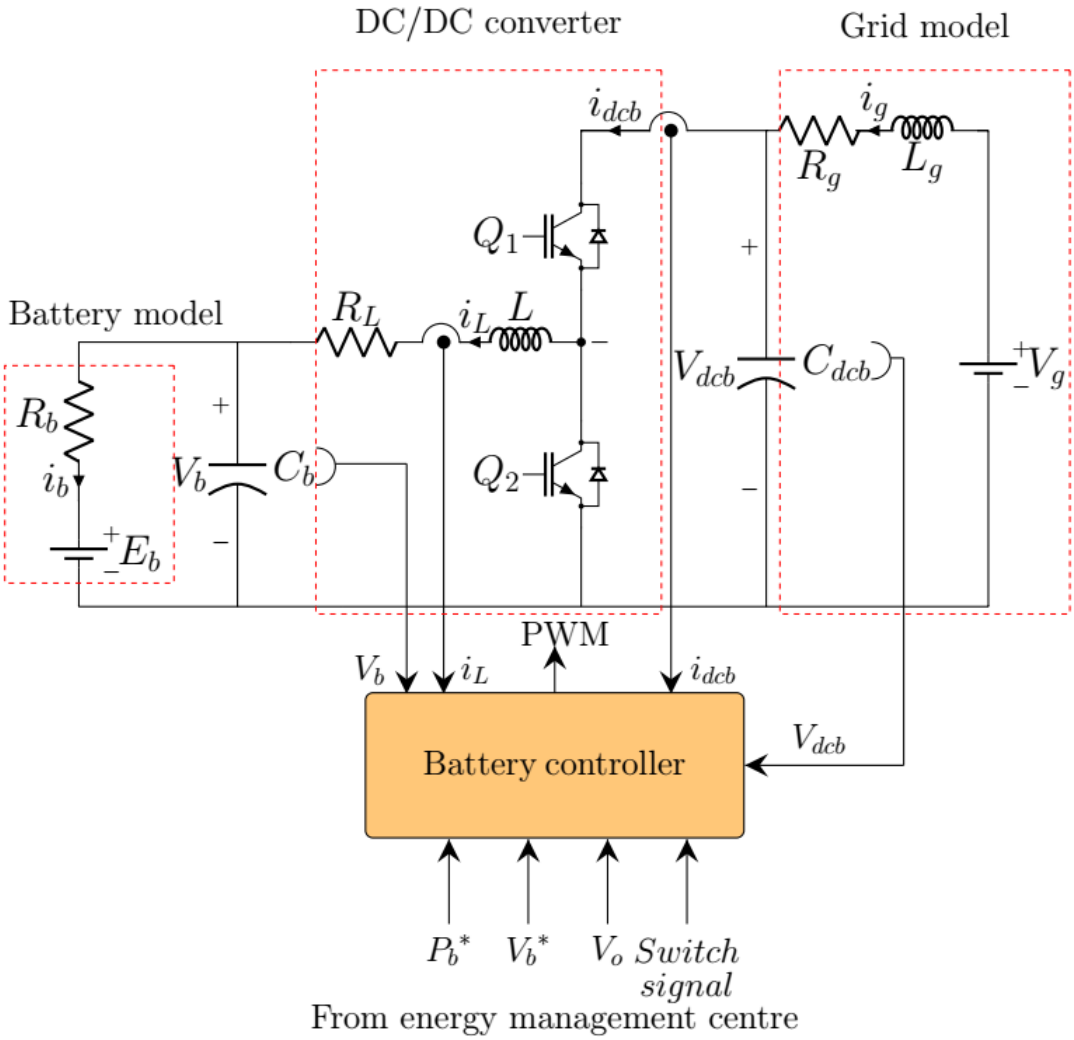

Fig. 5.4: Electric circuit of bidirectional DC-DC converter interfacing the battery to the aircraft DC bus

where

$$X = \begin{bmatrix} \Delta i_L(t) \\ \Delta v_b(t) \\ \Delta i_g(t) \\ \Delta v_{dcb}(t) \end{bmatrix}, A = \begin{bmatrix} \frac{-R_L}{L} & \frac{-1}{L} & 0 & \frac{D_1}{L} \\ \frac{1}{C_b} & \frac{-1}{C_b R_b} & 0 & 0 \\ 0 & 0 & \frac{-R_g}{L_g} & \frac{-1}{L_g} \\ \frac{-D_1}{C_{dcb}} & 0 & \frac{1}{C_{dcb}} & 0 \end{bmatrix}, B = \begin{bmatrix} 0 & 0 & \frac{V_{dcb}}{L} \\ \frac{1}{C_b R_b} & 0 & 0 \\ 0 & \frac{1}{L_g} & 0 \\ 0 & 0 & \frac{-I_L}{C_{dcb}} \end{bmatrix} \tag{5.12}$$

$$U = \begin{bmatrix} \Delta E_b(t) \\ \Delta V_g(t) \\ \Delta d_1(t) \end{bmatrix}, C = \begin{bmatrix} 1 & 0 & 0 & 0 \\ 0 & 1 & 0 & 0 \\ 0 & 0 & 1 & 0 \\ 0 & 0 & 0 & 1 \end{bmatrix}, D = \begin{bmatrix} 0 & 0 & 0 & 0 \\ 0 & 0 & 0 & 0 \\ 0 & 0 & 0 & 0 \end{bmatrix} \tag{5.13}$$

where

- C_b is the battery capacitor (F)
- C_{dcb} is the DC bus capacitor (F)
- R_{eq} is the sum of internal battery and inductor resistances (Ω)
- D_1 is the duty cycle of the upper switch
- V_{dcb} is the battery DC bus voltage (V)

The steady state solution of the system model (5.11) provides the system equilibrium points given by:

$$V_{dcb} = \frac{V_g R_{eq} + D_1 E_b R_g}{R_g D_1^2 + R_{eq}} \tag{5.14}$$

$$V_b = \frac{E_b R_g D_1^2 + D_1 V_g R_b + E_b R_L}{R_g D_1^2 + R_{eq}} \tag{5.15}$$

$$I_g = I_{dcb} = \frac{-D_1(E_b - D_1 V_g)}{R_g D_1^2 + R_{eq}} \tag{5.16}$$

$$I_L = I_b = \frac{-E_b + D_1 V_g}{R_g D_1^2 + R_{eq}} \tag{5.17}$$

It should be noted from (5.17) that the direction of the inductor current depends on the relationship between the duty cycle, the battery voltage, and the DC bus voltage. Fig. 5.5 shows the relationship between the duty cycle and the inductor current. The value of the duty cycle D_0 at zero inductor current is given by 5.18.

$$D_0 = \frac{E_b}{V_g} \tag{5.18}$$

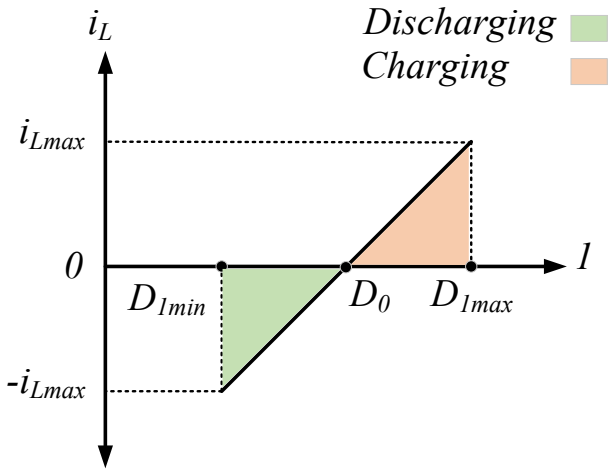

Fig. 5.5: Change of inductor i_L current with respect to duty cycle D

In buck mode, the inductor current is positive and hence the duty cycle should be higher than D_0. In boost mode the inductor current is negative and therefore, the duty cycle is smaller than D_0.

5.4 Proposed Battery Controller Design

The proposed battery control scheme as well as the energy management strategy for regulating the charging/discharging process are discussed in this section. To aid in controllers' gain design, the transfer functions of linearized plants for inner and outer loops are derived.

5.4.1 Control Scheme

Fig. 5.6 shows the proposed controller structure of the battery. The structure includes two parts: the inner and the outer loops. The inner loop function is to control the inductor current i_L. The reference inductor current is compared with the actual current to generate the corresponding duty cycle, which in its turn generates the modulating signal that is used by PWM to generates gate pulses of the switches. The outer loop is made up of DC output power, battery voltage, and DC voltage controllers (W_p, W_b and W_v).

In case of failure of any power generation channel, as mentioned in Section (3.2.1), a

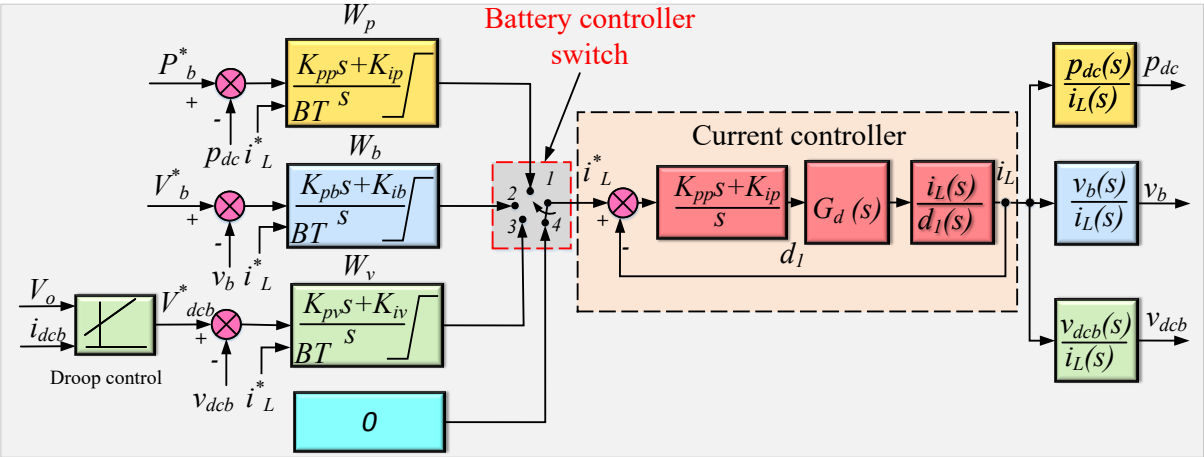

Fig. 5.6: Proposed battery controller with their associated control plants

DC power controller is employed so that the battery covers the load power deficit. In an emergency scenario (all power generation channels failed), the DC voltage controller is selected because the DC power controller is not effective for keeping the DC bus voltage within standard's limits. Therefore, the DC bus voltage is controlled based on the droop control method, to generate the reference voltage for the DC voltage controller. The reference voltage of the converter can be given as in (5.19).

$$V_{dcb}{}^{*} = V_o - i_{dcb}R_{db} \tag{5.19}$$

where,

- V_o is the no-load system voltage
- i_{dcb} is the DC bus current
- R_{db} is the droop gain
- V^*_{dcb} is the reference battery DC bus voltage (V)
- P^*_b is the reference DC power (W)
- V^*_b is the reference battery voltage
- P_{dc} is the battery DC power (W)

For the charging process, the CC-CV method is chosen for the Li-ion battery according to the manufacturer's recommendation. The DC power controller is selected to charge

the battery pack with constant current up to SoC_{max1}, then the battery voltage controller is applied to keep the battery voltage at its maximum limit and continue charging until SoC_{max} achieved. To ensure smooth transitions between the controller outputs, the BT algorithm is employed for all three controllers [100]. This algorithm takes into account the output i_L^* and maintains each controller's integrator states to be of similar values. The system delay is represented by the delay function $G_d(s)$ and is given by (5.20).

$$G_d(s) = \frac{1}{T_d s + 1} \tag{5.20}$$

where T_d is the time delay due to the inverter and the digital controller, which is calculated as 1.5 times the sampling time [110].

5.4.2 Energy Management Strategy

The role of the battery EMS is to manage the charging and discharging process of the battery, taking into consideration the various limitations, such as maximum charging/discharging current, full charge voltage, and minimum and maximum SoC with different operation modes. Fig. 5.7 shows the flowchart of the EMS. The battery discharges when there is a shortage in power generation and its SoC is above the minimum predefined value, while the battery charges when the SoC is below the minimum value and enough generated power is available. In case of a shortage of generated power and it being necessary to charge the battery, the EM strategy can decide to shed some Low Priority Loads (LPLs) and/or some Medium Priority Loads (MPLs) to allow the battery charging, otherwise charging cannot take place. The reference charging/discharging power, reference battery voltage, no-load system voltage, and switching signal are sent from the Energy Management Center (EMC), based on the operation mode of the system. The Finite State Machine (FSM) method is used to implement the EM strategy using Matlab/Stateflow, since this is easy to use as it is a graphical language and includes powerful and fast algorithms [91].

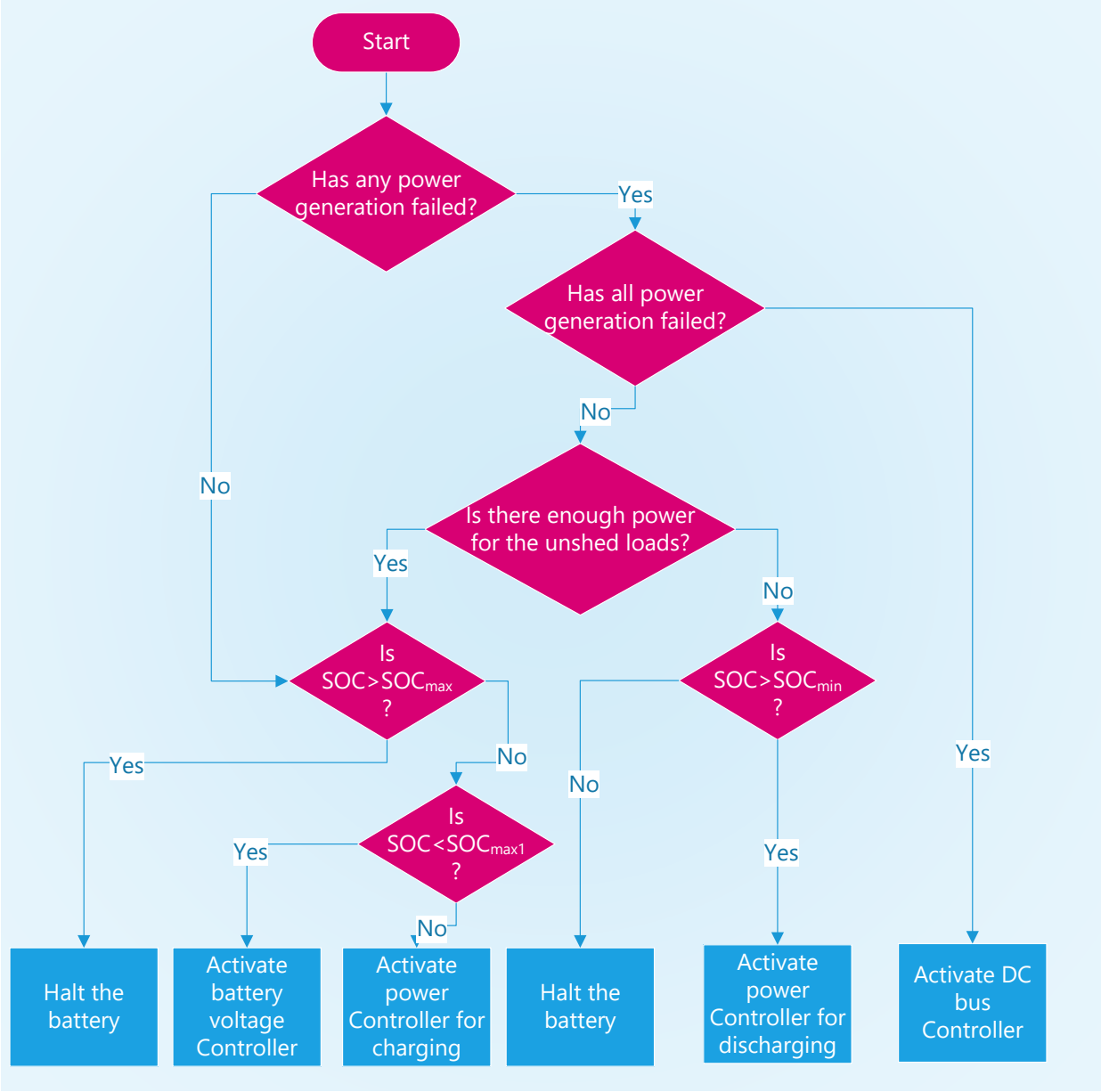

Fig. 5.7: Energy management strategy

5.4.3 Controller Design

5.4.3.1 Inner current loop

Using Taylor's series expansions, the transfer function of the linearized plant between the inductor current and the duty cycle, using (5.11) is given by:

$$\frac{\delta i_L}{\delta d_1} = \frac{a_1 s^3 + a_2 s^2 + a_3 s + a_4}{b_1 s^4 + b_2 s^3 + b_3 s^2 + b_4 s + b_5} \tag{5.21}$$

while the linearized transfer function between DC bus voltage and duty cycle can be obtained as:

$$\frac{\delta v_{dcb}}{\delta d_1} = \frac{c_1 s^3 + c_2 s^2 + c_3 s + c_4}{b_1 s^4 + b_2 s^3 + b_3 s^2 + b_4 s + b_5} \tag{5.22}$$

Fig. 5.8 and Fig. 5.9 depict the linearised plants' poles/zeros map in (5.21) and (5.22). The open-loop transfer function between battery current and the duty cycle is stable, however, the transfer function between DC voltage and duty cycle has an RHP zero, preventing high performance from being achieved.

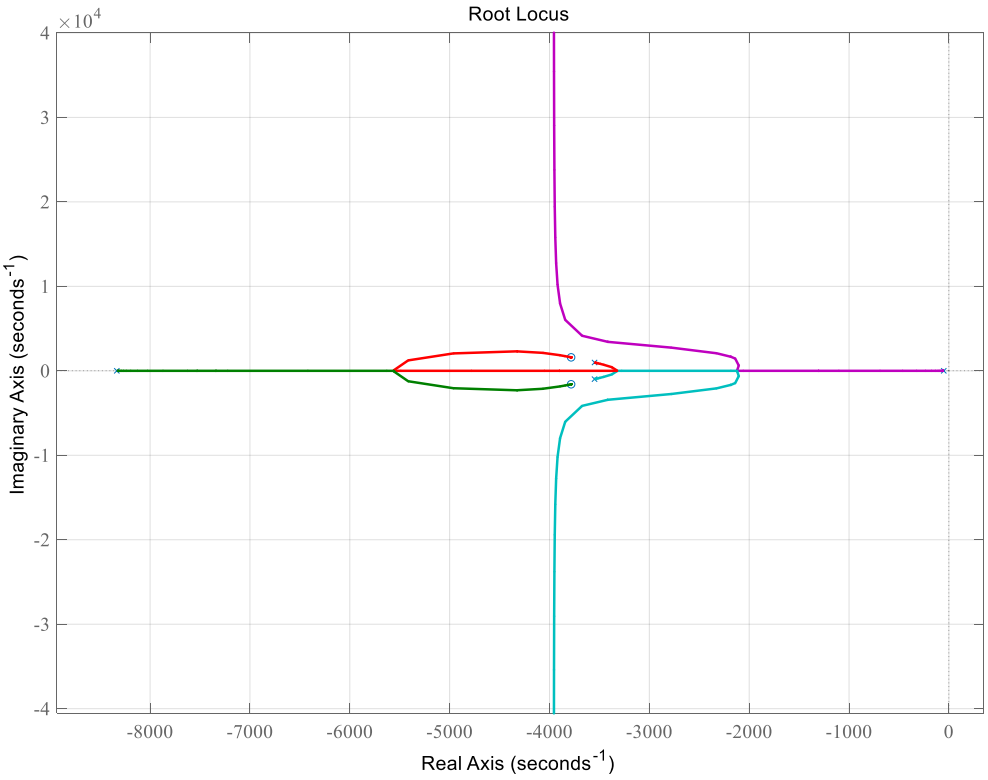

Fig. 5.8: Poles/zeros map of the linearized plant (5.21)

5.4.3.2 Outer loops

The DC power control, DC bus voltage control, and battery voltage control are achieved indirectly through the cascaded outer control loops. The transfer functions of linearized plant between DC bus voltage and battery voltage and inductor current can be expressed respectively as follows:

$$\frac{\delta v_{dcb}}{\delta i_L} = \frac{c_1 s^3 + c_2 s^2 + c_3 s + c_4}{a_1 s^3 + a_2 s^2 + a_3 s + a_4} \tag{5.23}$$

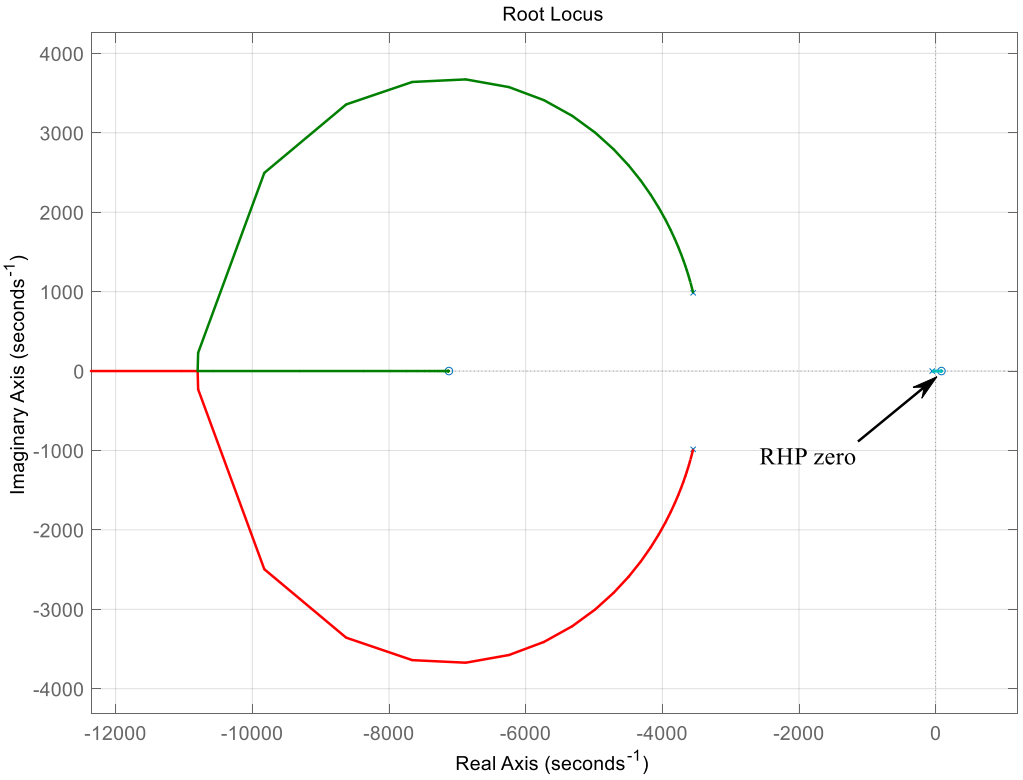

Fig. 5.9: Poles/zeros map of the linearized plant (5.22)

$$\frac{\delta v_b}{\delta i_L} = \frac{R_b}{C_b R_b s + 1} \tag{5.24}$$

while the transfer function of the linearized plant between DC power and inductor current can be obtained by linearizing the power equation in (5.25).

$$p_{dc} = v_{dcb}.i_{dcb} \tag{5.25}$$

The result of linearization gives the required linearised transfer function as (5.26).

$$\frac{\delta p_{dcb}}{\delta i_L} = \frac{d_1 s^2 + d_2 s + d_3}{e_1 s + e_2} \tag{5.26}$$

where the coefficients $a_1 - a_4, b_1 - b_5, c_1 - c_4, d_1 - d_3$ and $e_1 - e_2$ are detailed in the Appendix B.1. It should be noted that the DC voltage and DC power transfer functions in boost mode have RHP zeros. The RHP zero restricts the achievement of high dynamic performance and makes the control design a challenging task.

5.4.3.3 Controllers Gains Calculation

Choosing the operating point I_L= -1000A (maximum discharging current of battery pack), V_g=270V and E_b=135V, then from steady state equations (5.15) to (5.17), the steady state values are derived: D_1=0.3117, V_{dcb}=351.6V, V_b=110.4V, and I_g=-311.7 A. Using the parameters of the system under study as shown in Table 5.1, the transfer functions in (5.21) to (5.26) can be obtained as:

$$\frac{\delta i_L}{\delta d_1} = \frac{2.748e-11s^3 + 2.397e-05s^2 + 0.1776s + 381.2}{8e-17s^4 + 7e-11s^3 + 5e-07s^2 + 0.001s + 0.09} \tag{5.27}$$

$$\frac{\delta v_{dcb}}{\delta d_1} = \frac{4.22e-11s^3 + 3.68e-05s^2 + 0.2598s - 1.709}{8e-17s^4 + 7e-11s^3 + 5e-07s^2 + 0.001s + 0.09} \tag{5.28}$$

$$\frac{\delta p_{dcb}}{\delta i_L} = \frac{-2.471e-07s^2 - 0.2137s + 0.8868}{2.471e-07s + 0.2137} \tag{5.29}$$

$$\frac{\delta v_b}{\delta i_L} = \frac{0.0246}{1.156e-6s + 1} \tag{5.30}$$

Four PI controllers are employed to control the inductor current, DC power, DC bus voltage, and battery voltage. The PI controller is designed using Gauss Newton-based design algorithm to achieve the desired control specified in Table 5.2. It is recommended for the outer loops to be much slower than the inner current loop to ensure good control performance of both loops [35]. Fig. 5.10 and Fig. 5.11 show the step and frequency response of the DC/DC converter control loops at the desired operating operation when a step reference is applied. It is clearly seen that the desired specification is achieved,

Table 5.1: System under study parameters value

Parameter	V_g	V_b	R_g	L_g	C_{dcb}	L	R_b	R_L	C_b	f_{sw}
Value	270 V	135 V	260mΩ	36.5μH	2 mF	1 mH	24.6 mΩ	0.041 mΩ	47μF	5 kHz

Table 5.2: Desired specification of controllers and corresponding gains value

Controller	W_c	W_p	W_v	W_b
Bandwidth (Hz)	1000	10	10	10
Phase margin (degree)	45	45	45	45
K_p	0.0175	0	0	0
K_i	14.8	0.34	-560	2600

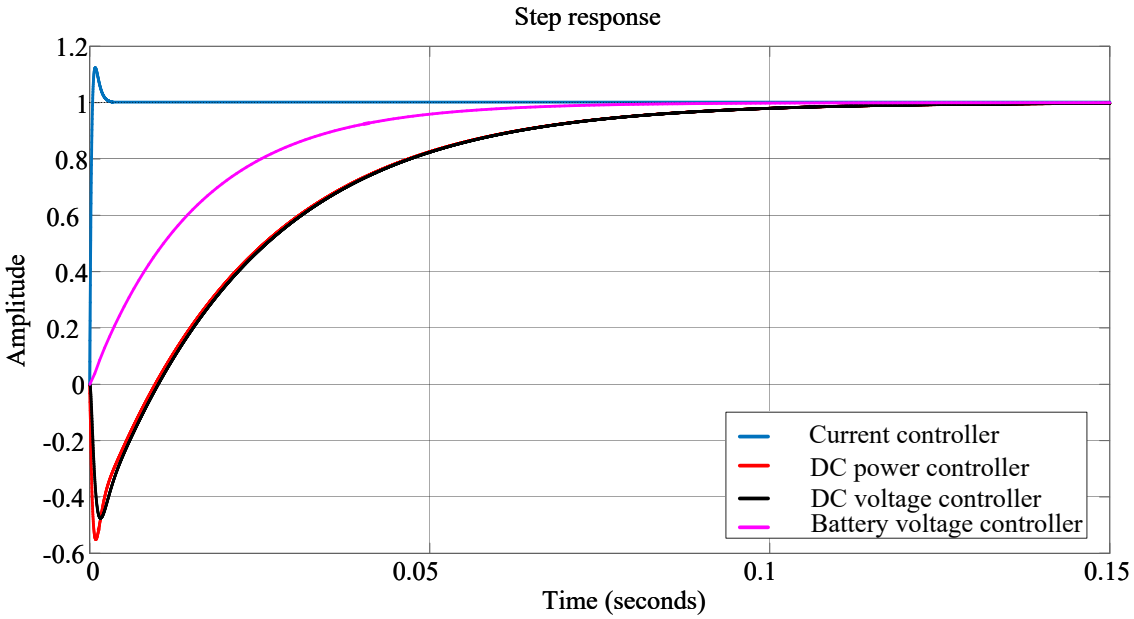

Fig. 5.10: Step response of inner and outer control loops

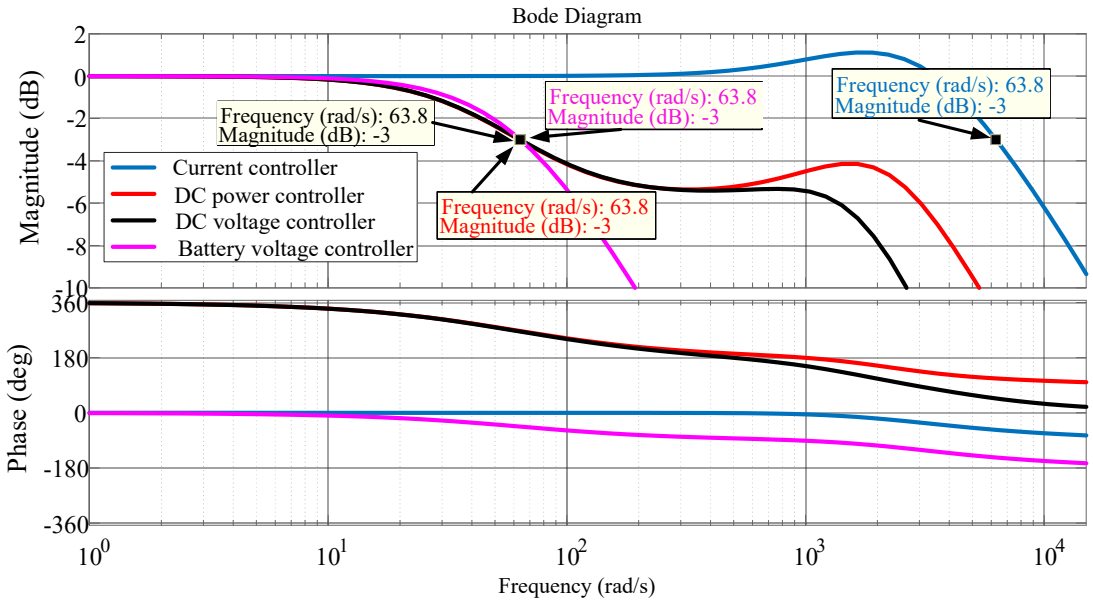

Fig. 5.11: Frequency response of inner and outer control loops

for the current controller the bandwidth is 1 kHz and 10 Hz for the other controllers. It should be noted that the effect of non-minimum phase behaviour in DC power and DC bus voltage plants appears in the step response as undershoot at the beginning. As suggested in Chapter 4, the ADRC technique can provide a potential solution for non-minimum phase systems [110].

5.5 Simulation results

In order to demonstrate the performance of the proposed battery system under different operating scenarios, a simulation was conducted using MATLAB®/Simulink®. It is assumed that the grid consists of two generators, namely G_1 and G_2, as shown in Appendix D. The generator has two values "1" and "0" for no-fault and fault statuses, respectively. The initial SoC of the battery is chosen to be 70%, the discharge power is 50 kW, the charging power is 30 kW, this is equivalent to 10 A (5C) charging current for each branch, and the generators' statuses are equal to 1. Therefore, the EMS decides to charge the batteries with constant current until 80% by activating the power controller as shown in Fig. 5.12 (b). When the SoC reaches 80%, at 100s, the EMS activates the

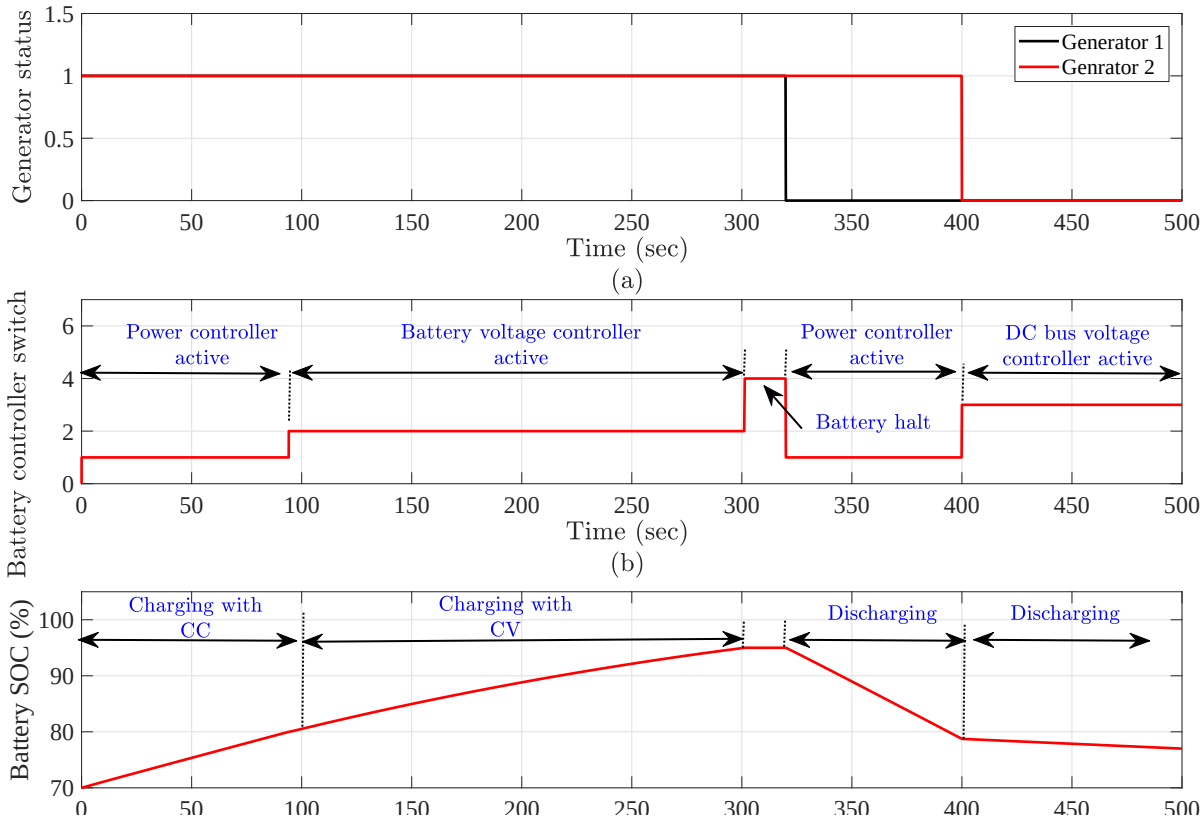

Fig. 5.12: Time response: (a) Generator status, (b) Battery controller switch signal, (c) Battery SOC

battery voltage controller to keep the battery voltage at its full charge value, as shown in Fig. 5.13 (c). Therefore, the battery current is decreased to keep the battery charging

slowly, as shown in Fig. 5.13 (a). Once the battery SoC reaches the maximum value of 95%, the EM strategy sends a signal to the switch to halt the battery.

At time 320s, a fault in generator 1 occurs, hence the EM strategy activates the power controller to allow the battery to discharge with 50 kW, as shown in Fig. 5.14 (c). It should be noted that the grid voltage is greater than the battery DC bus voltage in charging mode. This means that the direction of power flow is from grid to battery in charging mode, while in discharging mode the battery DC bus voltage is greater than the grid voltage, to push the power from battery to grid, as shown in Fig. 5.14 (a). To test the performance of the DC voltage controller, a fault in generator 2 at time 400s is applied to simulate an emergency scenario. In response to this fault, the EM strategy activates the DC bus voltage controller. The controller keeps the DC bus voltage at 270 V while supplying the 4.50 kW load, as shown in Fig. 5.14 (a). The battery voltage

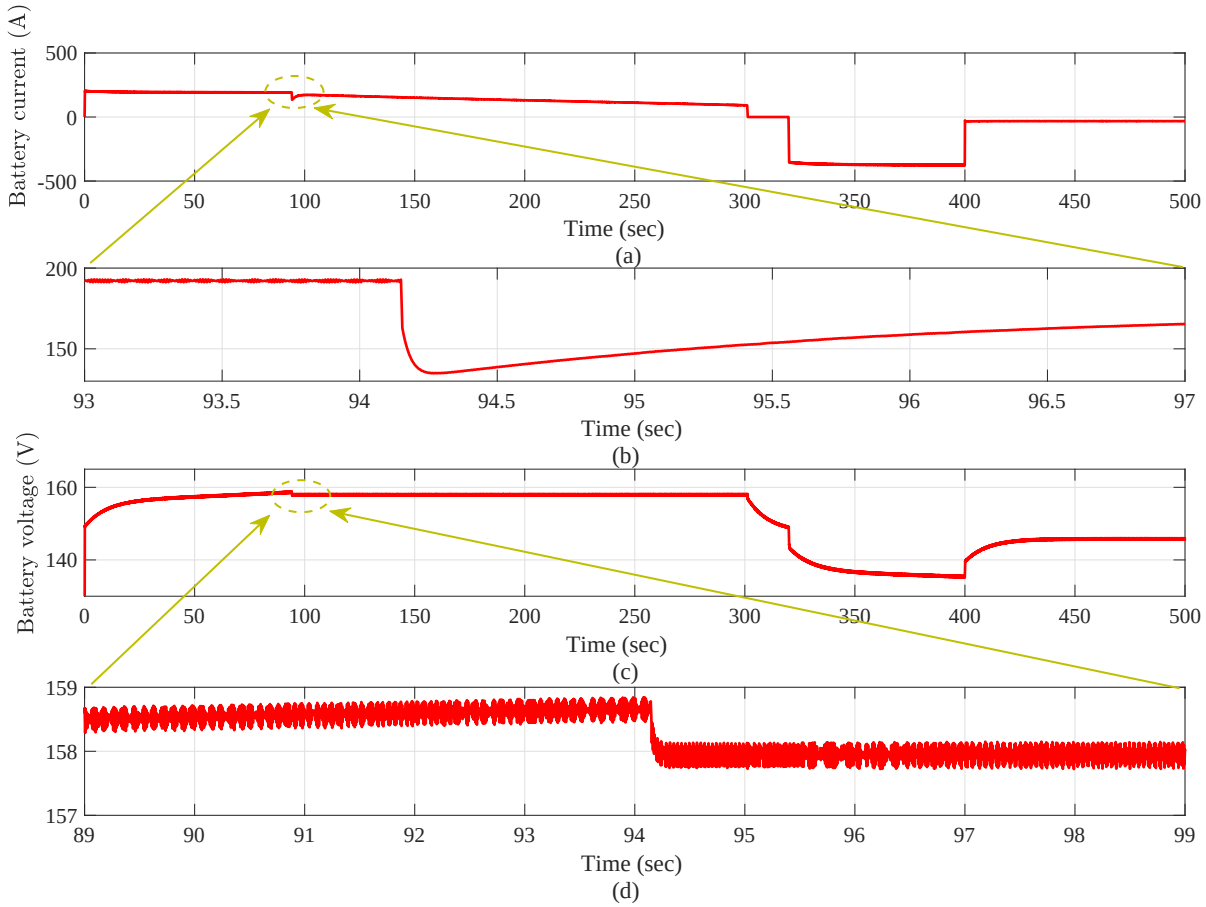

Fig. 5.13: Time response: (a) Battery current, (b) Zoom in of battery current, (c) Battery voltage, and (d) Zoom in of battery voltage

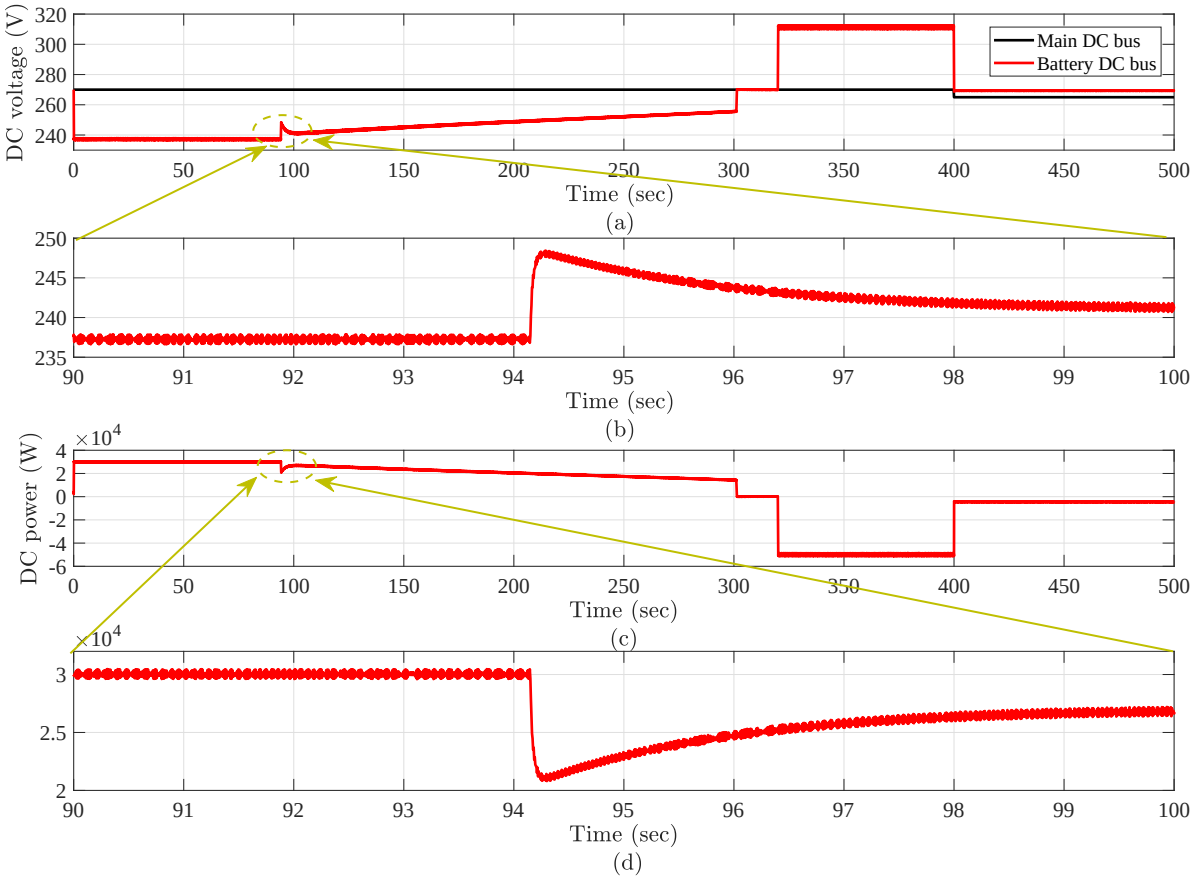

Fig. 5.14: Time response: (a) DC voltage, (b) Zoom in of DC voltage, (c) Dc power, and (d) Zoom in of DC power

increased compared to the previous scenario due to the reduction of the voltage drop at the internal battery resistance. The simulation results prove the effectiveness of the proposed controller under different situations.

5.6 Conclusion on Chapter 5

In this chapter, a novel battery control scheme was proposed, with the strategy to cover the concept of four functionalities: battery current, DC power, DC bus voltage, and battery voltage control. The lithium-ion battery was chosen for this thesis because it has superior characteristics such as high energy density and long life cycles compared to other battery types. The modified Shepherd model is employed to model the Lithium-ion battery used in this study and its associated parameters are found for the chosen battery. The CC-CV charging/discharging method is used because it is simple to implement and allows for high capacity utilization. The CC-CV approach is implemented using a cascaded control system arrangement because it allows for separate design and verification of each control loop and effectively limits the battery current controller by saturating the battery voltage controller. The inner loop is the current controller, and the outer loop is the battery voltage controller/DC power/DC bus voltage. The small-signal control plants for the controllers were derived for the control design purpose. The desired specifications of the controllers are defined and the corresponding PI parameter values were obtained. It was observed that non-minimum phase characteristics were inherent for both DC power and DC bus voltage plants, which meant limited high-performance achievement for the associated controllers. Simulations were conducted in order to demonstrate the control operation for each of the functionalities. The novel battery controller will be integrated with the overall electric power system of the aircraft, allowing an investigation of control robustness in different flight conditions and of the supervisor control strategy of the EPS. By integrating the proposed battery controller with the overall EPS, the vital loads can be continuously powered even under emergency circumstances by activating the DC bus voltage controller. Furthermore, based on the proposed EM strategy, the other functions can be fulfilled by activating the other controllers, such as battery voltage and DC power controllers.

Chapter 6

Onboard Microgrid Droop Control to Minimize Total Losses

This chapter will investigate the optimal droop gains design approach to achieve minimum EPS losses (maximum system efficiency). An onboard Microgrid (MG), based on a common DC bus with multiple-sources and multiple-loads is studied considering transmission line losses as well as converter losses for the common types of loads such as CIL, CCL, and CPL. The converter losses model is established to support the optimal droop gain selection. The optimal droop gains are analytically derived for the mentioned load types. The effectiveness of the proposed design method is then verified using detailed simulations in a Matlab®/Simulink® environment and evaluated experimentally using a laboratory DC microgrid test rig.

6.1 Introduction

From the control point of view, the PC's primary control can be divided into an inner loop (voltage/current control) and outer droop control, the latter of which is used for ensuring desirable load-sharing [131]-[132]. Droop control is a decentralized control method that is widely accepted in DC microgrids due to its modularity, reliability, and ability to achieve load-sharing without communication links. Based on these, reliable system control can be realized [133]–[135]. The idea behind droop control is to deliver the required power/current to the DC bus by linearly reducing the DC voltage reference

with any increase in output current [136]–[138]. This can be achieved by adding a virtual resistance to the converter controller. This virtual resistance is also known as droop gain, droop constant, or droop coefficient [139]. However, this type of conventional droop control has two limitations. The first is that the output voltage of each converter cannot be the same because the line resistance variations during operation affect the output current-sharing accuracy [140]. The second limitation of conventional droop control is that the DC bus voltage deviation increases with the load due to the droop action. These two limitations are analysed in detail in [80],[141].

Thus, the challenge with droop control is related to selection of appropriate droop gains to achieve any required power-sharing, to improve DC bus voltage regulation, and to reduce power system losses. By using a large droop gain, the power-sharing between sources is improved [141], but this degrades the voltage regulation and increases the system losses if sources with different ratings are used. On the other hand, if a droop gain is small, the voltage regulation is improved, but the power-sharing will be deteriorated, especially under heavy loads. Therefore, a compromise between power-sharing, voltage regulation, and system losses reduction should be conducted using, for example, a multi-objective optimization of droop gain design strategy. Previous research work has dealt with this issue and will be summarized below.

The authors in [142] present a decentralized inverse-droop control to achieve current-sharing between parallel DC-DC converters. This is accomplished by raising the output voltage reference as the load absorbs more power. Each module is self-contained, and there is no need to use a supervisory controller or communication. Non-linear droop control is proposed in [133], where the droop gain is set as a function of the converter output current, and its value increases when the output current increases. As a result, there is a reduction in the effect of DC voltage sensor accuracy and of the resistance of cables on voltage regulation and load-sharing. In [143], the equivalent droop gains are calculated automatically based on loading conditions. When the load current increases, the equivalent droop gains are automatically increased to improve the current-sharing. In [144], the droop gains and the no-load voltage of source converters are optimized to minimize the current-sharing error and the voltage deviation from the nominal grid voltage. This is done using a particle swarm optimization technique.

In [145] the droop parameters are optimized to minimize the current-sharing error and the transmission line power losses. This paper does not consider the converter losses in the optimization algorithm. Meanwhile, the authors in [133] investigate the system efficiency of parallel converters with linear droop and inverse parabolic droop methods. The transmission line losses and power conversion losses are both considered. By examining the efficiency and load-sharing curves, the non-linear droop was found to provide better load-sharing under a heavier load, while the efficiencies for linear and non-linear droop control are almost identical.

In [146], a droop gain optimization method is presented to improve the operational efficiency of a system with parallel DC-DC converters. The optimization uses a Genetic Algorithm at the tertiary controller level to find the optimal sharing ratio. The converter losses are taken into account, with the MATLAB curve-fitting tool used to transform the experimental data for converter efficiency into an analytical function dependent on the converter current. Although this proposed method improves the system efficiency of the parallel converter system, it requires communication between converters to collect the system measurements and transmit them to the tertiary level where the optimization decisions are performed. A complex multi-objective optimization-based intelligent computation approach for selecting the optimal droop coefficients for energy sources in an islanded DC microgrid is presented in [147]. The proposed method takes into consideration the system voltage regulation, enhanced current-sharing among energy sources, and total system losses minimization, however, only transmission line losses are considered.

Based on this review of the the previous literature, the existing droop gain design methods mostly depend on computationally intensive control algorithms. In this chapter, a simple, explicit, and analytical design method is proposed to define droop gains that lead to minimization of power losses (including transmission line and converters losses) for the common types of loads. The optimal droop gains can be calculated by relying only on the knowledge of converters' power losses parameters.

6.2 Modelling and Analysis of Single DC Bus EPS with i Paralleled Converters

A single DC bus-based multiple-sources EPS is used for this study, as shown in Fig. 6.1. It consists of i sources feeding a common DC bus through i converters and cables. The common DC bus supplies power to different types of loads. A generalized voltage model for an i converter-based system supplying a resistive load is given in (6.1):

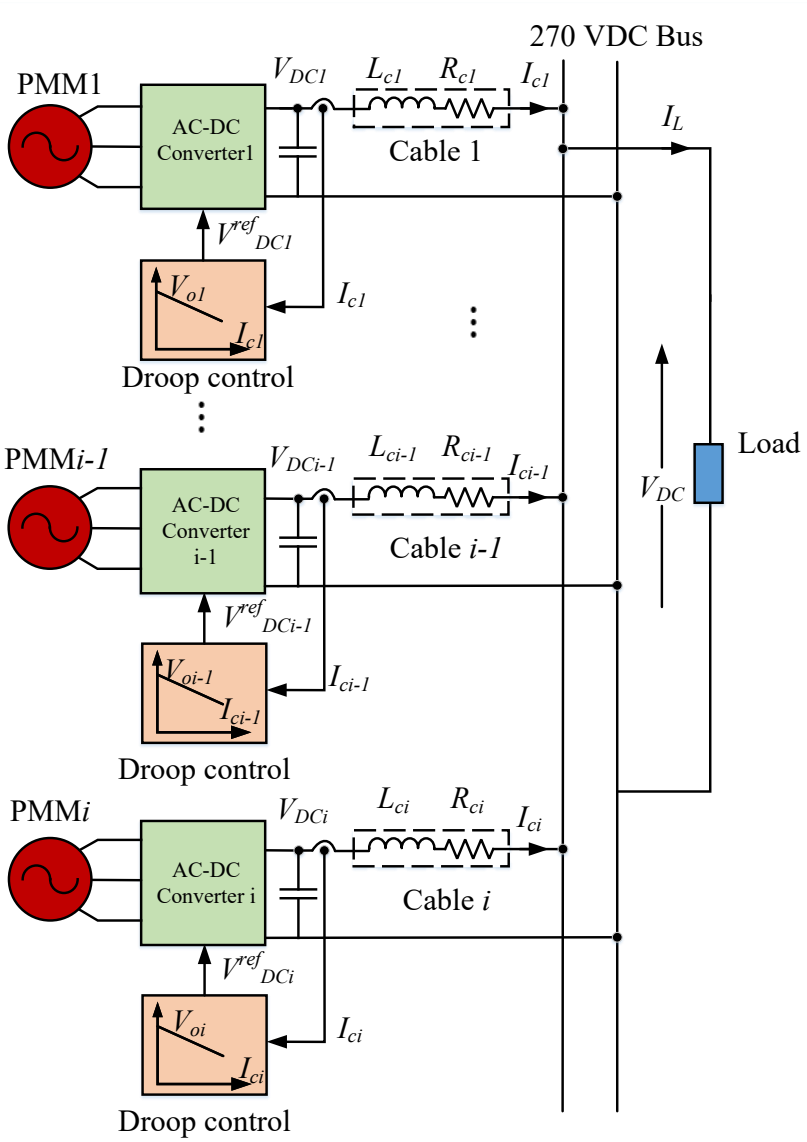

Fig. 6.1: DC microgrid power system of the system under study

.

$$V_{DCi}^{ref} = V_{oi} - I_{ci}R_{di} \tag{6.1}$$

where V_{DCi}^{ref} refers to the output voltage reference of source i, V_{oi} is the no-load output voltage of the i^{th} converter, and I_{ci} and R_{di} represent, respectively, the output current and virtual resistance representing the effect of the droop control. By applying Kirchhoff's voltage law to the equivalent circuit of the i converter-based DC microgrid with a resistive load, as shown in Fig. 6.2, the steady-state model of the system satisfying (6.1) is given by:

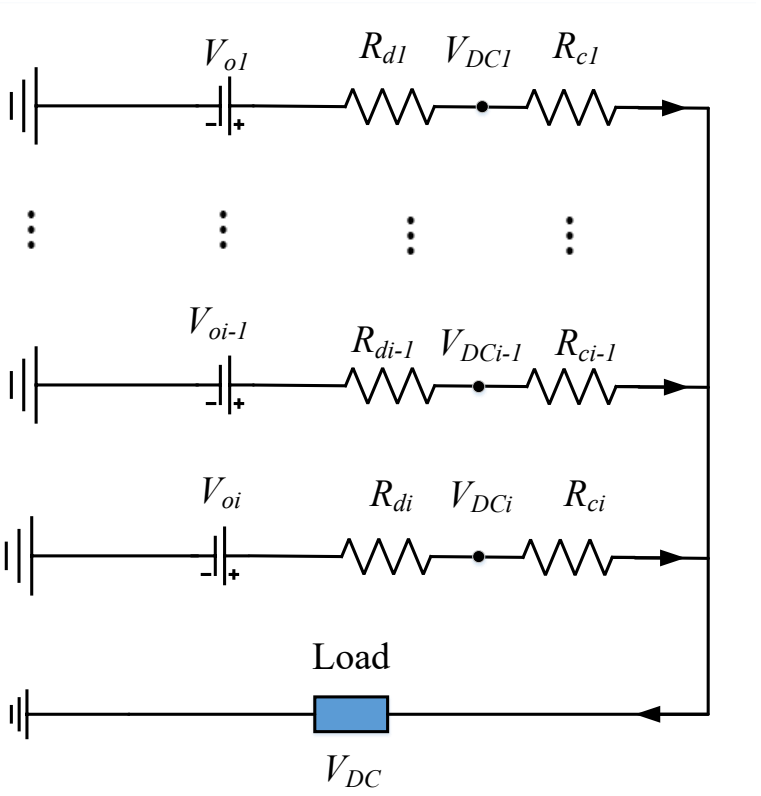

Fig. 6.2: Equivalent circuit of i parallel converter-based DC microgrid of the system under study

.

$$\begin{aligned} V_{o1} - I_{c1}R_1^{'} - I_L R_L &= 0 \\ &\vdots \\ V_{oi} - I_{ci}R_i{}' - I_L R_L &= 0 \end{aligned} \tag{6.2}$$

$$I_L = I_{c1} + I_{c2} + ... + I_{ci} \tag{6.3}$$

where $R_i^{'} = R_{di} + R_{ci}$, and R_{c1}, R_{ci}, I_L and R_L are the Transmission Line Resistances (TLR) of the first converter, the TLR of i^{th} converter, the common DC bus load current,

and the load resistance, respectively. Using (6.2), the current share of each converter can expressed as:

$$\begin{aligned} I_{c1} &= \frac{V_{o1} - I_L R_L}{R_{d1} + R_{c1}} \\ &\vdots \\ I_{ci} &= \frac{V_{oi} - I_L R_L}{R_{di} + R_{ci}} \end{aligned} \tag{6.4}$$

By assuming $V_{o1} = V_{o2} = ... = V_{oi}$, the converters' current sharing ratio in the steady-state between the i^{th} converter and the master converter (number 1) can be given as:

$$\frac{I_{ci}}{I_{c1}} = \frac{R_{d1} + R_{c1}}{R_{di} + R_{ci}} \tag{6.5}$$

It can be seen from (6.5) that load-sharing depends on both droop gains and the cable resistances. Equation (6.5) is valid for the load current-sharing of any type of load, including CCL, CIL, and CPL, as the current is distributed between converters based on the source's equivalent resistance (i.e., the sum of the droop gains and cables resistances). Optimal load current-sharing to achieve a specific set of optimization objectives can, therefore, be achieved by selecting suitable values for the converter droop gains.

6.3 Converter Power losses model

The losses of a given power converter can be categorized into switching and conduction losses [148]. Switching losses depend on the switching frequency, operating voltage, and current of the converter, while conduction losses are proportional to the converter output current. For simplicity, if can be assumed that the losses of the converter may be considered to be the sum of the two main parts of no-load losses and copper losses. A streamlined converter losses model is proposed as:

$$P_{losses} = P_{noload} + I_c^2 R_{es} \tag{6.6}$$

where R_{es}, P_{noload}, and I_c denote the Equivalent Series Resistance (ESR) representing the conduction losses of the converter, the no-load losses, and the converter output DC current, respectively. The no-load losses are represented as a percentage of the converter's total losses at the nominal operating point, as in (6.7), where S_r is the split ratio:

$$S_r = \frac{P_{noload}}{P_{lossesn}} \tag{6.7}$$

At nominal power, the converter efficiency is defined as in (6.8), where P_n is the nominal output power:

$$\zeta_n = \frac{P_n}{P_n + P_{lossesn}} \tag{6.8}$$

Substituting (6.7) and (6.8) into (6.6), the generalized model of the converter equivalent series resistance is expressed as:

$$R_{es} = \frac{(\frac{P_n}{\zeta} - P_n)(1 - S_r)}{I_{cn}^2} \tag{6.9}$$

To validate the accuracy of the proposed converter losses model in (6.6), the efficiency curve of an ABB string inverter [149] for the parameters shown in Table 6.1 is compared to the efficiency calculated using the proposed model in (6.6). Fig. 6.3 (a) shows the efficiency curves of the inverter calculated using the proposed model from (6.6), with the data listed in Table 6.1 at different split ratios (from 10% to 30%), and the actual converter efficiency curve obtained from the converter datasheet. It can be seen that the efficiency curve at a 15% split ratio matches the efficiency curve given in the datasheet [149] as it provides less average error value 4.83% over a full range of loading as sown in Fig. 6.3 (b).

Table 6.1: Technical Data for ABB String Inverter [149]

Model	ABB string inverters PRO-33.0-TL-OUTD
Manufacture	ABB
Switch type	IGBT
Rated DC input voltage	580 V
Rated DC input current	58 A
Rated DC input power	33700 W
Rated AC output voltage	400 V
Rated AC output current	50.3 A
Rated AC output power	33000 W

The good agreement between the actual efficiency curve and the efficiency curves calculated by (6.6) validates the accuracy of the model proposed by (6.6), hence will be used for single DC bus multiple-sources multiple loads power losses evaluation and optimization in this chapter.

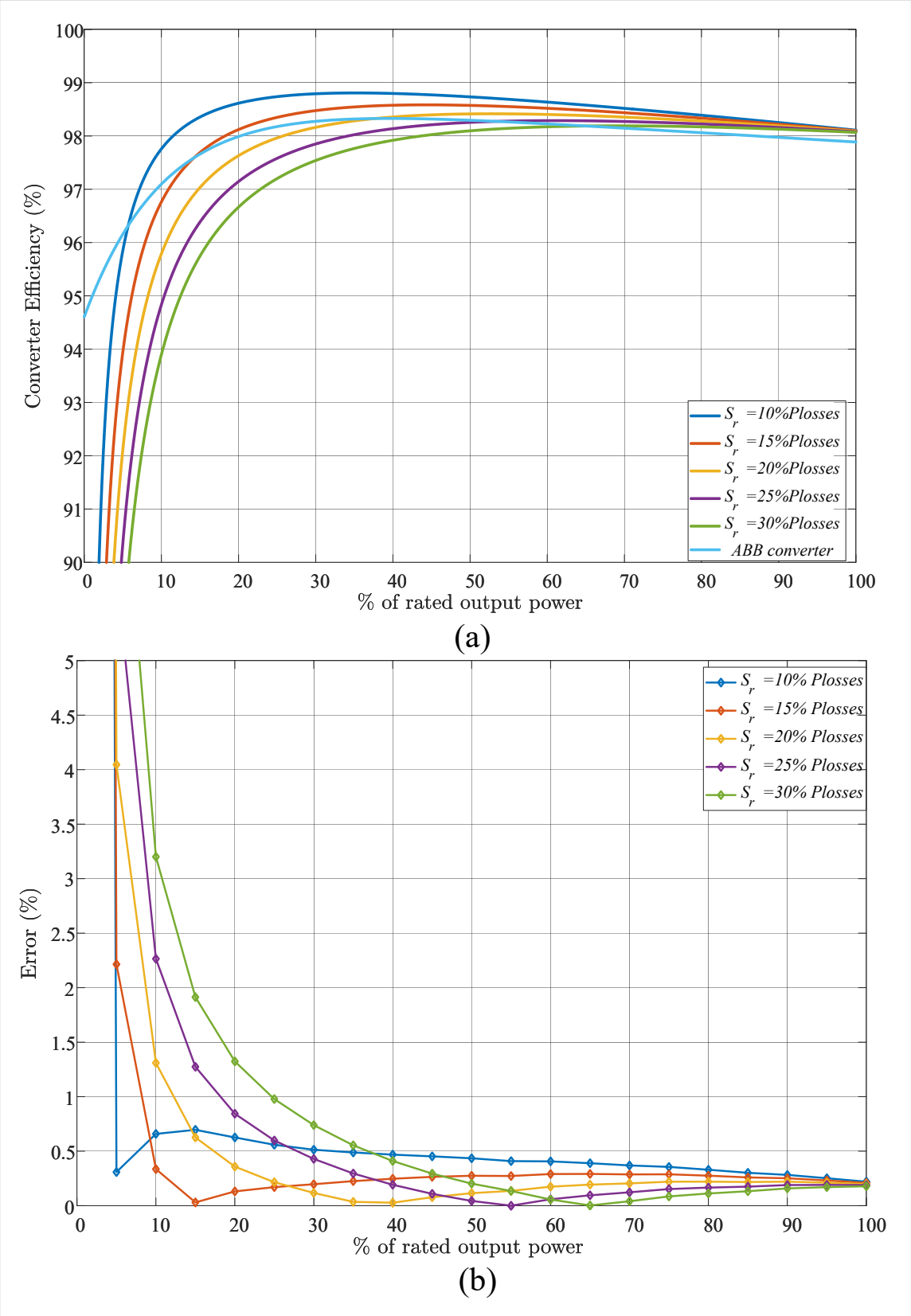

Fig. 6.3: Converter efficiency curves with different split ratios

6.4 Proposed Method for Analytical Based Optimal Droop Gains Selection

The total power losses of a single DC bus multiple-sources multiple-loads EPS are a combination of converter losses and transmission line losses, with the converter losses represented by the proposed model in (6.6). The total power losses of the i converter system can be expressed as:

$$P_{losses}(I_{c1}, I_{c2}, ..., I_{ci}) = \sum_{i=1}^{n} P_{no-loadi} + I_{ci}^2 R_i \tag{6.10}$$

where ($R_i = R_{ci} + R_{esi}$) is the sum of the converter ESR and the TLR. From (6.10), the optimal current sharing for the i^{th} converters, I_{ci}, for minimum power losses is obtained using the Lagrange multiplier method, which is a strategy for finding the local maxima and minima of a non-linear function subject to equality constraints [150]. The Lagrangian function defined for the system power losses minimization problem is formulated as:

$$\mathcal{L}(I_{c1}, ..., I_{ci}, \lambda) = P_{losses}(I_{c1}, ..., I_{ci}) - \lambda.g(I_{c1}, ..., I_{ci}) \tag{6.11}$$

where λ is a Lagrange multiplier and g is the constraints functions that can be expressed as:

$$g(I_{c1}, ..., I_{ci}) = I_L - \sum_{i=1}^{n} I_{ci} \tag{6.12}$$

Hence, the Lagrange optimization function can be expressed as:

$$\mathcal{L}(I_{c1}, ..., I_{ci}, \lambda) = \sum P_{no-load} + I_{c1}^2 R_1 + ... + I_{ci}^2 R_i - \lambda[I_L - (I_{c1}, ..., I_{ci})] \tag{6.13}$$

To find the critical points of $\mathcal{L}$, the gradient of $\mathcal{L}$ is set to equal a zero vector:

$$\bigtriangledown_{I_{c1},...,I_{ci},\lambda} \mathcal{L}(I_{c1}, ..., I_{ci}, \lambda) = 0 \tag{6.14}$$

The solution in (6.14) gives converters optimal current-sharing ($I_{c1o}, ..., I_{cio}$). The expression of the load current I_L in (6.13) depends on the load type. Different types of loads have been considered (CIL, CCL and CPL).

6.4.1 Optimal Droop Gains for Constant Current Load

In the case of CCL, the gradients of the Lagrange optimization function in (6.14) concerning the converter currents are given as:

$$\begin{cases} 2I_{c1}R_1 - \lambda = 0 \\ \vdots \\ 2I_{ci}R_i - \lambda = 0 \end{cases} \tag{6.15}$$

From (6.15), the optimal current-sharing of all converters is given as:

$$\begin{cases} I_{c1} = \frac{\lambda}{2R_1} \\ \vdots \\ I_{ci} = \frac{\lambda}{2R_i} \end{cases} \tag{6.16}$$

From (6.16), the ratio of the optimal current-sharing of the i^{th} converters I_{ci} with respect to the master converter current sharing I_{c1} is obtained by:

$$\frac{I_{ci}}{I_{c1}}\bigg|_{opt} = \frac{R_1}{R_i} = \frac{R_{c1} + R_{es1}}{R_{ci} + R_{esi1}} \tag{6.17}$$

It is clear from (6.17) that the optimal current-sharing ratio between any two converters is inversely proportional to the respective sum of the ESR of the converter and the TLR. Comparing (6.17) and (6.5), it can be seen that the converters' droop gains can be selected to achieve optimal current-sharing, as in (6.17). By equating the left-hand sides of (6.17) and (6.5), optimal droop gains can be obtained as a function of converter equivalent resistance and transmission line resistance:

$$\frac{(R_{c1} + R_{es1})}{(R_{ci} + R_{esi})} = \frac{(R_{d1-opt} + R_{c1})}{R_{di-opt} + R_{ci}} \tag{6.18}$$

where R_{di-opt} is the optimal droop gain of the i^{th} converter as a function of R_{d1-opt} of converter No 1. R_{di-opt} is as given in (6.19):

$$R_{di-opt} = (R_{d1-opt} + R_{c1})\frac{(R_{ci} + R_{esi})}{(R_{c1} + R_{es1})} - R_{ci} \tag{6.19}$$

It is noted from (6.19) that the optimal value of droop gain for the i^{th} converter depends on the selected droop gain value for converter No.1, the ESR of each converter, and the

value of the TLR between the converter and the DC bus. This indicates the existence of multiple optimal solutions for droop gains selections. One of the many optimal solutions of (6.18) is setting droop gains for all converters equal to their ESR, as in (6.19) and (6.20). The advantage of this solution is that the optimal droop gains can be set by relying only on information about the power losses of the converter.

$$R_{d1-opt} = R_{es1} \;\; \& \;\; R_{di-opt} = R_{esi} \tag{6.20}$$

On the other hand, from (6.19), if R_{c1} and R_{ci} are very small compared to the converter ESR, they can be ignored, and then the relation between R_{di-opt} and R_{d1-opt} can be simplified as in (6.21):

$$R_{di-opt} \sim R_{d1-opt}\frac{R_{esi}}{R_{es1}} \; and \; R_{di-opt} > R_{esi} \tag{6.21}$$

From (6.21), the optimal droop gains can also be calculated based only on the ESR of the converters, with no need for any additional information about the TLRs. However, the effect of ignoring the TLRs will be significant if the selected optimal droop gains are very small. It should be noted from (6.21) that one of the droop gains selections is the same as in (6.20), which gives the minimum system losses.

To test the proposed algorithm, a system with 2 converters is considered, Fig. 6.4(a) shows the relationship between the optimal values of R_{d2} and R_{d1} for the two converter system parameters listed in Table 6.2, Case1, when TLRs are taken into consideration (black line) or ignored (red line). The current of each converter is calculated based on the current division law [151], then the losses are obtained based on the no-load losses, the resistance of the converter, and the transmission lines resistances. The DC bus voltage is calculated using the DC bus droop characteristic. The design specification objectives were to achieve minimum system power losses for different combinations of converters, i.e. using converters with the same power ratings or different power ratings and a variety of efficiencies, and complying with the MIL-STD-704F standards. The intersection between the two lines gives the special optimal solution for R_{d2} and R_{d1}, where they are set to be equal to the corresponding converter ESRs, as in (6.20). Fig. 6.4 (c) and (d) show the DC bus voltage variation and system power losses with respect to the droop gain R_{d1} for the two droop gain designs (black and red lines) shown in Fig. 6.4(a).

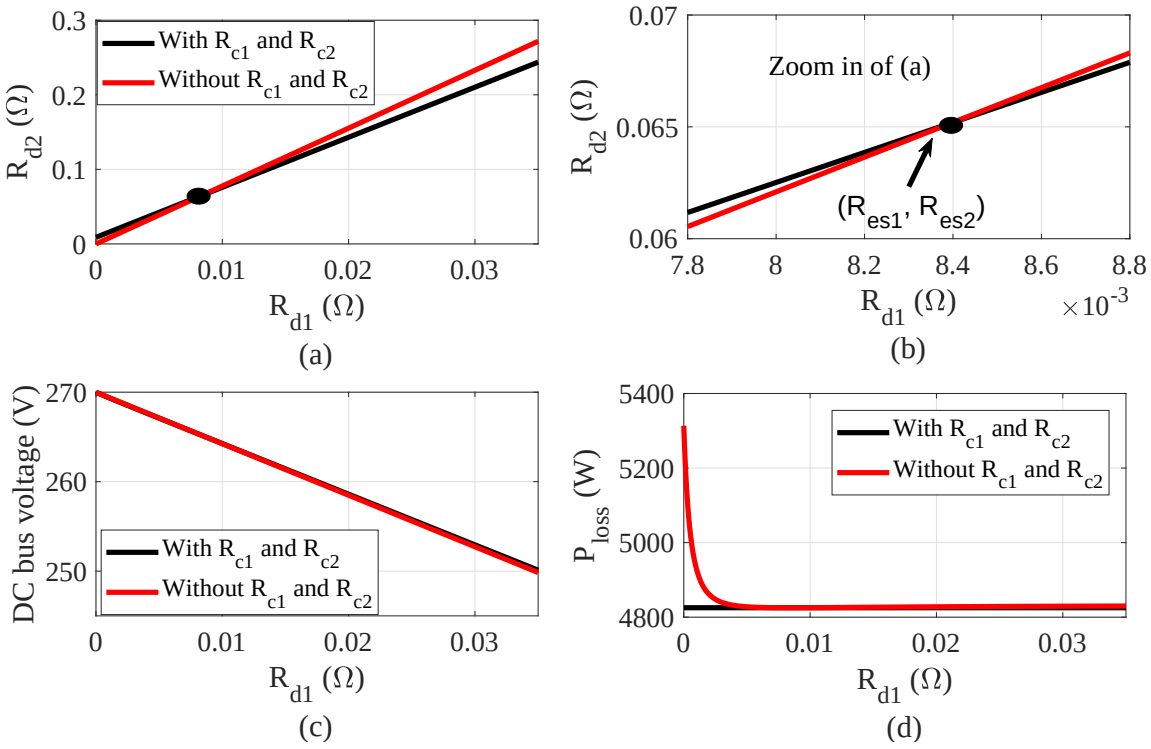

Fig. 6.4: Optimal droop gains for constant current load system at I_L=650 A, a) optimal droop gains, b) Total system losses, c) DC bus voltage, and d) Zoom in of (a)

Clearly, from Fig. 6.4(d), the selected values of the droop gains using (6.21) are smaller than the values of the intersection point in Fig. 6.4(a), the system power losses (red line) significantly increase and deviate from the optimal (black line). If the values of the selected droop gains are higher, the system power losses (red line) converge to the optimal power losses (black line) and they become exactly equal at the intersection point of the lines in Fig. 6.4(a). By increasing the values of the droop gain further, the difference between the power loss lines (red and black) can be seen to be quite small, potentially insignificant. Therefore, for values of R_{d1} higher than the value at the intersection point of Fig. 6.4(a), (6.21) can be used to calculate optimal droop gains without the need of any information about the TLRs.

6.4.2 Optimal Droop Gains for Constant Resistive Load

The load current in case of resistive load can be given as:

$$I_L = \frac{V_{DC}}{R_L} \tag{6.22}$$

Table 6.2: Converters Data and Optimal Droop Gains Values

	Case (1)	Case(2)	Unit
P_{n1}	150	150	kW
P_{n2}	50	150	kW
ζ_1	98	98	%
ζ_2	95	95	%
ζ_{cable1}	99.5	99.5	%
ζ_{cable2}	99.5	99.5	%
$P_{noload1}$	459.18 8	459.18	W
$P_{noload2}$	394.74	1184.2	W
R_{es1}	0.0084	0.0084	Ω
R_{es2}	0.0652	0.0217	Ω
R_{c1}	0.0024	0.0024	Ω
R_{c2}	0.0073	0.0024	Ω
$I_{c1rated}$	555.6	555.6	A
$I_{c2rated}$	185.2	555.6	A

The DC bus voltage can be expressed as a function of all converters currents as:

$$V_{DC} = V_o - \frac{1}{n}(I_{c1}R_1^{'} + ... + I_{ci}R_i^{'}) \tag{6.23}$$

By substituting (6.22) and (6.23) into (6.13), the gradients of the Lagrange optimization function with respect to the converter currents are obtained as:

$$\begin{cases} 2I_{c1}R_1 - \lambda\left(\frac{R_1^{'}}{nR_L} + 1\right) = 0 \\ \vdots \\ 2I_{ci}R_i - \lambda\left(\frac{R_i^{'}}{nR_L} + 1\right) = 0 \end{cases} \tag{6.24}$$

The solution of (6.24) gives the current sharing of all converters as in (6.25).

$$\begin{cases} I_{c1} = \frac{\lambda}{2R_1}\left(\frac{R_1^{'}}{nR_L} + 1\right) = 0 \\ \vdots \\ I_{c1} = \frac{\lambda}{2R_1}\left(\frac{R_i^{'}}{nR_L} + 1\right) = 0 \end{cases} \tag{6.25}$$

From (6.25) the optimal current sharing of i^{th} converters I_{ci} with respect to the master converter current sharing I_{c1} is given by:

$$\left.\frac{I_{ci}}{I_{c1}}\right|_{opt} = \frac{R_1}{R_i}T_1 \tag{6.26}$$

Where

$$T_1 = \frac{R_1{}' + nR_L}{R_i{}' + nR_L} \tag{6.27}$$

The term T_1 depends on the value of load resistance, the number of converters, the droop gains, and the TLRs. If nR_L is considered to be very large compared to $(R_1)'$ and $(R_i)'$ then the term T_1 can be consider to be equal to 1 and the ratio between I_{ci} and I_{c1} becomes equal to the ratio between R_1 and R_i, similar to (6.17), which was derived for the CCL case. In this case, the optimal current share is only dependent on the TLRs and ESRs of the converters, similarly to the constant current case. By comparing (6.26) and (6.5) the optimal droop gains can be defined using (6.28):

$$\frac{R_1}{R_i}T_1 = \frac{R_{d1-opt} + R_{c1}}{R_{di-opt} + R_{ci}} \tag{6.28}$$

From (6.28), R_{di-opt} can be expressed as function in R_{d1-opt} and load parameters:

$$R_{di-opt} = -\frac{(R_{ci} + R_{esi})(R_{d1-opt} + R_{c1})(R_{ci} + nR_L) - R_{ci}(R_{c1} + R_{es1})(R_{c1} + R_{d1-opt} + nR_L)}{(R_{ci} + R_{esi})(R_{d1-opt} + R_{c1}) - (R_{c1} + R_{es1})(R_{c1} + R_{d1-opt} + nR_L)} \tag{6.29}$$

The relation between R_{di-opt} and R_{d1-opt} in (6.29) for the resistive load case is plotted and shown in Fig. 6.5 (a), black line, while the red line shows the results when ignoring the TLR.

In comparison, the results for the CCL case are shown in Fig. 6.4 and for the CRL case are shown in Fig. 6.5, which are quite similar. It is noted that with an increase of the optimal droop gains, the EPS losses (red line in Fig. 6.5 (a)) are nearly equal to the optimal power losses (black line) as long as the optimal droop gains are selected to be larger than the values corresponding to this intersection point (Fig. 6.5 (a)). Hence, ignoring TLR during the optimal droop gains design is also valid for the CRL case since the converter ESR is significantly higher than the TLR. Therefore, the optimal droop gain can be calculated using the following simplified relationship:

$$R_{di-opt} \sim R_{d1-opt}\frac{R_{esi}}{R_{es1}} \; and \; R_{di-opt} > R_{esi} \tag{6.30}$$

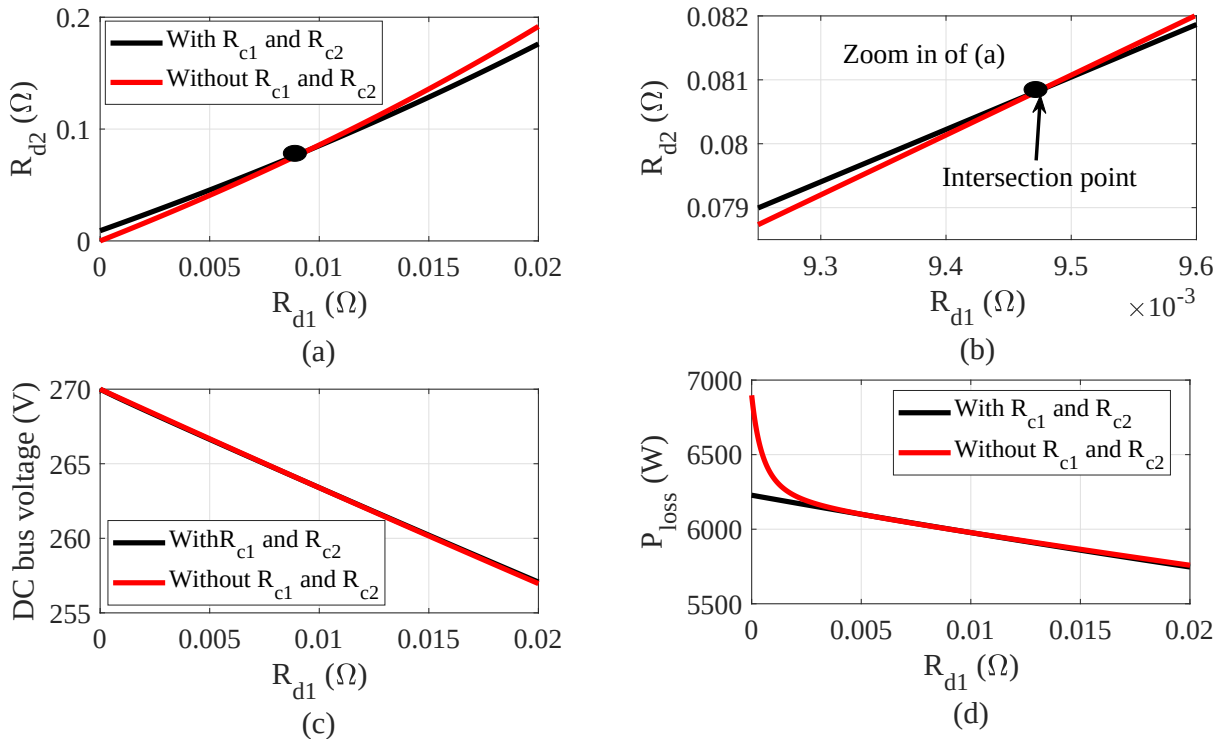

Fig. 6.5: Optimal droop gains for resistive load system at R_L=0.5Ω a) Optimal droop gains, b) Total system losses, c) DC bus voltage, and d) Zoom-in of (a)

As the selected value for R_{d1-opt} is increased, the corresponding optimal value R_{di-opt} also increases. Thus the converter currents are decreased and hence, the system losses are decreased as shown in Fig. 6.5 (b). However, it should be noted that the total system losses remain minimal for each new selected set of the optimal droop gains values.

6.4.3 Optimal Droop Gains for Constant Power Load

Equation (6.31) describes the load current using constant power load assumption:

$$I_L = \frac{P_{CPL}}{V_{DC}} \tag{6.31}$$

where P_{CPL} is the power of the load and V_{DC} is given in (6.23). Substituting (6.30), and (6.23) into (6.13), the gradients of the Lagrange optimization function with respect to the

converter currents are expressed as:

$$\begin{cases} 2I_{c1}R_1 - \lambda\left(\frac{\frac{P_{CPL}R_1^{'}}{n}}{\left(V_o-\frac{1}{n}(I_{c1}R_1^{'}+...+I_{ci}R_i{'})\right)^2}+1\right)=0 \\ \vdots \\ 2I_{ci}R_i - \lambda\left(\frac{\frac{P_{CPL}R_i^{'}}{n}}{\left(V_o-\frac{1}{n}(I_{c1}R_1^{'}+...+I_{ci}R_i{'})\right)^2}+1\right)=0 \end{cases} \tag{6.32}$$

Solving (6.32) gives the optimal current sharing of converter i^{th} I_{ci} with respect to the master converter current I_{c1} as:

$$\left.\frac{I_{ci}}{I_{c1}}\right|_{opt} = \frac{R_1}{R_i}T_2 \tag{6.33}$$

Where

$$T_2 = \frac{\left(\frac{P_{CPL}R_i^{'}}{n}+\left(V_o-\frac{1}{n}(I_{c1}R_1^{'}+...+I_{ci}R_i{'})\right)^2\right)}{\left(\frac{P_{CPL}R_1^{'}}{n}+\left(V_o-\frac{1}{n}(I_{c1}R_1^{'}+...+I_{ci}R_i{'})\right)^2\right)} \tag{6.34}$$

The term T_2 depends on the DC microgrid parameters and the value of load power. The numerator and denominator of T_2 are nearly equal, as the difference between the $(R_i^{'})$ values and the value of $(R_1^{'})$ is not large, hence $T_2 \sim 1$. Therefore, the optimal current sharing is dependent on the values of the ESRs of the converters and the TLRs. The optimal droop gains can be selected by comparing (6.33)and (6.5) and this results in (6.35):

$$\frac{R_1}{R_i}T_2 = \frac{R_{d1-opt}+R_{c1}}{R_{di-opt}+R_{ci}} \tag{6.35}$$

From (6.35), for CPL case, the optimal droop gain R_{di-opt} can be expressed as a function in R_{d1-opt} as in (6.36).

$$R_{di-opt} = \frac{(R_{c1}+R_{es1})(V_o - I_{c1}(R_{d1-opt}+R_{c1}))^2 - \sqrt{b} + 2P_{CPL}nR_{ci}(R_{c1}+R_{es1})}{2\frac{P_{CPL}}{n}(R_{c1}+R_{es1})} \tag{6.36}$$

where b is given in Appendix B.5. Fig. 6.6 shows the results when the optimal droop gain of converter 1 is changed from 0.001 to 0.020 Ω and the optimal droop gain of converter 2 is calculated using (6.36) and the system parameters listed in Table 6.2. The two converters were supplying a constant power load of 150 kW. The relationship of the droop gains, the system power losses, and the DC bus voltage shown in Fig. 6.6 (d and c) are found to be similar to the results shown in Fig. 6.4 and Fig. 6.5 for constant current and resistance loads cases. It can also be concluded that using larger optimal droop gains, calculated

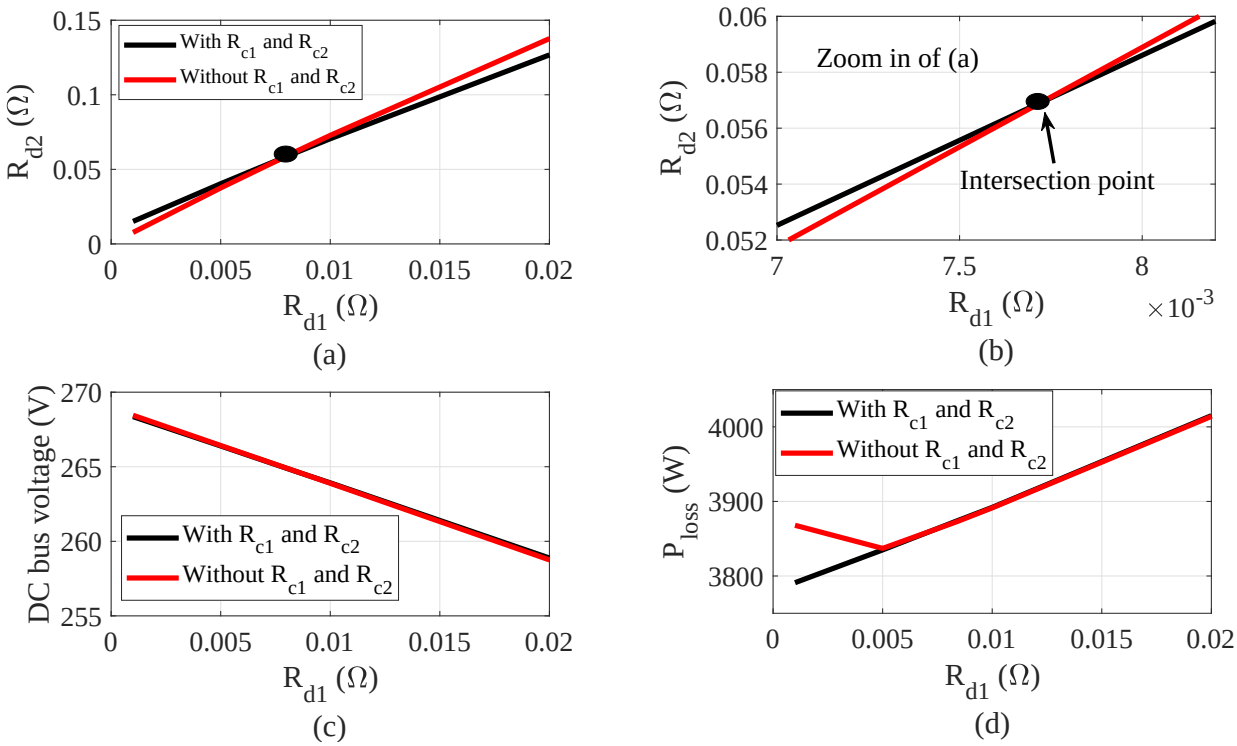

Fig. 6.6: Optimized droop gains for constant power load (150 kW) using two converter system a) Optimal droop gains, b) Total system losses, c) DC bus voltage, and d) Zoom in of (a)

according to (6.36), whilst ignoring TLRs will give nearly optimum system power losses. Therefore, the optimal droop gain for CPL can be also calculated using (6.30).

6.4.4 Optimal Droop Gains for Mixed Loads

In this case, the load is a combination of CPL, CCL, and CRL and the load current can be expressed as:

$$I_L = \frac{P_{CPL}}{V_{DC}} + \frac{V_{DC}}{R_L} + I_{cc} \tag{6.37}$$

where I_{cc} is the current of CCL and V_{DC} is given by (6.23). The gradients of the Lagrange optimization function with respect to the converter currents are given as:

$$\begin{cases} 2I_{c1}R_1 - \lambda\left(\dfrac{\frac{P_{CPL}R_1'}{n}}{\left(V_o - \frac{1}{n}(I_{c1}R_1' + \ldots + I_{ci}R_i')\right)^2} + \dfrac{R_1'}{nR_L} + 1\right) = 0 \\ \qquad\qquad \vdots \\ 2I_{ci}R_i - \lambda\left(\dfrac{\frac{P_{CPL}R_i'}{n}}{\left(V_o - \frac{1}{n}(I_{c1}R_1' + \ldots + I_{ci}R_i')\right)^2} + \dfrac{R_i'}{nR_L} + 1\right) = 0 \end{cases} \tag{6.38}$$

Solving (6.38) gives the optimal current sharing of the i^{th} converter, I_{ci}, with respect to the master converter current I_{c1} as:

$$\frac{I_{ci}}{I_{c1}}\bigg|_{opt} = \frac{R_1}{R_i}\left(\frac{T_{11}+T_{12}+1}{T_{i1}+T_{i2}+1}\right) \tag{6.39}$$

where

$$\begin{aligned} T_{11} =& \frac{\frac{P_{CPL}R_1^{'}}{n}}{\left(V_o - \frac{1}{n}(I_{c1}R_1^{'} + ... + I_{ci}R_i{'})\right)^2}, \\ T_{12} =& \frac{R_1^{'}}{nR_L}, \\ T_{i1} =& \frac{\frac{P_{CPL}R_i^{'}}{n}}{\left(V_o - \frac{1}{n}(I_{c1}R_1^{'} + ... + I_{ci}R_i{'})\right)^2}, \\ T_{i2} =& \frac{R_i^{'}}{nR_L} \end{aligned} \tag{6.40}$$

The terms T_{11} and T_{i1} are nearly equal to each other, and are similar to T_{12} and T_{i2}, therefore, the optimal current sharing for multiple types of loads connected to the DC bus will depend on the ESRs of converters and the TLRs, and can be obtained as in (6.17).

6.5 Validation of The Optimal Droop Gains Design Method

In order to validate the optimal droop gains design, different scenarios for utilizing the microgrid structure and component characteristics are investigated. The droop gains design for a microgrid with converters of different power ratings and efficiencies is considered. The design for a set of converters with the same power ratings and different efficiencies is also investigated. The system power losses when using the optimal droop gains obtained by the proposed design method are estimated and compared to the power losses when using the droop gains designed using the conventional and non-linear droop gains design approaches. The converter's behavior is represented by a simplified first-order dynamic system, as shown in Fig. 6.7. It should be noted that the single DC bus multiple-sources multiple-loads model used for validation is the same model as was used for optimization in Fig. 6.1. The simulation is carried out in MATLAB®/Simulink®, and

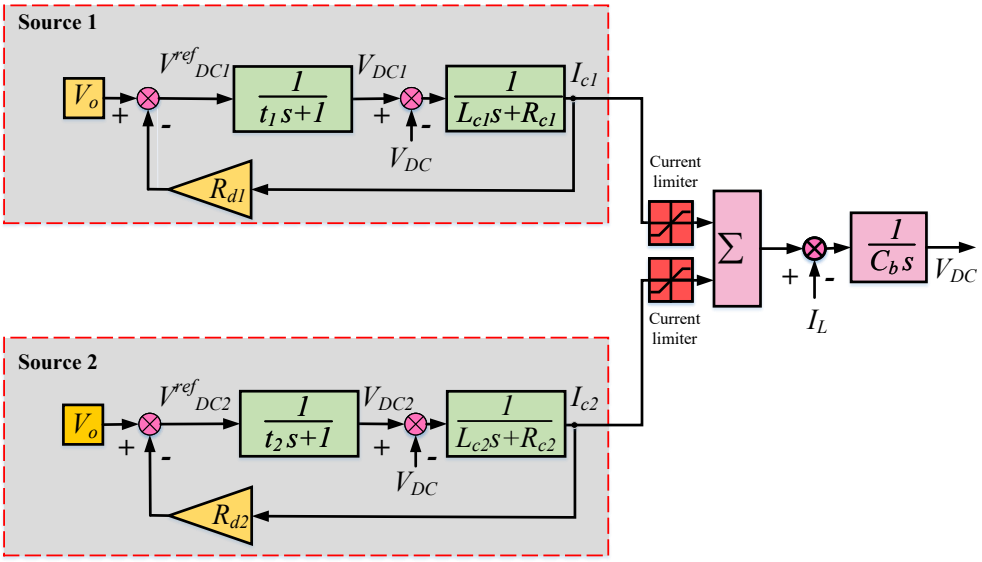

Fig. 6.7: Voltage mode droop-controlled converters scheme [136]

the system parameters used are given in Table 6.3. The converter no-load losses (split ratio) are assumed to be 15 % of its total losses at the nominal operating point according to recommendation of Section 6.3. The total system losses are estimated by simulation when using the optimal droop design in (6.20) and the results are compared to the estimated power losses when the droop gains used are designed following the conventional design approach as in (6.41) [80], and the non-linear droop gains design approach [133].

$$R_{di} = \frac{\triangle V_{max}}{I_{cimax}} \tag{6.41}$$

where $\triangle V_{max}$ and I_{cimax} are the maximum allowable voltage drop and the maximum output current of converter i, respectively. The maximum allowable voltage can be found using the standards (10% of 270 V DC) in [19]. Equation (6.41) is used and the values of

Table 6.3: Electric Power System Parameters

Parameter	Symbol	Value	Unit
DC link capacitor	C_b	0.8	μF
DC link bus voltage	V_L	270	V
Line inductance	$L_1 - L_2$	1	μH
Time constant of converter	$t_1 - t_2$	1	ms
Maximum allowable voltage degradation	$\triangle V_{max}$	5	%

these droop gains are given in Table 6.4.

Table 6.4: Conventional and Optimal Droop Gains Values

	Case (1)	Case(2)	Unit
R_{d1}	0.0243	0.0243	Ω
R_{d2}	0.0729	0.0243	Ω
R_{d1-opt}	0.0084	0.0084	Ω
R_{d2-opt}	0.0652	0.0217	Ω

6.5.1 Case 1: Different Converter Ratings and Different Efficiencies

Fig. 6.8 (a) shows the estimated total losses for a system with two converters having different power ratings and efficiencies. It is noted, for example, that the losses are the smallest using the optimal droop gains at the load current of 600A. At this point, the losses are reduced by 23% compared to the conventional droop gains designed case and by 15.5% compared to the non-linear droop gains case. The achieved losses reduction is due to the adjustment of each converter current according to its equivalent resistance. Fig. 6.8 (b) shows the voltage regulation of the DC bus. As an additional advantage, the proposed method provides improved voltage regulation at different load conditions compared to the other methods e.g. by 4.5% at 600A. In terms of load-sharing between converters, the conventional and non-linear droop gain design methods provide almost equal load-sharing per unit, while the proposed method gives nearly half the load-sharing per unit between converters at light load as the ratio depends on the losses of the converters, shown in Fig. 6.8 (c). This is acceptable, as long as the converters remain working within their current limits. This ratio closes to one as the load increases.

At maximum load, the current is 741 A, which is equivalent to the sum of two converters' rated currents; the system losses, and the current-sharing ratio is similar to the other methods. This is because the two converters are delivering their nominal currents to the load.

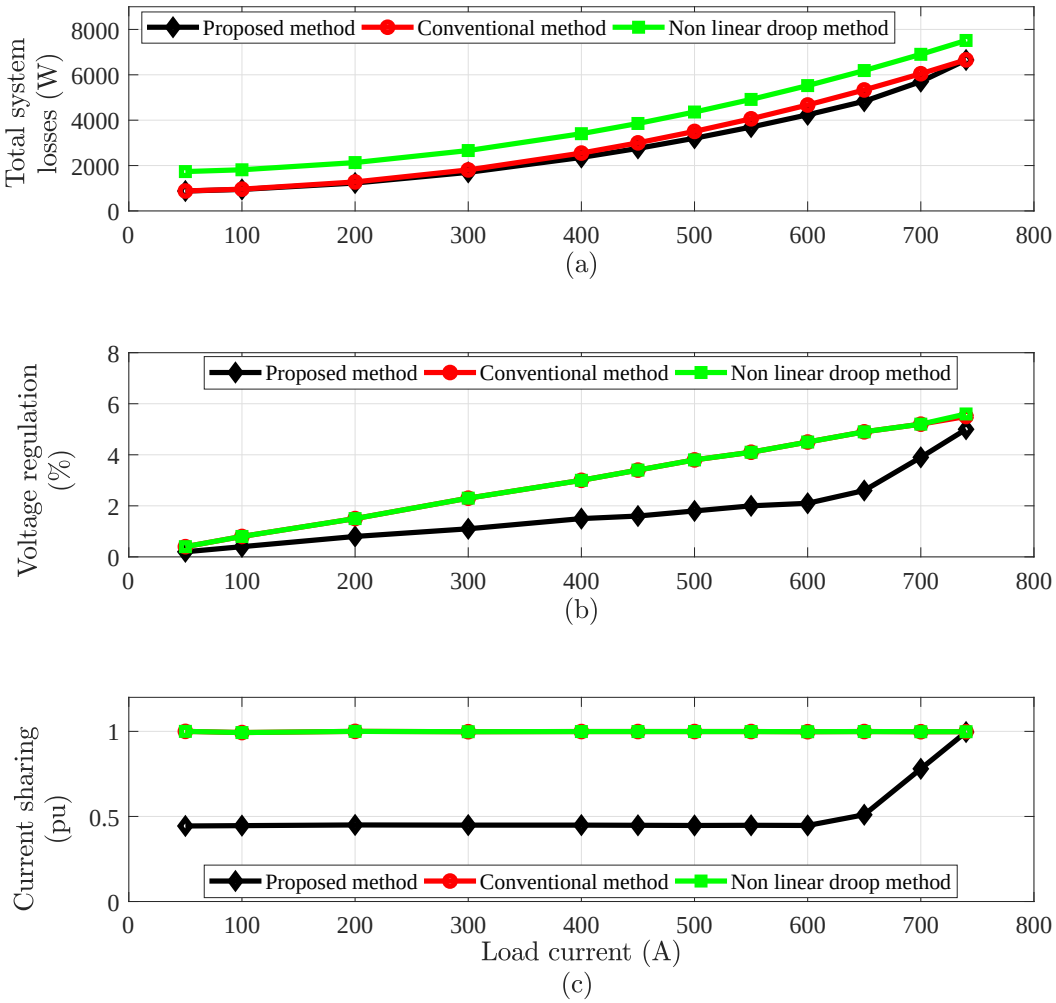

Fig. 6.8: Variation of system losses, DC bus voltage, and converters output currents with load current for case (1), (a) system losses, (b) DC bus voltage regulation and (c) Current sharing ratio

6.5.2 Case 2: Identical Converter Ratings and Different Efficiencies

In this case, the converters used have the same ratings but different efficiencies, it means that the converters have different equivalent resistances in the loss model and no load power. Fig. 6.9 (a) shows the total system losses. The losses of the proposed design method can be seen to be less than of the conventional or the non-linear droop

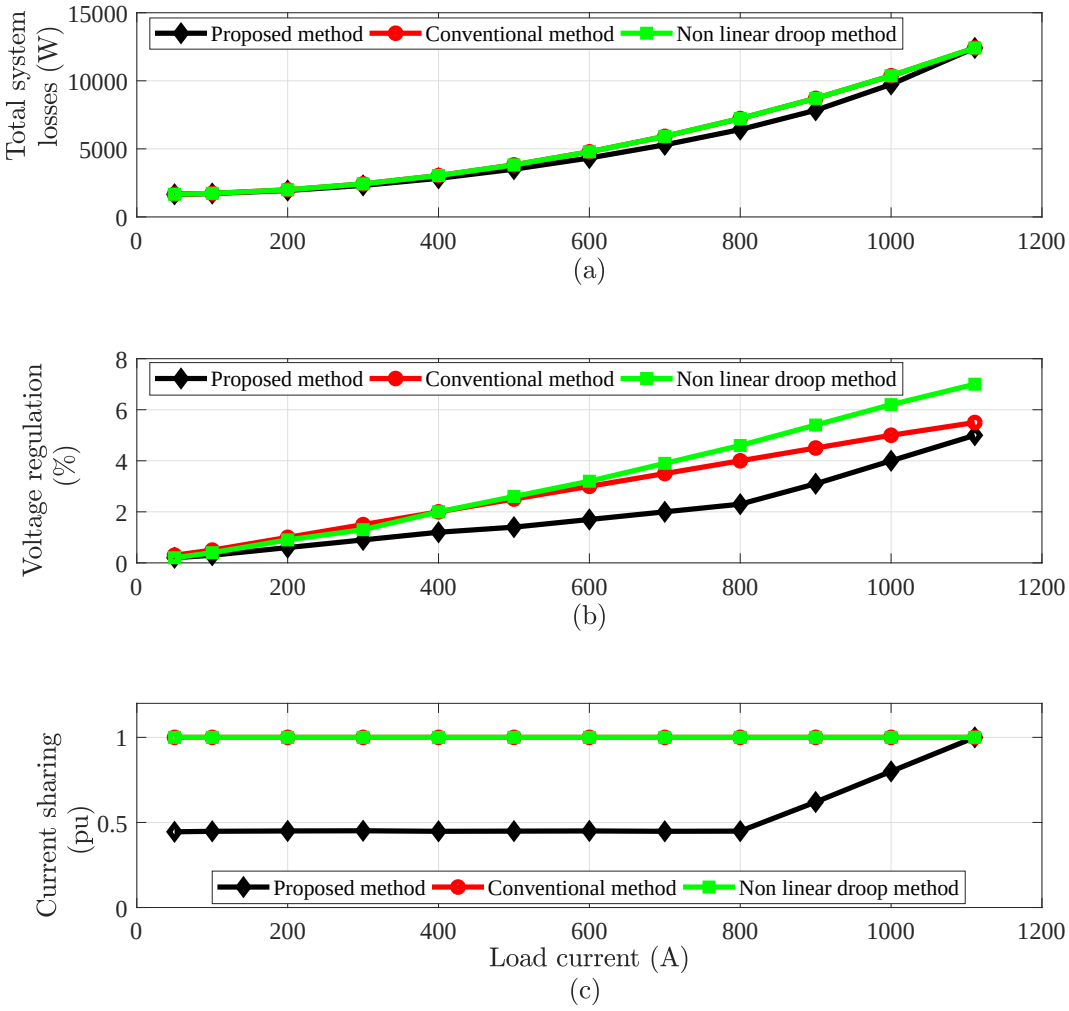

Fig. 6.9: Variation of system losses, DC bus voltage, and converters output currents with load current for case (2). (a) System losses, (b) DC bus voltage regulation, and (c) Current sharing ratio

gains design methods. E.g., at a load current of 900A, there is a 10% reduction in losses compared to both the other methods. This reduction in system losses is achieved because the currents are redistributed based on the value of the equivalent resistance of each converter. At light load conditions, the reduction in losses is small compared to heavy load conditions. Fig. 6.9 (b) demonstrates the voltage regulation of a DC bus, where the voltage regulation of the proposed method is improved by 1.6% and 2.3% for the same operating point compared to conventional and non-linear methods respectively, and this is

due to the adjustment of the converters' currents sharing. The load-sharing ratio between the two converters for the three methods is shown in Fig. 6.9 (c). Here, the proposed method provides a half sharing ratio at light load and almost equal sharing for a heavy load, while the other methods provide equal load-sharing across all loads.

6.6 Experimental Results

An experimental rig has been used to verify the findings in this chapter. A prototype consisting of two parallel AFE converters to represent the two sources in the EPS was built in the laboratory, as depicted in Fig. 6.10. Two identical power converters (SEMIKRON's IGBT power Stack-SEMIKUBE: IGD-1-424-P1N4-DL-FA [152]) are connected to the DC bus. The sensor signals (voltage sensor/current sensor) are sent back from the converter to the microprocessor employing the interface boards. The control platform is a DSP (Texas Instruments, TMS320F28379D DSP Kit). A detailed description of each component of the prototype subsystem is shown in Appendix C.2. The conventional and optimal droop gains for converter 1 and converter 2 are calculated using (6.41) and (6.20), and their values are given in Table 6.5. Two loading cases, 40 Ω resistive load and 40 Ω resistive load in parallel with CPL of 1 Kw are investigated. The DC bus voltage is kept constant

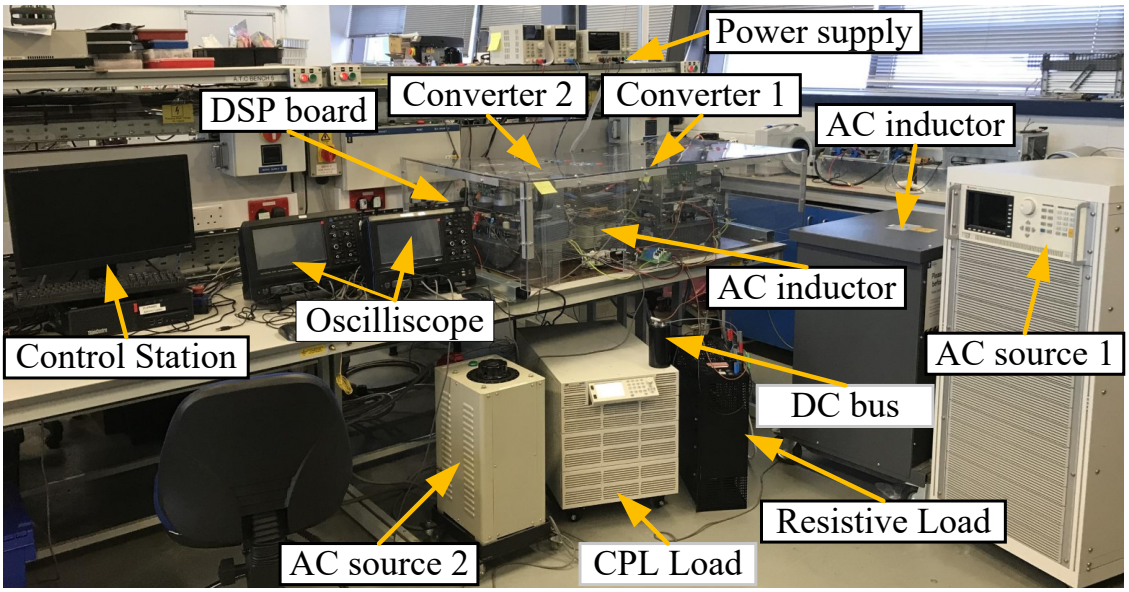

Fig. 6.10: Experimental setup

Table 6.5: Conventional and Optimal Droop Gains Values for Experimental Tests

Symbol	Value	Unit
R_{d1}	0.729	Ω
R_{d2}	0.729	Ω
R_{d1-opt}	0.3833	Ω
R_{d2-opt}	0.2529	Ω

at 270 V during all tests to ensure that the power consumed by the load is the same. Consequently, the comparison of system losses between both methods is considered to be fair and accurate.

Fig. 6.11 and Fig. 6.12 show the results with the 40 Ω resistive load for the conventional and proposed design methods. By using the conventional design method both converters share the load power almost equally, as indicated in Fig. 6.11 (c). The difference between them can be explained as the difference between TLRs. Fig. 6.12 (c) shows the DC currents of both converters under application of the proposed method. As shown, converter 2 supplies higher power than converter 1, as it has a small ESR. Therefore, the load-sharing ratio is nearly half as shown in Table 6.6. In terms of system losses, the proposed method provides lower losses, and the reduction in system losses is calculated based on the difference between the AC input power and the load consumed constant power in both methods, shown in Fig. 6.12 (d); (this was found to be 1580-1559=21 W, (0.65%)).

Table 6.6: Measurements with 40 Ω Resistive Loads

Load value	Measurements	Conventional method	Proposed method
40 Ω	I_{dc1} (A)	3.1	2.4
	I_{dc2} (A)	3.3	4.1
	Sharing ratio	0.936	0.585
	V_{dc} (V)	270	270
	System losses (W)	1580	1559

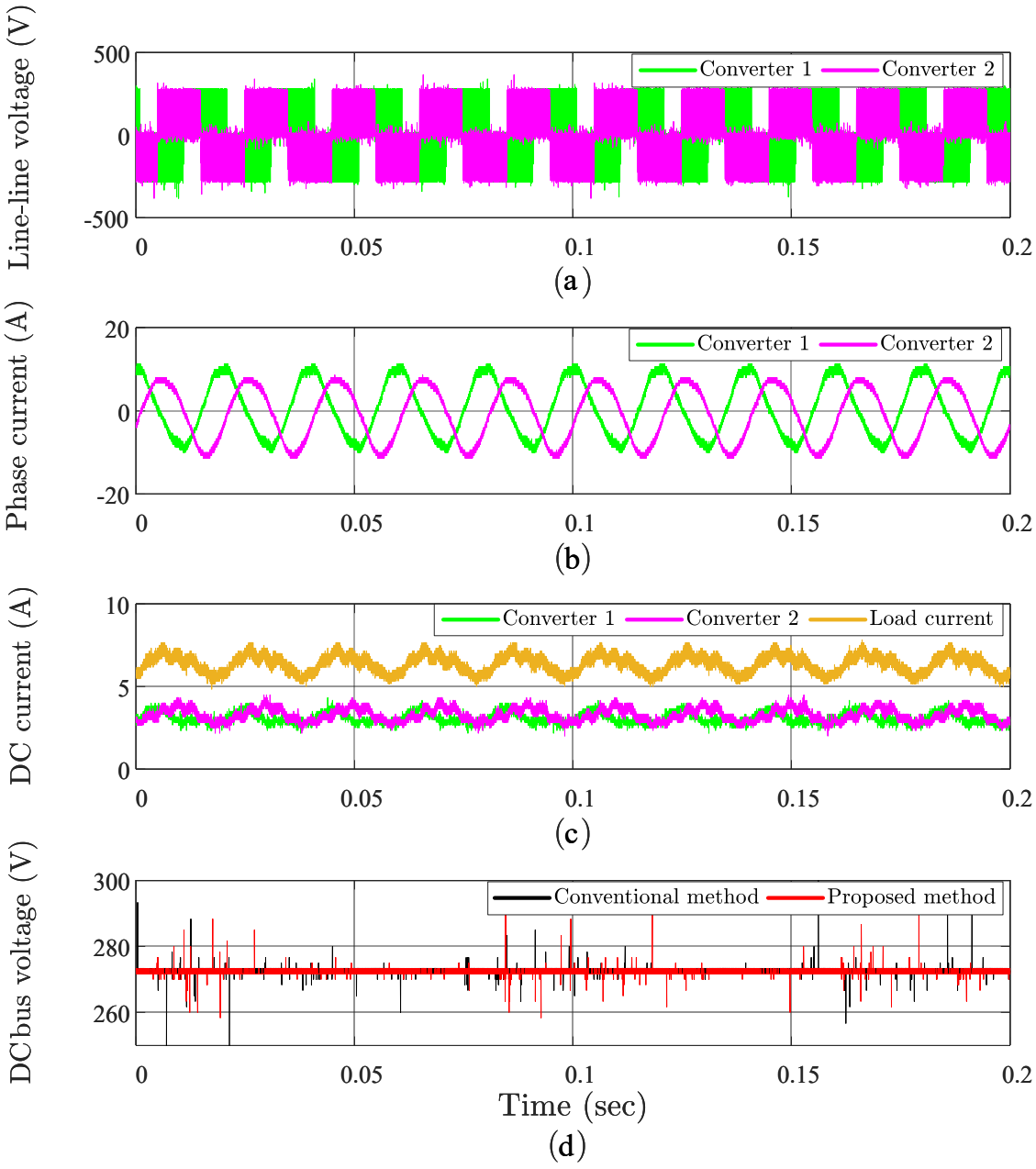

Fig. 6.11: Experimental results with 40 Ω CIL using the conventional design approach

Fig. 6.13 and Fig. 6.14 show the results using different load types with CPL and CIL, which are connected to the DC bus simultaneously. The value for CIL is 40 Ω and for CPL it was increased in two steps of 500 W each. The system was initialized with 40 Ω resistive load, after which the first 500 W CPL is connected, followed by the second 500 W CPL. The load is then decreased again, reversing this operation, the first 500 W

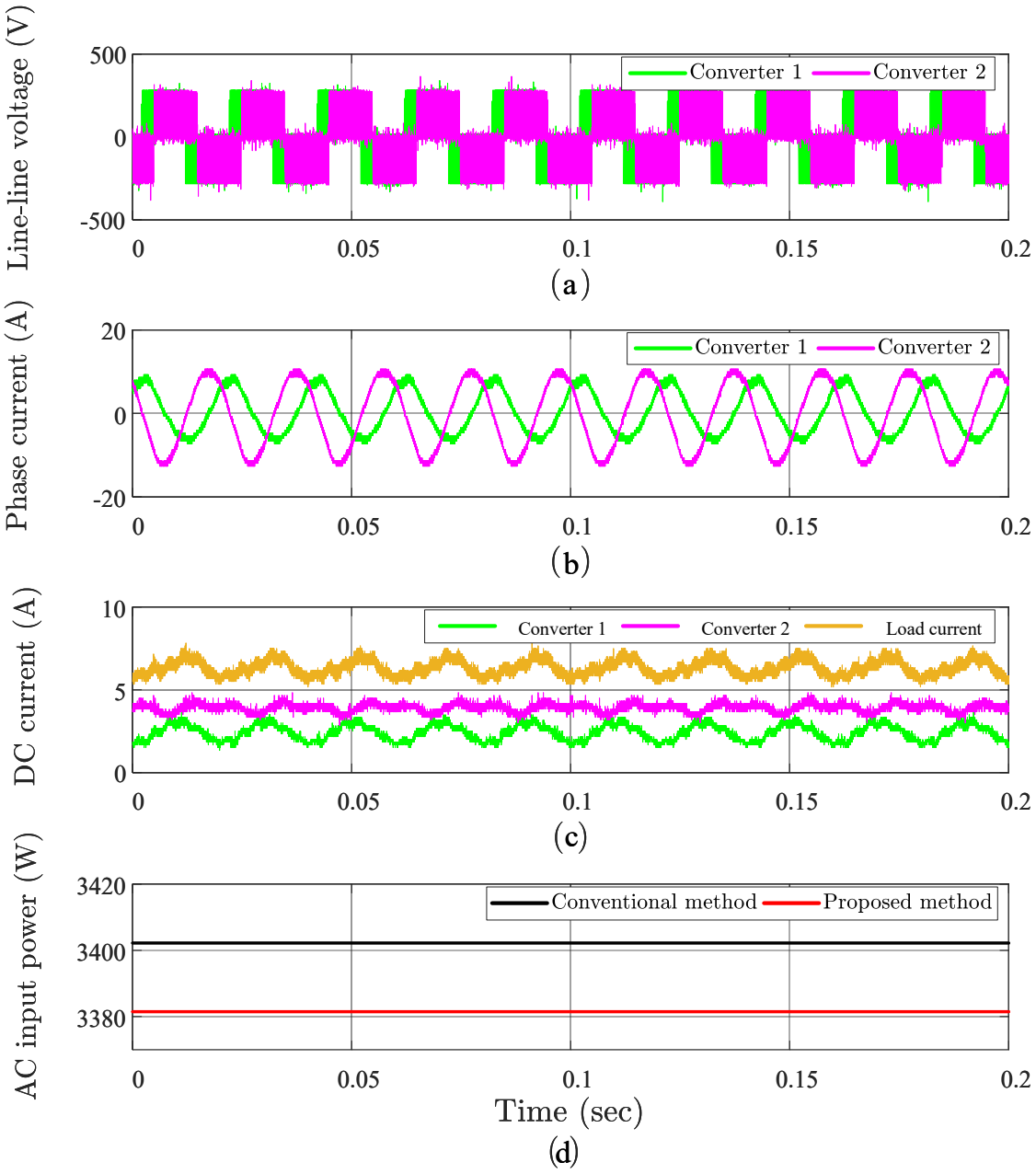

Fig. 6.12: Experimental results with 40 Ω CIL using the proposed design approach

CPL is disconnected, followed by the second 500 W CPL, as shown in Fig. 6.13 (c) and Fig. 6.14 (c). The system losses are calculated for the three load cases, with the proposed method providing the smallest losses values. Fig. 6.14 (d) shows that the reductions in system losses were found to be 21 W (0.65%), 56 W (1.47%), and 67 W (1.52%), for 40 Ω, 40 Ω with 500 W CPL, and 40 Ω with 1000 W CPL cases, respectively. It should be

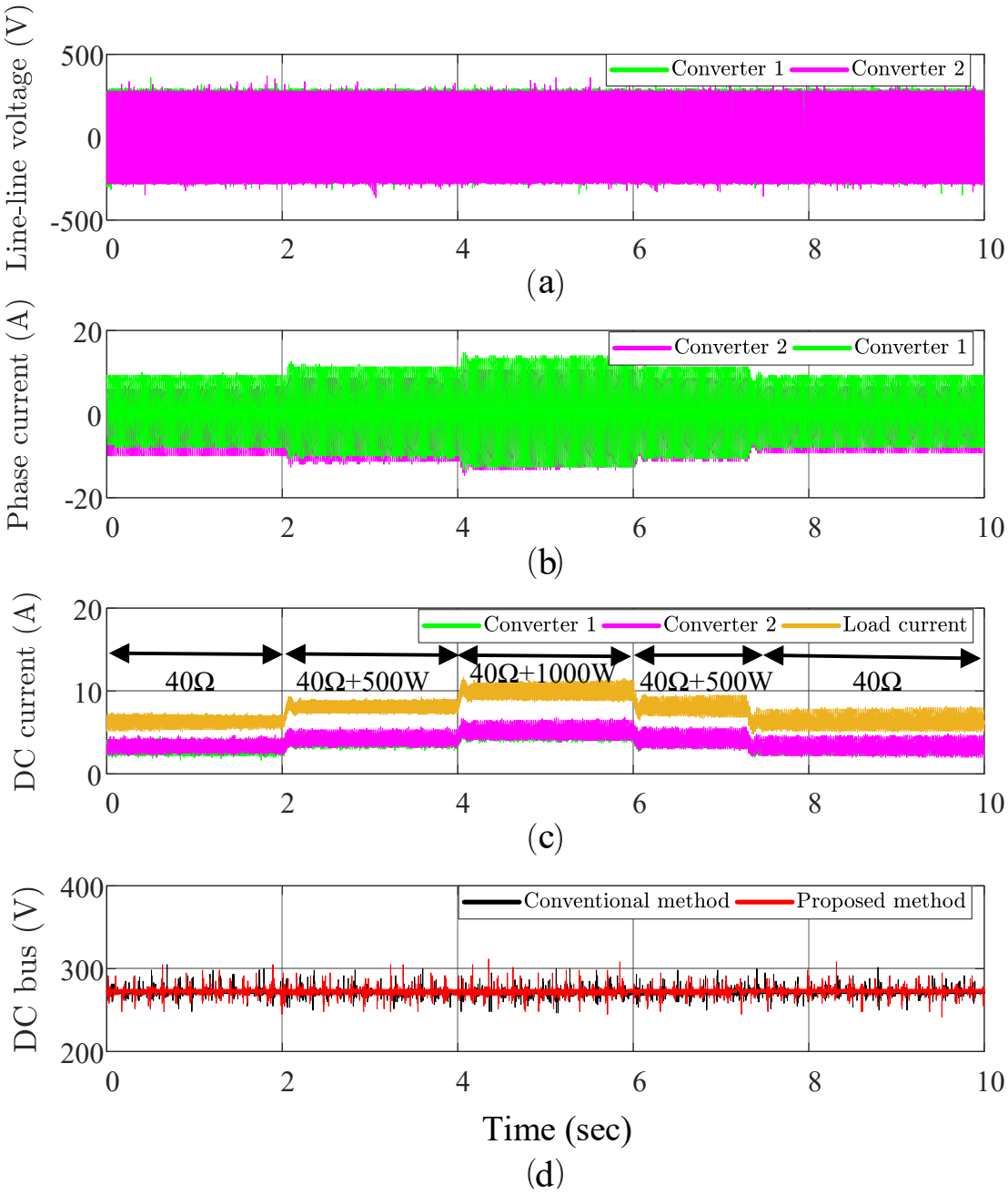

Fig. 6.13: Experimental results with 40 Ω CIL and CPL with conventional design approach

noted that as the load power increased, the percentage of system losses reduction also increased. In summary, the experimental results demonstrate the effectiveness of the proposed design method.

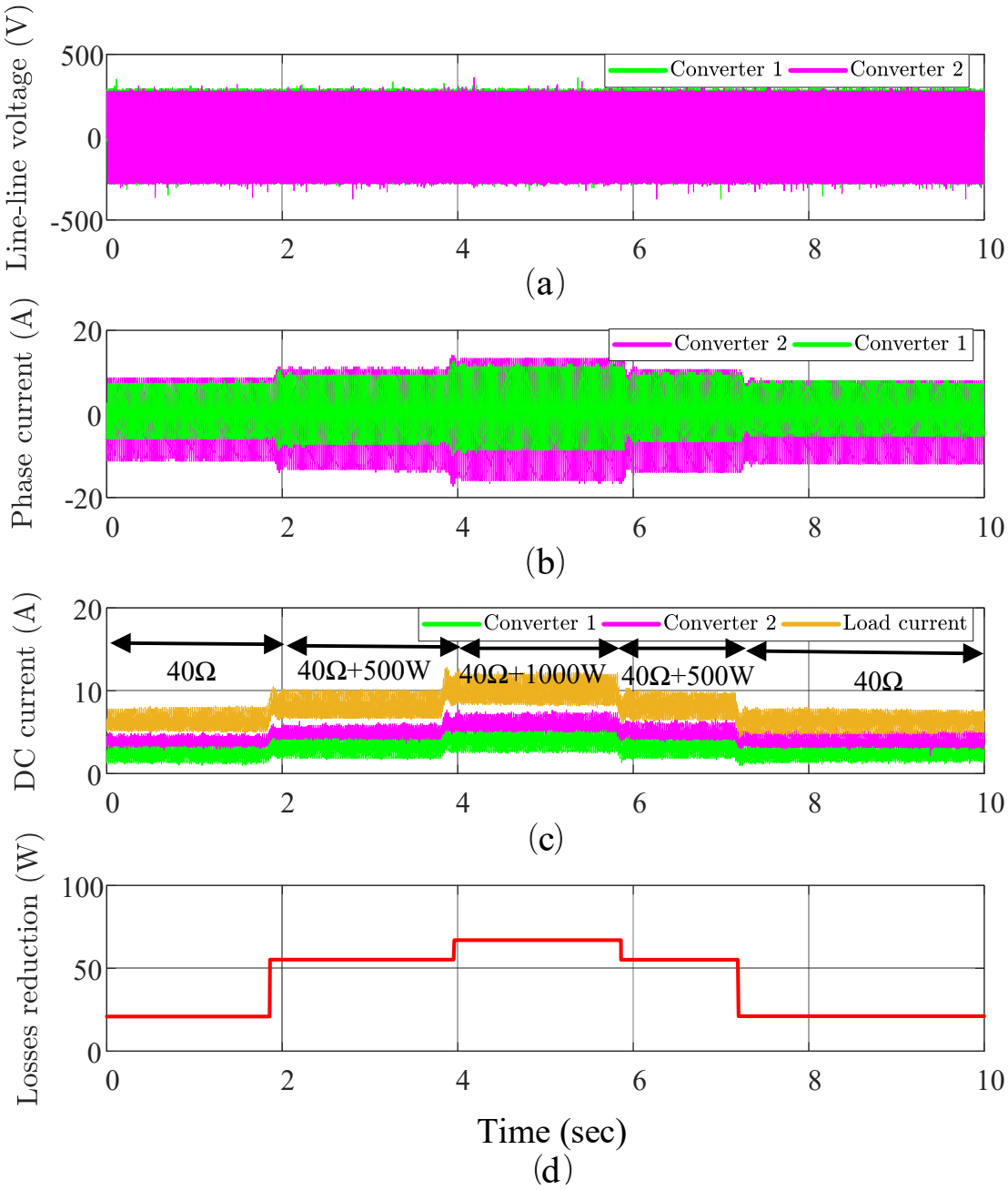

Fig. 6.14: Experimental results with 40 Ω CIL and CPL with proposed design approach

6.7 Conclusions on Chapter 6

This chapter presents a method for optimal droop gains selection to minimize the power losses in a single DC bus multiple-sources multiple-loads microgrid considering the converters and transmission line losses for different load types i.e. CCL, CIL, and CPL. A converter power losses model was adopted for the droop gain design optimization. The main findings of the study of analytical based optimal droop gains design for the three different types of loads can be summarized as:

- Optimal droop gains can be calculated relying only on the knowledge of equivalent series resistance of converters for all types of loads.
- For all three types of loads, the optimal droop gains of the i^{th} converters are found. It is shown that the minimum system losses can be achieved by choosing the optimal droop gains equal to their corresponding ESR.
- It is shown that as the optimal droop gains vary, the system loss behaviour depends on the gain and the load type. Namely, for CCL, the losses are kept constant, for CPL the losses are increased and for CIL the losses are decreased with droop gains increase.

According to the proposed method, there are multiple optimal solutions for droop gains. As derived, one of the optimal gains sets is found when the droop gains are equal to the corresponding equivalent series resistances of the feeding converters. This leads to a solution that does not require any information about the transmission lines or other converters in the system, but only about the power losses model of the local converter.

The proposed method of droop gains optimization was validated by simulation using a streamlined dynamic model of the single DC bus multiple-sources multiple-loads microgrid and the converters. The validation results confirmed the effectiveness of the optimal design approach in reducing the total system power losses and improving the voltage regulation of the single DC bus multiple-sources multiple-loads MG system, as expected. The proposed optimal droop gain design approach will be used as a power-sharing method between the multiple sources in the single DC bus architecture to aid the energy management strategy of the overall EPS system presented in Chapter 8.

Chapter 7

Multi-Objective Droop Gain Design based-on Artificial Neural Network

In Chapter 6 the criteria of the optimal droop gains design focused on system losses minimization and ignored issues related to voltage regulation and current sharing. In contrast, this chapter will present a new approach for optimal droop gains design in a single DC bus multiple-sources and multiple-loads onboard microgrid to achieve multiple objectives, such as minimum system losses, improved voltage regulation, and improved current sharing of power converters, using an ANN. First, the procedures used for data generation needed in the training the ANN are discussed, then the structure of the ANN and training method are presented, and then the final proposed ANN-based droop gain design approach is tested in simulation to confirm the improved performance.

7.1 Introduction

As discussed in Chapter 6, there is a trade-off between improved power-sharing, improved voltage regulation, and system losses reduction, which is illustrated by Fig. 7.1. Therefore, a multi-objective droop gain design strategy seems to be very beneficial and was therefore undertaken in this study. An Artificial Intelligence (AI) approach is considered as the best candidate to deal with such a complex problem, where AI could replace the original system with a surrogate model that can reduce the design time significantly [153]. The ANN method is the most actively researched area for AI applications in power

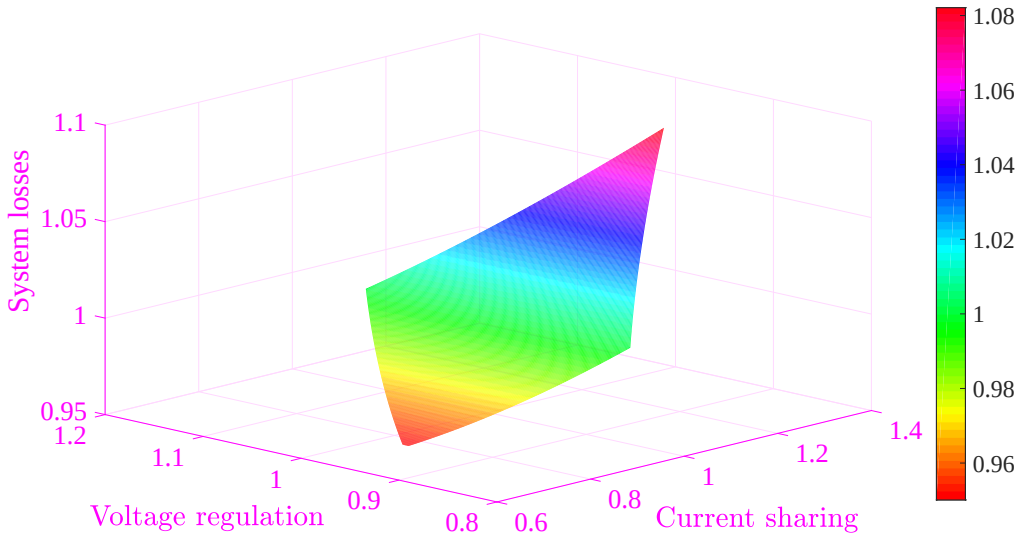

Fig. 7.1: The trad off between different optimisation objectives

electronics systems due to the flexibility of its structure to integrating other AI techniques for performance improvement. Furthermore, the remarkable developments in computer hardware provide room for the neural network (NN) to handle complex tasks related to power electronic systems in a seamless manner [154]. The ANN is a deep learning approach that has developed from the concept of biological neural networks of the human brain, but ANN accepts only numeric and unstructured data and can be used to model complicated systems. Fig. 7.2 presents a typical biological neuron which consists of the following four parts [154], [155]:

- Dendrites: responsible for receiving the data from other connected neurons.
- Soma or Cell body: the neuron's cell body, responsible for processing information received from dendrites.
- Axon: similar to a cable that transmits information between neurons.
- Synapses: the link between the axon and the dendrites of other neurons.

The ANN collects together a large number of units that are connected in some way to allow communication between them. These units, also known as nodes or neurons, are simple processors that work in a parallel fashion. The neurons are connected via a connection link. Each connection link has a weighting factor that contains data about

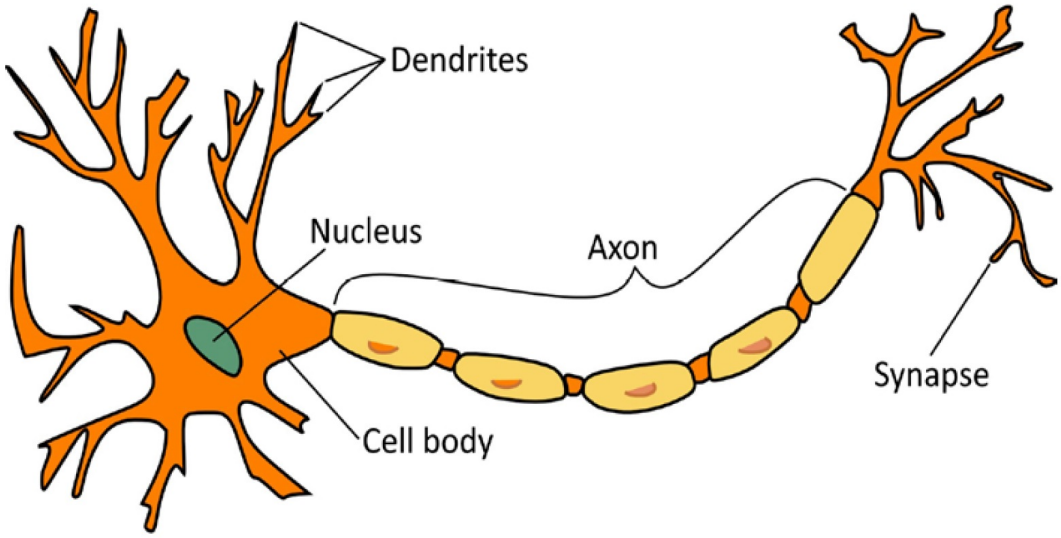

Fig. 7.2: Schematic diagram of a Biological neuron

the input signal. The weighting factor usually amplifies or attenuates the signal that is being communicated. The input signals and the associated weighting factor are the most important information required for a neuron to solve a particular problem[156].

Each neuron has an internal state, which is called an activation signal/function. An activation function is used to add non-linearity to data. Introducing non-linearity aids in the identification of complicated underlying patterns. It can also be used to scale a value to a specific range. The sigmoid activation function, for example, scales the value between 0 and 1. Each neuron has a bias to adjust the output along with the weighted sum of the inputs to the neuron. The bias is a constant which helps the model to fit the given data. The input signals and the activation rule are combined to produce the output signals, which can be sent to other units as shown in Fig. 7.3 [154].

A neural network with a single layer is called a perceptron. A multi-layer perceptron is called an ANN. The neural network can have any number of layers and each layer can have one or more neurons connected with every other neuron [154].

Learning or training of an ANN can be achieved by modifying the weights of the connections between the neurons of a specified network. Learning in an ANN can be classified into three categories namely; supervised learning, unsupervised learning, and reinforcement learning [154].

In supervised learning, the training of the ANN is done under the supervision of a

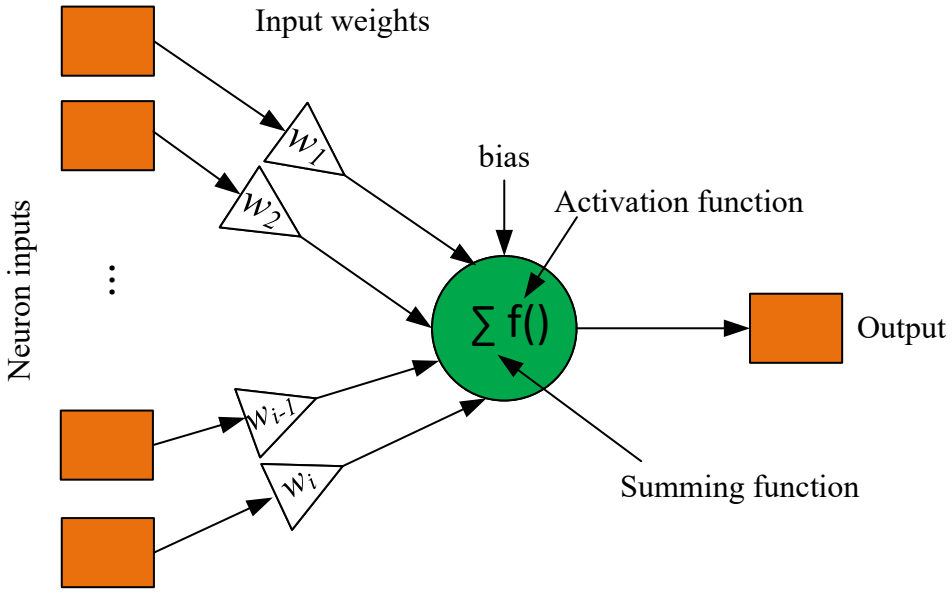

Fig. 7.3: Schematic diagram of the perceptron

teacher – a way by which it can determine the desired output vector for each input in the training data, either as the vector itself or a method by which it can be determined. Each input vector is fed into the network and it generates an output vector. A comparison between this output vector and the desired output vector is made. If the actual output does not match the desired output vector, an error signal is generated. Consequently, the weights are modified based on this error signal until the actual output matches the desired output as shown in Fig. 7.4

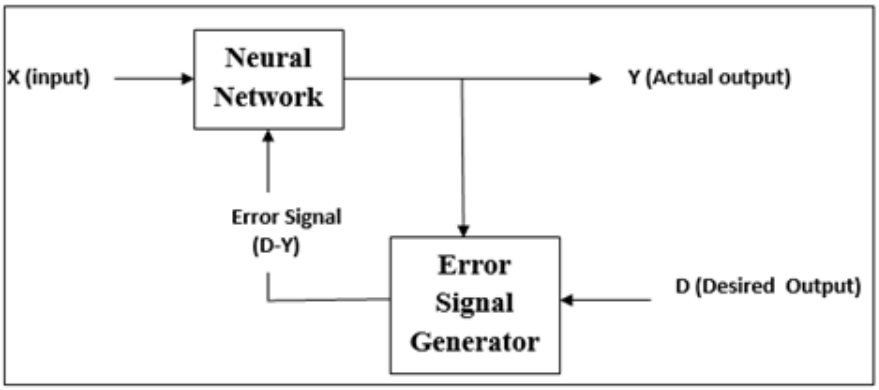

Fig. 7.4: Supervised learning of ANN [154]

Unsupervised learning is done without the supervision of a teacher. Clusters are formed by combining input vectors of similar types. When a new input pattern is applied, the neural network responds with an output response reflecting the input pattern's class. There is no feedback from the environment about what the desired outcome should be or whether it is correct. As a result, in this sort of learning, the network must find patterns and characteristics from the input data, as well as the relationship between the input and output data as depicted in Fig. 7.5.

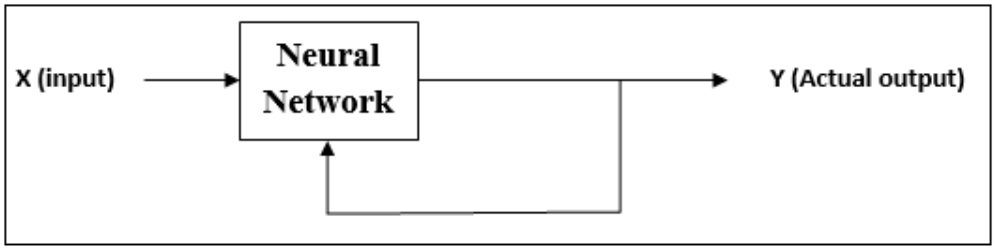

Fig. 7.5: Unsupervised learning of ANN [154]

Reinforcement learning is similar to supervised learning. The network receives some feedback from the environment during its training under reinforcement learning, stating how good/bad the result is, rather than telling it the correct result. As a result, this resembles supervised learning in certain ways. However, the feedback is evaluative rather than instructive, implying that there is no teacher present, as in supervised learning. After getting the input, the network adjusts the weights to obtain better information in the future, as presented in Fig. 7.6

The ANN can be classified into two main topologies, Feed forward Neural Networks (FFNN) and Feedback Neural Networks (FBNN). In the FFNN, each layer's nodes are linked to the nodes of the previous layers. Different weights are placed on the connections. The signal can only go in one direction, from input to output, because there is no feedback loop. In contrast the FBNN has feedback paths, which means the signal can flow in both directions using loops. As a result, it is a non-linear dynamic system, which changes continuously until it reaches a state of equilibrium.

The FFNN is the most frequently employed type of conventional ANN in power electronics applications due to its simplicity. A detailed review of machine learning-based

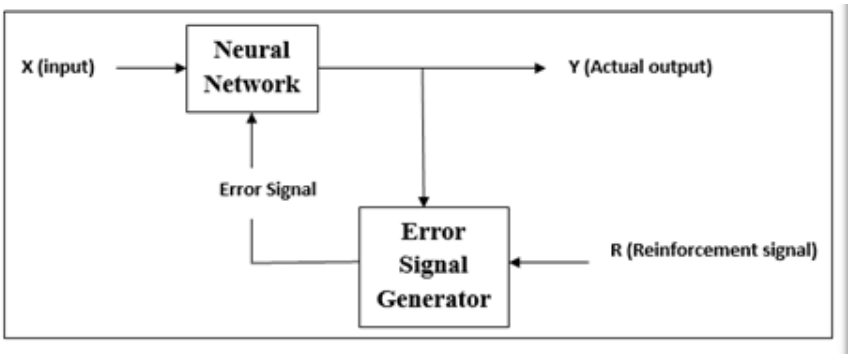

Fig. 7.6: Reinforcement learning of ANN [154]

approaches such as recurrent neural networks (RNNs), FFNNs, and support vector machine (SVM) in the estimation of battery state is provided in [155].

In this chapter, a possible solution is proposed for designing the optimal droop gains for minimum system losses, improved voltage regulation, and better current sharing, employing the ANN to reduce run-time computation. The desired ANN can be trained by exploring all of the combinations of the droop gains in the design space. Thereafter, the trained neural network is used to predict the optimal droop gains combination that will ensure minimum system losses, improved voltage regulation and accurate/desired current sharing, as defined by the user.

7.2 Proposed ANN-based Droop gain Design Approach

Fig. 7.7 provides a flow chart showing the steps of the ANN-based droop gain design approach. The first step involves the collection of data from detailed simulations of the MEA EPS model, including the actual model of the PMM-based generators and AFE converters, and their associated controllers for every combination of the design parameters, leading to a diagram as shown in Fig. 6.1. Then, at the 2nd step, using this data, the ANN is trained to become a surrogate model of the MEA EPS model. The training is based on user-defined desired balances between power system losses, voltage regulation, and current sharing. Based on this, the optimal droop gains can be predicted very quickly

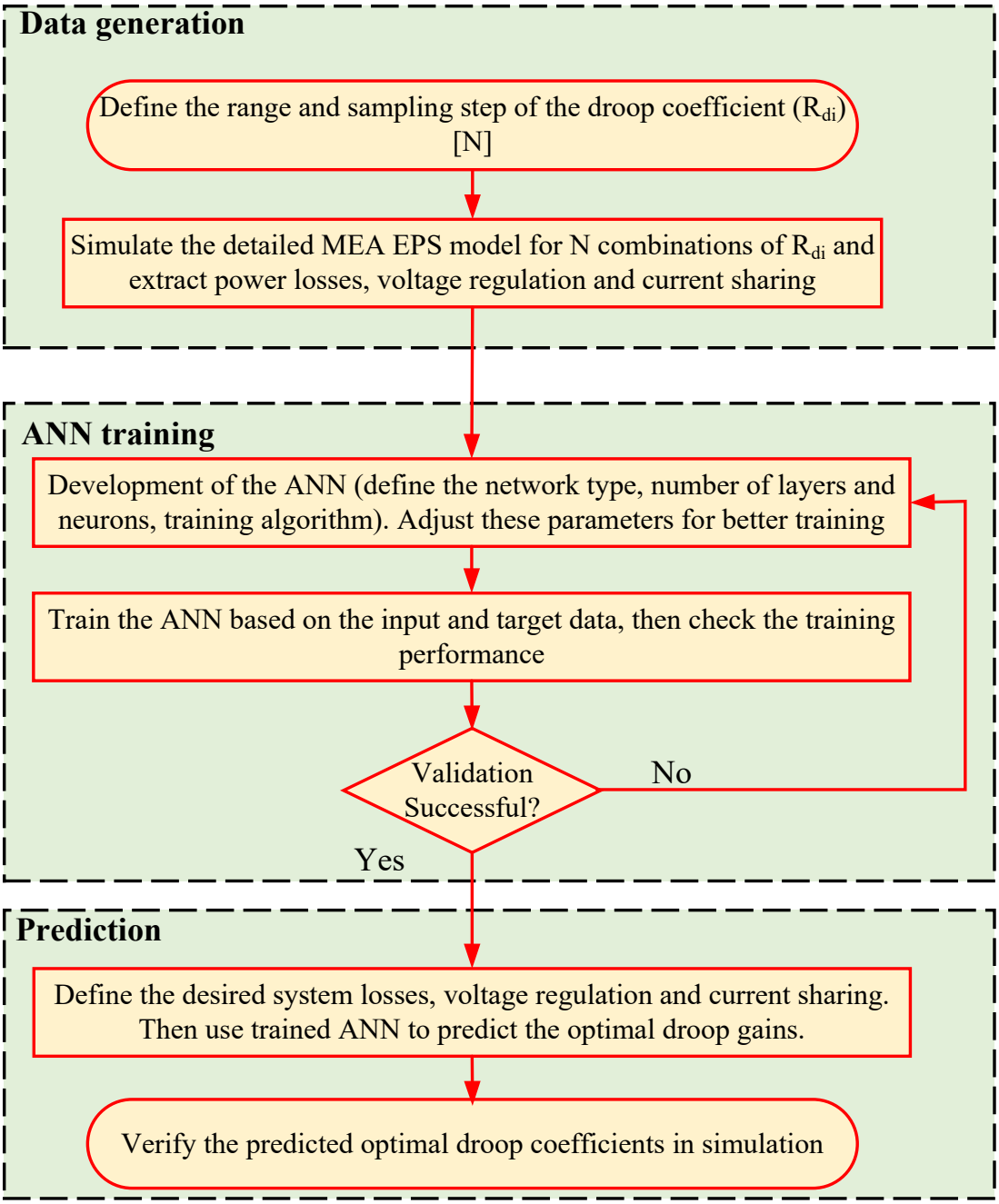

Fig. 7.7: Flowchart for the design of the droop gain using ANN method

.

and accurately. It is noteworthy that the data generation and training of the ANN needs to be carried out only once using the detailed system model parameters.

7.2.1 Procedure for Data Generation

The detailed MEA EPS system control model which is used as the case study in this Chapter (Fig. 6.1) was developed using MATLAB® /Simulink® and the corresponding code is shown in Appendix D. The MEA EPS and equivalent DC cable parameters used for simulation are given in Table 7.1. The droop gain sweep range is selected to cover ± 10% of the conventional droop gains to ensure a feasible design space with high fidelity. This implies that, after training, the obtained optimal droop coefficient can be applied in a practical situation. The sampling step for droop gain was set to 1e-4, which leads to 59536 samples. The data generated from the simulations at 300A load current was used as the input-target sample data to train the ANN. At high current, the losses, voltage regulation, and current sharing have significant values and this will aid in training accuracy. At this data generation step, the relationship between the droop coefficients, system losses,

Table 7.1: Converters Data and Optimal Droop Gains Values

Parameter	Symbol	Value	Unit
Converter1 rated power	P_{n1}	45	kW
Converter2 rated power	P_{n2}	45	kW
Converter1 efficiency	ζ_1	98	%
Converter2 efficiency	ζ_2	96	%
Converter1 no load losses	$P_{noload1}$	138	W
Converter1 no load losses	$P_{noload2}$	282	W
Converter 1 equivalent series resistance	R_{es1}	0.0281	Ω
Converter 2 equivalent series resistance	R_{es2}	0.0574	Ω
TL1 resistance	R_{c1}	0.0081	Ω
TL2 resistance	R_{c2}	0.0081	Ω
Converter 1 rated current	$I_{c1rated}$	170	A
Converter 2 rated current	$I_{c2rated}$	170	A
Converter 1 droop gain	R_{d1}	0.0810	Ω
Converter 2 droop gain	R_{d2}	0.0810	Ω

voltage regulation and current sharing between converters can be represented as in (7.1).

$$y = F_1(x) \leftrightarrow (P_{losses}, I_{sh}, \Delta V_{dc}) = F_1(R_{d1}, R_{d2}) \tag{7.1}$$

where R_{d1} and R_{d2} are the droop coefficient combinations within the design space used for multiple simulations and ΔV_{dc}, P_{losses} and I_{sh} are the voltage regulation, system losses and current sharing obtained from each of the simulations. It should be noted that the minimum limit for the ANN corresponding to minimum droop gain (i.e. inputs system losses and voltage regulation) as a function of load current I_L after fitting the data obtained from offline calculations has been found to be as follows:

$$P_{losses} = 0.00285 * I_L \tag{7.2}$$

$$\Delta V_{dc} = 0.00285 * I_L \tag{7.3}$$

while for the current sharing ratio it was found that the minimum value is not affected by load variations and is kept at the constant value of 0.75 .

7.3 Structure and Training of the ANN

In this section, the FFNN structure is selected to train the ANN due to the static relationship between the input and output data, which makes it easy to build with a simple optimizing algorithm as shown in Fig. 7.8 [157]. A static neural network merely feeds the input vector forward and the weights are fixed after training, whereas a dynamic neural network includes feedback from the output to the input or between layers hidden inside the network [158]. Users do not need to specify the functional relationship between the model inputs-outputs because the powerful FFNN will learn it automatically by tuning its internal training parameters (i.e. weights and bias). A detailed description of the FFNN can be found in [158]. The neurons in each layer process the information they receive from the previous layer. The outputs of a neuron are calculated using the outputs of all layers before it, multiplied by associated weights and summed together with a bias term. In this study, the algorithm used in training the ANN (Levenberg-Marquardt method [159]) and the training process are implemented in MATLAB's Neural Network Toolbox [159]. The ANN structure is made up of three layers with 3 neurons in the input layer, 10

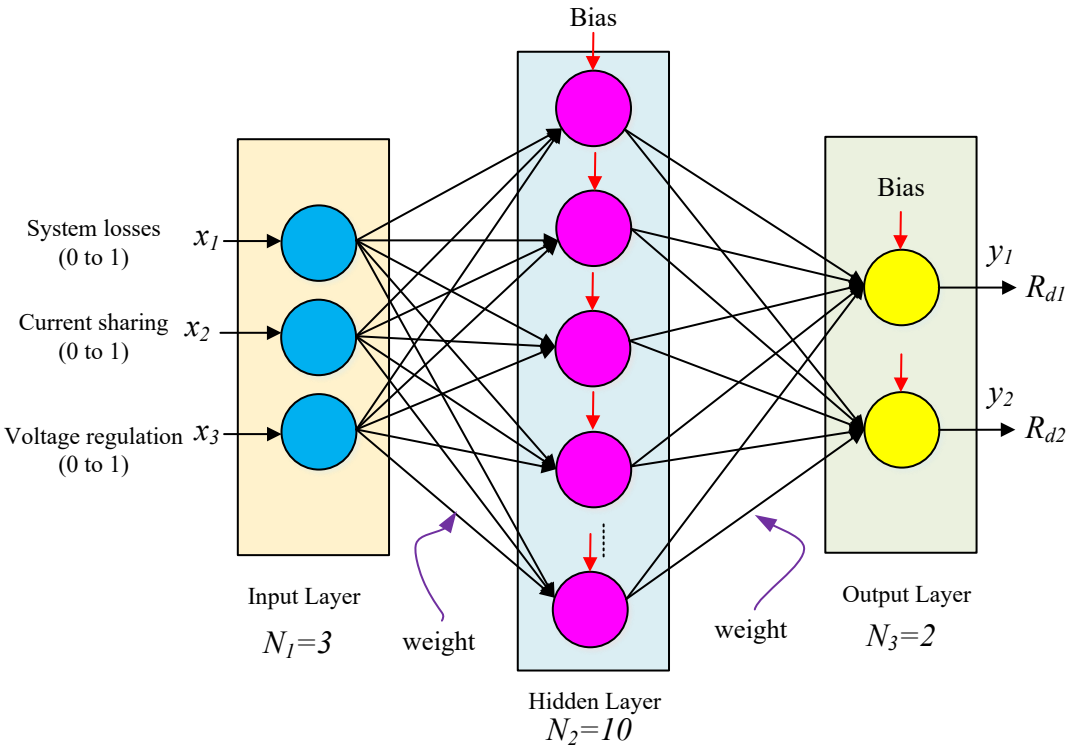

Fig. 7.8: Structure of the three-layer FFNN which serves as a surrogate model of the MEA EPS model shown in Fig. 6.1

.

neurons in the hidden layer, and 2 neurons in the output layer. At this training stage, the relationship between the droop coefficients, system losses, voltage regulation, and current sharing between converters can be represented as in (7.4).

$$y = F_2(x) \leftrightarrow (R_{d1}, R_{d2}) = F_2(P_{losses}, I_{sh}, \Delta V_{dc}) \tag{7.4}$$

The output of a neuron in the input layer ($l = 1$) can be calculated as $z_i^1 = x_i, i = 1, .., N_1$, while the output of neuron i in the hidden layer ($l = 2$) can be given as:

$$z_i^2 = \sigma\left(\sum_{j=1}^{N_1} \omega_{ij}^2 z_j^1 + b_i^2\right), i = 1, ..., N_2 \tag{7.5}$$

Finally, the output of a neuron in the output layer ($l = 3$) can be obtained as:

$$y_i = \sigma\left(\sum_{j=1}^{N_2} \omega_{ij}^3 z_j^2 + b_i^3\right), i = 1, ..., N_3. \tag{7.6}$$

where ω_{ij} is the weight, b_i is the bias and σ is an activation function that usually takes the form of a sigmoid function as following [157]:

$$\sigma(\gamma) = 1/(1 + e^{-\gamma}) \tag{7.7}$$

It is important to mention that the choice of the number of neurons used in the hidden layer(s) to train the ANN has a significant impact on the performance of the ANN (for avoiding over fitting or under fitting). As a rule of thumb, it is recommended that one starts with a relatively small number of neurons and then increases it gradually based on using the observed training error [153]. This is a trial-and-error process and can be carried out very fast since the training can be completed within a few seconds (based on using a standard office PC). It should be noted that the inputs for the ANN here are the desired system losses, voltage regulation, and current sharing, while the outputs are the corresponding optimal droop gains.

7.4 Application and Validation of the Proposed Design Approach

To demonstrate the effectiveness of the optimal droop gain design using the ANN approach, a simulation test has been conducted using Matlab® /Simulink® models given in Appendix D and the system parameters used are given in Table 7.1. Two tests are carried out to illustrate the compromises between different optimization objectives. In the first test, the desired design requirement is to achieve minimum system losses with a small sacrifice of equal current sharing and improved voltage regulation. Therefore, (7.3) is used to set the minimum system losses and voltage regulation values while the current sharing (i_2/i_1) is set to the minimum value of 0.75. A step-change in load current [50, 100, 150, 200, 250, 300, 340] has been applied. By changing the load current, the minimum limits of system losses and voltage regulation are changed, and as a result, the corresponding droop gains change as shown in Fig. 7.9. Fig. 7.10 shows the converters' currents under droop gains generated from the ANN. It can be seen that the current sharing between the converters is achieved according to the generated droop gains from the ANN, for example, at a load current of 200A, the ratio was found to be 0.75. Fig. 7.11 presents

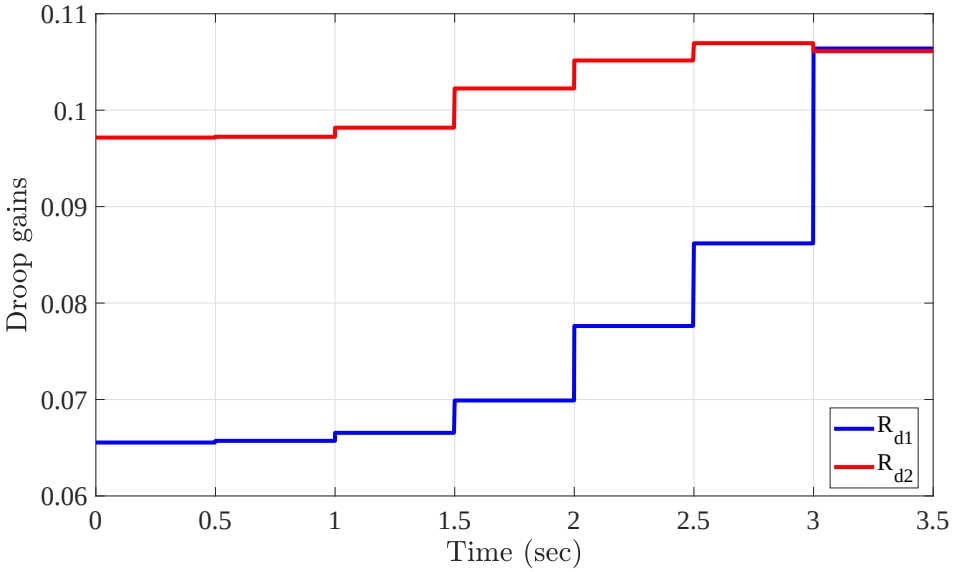

Fig. 7.9: Variation of droop gains with load current for test 1

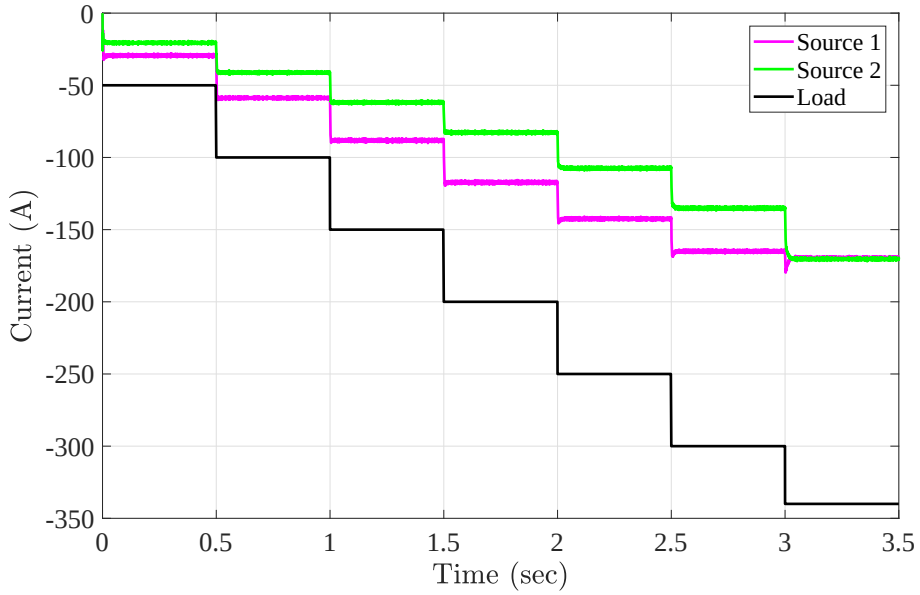

Fig. 7.10: Variation of sources currents with load current change using proposed method for test 1

the converters' currents with a traditional design approach, that provides equal current sharing in all loading cases. In comparison to the traditional method, at light loading the sharing is almost equal to the minimum predefined value of 0.75, while increasing the loading means that the sharing ratio changes towards 1 which means equal currents, as seen in Fig. 7.12.

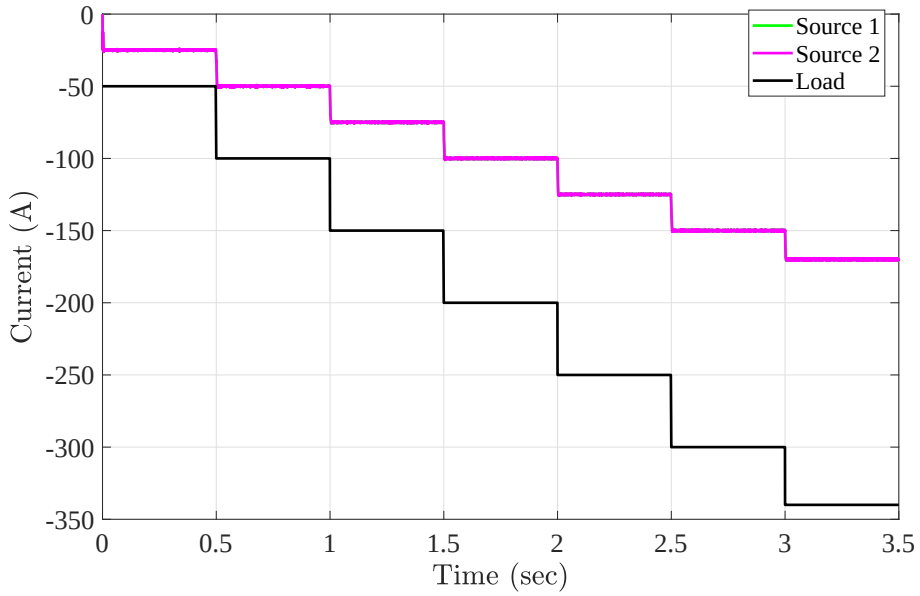

Fig. 7.11: Variation of sources currents with load current change using conventional method [80]

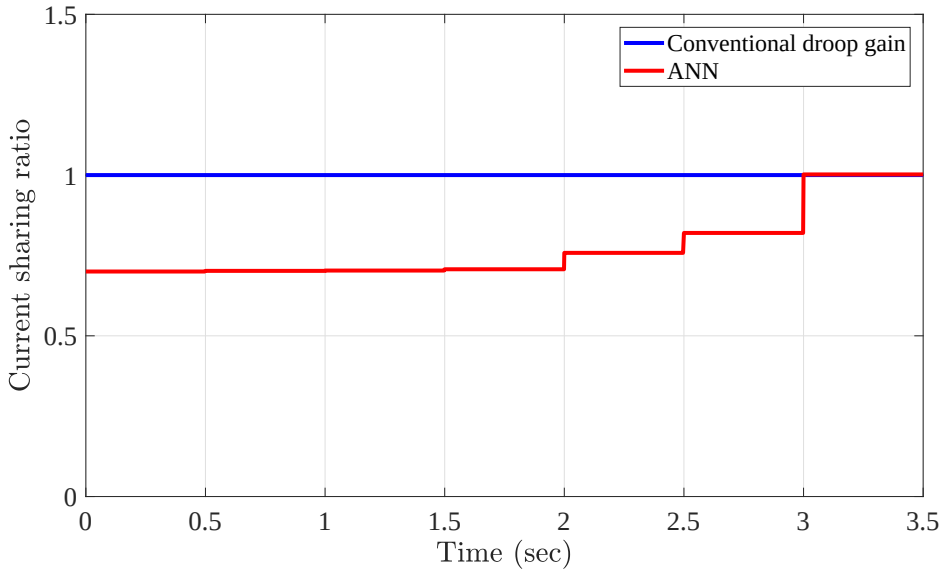

Fig. 7.12: Variation of current sharing with load current for test 1

Fig. 7.13 shows how the total system losses vary with load current for both methods. From this figure, the losses of the proposed design method are less than the conventional method e.g. at load current 300A, the observed reduction in losses is 5% (135W in the simulated scenario). This reduction in system losses is achieved because the currents are redistributed based on the value of the equivalent resistance of each converter. At light

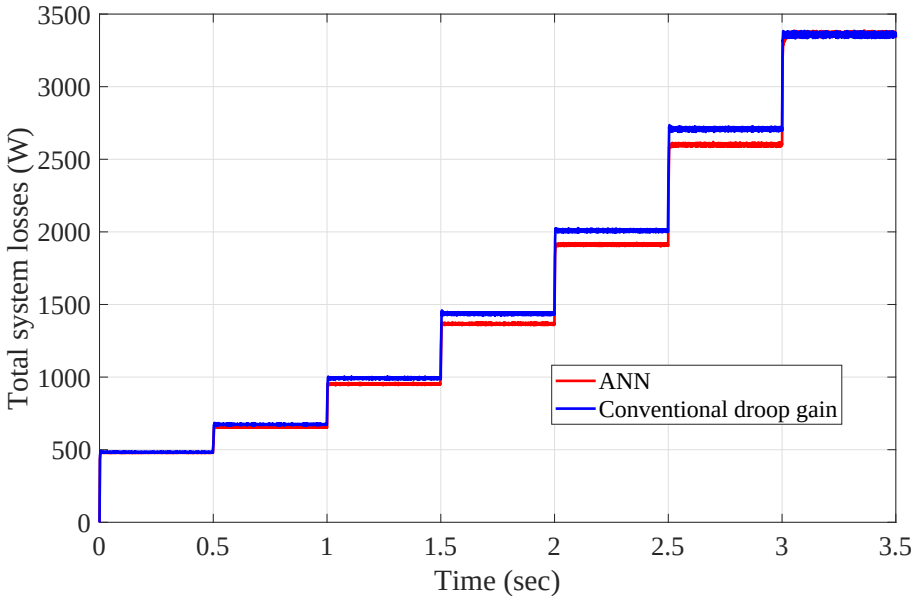

Fig. 7.13: Variation of system losses with load current for test 1

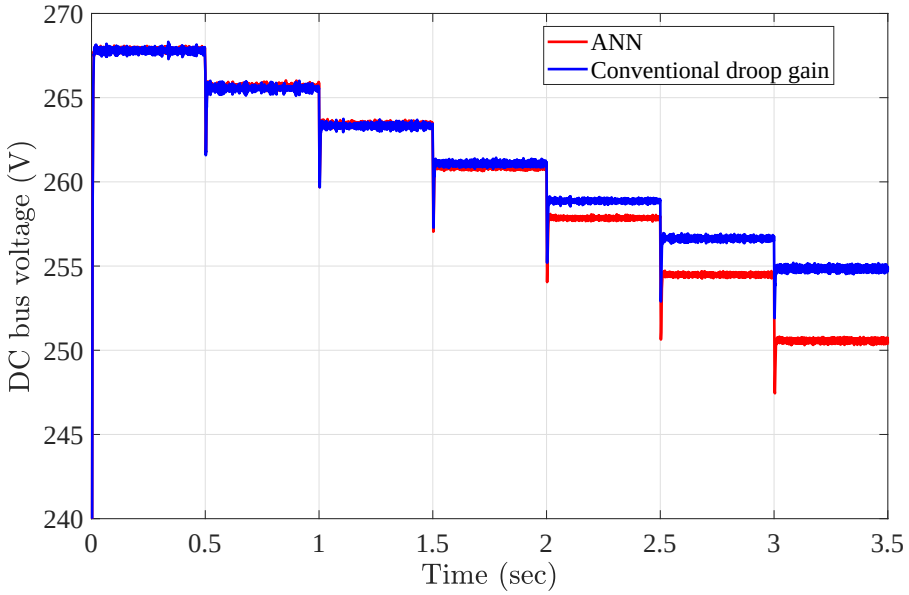

Fig. 7.14: Variation of DC bus voltage with load current for test 1

load, the reduction in losses is small compared to the heavy load condition, as the no-load losses are dominant. In terms of voltage regulation of the DC bus, it can be seen that for the proposed method this is slightly degraded, by 0.75%, which is due to the adjustment of the converters' currents, as shown in Fig. 7.14.

In contrast, in test 2 the desired design requirements are: equal current sharing, small sacrificing of system losses minimization and improved voltage regulation. Hence, the

input values of the trained ANN P_{losses}, I_{sh} and ΔV_{dc} are 0.90, 1 and 0.90, respectively. Fig. 7.15 shows the predicted droop coefficients from the trained ANN when the load changes, and it can be seen that their values are constant during the test as the desired inputs are fixed. The converters' DC currents when the predicted droop gains are used are shown in Fig. 7.16. Moreover, the current sharing between both converters is

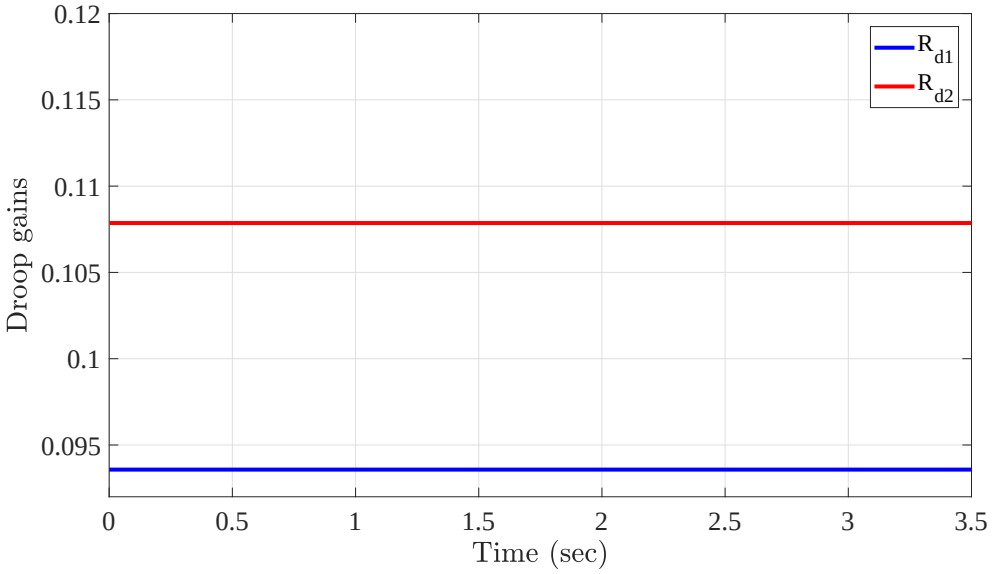

Fig. 7.15: Variation of droop gains with load current for test 2

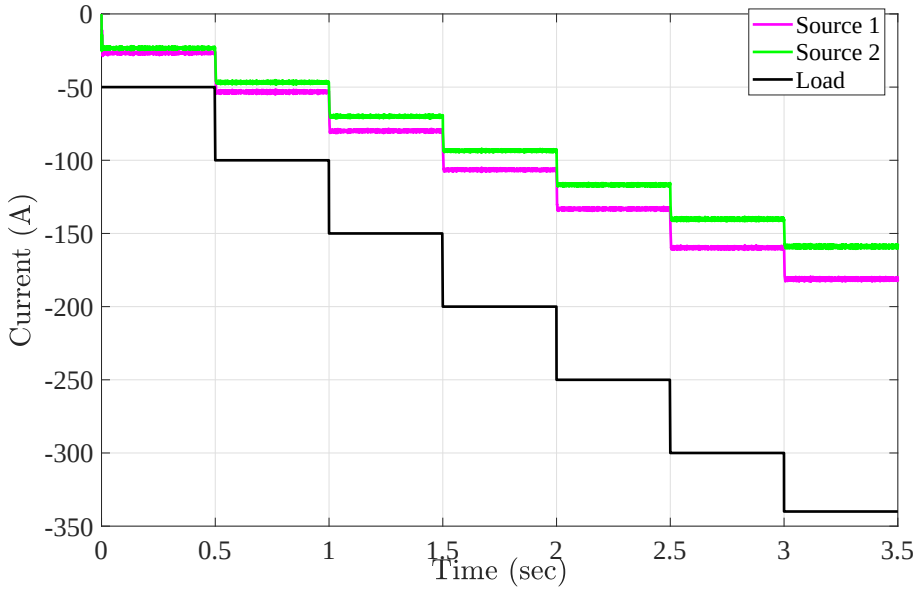

Fig. 7.16: Variation of sources currents with load current change using proposed method for test 2

improved compared to Fig. 7.10, for example at 200 A it was found to be 0.96. It can be seen from Fig. 7.17 that with the ANN approach the ratio is close to 1. Consequently, the desired requirements are achieved. In comparison to the results of losses reduction in test 1 (Fig. 7.13), the losses reduction in test 2 has decreased due to a low priority for loss minimization in this test. For example, at a load current of 300 A, the losses reduction is 2700-2630=70W (2.64%) compared to the conventional method as shown in

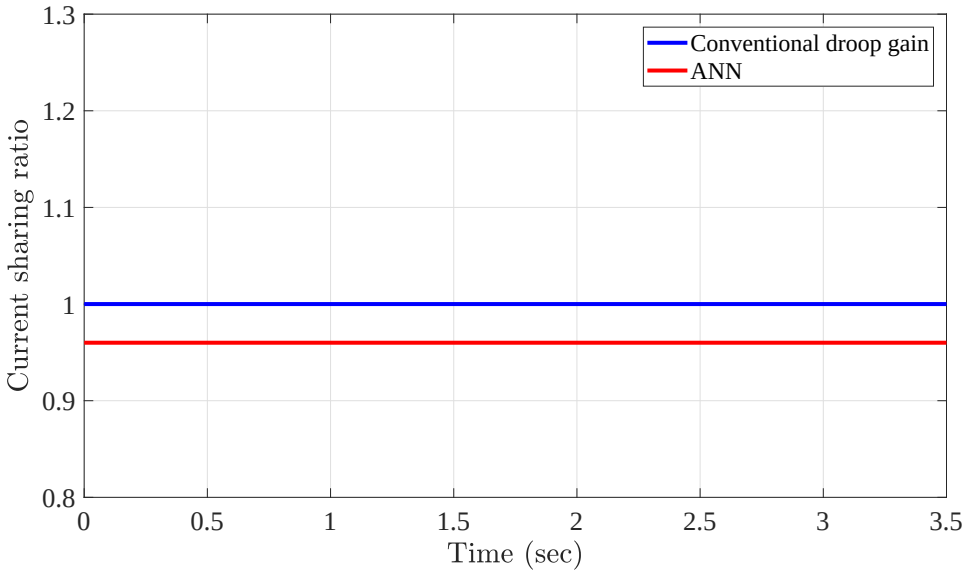

Fig. 7.17: Variation of current sharing with load current for test 2

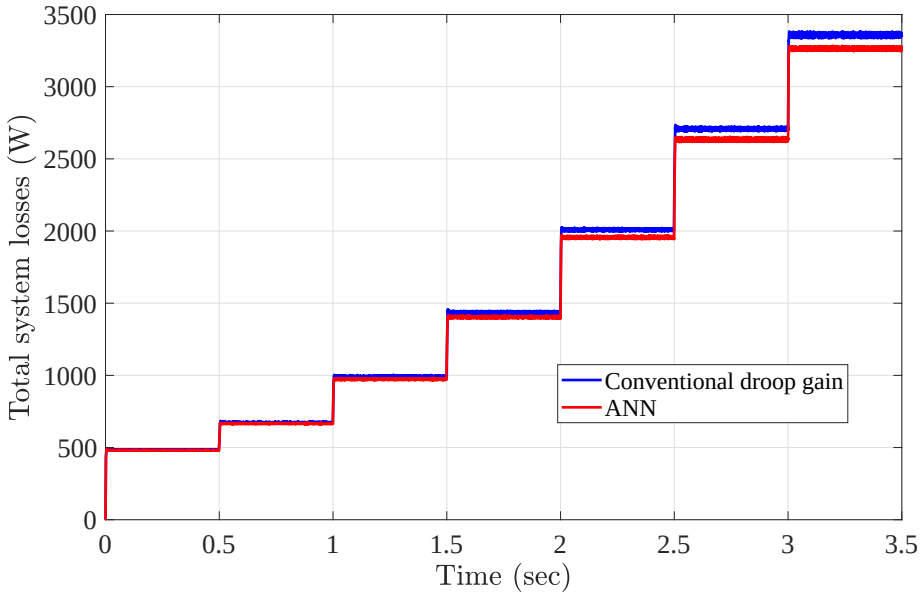

Fig. 7.18: Variation of system losses with load current for test 2

Fig. 7.18. The DC bus voltage variation under load changes is shown in Fig. 7.19, and it can be concluded that the voltage regulation with the ANN approach has deteriorated by 1.11% compared to test 1, as the current sharing is improved, leading to a larger voltage droop on converter equivalent resistance.

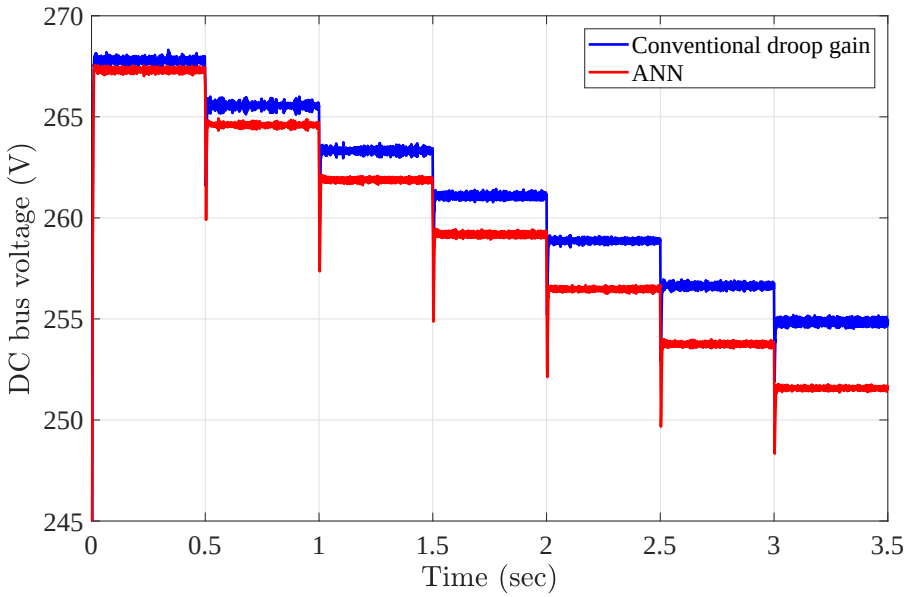

Fig. 7.19: Variation of DC bus voltage with load current for test 2

7.5 Conclusion

In this chapter, an ANN-based design of optimal droop gains for EPS losses minimization, improved voltage regulation, and improved current sharing among power converters is developed. The ANN can be used to predict the optimum droop gain combinations for any user-defined minimized system losses, voltage regulation, and current sharing within the design space in a fast and accurate manner. The proposed method doesn't incur any additional burden on the system, only measuring the load current for minimum limits calculation for the ANN inputs. Furthermore, by implementing the trained ANN online into the controller of each source, the corresponding optimal droop gain can be obtained directly for any ANN inputs for the given user-defined preferences.

The proposed ANN approach has been validated in time domain simulation with different tests that cover the potential of the trade-off between the different optimization objectives and it showed satisfactory performance in adjusting its outputs accordingly.

Similarly to the proposed design method which was presented in Chapter 6, optimal droop gains design using the ANN approach can be used as a power-sharing method for a single DC bus EPS that is required to implement the energy management strategy that will be introduced in Chapter 8. The difference between the two methods presented in Chapter 6 and this Chapter is that here the user has an option to select which objective/objectives need to be optimized.

Chapter 8

Energy Management for onboard EPS with Batteries Integration

Effective management to improve system efficiency (losses minimization) given the significant increases in the number and size of onboard sources and loads is considered to be one of the key challenges for an MEA EPS. Therefore, this Chapter presents an intelligent EM strategy, based on the optimal droop gain approach presented in Chapter 6, to minimize the total system losses for single DC bus multiple-sources multiple loads EPS. The assumptions for the proposed EM strategy are presented, followed by the discussion of all potential operating scenarios of the flight. The conditions for states transitions and the status of system components, switches, and variable settings are investigated. The FSM structure has been chosen to implement the control strategy to realize the EPS reconfiguration operation. The proposed EM strategy is implemented and simulated using Matlab/Simulink showing how it is able to manage the EPS under different operating conditions to reduce the system losses.

8.1 Introduction

In the EPS configuration shown in Fig. 8.1, the generators and their corresponding AFE converters and batteries are connected to the 270 DC bus by circuit breakers C1-C3. Different system configurations can be obtained by changing the status of the circuit breakers (open/closed). For example, when one of the power generation channels fails,

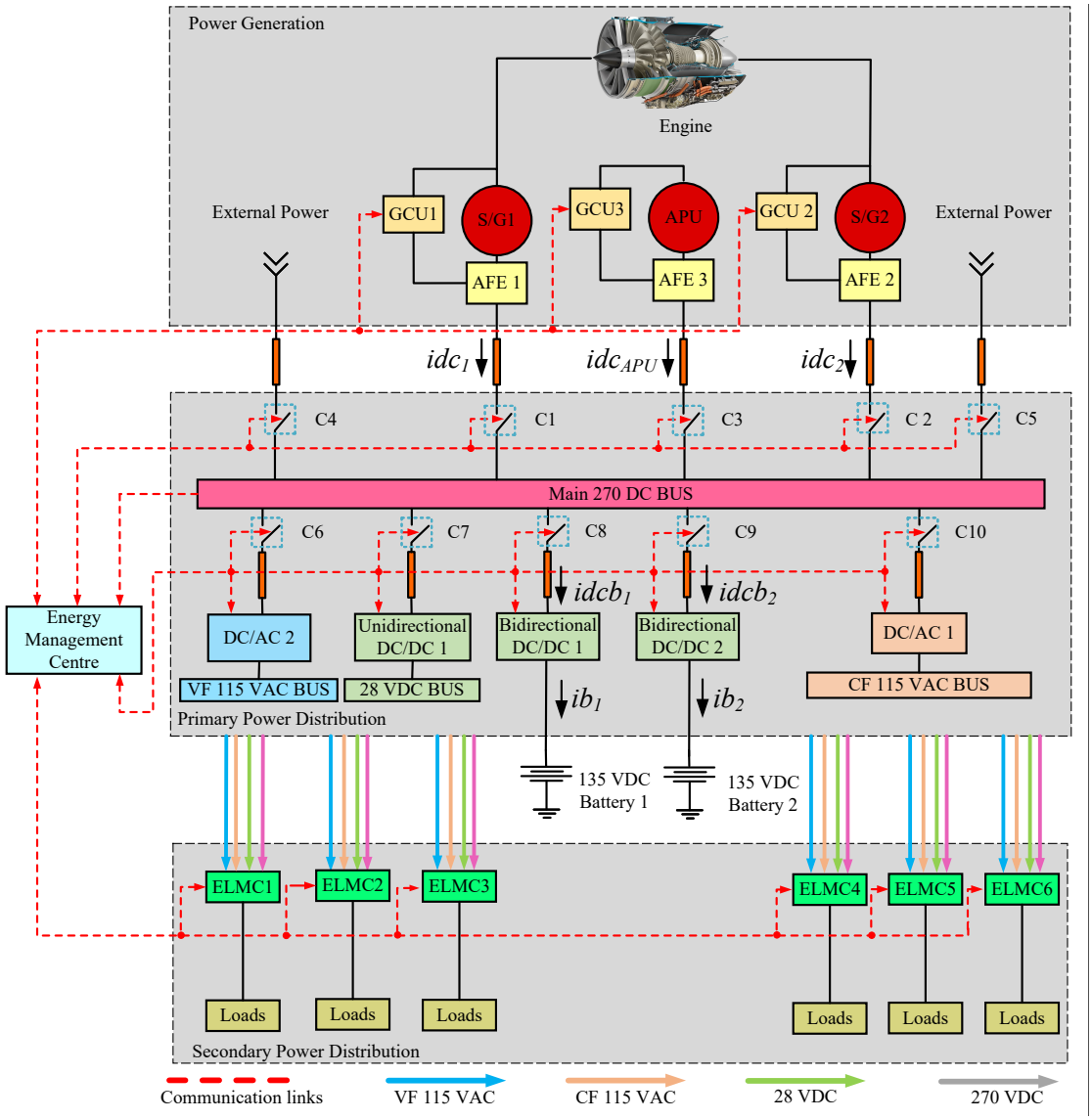

Fig. 8.1: Single Bus EPS architecture

the APU or battery system may be used to supply some emergency buses to enable safety-critical system operation. The EM strategy is required to manage the power flow distribution and EPS reconfigurations, setting a new power path and ensuring safe operation under different operating scenarios. In [88] a control strategy to manage the power flow in the EPS and to ensure continuous power supply to the high priority loads under different converter failure conditions is presented. The proposed strategy is applied through a smart controller and the control logic is implemented using the FSM approach. The actions taken by the controller under different operating conditions are dependent on the state of charge of the batteries. In [160] the balance between the

power available from the aircraft power supply (gas turbine generator and storage device) and power demands, while minimizing the operation cost including fuel and battery operation cost, is formulated as a mixed-integer nonlinear programming (MINLP) power management problem for MEA civil aircraft. The outputs of the MINLP are the optimal active power generation, load management, and battery charging/discharging status. In [161] a power allocation and load management method to minimize the load shedding is presented. The management problem is formulated as Mixed-Integer Quadratic Problem (MIQP) where the decision variables are the generator output power, load connections, and battery charging schedules. To the best of the author's knowledge, this Chapter will cover the gap between introducing an intelligent energy management strategy to ensure uninterruptible power supply to safety-critical loads and considering system losses minimization (converters and transmission lines losses), exploiting the thermal capability (overload) of generators, considering variable load priority during flight phases, and schedules for battery charging/discharging, to supply safety-critical and non-critical loads during different failure scenarios.

8.2 Proposed Energy Management Strategy

This section outlines the proposed control strategy. As mentioned in Section (2.6), this strategy aims to ensure uninterrupted power to the HPLs. Moreover, the batteries are employed to supply the medium priority loads during generator failures in addition to their basic functions such as providing power to start the APU and supporting ground operations (refueling, powering the braking system when the aircarft is towed, etc). Moreover, keeping also the batteries SoC within the pre-set values. The assumptions for EM strategy investigated in this study are:

1. Electrical loads can be either powered or shed (on/off). Loads can be regulated continuously or intermittently.

2. Generators can operate above their nominal power ($110\%P_n$) for a short time (5 minutes). This overload capacity can therefore be exploited.

3. The EPS can be reconfigured, using switches, to find the appropriate power path

for each load to be fed in different situations.

4. Storage devices can both absorb and supply the referenced power (when available).

5. The APU generator will come into operation in case of the failure of the one of the main generators. The APU generator can run in parallel with the remaining main generator.

6. The APU generator is used to provide power to the power users during ground operation.

From the discussion in Section 2.6 it can be seen that the EPS is a dynamic system, i.e. continuously having to react to external and internal stimuli. Therefore, based on [89], [162], the use of FSM is considered as a solution to improve EPS energy management. In FSM, the behaviour of the system can be modelled as a set of states and transitions between states. From a mathematical point of view, the FSM can be seen as:

$$f\left(\sum, S, s_0, \delta, F\right) \tag{8.1}$$

where $\sum$ represents a finite set of symbols, S is a finite set of states, s_0 is the initial state, so that $s_0 \in S$, δ is a state transition function:

$$\delta : S \times \sum \rightarrow S \tag{8.2}$$

Here F is the finite set of final states. An example of the formulation is depicted in Fig. 8.2. The following equations describe the system in Fig. 8.2. The inputs are:

$$\sum = [\varepsilon] \tag{8.3}$$

The states can be expressed as:

$$S = [s_0, s_1, s_2] \tag{8.4}$$

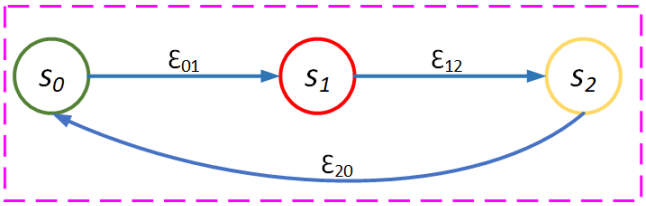

Fig. 8.2: Example of reactive system

The transition function δ that define mapping between cartisian product of the set of states S and the language symbols $\sum$ into the set of states S is given by:

$$\delta = [s_0/\varepsilon_{01} \rightarrow s_1, s_1/\varepsilon_{12} \rightarrow s_2, s_2/\varepsilon_{20} \rightarrow s_0] \tag{8.5}$$

For example, if the current state is s_0 and the input is ε, the next state will be s_1 and so on.

The final state can be given as:

$$F = s_2 \tag{8.6}$$

Since the theory of FSM has been introduced, it can be applied to the EPS in order to set a management strategy. The states for the EPS under study were established based on the status of the main generators and APU, as well as generator overload availability, and battery SoC. The status of the generator health is represented by one numbers: "0" for faulty and "1" for unfaulty. Similarly, all generators' overload periods are assigned one of two possible values: "0" for not overloaded and "1" for overloaded. In charge mode, the battery's SoC is "0," while in discharge mode, it's "1". Table 8.1 shows the 32 (2^5) possible outcomes based on these variables. It can be seen that there are 12 states that are inapplicable since they contradict the proposed EM's assumptions, and 8 states are duplicated and can be merged with comparable states, leaving 12 states that will be detailed in-depth in the following section. These 12 possibles/states can be grouped under five main operation scenarios i.e. normal scenario, one power generation channel fails and APU is running, one power generation channel fails and APU fails, both power generation channel fail and APU is running, and both power generation fail and APU fails.

8.2.1 Normal scenario

- **State 1 (ST1): No fault of main generators, all loads connected and supplied, and APU is off**

  In this state, there is no fault in the power generation channels and the Energy Management Centre (EMC) role is to send a message to ELMC to connect the loads according to each flight phase. If the EPS was operating in a different scenario and a transition to ST1 happened then, the EMC should shut down the APU if it

Table 8.1: All possible states combinations

No	G1	G2	APU	Overload (OL)	SoC	State	Description
1	0	0	0	0	0	NA	G1& G2 off & APU off & not overloaded & charge
2	0	0	0	0	1	ST 11/12	G1 & G2 off&APU off & not overloaded & discharge
3	0	0	0	1	0	NA	G1 & G2 off & APU off & not overloaded & charge
4	0	0	0	1	1	ST11/12	G1 & G2 off & APU off & overloaded & discharge
5	0	0	1	0	0	ST5	G1 & G2 off & APU on & not overloaded & charge
6	0	0	1	0	1	ST2	G1 & G2 off & APU on & not overloaded & discharge
7	0	0	1	1	0	ST4	G1 & G2 off & APU on & overloaded & charge
8	0	0	1	1	1	ST3	G1 & G2 off & APU on & overloaded & discharge
9	0	1	0	0	0	ST9	G1 off & G2 on & APU off & not overloaded & charge
10	0	1	0	0	1	ST6	G1 off & G2 on & APU off & not overloaded & discharge
11	0	1	0	1	0	ST8	G1 off & G2 on & APU off & overloaded & charge
12	0	1	0	1	1	ST7	G1 off & G2 on & APU off & overloaded & discharge
13	0	1	1	0	0	ST10	G1 off & G2 on & APU on & not overloaded & charge
14	0	1	1	0	1	NA	G1 off & G2 on & APU on & not overloaded & discharge
15	0	1	1	1	0	ST10	G1 off & G2 on & APU on & overloaded & charge
16	0	1	1	1	1	NA	G1 off & G2 on & APU on & overloaded & discharge
17	1	0	0	0	0	ST9	G1 on & G2 off & APU off & not overloaded & charge
18	1	0	0	0	1	ST6	G1 on & G2 off & APU off & not overloaded & discharge
19	1	0	0	1	0	ST8	G1 on & G2 off & APU off & overloaded & charge
20	1	0	0	1	1	ST7	G1 on & G2 off & APU off & overloaded & discharge
21	1	0	1	0	0	ST10	G1 on & G2 off & APU on & not overloaded & charge
22	1	0	1	0	1	NA	G1 on & G2 off & APU on & not overloaded & discharge
23	1	0	1	1	0	ST10	G1 on & G2 off & APU on & overloaded & charge
24	1	0	1	1	1	NA	G1 on & G2 off & APU on & overloaded & discharge
25	1	1	0	0	0	ST1	G1 on & G2 on & APU off & not overloaded & charge
26	1	1	0	0	1	NA	G1 on & G2 on & APU off & not overloaded & discharge
27	1	1	0	1	0	ST1	G1 on & G2 on & APU off & overloaded & charge
28	1	1	0	1	1	NA	G1 on & G2 on & APU off & overloaded & discharge
29	1	1	1	0	0	NA	G1 on & G2 on & APU on & not overloaded & charge
30	1	1	1	0	1	NA	G1 on & G2 on & APU on & not overloaded & discharge
31	1	1	1	1	0	NA	G1 on & G2 on & APU on & overloaded & charge
32	1	1	1	1	1	NA	G1 on & G2 on & APU on & overloaded & discharge

is running, unshed the loads if they were shed, and charge the batteries if their $SoC < SoC_{max}$. Fig. 8.3 shows ST1 with simplified and reduced scale EPs.

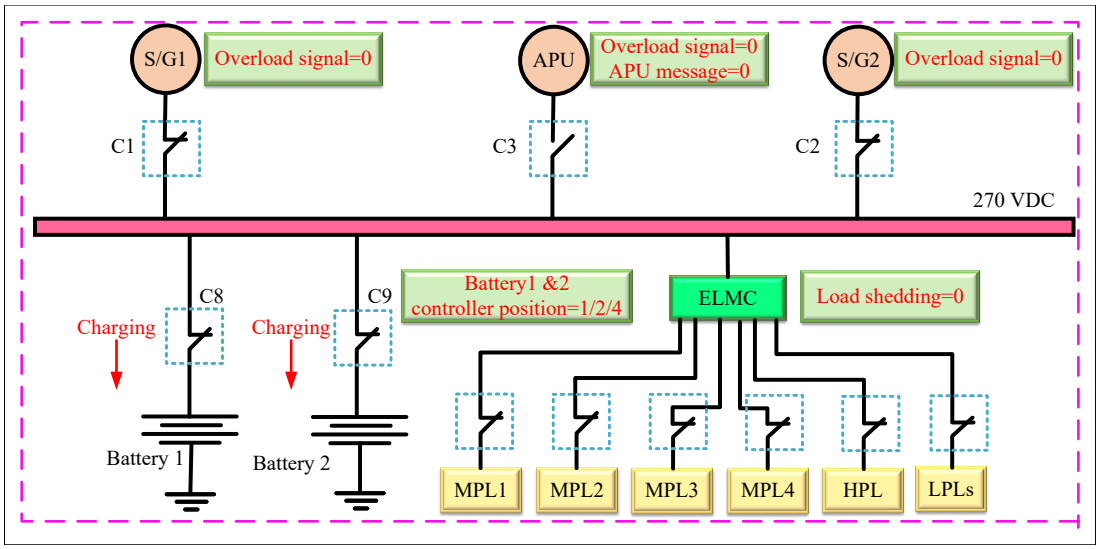

Fig. 8.3: ST1 illustration on simplified EPS

8.2.2 Both Power Generation Channels Fail and APU is Started Scenario

- **State 2 (ST2): Main generators failed and APU is running for up to 5 minutes**

  In this state as shown in Fig. 8.4, both main power generation channels failed and APU is running. The APU can be overloaded by 10% for 5 minutes and batteries can be used to supplement power until discharging to the the lower limit SoC_{min}.

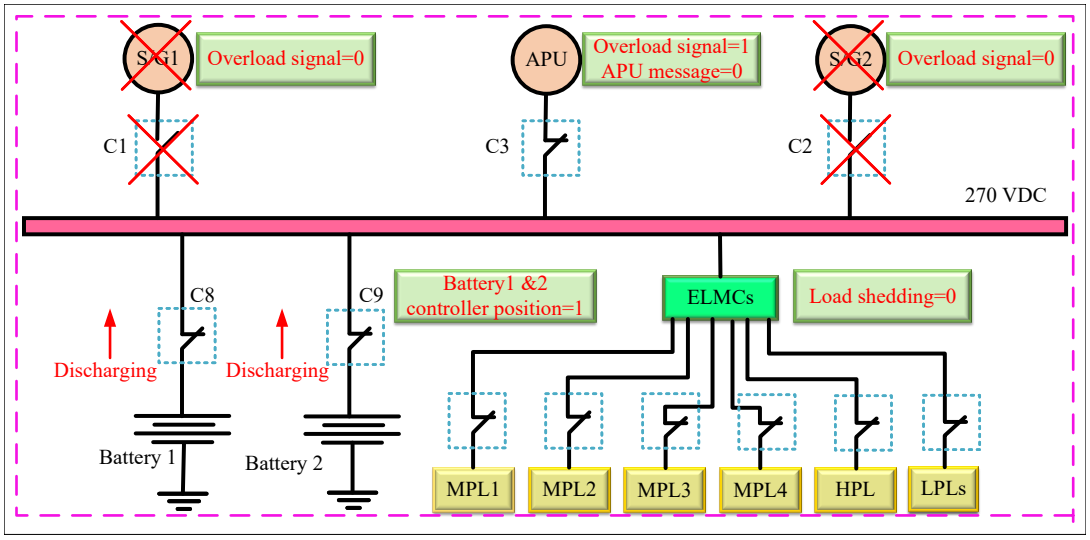

Fig. 8.4: ST2 illustration on simplified EPS

- **State 3 (ST3): Main generators failed, APU overloaded for more than 5 minutes, batteries are discharging, and low priority loads are shed.**

  Here, the APU overloading in ST2 has occured for more than 5 minutes, but the batteries still have enough energy to supply the critical loads. Therefore, the batteries continue to supply power hence, discharge further. However the low priority loads are shed as depicted in Fig. 8.5.

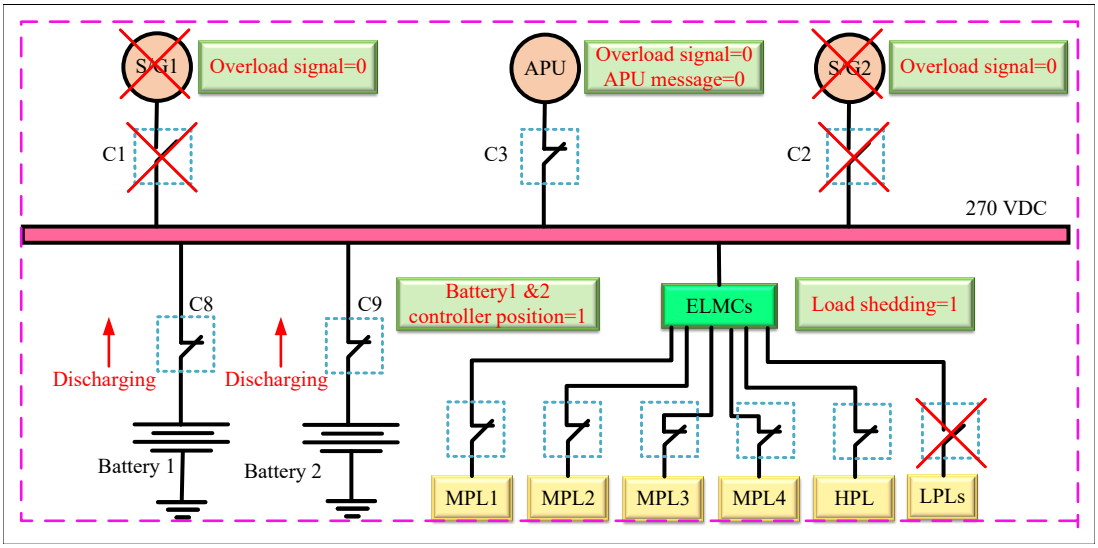

Fig. 8.5: ST3 illustration on simplified EPS

- **State 4 (ST4): Main generators failed, APU overloaded for more than 5 minutes, batteries permitted to charge, all LPLs and some MPLs shed**

  This state is reached from ST3 if the batteries were discharging and reached the lower limit SoC_{min}, so that they could no longer provide power, and the APU can still provide its rated power (250kW). The LPLs and MPL1 and MPL2 are all shed in this state to reduce the power requirements as shown in Fig. 8.6. If there is surplus power after shedding, the batteries can be recharging.

- **State 5 (ST5): Main generators failed, APU overloaded for less than 5 minutes, batteries charging, and LPLs and some MPLs shed.**

  If the overloading time does not exceed 5 minutes and the batteries are discharging, then the EMC allows the APU to continue to run with 10% overloading condition. The low and MPL1 and MPL2 are all shed in this state, to reduce the power

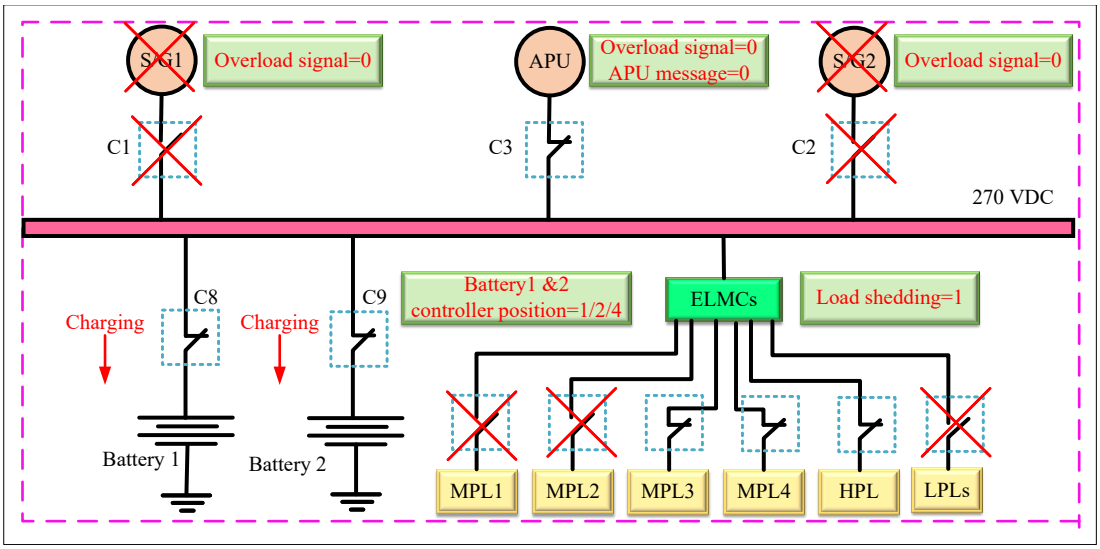

Fig. 8.6: ST4 illustration on simplified EPS

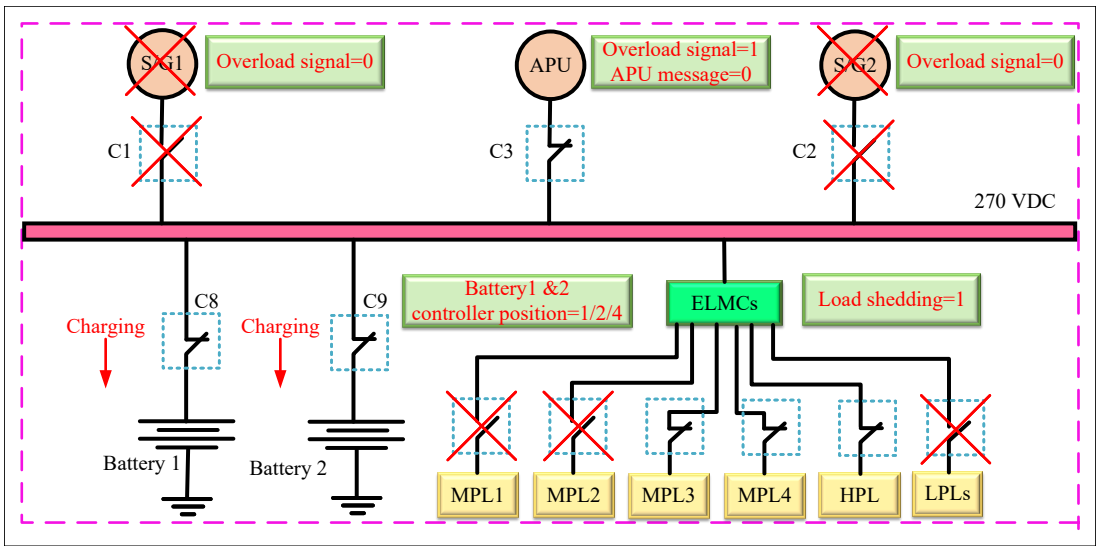

Fig. 8.7: ST5 illustration on simplified EPS

requirements. If there is surplus power after the shedding, the batteries can be charging. Fig. 8.7 shows ST5 with simplified and reduced scale EPs.

8.2.3 One Power Generation Channel Fails and APU Fails Scenario

- **State 6 (ST6): One generator running with 10% overload up to 5 minutes, batteries discharging ($SoC \geq SoC_{min}$), and no shedding**

  Only one of the main generators is working as represented in Fig. 8.8, and is allowed

to be overloaded by 10 % for 5 minutes with batteries discharging at their maximum rates to cover the shortage in power demand.

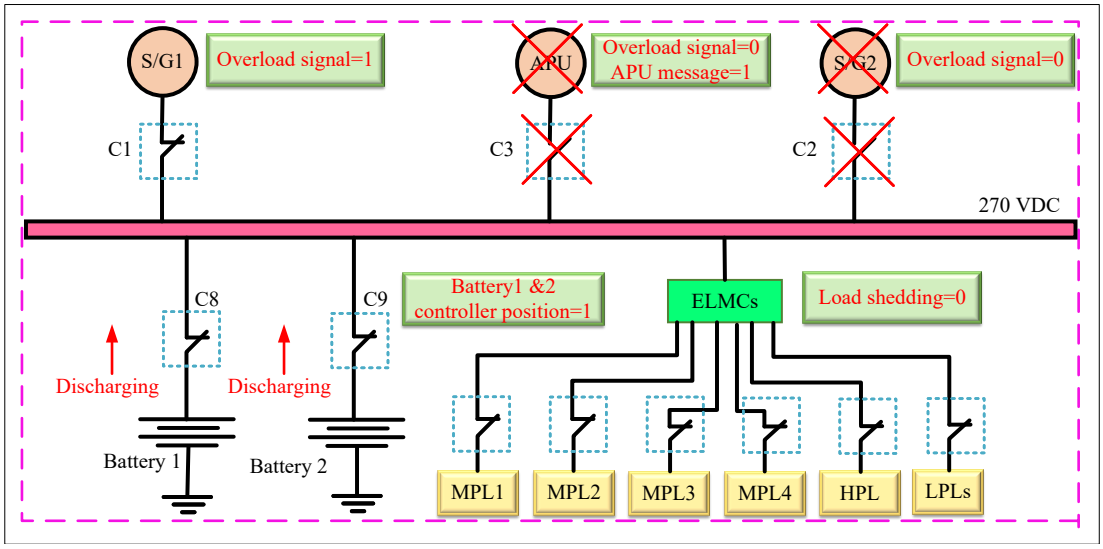

Fig. 8.8: ST6 illustration on simplified EPS

- **State 7 (ST7): One generator running, batteries discharging ($SoC \geq SoC_{min}$), healthy generator is overloaded for more than 5 minutes, and low priority loads shed**

  Once the overloading time of healthy generator reaches 5 minutes and the SoC of the batteries is above their minimum values, the operating point will move to ST8, in which case the batteries will discharge until their minimum SoC values, and LPLs are shed as shown Fig. 8.9.

- **State 8 (ST8):One generator running, no overload, batteries charging ($SoC \leq SoC_{min}$), LPLs and some MPLs shed**

  In this operating state as depicted in Fig. 8.10, the batteries are fully discharged and the available generating power is equal to 250 kW. Therefore, the LPLs and MPL1 and MPL2 are shed and the batteries will charge until their maximum values.

- **State 9 (ST9): One generator running in overload (< 5 minutes), batteries charging ($SoC < SoC_{max}$), LPLs and MPLs shed**

  If the overloading time has not reached the limit (5 minutes) and the batteries have been discharging below SOC_{min}, then the system is in ST9. The healthy generator

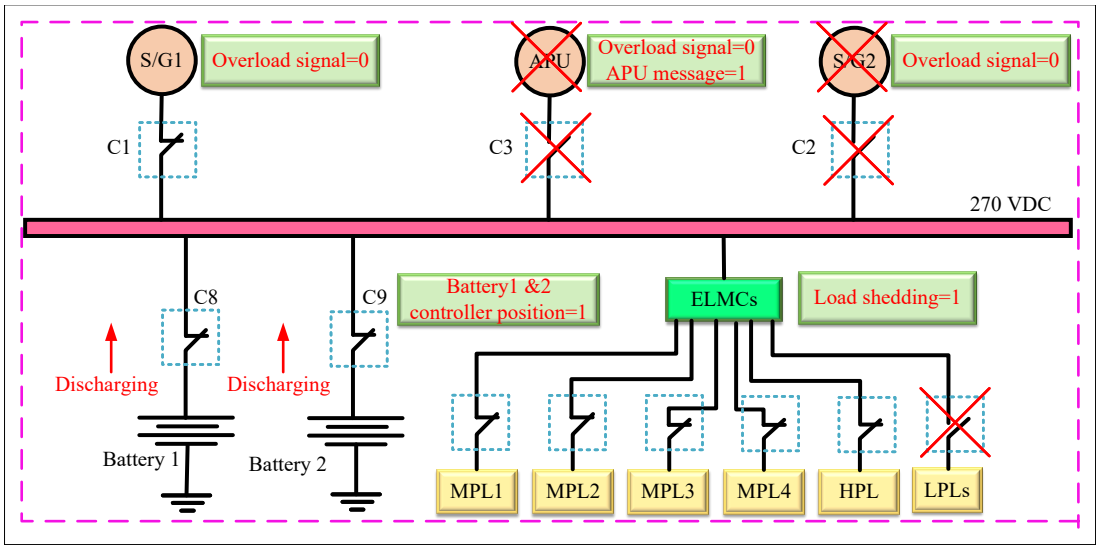

Fig. 8.9: ST7 illustration on simplified EPS

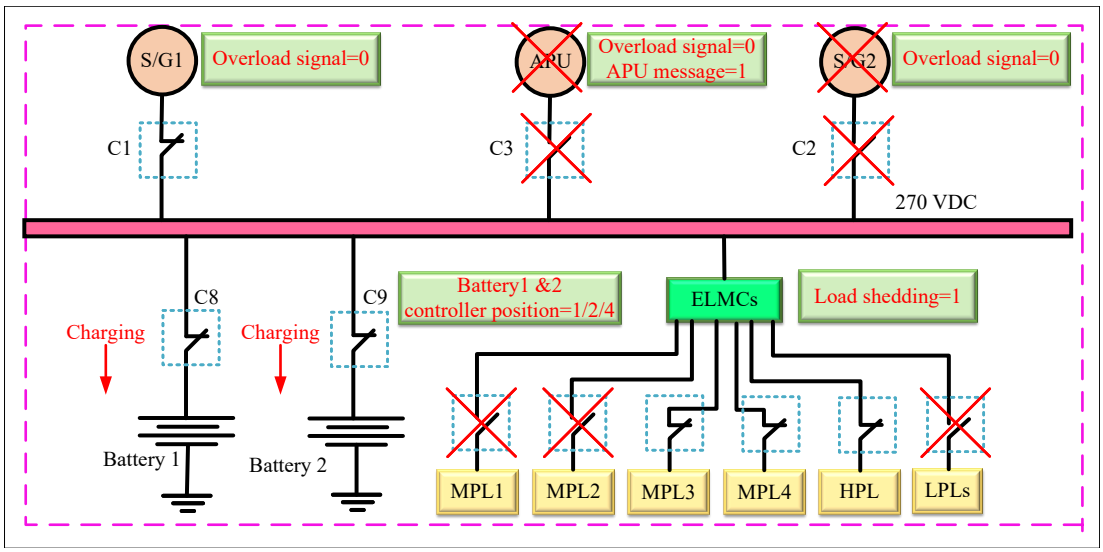

Fig. 8.10: ST8 illustration on simplified EPS

is overloaded by up to 10%. The LPLs and MPL1 and MPL2 are all shed in this state, to reduce the power requirements. If there is power surplus after the load shedding, the batteries can be recharging. Fig. 8.11 illustrates ST9 with simplified and reduced scale EPs.

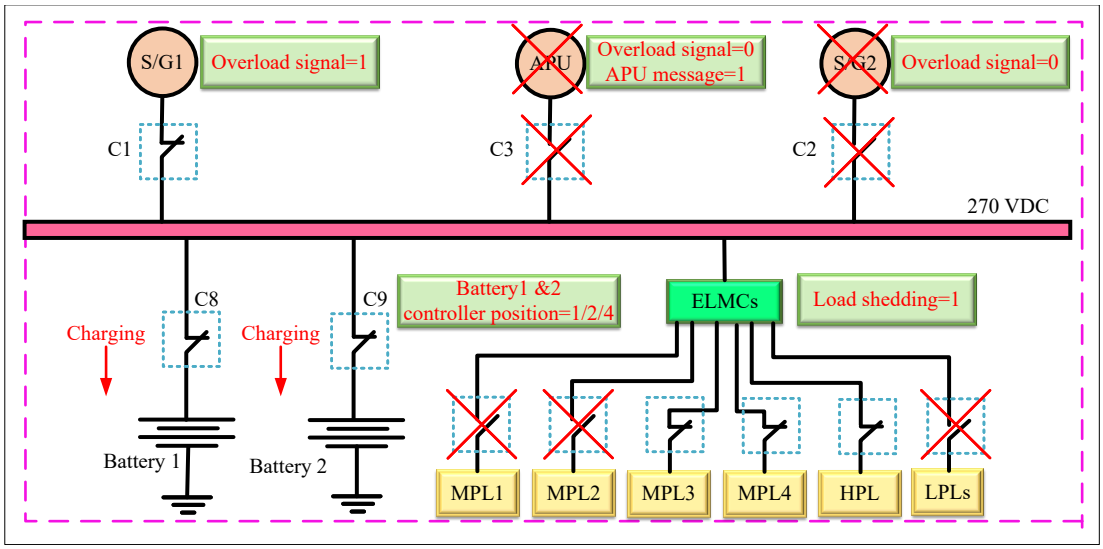

Fig. 8.11: ST9 illustration on simplified EPS

8.2.4 One Power Generation Channel Fails and APU is running Scenario

- **State 10 (ST10): One generator and APU running and not overloaded, batteries charging, loads unshed.**

  In this state, the APU has started, it is similar to the normal scenario (ST1). Therefore, the loads which were shed in previous scenarios are reconnected and the EMC will not allow the healthy generator to be overloaded any longer, and the batteries will charge until SoC_{max} as shown in Fig. 8.12.

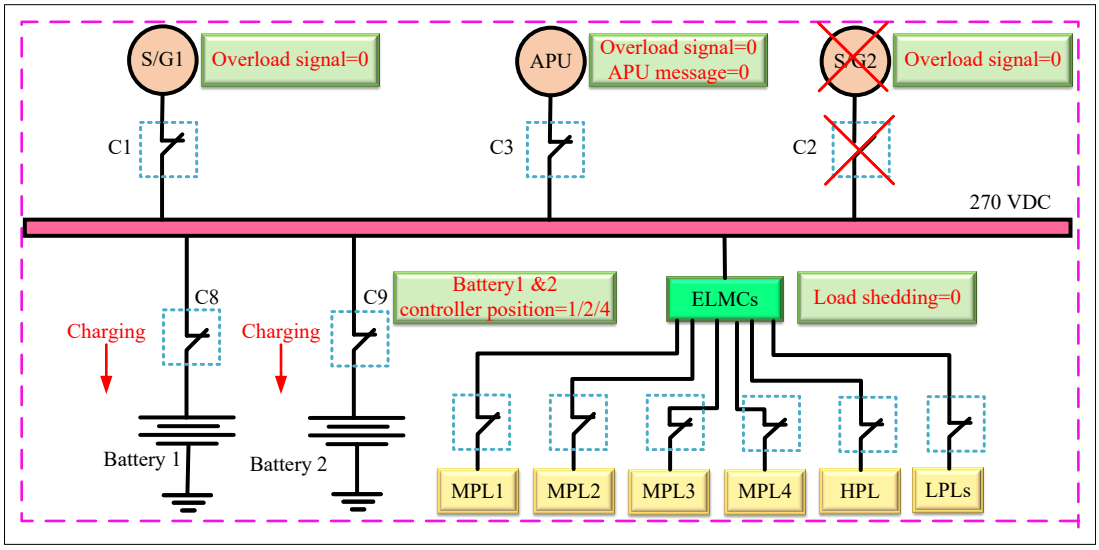

Fig. 8.12: ST10 illustration on simplified EPS

8.2.5 Both Main Power Generation Channels Fail and APU Fails or not started Scenario (Emergency)

- **State 11 (ST11): Main generators and APU fail and SoC is less than SoC_{min}.**

  In this state, all power sources except batteries have failed as shown in Fig. 8.13, and the batteries supply the critical loads only, to allow the aircraft to land safely.

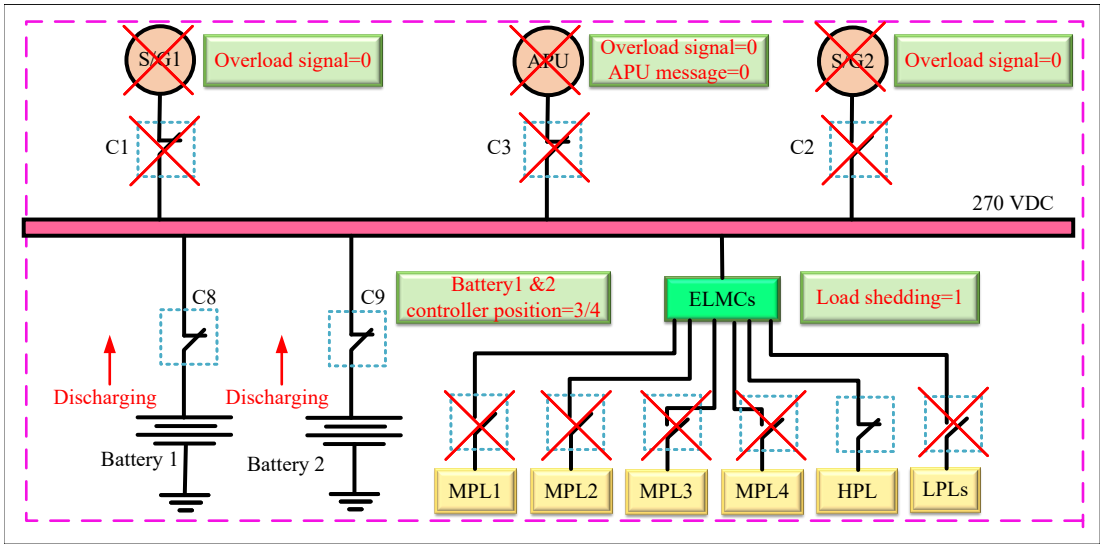

Fig. 8.13: ST11 illustration on simplified EPS

- **State 12 (ST12): Main generators and APU failed and SoC is greater than SoC_{min}.**

  If there is enough energy in the batteries, this can be exploited by supplying MPL1 and or MPL2. Fig. 8.14 represents ST12 with simplified and reduced scale EPs.

Fig. 8.15 shows the EM strategy adopted in this work. The EM strategy coveres all operation modes, which includes normal, failure of one power generation channel, failure of both power generation channel, and emergencies with their associated states. Moreover, the conditions for transitions between states will also be explained in the next section.

As is clear in the figure, there is a reciprocal transition between the major scenarios, and the directions of the arrows illustrate this. The transition will occur between the main scenario firstly, and subsequently between the inside states. For example, if the system is

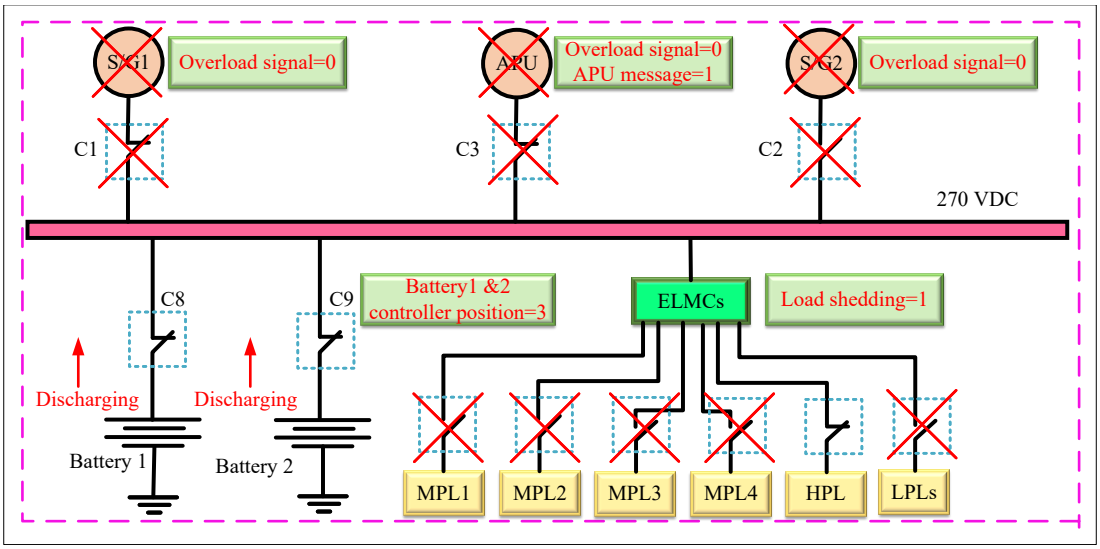

Fig. 8.14: ST12 illustration on simplified EPS

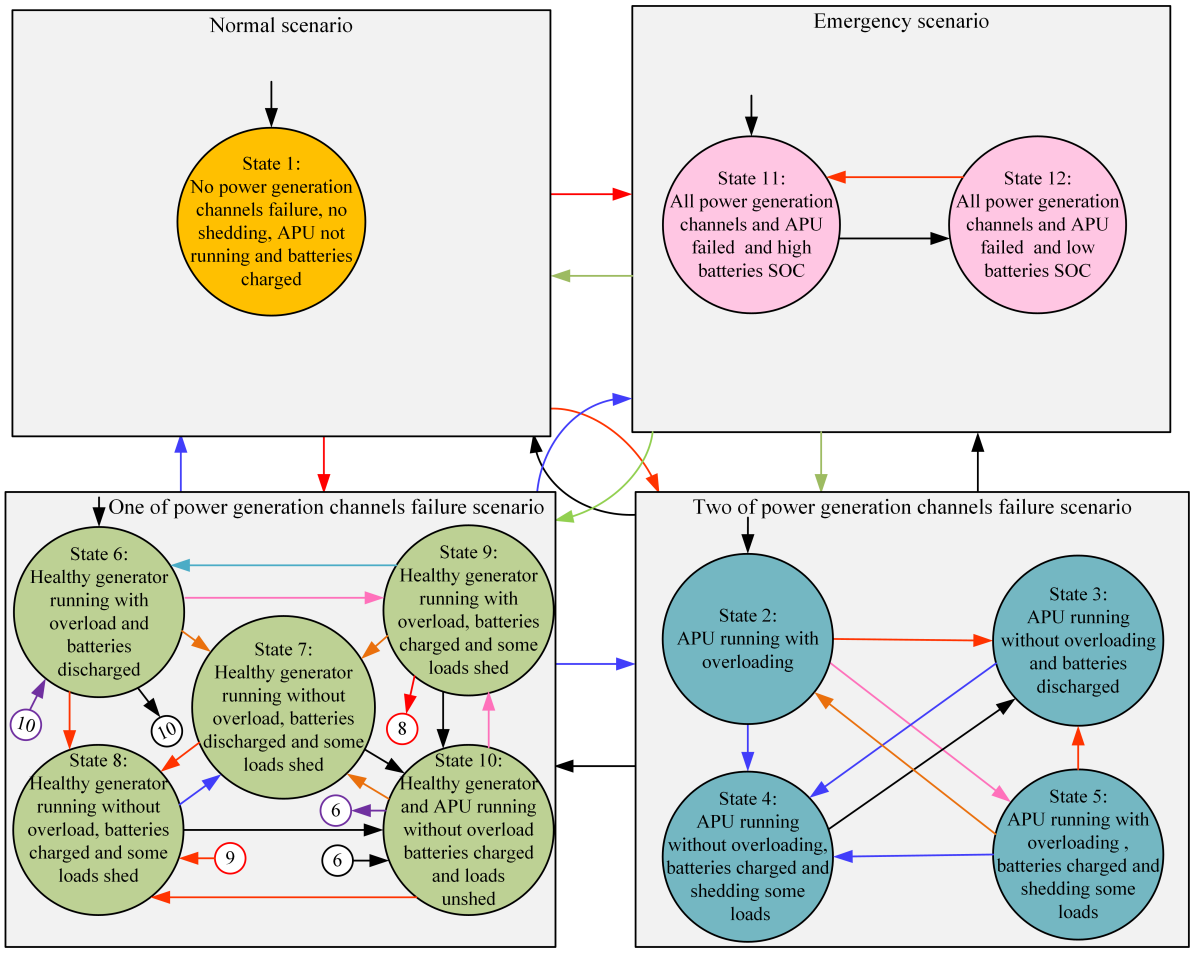

Fig. 8.15: Power distribution state diagram

operating in the normal scenario and both main generators and APU fail, the EM system will switch to the emergency scenario. There are two states in the emergency scenario,

ST11, and ST12, which are selected dependent on the SoC of the batteries. The same goes for the other direction. The EM system will return to normal operation once the fault has been cleared. However, if one of the main generators fails whilst the other was already unfaulty, the EM system will switch to the "one of the main generators failure scenario," and the EM system will start at ST6 and move from and to any state within this main scenario as shown by the directions of the arrows, depending on the specified conditions. However, if the other generator fails while the APU continues to operate, the EM system will switch to ST2 and begin with the scenario "both main generators fail while APU is running". The internal transition is carried out in the same manner as described earlier. While in this scenario if an APU fails, it will switch to the emergency scenario, and if one of the main generators' faults has been cleared, it will move to the scenario "one of the main generators fail".

8.2.6 State Transition

The conditions for transition between the different states (summarised in Table 8.2) are defined by the status of generators, APU overload, and SoC of batteries. Table 8.3 shows the status of the generator during different scenarios, e.g. if SG1 and SG2 status is normal, the EPS operates in ST1. Table 8.4 indicates the status of switches, load shedding signal, overload signal, APU message, and a reference voltage and power values sent to the controllers. The value 0 indicates the switch is off/open and the value 1 refers to the switch being closed. The battery controller switch has 4 control positions (1 to 4); DC power, battery terminal voltage, DC bus voltage, and halt, respectively [163]. The maximum charging power P_{charge} is chosen here to be 30 kW (corresponding to 5C) for each battery pack and the maximum discharge power $P_{discharge}$ to be 75 kW as each battery pack is designed to supply one part of the MPLs in the worst-case scenario (based on Table 3.1, the maximum of the MPLs is 328 kW and one part is 82 kW). The reference voltage for the battery cascaded voltage controller V_{dcn} is set to 270V.

In conclusion, the EPS states for the proposed EM strategy, and the implementation of the proposed EM method utilizing the FSM technique have been presented. The criteria for transitions between the distinct states were also described, based on the status of EPS variables such as generator status. The effectiveness of the proposed EM strategy will be

Table 8.2: Conditions for states transition for the different scenarios

Transition from	Condition	Transition to
Normal scenario (state 1)	Failure of two main generator	state2
Normal scenario (state 1)	Failure of one main generator	state 6
Normal scenario (state 1)	Failure of two main generator and APU	state 11
One of power generation channels failure scenario (any states)	Fault of power generation channels is cleared	state 1
One of power generation channels failure scenario (any states)	Other power generation channels are failed & APU is started	state 2
One of power generation channels failure scenario (any states)	Other power generation channels are failed & APU is failed/not started	state 11
Two of power generation channels failure scenario (any states)	Fault of power generation channels is cleared	state 1
Two of power generation channels failure scenario (any states)	One of power generation channels fault is cleared	state 6
Two of power generation channels failure scenario (any states)	APU is failed/not started	state 11
Emergency scenario (any states)	If both of power generation channels fault is cleared	state 1
Emergency scenario (any states)	If any one of power generation channels fault is cleared	state 6
Emergency scenario (any states)	If both of power generation channels failed and APU running	state 2
state 2, state 5	$APU_{OL} = 1$ & $SoC_{1,2} > SoC_{min}$	state 3
state 2, state 5, state 3	$APU_{OL} = 1$& $SoC_{1,2} < SoC_{min}$	state 4
state 2	$APU_{OL} = 1$ & $SoC_{1,2} < SoC_{min}$	state 5
state 4	$APU_{OL} = 1$& $SoC_{1,2} > SoC_{max}$	state 3
state 5	$APU_{OL} = 0$& $SoC_{1,2} > SoC_{max}$	state 2
state 6, state 9, and state 10	$SG_{OL} = 1$& $SoC_{1,2} > SoC_{min}$ & APU is not started	state 7
state 8	$SG_{OL} = 1$ & $SoC_{1,2} > SoC_{max}$ & APU is not started	state 7
state 6, state 7, state 9, and state 10	$SG_{OL} = 1$ & $SoC_{1,2} < SoC_{min}$ & APU is not started	state 8
state 6, state 10	$SG_{OL} = 0$& $SoC_{1,2} > SoC_{min}$	state 9
state 6, state 7, state 8, and state 9	$APU = 1$	state 10
state 10	APU is failed & $SG_{OL} = 0$ & $SoC_{1,2} > SoC_{min}$	state 6
state 9	APU is not running & $SG_{OL} = 0$ & $SoC_{1,2} > SoC_{max}$	state 6
state 11	All power generation channels are failed & $SoC_{1,2} > SoC_{min}$	state 12
state 12	All power generation channels are failed & $SoC_{1,2} < SoC_{min}$	state 11

Table 8.3: Status of generators, batteries SoC and overloading time during different scenarios

Scenario	Normal	Two of Power Generation channels failure				One of power generation channels failure					Emergency	
State	State 1	State 2	State 3	State 4	State 5	State 6	State 7	State 8	State 9	State 10	State 11	State 12
G1 status	N	F	F	F	F	F	N/F	N/F	N/F	N/F	F	F
G2 status	N	F	F	F	F	F	N/F	N/F	N/F	N/F	F	F
APU status	NR	N	N	N	N	NR/F	NR/F	NR/F	NR/F	N	F	F
State of charge	Do not care	$>SoC_{max}$	$>SoC_{min}$	$<SoC_{min}$	$<SoC_{min}$	$>SoC_{min}$	$>SoC_{min}$	$<SoC_{min}$	$<SoC_{min}$	Do not care	$<SoC_{min}$	$>SoC_{min}$
Overload period	Non	Not reached	Reached	Reached	Not reached	Not reached	Reached	Reached	Not reached	Non	Non	Non
	N= Normal, F= Failure, NR= Not running											

Table 8.4: System switches and variables settings

Scenario	Normal	Two of Power Generation channels failure				One of power generation channels failure					Emergency	
State	State 1	State 2	State 3	State 4	State 5	State 6	State 7	State 8	State 9	State 10	State 11	State 12
SSPC1 switch	1	0	0	0	0	0/1	0/1	0/1	0/1	0/1	0	0
SSPC2 switch	1	0	0	0	0	0/1	0/1	0/1	0/1	0/1	0	0
SSPC3 switch	0	1	1	1	1	0	0	0	0	1	0	0
SSPC8 switch	0/1	1	1	1	1	1	1	1	1	1	1	1
SSPC9 switch	0/1	1	1	1	1	1	1	1	1	1	1	1
Load shedding	0	1	1	1	1	0	1	1	1	0	1	1
Overload signal	0	1	0	0	1	1	0	0	1	0	0	0
APU message	0	0	0	0	0	1	1	1	1	0	1	1
Battery controller switch	1/2/4	1	1	1/2/4	1/2/4	1	1	1/2/4	1/2/4	1/2/4	3/4	3
Battery 1 reference power	$P_{chn}/0$	P_{dischn}	P_{dischn}	P_{chn}	P_{chn}	P_{dischn}	P_{dischn}	P_{chn}	P_{chn}	P_{chn}	0	0
Battery 2 reference power	$P_{chn}/0$	P_{dischn}	P_{dischn}	P_{chn}	P_{chn}	P_{dischn}	P_{dischn}	P_{chn}	P_{chn}	P_{chn}	0	0
Battery 1 reference voltage	V_{dcn}											
Battery 2 reference voltage	V_{dcn}											

verified in the following section.

8.3 Simulation Results

This section applies the EM strategy proposed in Section 8.2. The EM is responsible for supplying uninterruptible power to the HPLs under all circumstances by appropriately reconfiguring the EPS, utilising the batteries for powering medium priority loads when a shortage in generated power has occurred in addition to their usual functions.

The optimal droop gains design which was developed in Chapter 6 is used here as the power-sharing method between sources. This proposed power-sharing approach guarantees that the system losses under different EPS reconfigurations are minimized. The multifunction battery controller introduced in Chapter 5 is used to reschedule the charging and discharging of the batteries. The EPS shown in Fig. 8.1 is used for the verification study. The two main generators, the APU, and their corresponding converters are modelled as current sources and the average model of the battery converter is assumed

as shown in Appendix D. The batteries are used to start the APU and the remaining SoC of the battery pack is assumed to be 70 % after starting the APU. Different scenarios are considered i.e.

1. normal operation (no failures)
2. one power generation channel failure
3. both power generation channels failure

The droop gains design for the EPS with converters of different power ratings and different efficiencies is considered, as discussed in Chapter 6. The EPS parameters and ratings of converters are shown in Table 8.5. The total system losses using optimal droop gain design equation (6.30) and conventional droop gain design methods will be compared (6.41).

Table 8.5: Converters, transmission line data, and optimal droop gains values

	G1 Converter	G2 Converter	APU Converter	Battery 1	Battery 2
Rating (kW)	300	300	300	75	75
DC voltage (V)	270				
Rated current (A)	1112	1112	1112	278	278
efficiency (%)	98	95	97	97	95
Droop gain R_d	0.01214	0.01214	0.01214	0.0486	0.0486
Converter resistance R_{es} (Ω)	0.0042	0.0109	0.0064	0.0256	0.0435
No load losses (W)	918.38	2368.4	1391.4	347.9	592.1
Transmission losses (W)	0.0012	0.0012	0.0012	0.0049	0.0049

8.3.1 Normal Scenario

In this part of the study, a normal flight operation is investigated with scenario as given in Table 8.6. Fig. 8.16 and Fig. 8.17 show the simulation results for this scenario.

Table 8.6: Time and numbers of flight phases

Flight phase	Ground	Take off	Climb	Cruise	Descending	Loiter	Landing	Unit
Flight phase number	1	2	3	4	5	6	7	-
Time	t_1	t_2	t_3	t_4	t_5	t_6	t_7	-
Flight phase time	10	5	10	60	5	5	10	Minutes

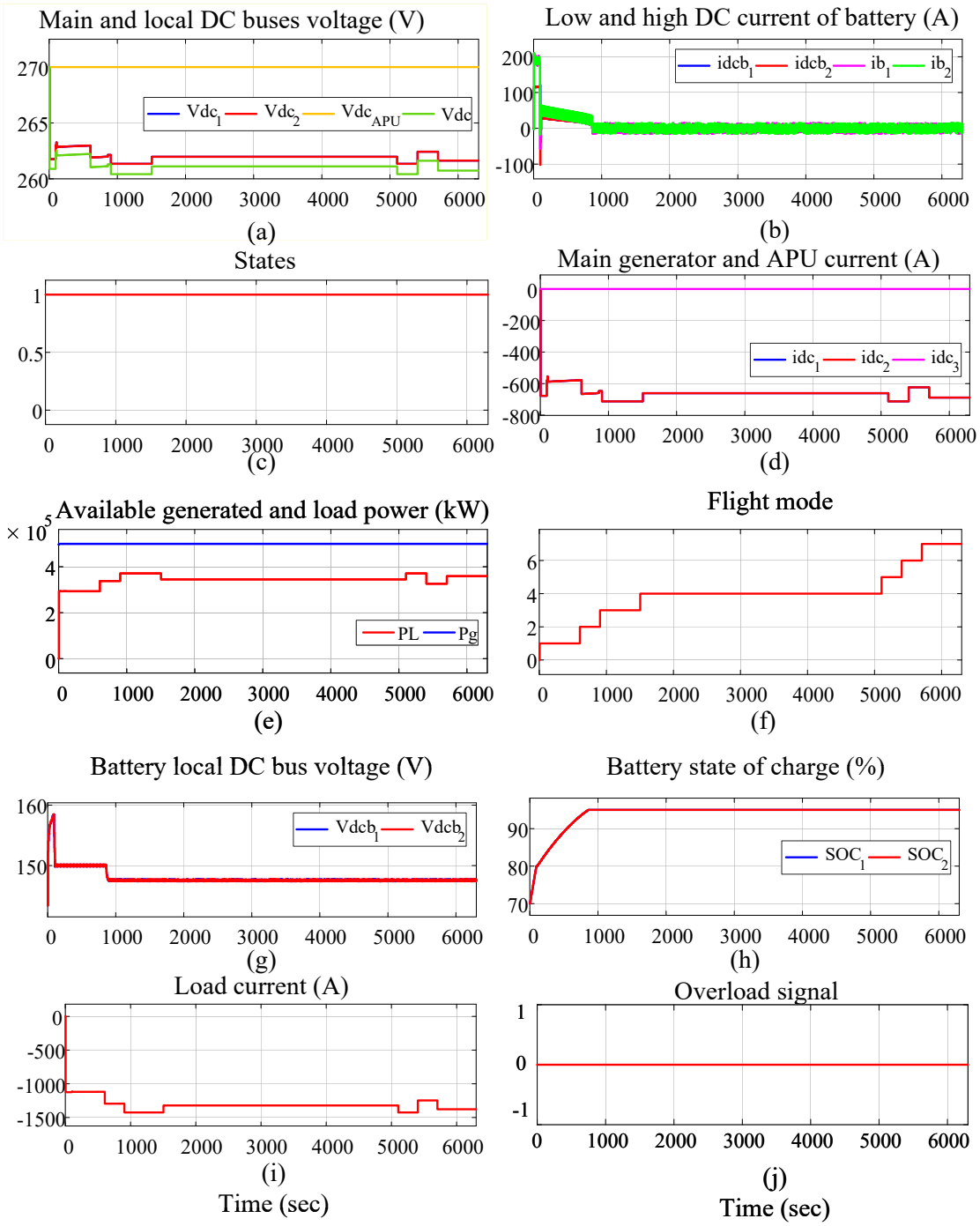

Fig. 8.16: Simulation results under normal flight scenario

In the beginning, the EMC sends the signals to the ELMCs to connect the ground loads during movement on the ground, e.g. taxiing, landing, towing, etc. Therefore, after starting the two main generators, they share the loads equally. If the *SoC* of the batteries is below (95%), then, the batteries are charged with constant current until

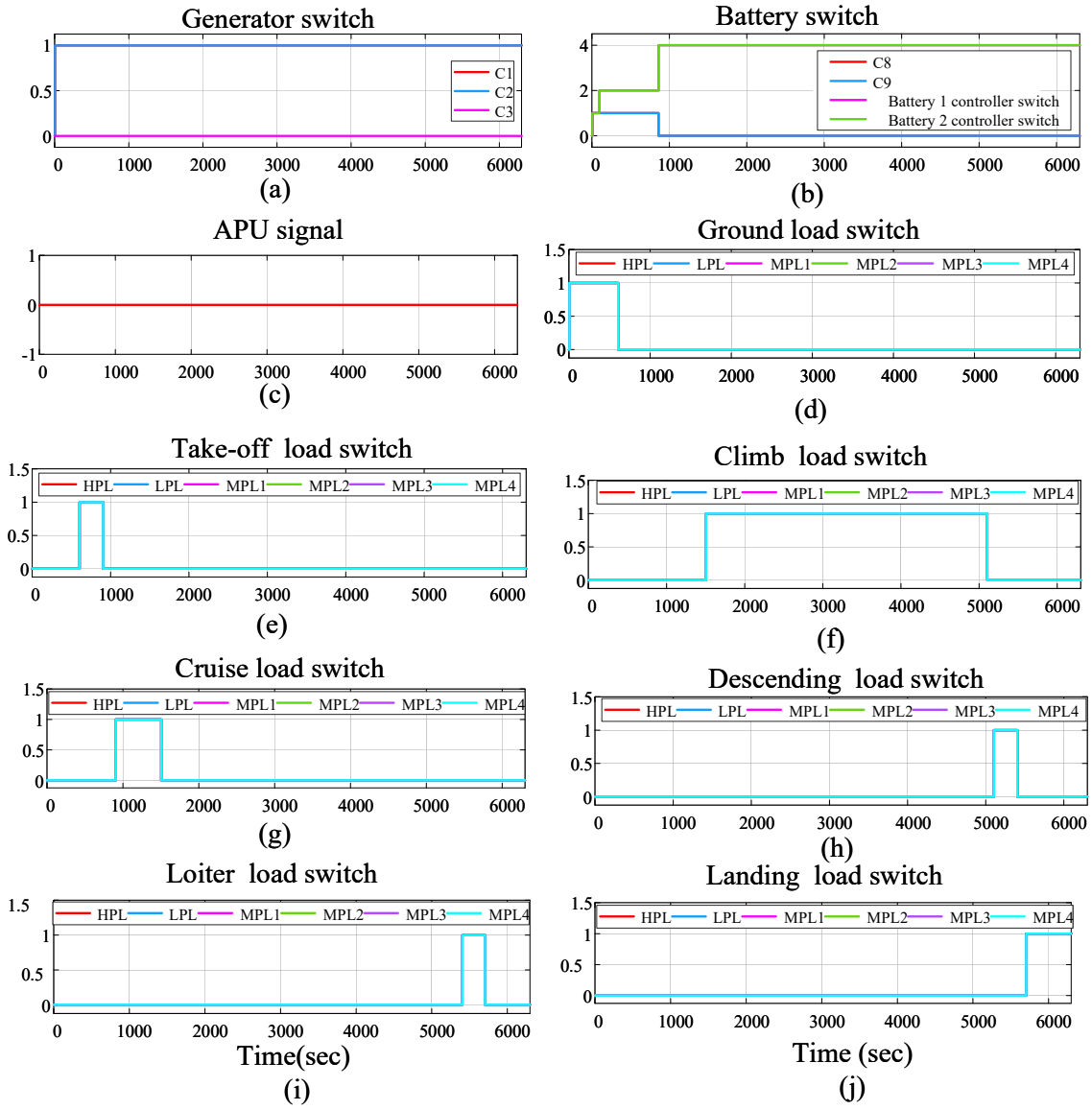

Fig. 8.17: Switching states, reference battery voltage, APU signal and overload signal under normal flight scenario

SoC_{max1}, which is assumed to be 80% in this study. The batteries continue charging up to SOC_{max} (95%) with constant voltage. The charging current of the battery according to the manufacturer's specifications, is limited by 20 A and the voltage is 148 V as shown in Fig. 8.16 (g). After SoC reaches 95%, the EMC stops the charging of the batteries. During the flight, the EMC sends signals to the ELMCs to manage the loads in each flight phase according to the corresponding time, as shown in Fig. 8.17. It should be noted that the DC bus voltage is kept within the limits of 250-280 V, according to MIL−STD−704F

[19] as evidenced by Fig. 8.16 (a).

Comparison between optimal (6.30) and conventional droop gains design for the power-sharing method between sources is also investigated. This comparison considers the total system losses including converters, transmission lines losses and battery losses (inductor and internal resistance) during the normal flight. It is clear from Fig. 8.18 that the proposed optimal droop gains design provides reduced energy losses in comparison to the conventional design. The total EPS energy losses under conventional droop control are 19.692 kWh while under the optimal one they are 17.366 kWh, i.e. they are reduced by 2.336 kWh (or 11.3%) during the flight.

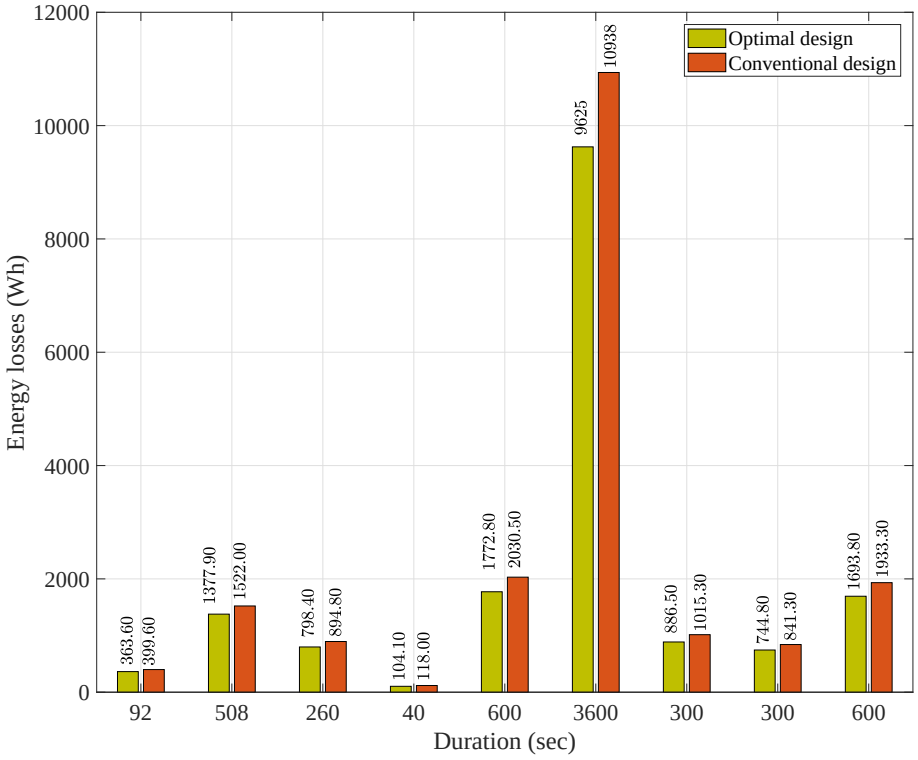

Fig. 8.18: Total system energy losses under normal scenario

8.3.2 One Power Generation Channel Fails and APU is Running/Fails case

The failure of the main generator 1 simulated covering STs 6, 7, 8, and 10. The simulation results are shown in Fig. 8.19 and Fig. 8.20. The flight started normally, as

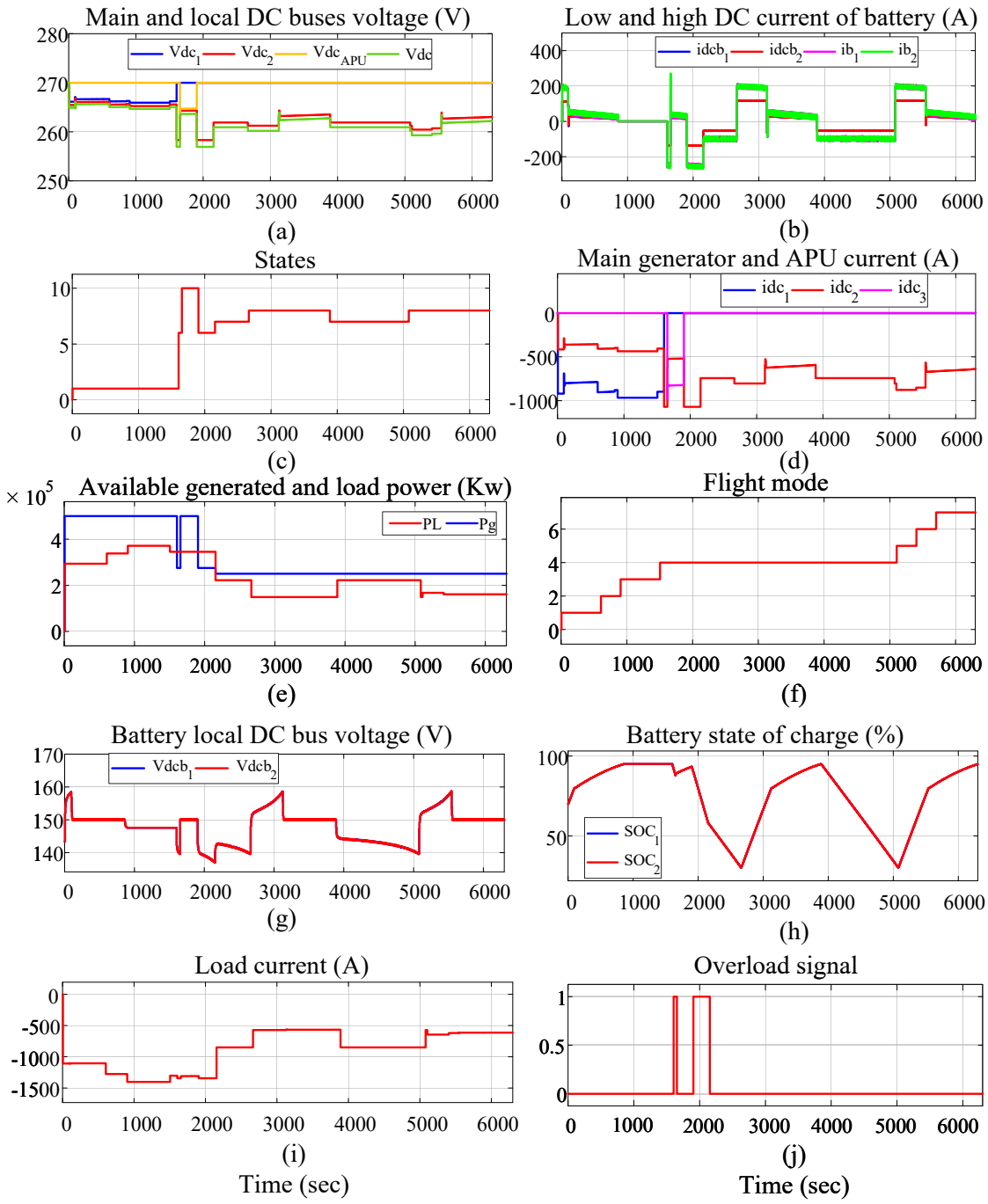

Fig. 8.19: Simulation results under one of power generation channel failure scenario

both main generators supplied the loads together, in addition to charging the batteries until these reach the maximum SoC value (95%). After reaching the maximum value, the charging stops. At t=1600s during the cruise, a fault in one of the main generators occurs. The EM responds to this fault by going into ST 6 directly. In this state, a signal is sent

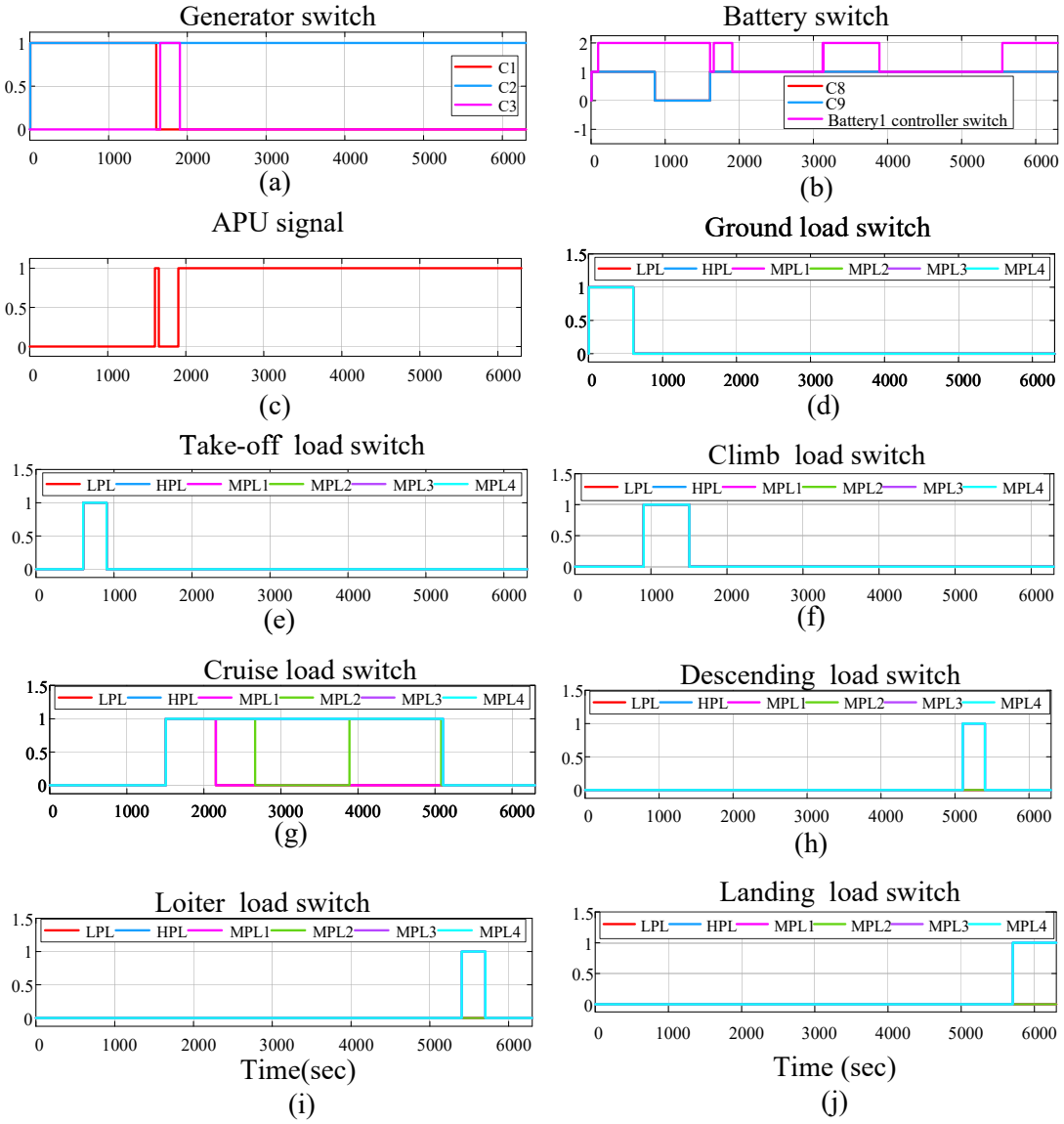

Fig. 8.20: Switching states, reference battery voltage, APU signal and overload signal under one of power generation channels failure scenario

to the backup generator to prepare to start and to share the loads, and the remaining healthy main generator is allowed to overload by 10%, and the battery to discharge. After 50s, the APU generator is ready to share the loads with the main generator. The overload of the main working generator is cleared, and the batteries are charging until they reach the maximum SoC values; this covers ST 10. At t=1900s a fault occurs in the APU generator, and in this case, the healthy main generator is allowed to overload again and the batteries are allowed to provide 70 kW of power (ST 6). As mentioned above,

the healthy generator is allowed to overload for a period of 300s (5 mins), at t=2200s this overload period expires, consequently the batteries need to supply the required power, gradually discharging until SoC drops to its minimum value (ST 7). At this point, the low priority loads are shed (ST 7). At t=2665s, the SoC reaches the minimum value (28%) for both batteries. Therefore, they will start charging after shedding LPLs and part1 and part two of MPLs (ST 8). At t=3920s, the $SoCs$ reach their maximum values and the EMC sends the signal to discharge the batteries (ST 7). Such a cycle of charging/discharging will continue until the end of the flight. It is clear from Fig. 8.19 (a) the main DC bus, local DC buses voltages are kept within the acceptable limits.

Fig. 8.21 shows the total system energy losses during the whole flight using conventional and optimal droop gains (6.30) design methods, and it is clear from this figure that the energy losses in the case of the conventional method are 21.094 kWh against 20.385 kWh in the case of the optimal design, a reduction of 709 Wh (4%) for the optimal design. Accordingly, the proposed method of optimal droop gain design gives fewer energy losses compare to the traditional method.

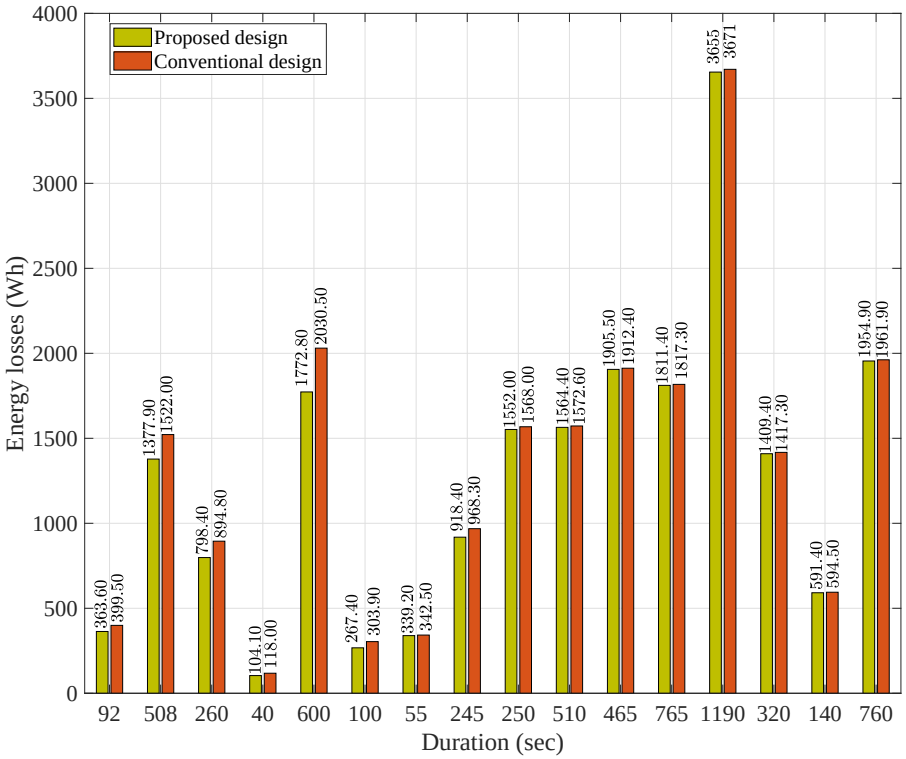

Fig. 8.21: Total system energy losses under one of power generation channel failure scenario

8.3.3 Both Power Generation Channels Fail and APU is Running/Fails case

The performance of the EPS under a failure of both main generators using conventional and optimal droop gains was evaluated as well. This scenario runs through STs 2, 3, 4, 5, 11, and 12. Fig. 8.22 and Fig. 8.23 show the simulation results. Initially, the aircraft flies normally (ST1) and at t=1600s during the cruise, the aircraft loses both main power generators simultaneously. According to the EM strategy the EMC commands to start APU. Until the APU started, the LPLs and MPLs are shed and the batteries are providing power supply to the HPLs, as the only offer for the pilot is to doing emergency landing (ST12).

The batteries' voltage controller is activated, replacing the batteries power control since it is critical to maintain the DC bus voltage at the correct level. After (100s from sending the command from the EMC,) the APU is ready to supply the loads, with overloading allowed, along with the batteries, and therefore all of the loads are unshed (ST2). The required total load power is 345 kW and the APU delivers 275 kW, therefore the batteries supply the difference, which is 70 kW. At t=1800s the APU also fails, so the EMC asks the ELMC to shed all of the loads apart from only MPL4 and the HPLs (ST12) which are supplied by the battery. When the SoC reaches its minimum value, MPL4 are also shed and only the HPLs are powered until the aircraft lands (ST11). It should be noted that the two battery systems are discharged with different currents because they have different optimal droop control gains, as shown in Fig. 8.22 (h).

At t=2700s the APU is back to work with the additional overload capability, so the available power is 275 kW. Therefore, the LPLs and MPL1 and MPL2 are unshed and the batteries start to recharged (ST5). The allowable overload period is ended at 2900s, and the EMC goes into ST3, at which point the batteries are supplying the deficit in power between the APU and the loads. Moreover, the LPLs and MPL1 and MPL2 are shed as shown in Fig. 8.23 (c). When the batteries are discharged below ($SoC < 28\%$), the EM moves to ST4, in which the LPLs, MPL1 and MPL2 are shed to allow the batteries to charge. At t=4430s the SoC of the batteries reaches the maximum value, therefore the system goes back into ST3. When the batteries SoC drops below their minimum values

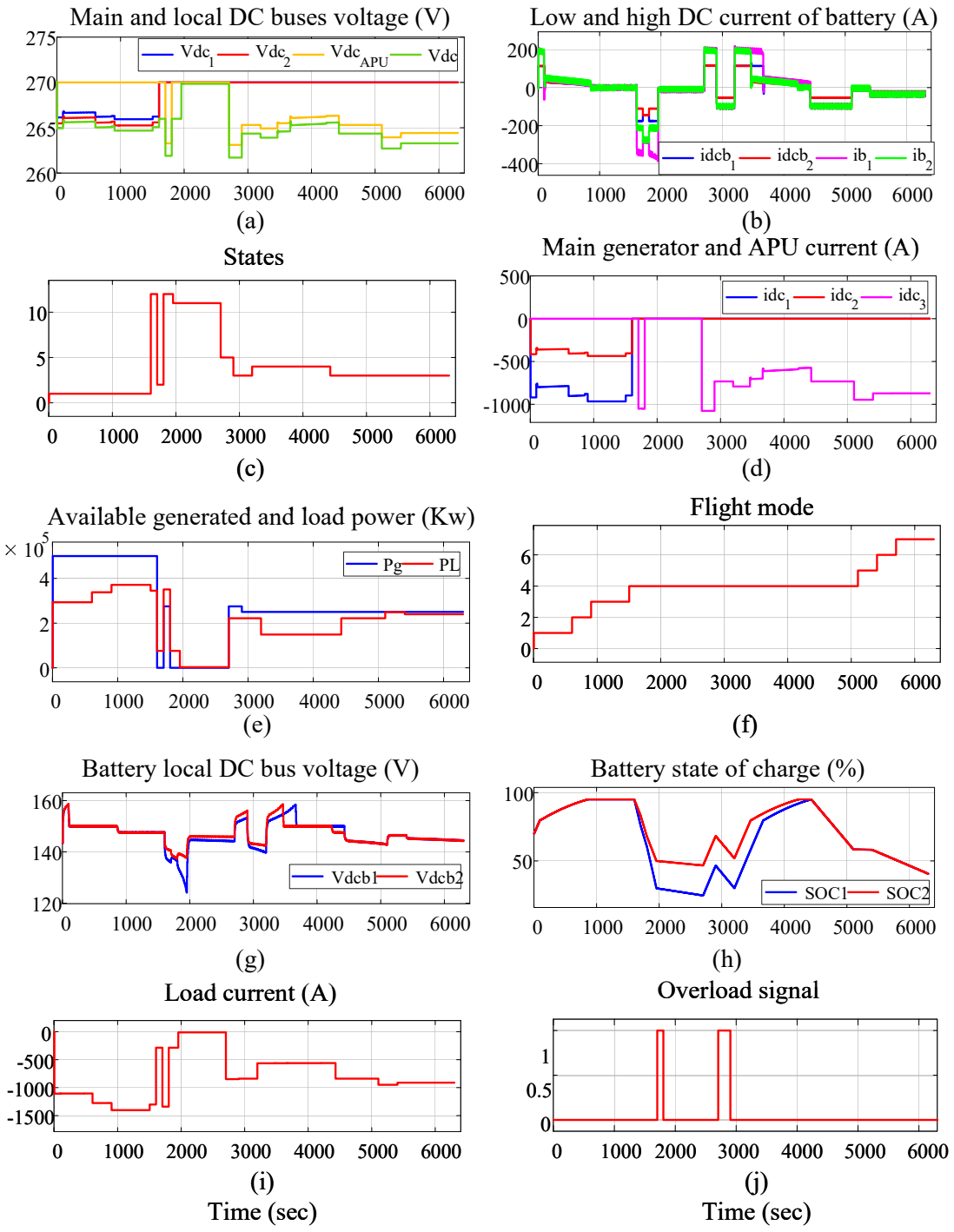

Fig. 8.22: Simulation results under both of power generation channel failure scenario

the EMC sheds the low and part one and part two of medium priority loads, and the batteries start to charge (ST4) again. It should be noted that the load current changes according to the loads for each flight phase, as shown in Fig. 8.22 (i). It is clear from the

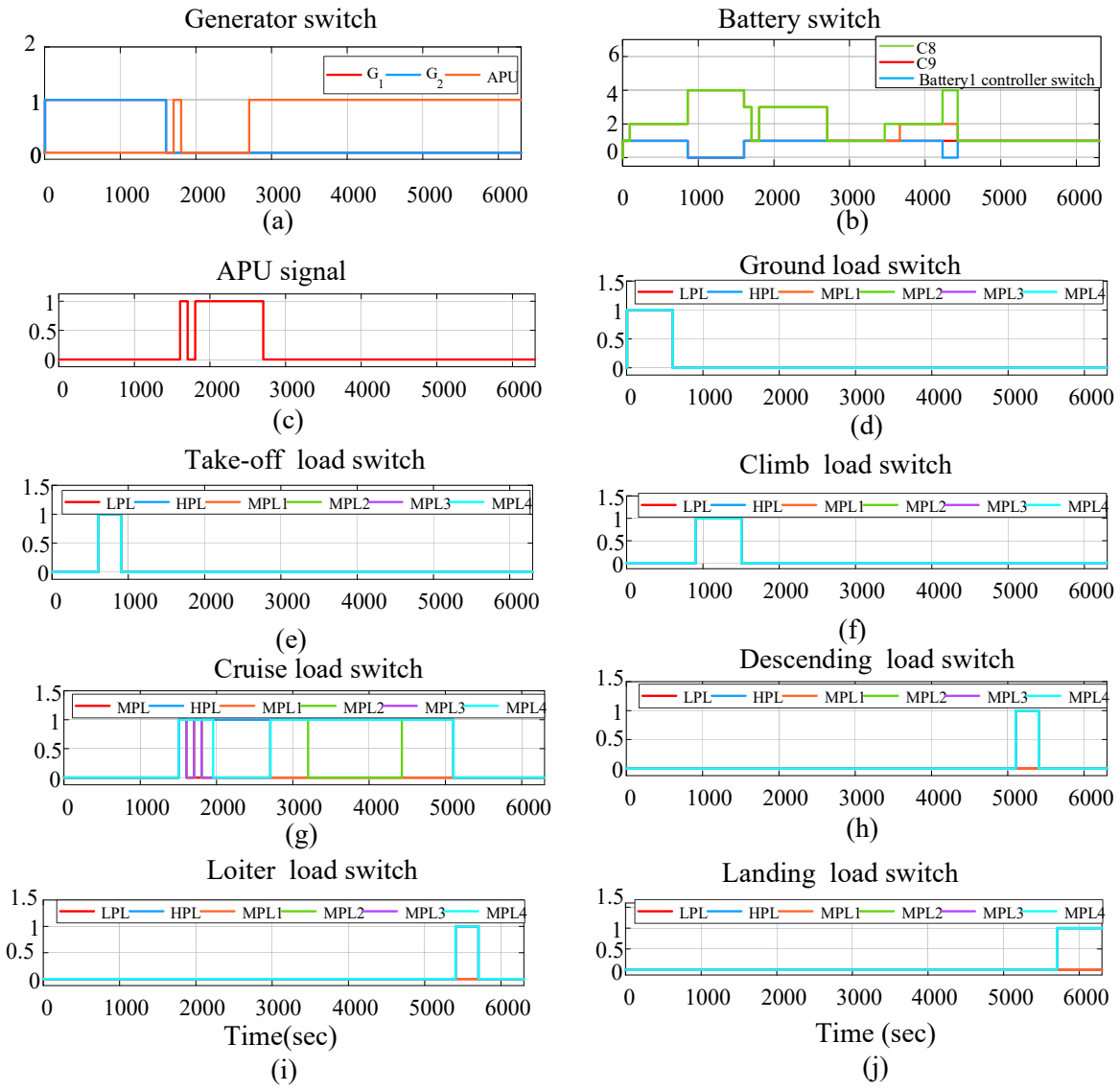

Fig. 8.23: Switching states, reference battery voltage, APU signal and overload signal under both of power generation channels failure scenario

results that the DC bus and local DC buses voltages are kept within the limits during the considered emergency case.

The total EPS energy losses using the conventional and the optimal droop gains design are calculated during each flight phase as shown in Fig. 8.24. These were 14.770 kWh for the conventional method but only 14.094 kWh for the optimal design method (6.30). This leads to a 676.6 Wh (3.4 %) reduction in energy losses in the studied scenario. It should be noted that the energy losses in some operation modes, i.e. ST3,

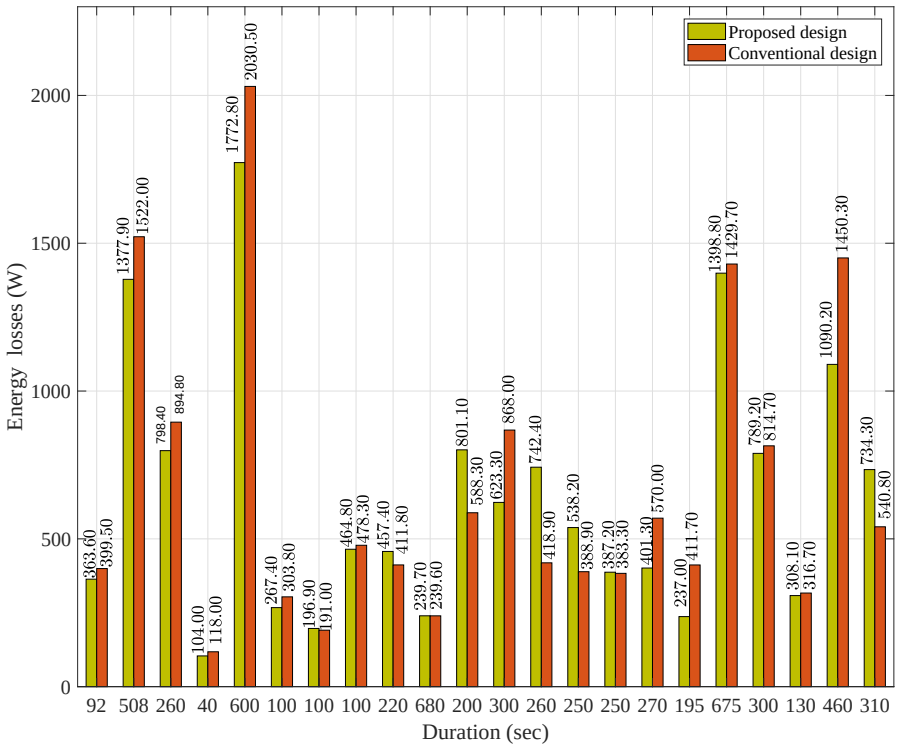

Fig. 8.24: Total system energy losses under both of power generation channel failure scenario

ST4, and ST11, using the optimal droop gains method are higher than the conventional method. This is because the batteries are charged/discharged with different power due to using different droop gains. The batteries are charged with constant power/voltage but they have different SoC, and this leads to the time of charging for batteries pack 1 being longer than pack 2 in the considered case. Moreover, the losses will be slightly higher than the conventional method as the battery packs are fully charged at the same time. However, in general, the total system losses when optimal droop gains are applied are smaller than with the conventional method if the whole flight is considered.

8.4 Conclusion on Chapter 8

In this chapter, a proposed intelligent EM strategy is presented to ensure that the HPLs will be continue to be supplied under different operating scenarios during the flight. The EM strategy takes into account the thermal capability of the power generation sources, the battery schedules, and variable load priorities for the representative EPS for future MEA. Furthermore, the proposed optimal droop gain presented in Chapter 6 to minimize the total system losses, used as a power-sharing method between sources, and the multi-function battery controller introduced in Chapter 5, are both used here. The control logic of the proposed strategy is implemented using a FSM, it is tested and verified using different operating scenarios for the complete flight, i.e. normal, loss of one of of the power generation channels, and loss of two of the power generation channels, using Matlab Simulink. The simulation results show that the proposed EM activates the correct state to always provide power for safety-critical loads for all fault conditions. Furthermore, it was confirmed that the proposed method reduces the total system energy losses in all studied cases compared to the conventional method, therefore the system efficiency is improved. By adopting the proposed EM strategy, the single DC bus architecture for MEA can be optimized.

Chapter 9

Conclusion and Future Work

9.1 Conclusion of this Research

MEA development trends are driven by a rise in fossil fuel prices and stricter environmental policies. Furthermore, advances in power electronics and fault-tolerant electrical machines are supporting this development. MEA developments improve weight, decrease drag as result of weight reduction, and fuel consumption of the aircraft, hence reducing the environmental impact of the aircraft. Other MEA benefits include increased reliability, easier prognostics and diagnostics, more flexibility, and lower overall costs. Among the potential advancements for the MEA concept, the promising single bus multiple sources with battery integration architecture with the aims of achieving improved fault tolerant proper/smart energy management and total system losses minimization is adopted in this study.

The thesis provides insight into the optimizing an EPS with single DC bus, multiple sources and battery integration, for the future MEA.

In Chapter 3, the pros and cons of the HVDC system for MEA were explored, as well as an overview of the chosen single bus-based topology. The power distribution system is divided into three levels: power generation, main power distribution, and secondary power distribution. In addition, each component's function was defined. A load analysis was performed to design the required generating capability and the number of power sources to ensure that power is delivered to all onboard loads. The loads were divided into three main categories based on their functions: LPL, MPL, and HPL. Following that, the main

component sizes were determined based on an examination of the load requirements and other criteria. The sizing of the main components of the under study EPS is essential for the validation of the proposed energy management strategy reported in Chapter 8 and for the proposed multifunction battery controller verification introduced in Chapter 5. During the flight, the main generator was designed to meet the highest continuous load requirements, with 33% additional power and 10% overload capacity for 5 minutes. As a result, it was determined that the main generator's capability should be 250 kW for the aircraft under study identified model. Regarding the APU capacity, choosing the same capacity for the APU as for the main generator was advised, for a more reliable EPS. When the generated power is insufficient, a battery storage system was designed to supply the emergency loads (HPLs), start the APU, and supply the MPL. A123's Nano phosphate lithium iron phosphate (LiFePO4) cell is considered, with a nominal battery stack voltage of 135 V. The battery system's maximum power output was found to be 75 kW for 5 minutes. Accordingly, each battery pack stores 6.765 kWh, resulting in a total weight of 62.32 kg when employing two battery packs.

In Chapter 4, a simple control technique for the starting mode, that aligned with the VVB control approach for the S/G system, is presented, allowing the S/G to operate in a wide speed range. The proposed control scheme uses a single current regulator to adjust the q-axis reference voltage and the d-axis voltage is calculated considering the maximum available voltage from the converter. The starter controller consists of a low speed controller to accelerate the machine up to the base speed and a high speed controller for operating above the base speed until self-sustaining engine speed is reached, then the VVB approach for generation mode is applied. A detailed analysis of the control strategy of the S/G is presented. It was discovered that the control plant for the starter mode has RHP zero, which limits the achievable high performance. As the loading and speed increase, the RHP zero slides closer to the origin. A solution to this problem was proposed, and its dynamic performance was tested and evaluated using MATLAB/Simulink. The control design process for the S/G power system was tested on a prototype experimental rig and the experimental setup was explained in detail. The controllers were adapted according to the specifications of the prototype and the key findings were reported. The simulation and experimental results show that the suggested control strategy can work at a

variety of speeds, in both starter and generator modes. Furthermore, the suggested control technique maximizes the utilization of DC bus voltage and increases machine efficiency. The proposed S/G system would be integrated with the overall EPS to perform its basic functions, e.g. starting the engine and supplying the onboard aircraft loads.

In Chapter 5, a novel battery control scheme was developed with the goal of addressing four concepts : battery current, battery voltage, DC power, and DC bus voltage control. In comparison to other battery types, the lithium-ion battery was chosen for this thesis because it offers superior properties such as high energy density and long life cycles. To represent the Lithium-ion battery, the modified Shepherd model is used, and its associated model parameters are found for the chosen battery. Due to its simplicity of implementation and maximum capacity utilisation, the CC-CV charging/discharging method is chosen. The cascaded control system configuration is selected to implement the CC-CV technique as it allows for sequential design and verification of each control loop and effectively limits the battery current controller by saturating the battery voltage controller. The controller's small-signal control plants were derived for the controller design process. To achieve high dynamic response, the controllers were designed and the values for the associated PI parameters were obtained. Similar to the findings in Chapter 4, non-minimum phase characteristics were shown to be inherent in both DC power and DC bus voltage plants, limiting the controllers ability to attain high performance. The control operation for each of the functionalities is demonstrated through simulations. In addition, the novel battery controller is integrated into the aircraft's overall EPS. This enables the investigation of control robustness under various flight conditions as well as of the EPS supervisor control approach. Using such a controller will guarantee that the critical loads remain powered in an emergency situation, by activating the DC bus voltage controller. Other functions, such as battery voltage control and DC power control, can also be fulfilled using the proposed EM method by activating their associated controllers.

In Chapter 6, a method for selecting optimal droop gains to reduce power losses in a single DC bus multiple-sources multiple-loads MG was proposed, taking into account converter and transmission line losses for various load types, such as CCL, CIL, and CPL. For the droop gain design optimization, a simple but sufficiently accurate converter power losses model was used. The following are the key findings of the analytical study

of optimal droop gains design for three different types of loads:

- Optimal droop gains can be calculated relying only on the knowledge of the equivalent series resistance of the converters for all types of loads.
- For all three types of loads, the optimal droop gain of the i^{th} converter is defined. It is shown that the minimum system losses can be achieved by choosing the optimal droop gains equal to their corresponding ESR.
- As the optimal droop gains increase, the variation in system losses depends on the type of load, i.e. for CCL the losses are constant, for CPL losses were increased and for CIL the losses were decreased.

There are numerous optimal droop gain solutions according to the proposed approach. Setting the droop gains equal to the corresponding equivalent series resistances of the feeding converters yields one set of optimal droop gains. This solution only needs to know the power losses model parameters of the local converter, and nothing about the transmission lines or other converters in the system. A streamlined dynamic model of the single DC bus multiple-sources multiple-loads microgrid, with the converters, was used to validate the proposed method of droop gains optimization. A small scaled lab rig prototype was used to conduct experimental testing to prove the proposed design process. The validation results showed the optimal design approach effectiveness in decreasing overall system power losses and improving voltage regulation of the single DC bus multiple-sources multiple-loads MG system, as predicted. To enhance the EM strategy of the overall EPS system provided in Chapter 8, the proposed optimal droop gain design methodology will be implemented as a power-sharing method between the multiple sources.

In Chapter 7, the design of optimal droop gain for system losses minimization, improved voltage regulation, and current sharing among power converters was developed, using an ANN-based technique. The training data for the ANN was created by running a loop simulation of the MEA EPS circuit with various droop gain combinations within a set design range. After training, the ANN can quickly and accurately predict the best droop gain combinations for any user-defined minimal system losses, voltage regulation,

and current sharing within the design space. The proposed solution places no additional strain on the system to perform this calculation, as it simply requires measuring the load current in order to calculate the ANN inputs. Furthermore, the associated optimal droop gain for any ANN inputs may be derived directly for the provided user-defined preferences by incorporating the trained ANN into the controller for each source. The proposed ANN method was tested using a time domain simulation with various tests in a case study. The tests addressed all aspects of the trade-off between the various optimal objectives, such as when current sharing, losses minimization or voltage regulation are given higher emphasis in the optimization.

In Chapter 8, a proposed intelligent EM strategy to ensure that the HPLs will be supplied under different operating scenarios during flight for the representative EPS for future MEA is presented. The EM strategy takes into account overload thermal capabilities of power generation sources, battery scheduling, and changing load priority. FSM was used to implement the proposed strategy's control logic and, it was tested and verified using Matlab/Simulink for a relevant whole flight mission, including normal operations, loss of one of the power generation channels, and loss of two of the power generation channels. According to the simulation results, the proposed EM always activates the correct state to provide power to safety-critical loads under all fault scenarios. Likewise, it was confirmed that the proposed method reduces overall system losses in all analysed scenarios when compared to the conventional way. Finally, the single DC bus architecture for MEA can be optimised by employing the proposed EM technique.

9.2 Future Work

This research project has addressed several research subjects in the field of energy management, S/G control, and control of power electronic converter interfaced EPS. The achieved results met all key technical requirements and the research generated multiple possibilities for follow-on studies. The following bullet points outline potential future work that could be expanded from the research presented in this thesis:

- Batteries are an essential component in the performance and safety of MEA. Accurately estimating SoC and State of Health (SoH) is crucial to keep the

Lithium-ion batteries to work in a safe state and to maximize their performance. Due to the battery being an electrochemical system, estimating its states is difficult as it has significant non-linearity and time-varying features. A developed online/offline SoC and SoH estimation technology could be investigated with the proposed multifunction controller presented in Chapter 4.

- In multiple spool generation, e.g. where HP and LP engine shafts are used to drive an electrical generators to exploit the engine power to supply ever-growing demand for more onboard electric power. The main challenge rising from using HP and LP spools is the effect of the wider speed range variation of the LP shaft in generation mode whereas the full power($N1_{max}$) to idle ($N1_{min}$) ratio can be more than 6:1. As a result, more research into the engine interface with the S/G system is needed.

- For optimal droop gain design in this study, only the converter and transmission line losses are considered for the analysis. A generalized loss model including the engine, generator, converters, battery and transmission line can be developed for possible load types and the analytical design and optimisation of droop gain can be investigated. Moreover, the switching losses ($P_{losses} = A+bI+CI^2$) can be included to give more comprehensive model for losses.

- Including into consideration the thermal and safety management of the battery, the system will be more complex and the energy management problem can be formulated as a convex optimization problem to meet the given objectives. Therefore, a neural network-based machine learning algorithm could be investigated to solve multi-objective energy management problems. The neural network could be trained using convex optimization outputs, and the trained neural network model would solve the convex optimization problem, according to simulation findings.

The abovementioned ideas could be interesting for the future studies and could lead to further improvements of the MEA electrical power system.

Chapter 10

Appendices

Appendix A

Inverse dqTransformation Convention

The three phase to dq frame transformation for field oriented vector control was explained in Section 4.2. The dq frame can be transformed back into three phase frame using the inverse dq transformation shown as:

$$\begin{bmatrix} x_a \\ x_b \\ x_c \end{bmatrix} = k_{abc} \begin{bmatrix} x_d \\ x_q \end{bmatrix} \tag{A.1}$$

where the inverse dq transformation coefficient, k_{abc}, is defined as:

$$k_{abc} = \begin{bmatrix} \cos(\theta) & -\sin(\theta) \\ \cos(\theta - \frac{2\Pi}{3}) & -\sin(\theta - \frac{2\Pi}{3}) \\ \cos(\theta + \frac{2\Pi}{3}) & -\sin(\theta + \frac{2\Pi}{3}) \end{bmatrix} \tag{A.2}$$

Appendix B

Linearisation approach

The following subsections show the coefficients of the linearised transfer functions that were large to be fitted with the core thesis content.

B.1 Battery Current controller

$$a_1 = R_b C_b C_{dcb} L_g V_{dcb}$$
$$a_2 = R_b R_g C_b C_{dcb} V_{dcb} + L_g C_{dcb} V_{dcb} - R_b C_b L_g D_1 I_L$$
$$a_3 = R_b C_b V_{dcb} + R_g C_{dcb} V_{dcb} - R_b R_g C_b D_1 I_L - L_g D_1 I_L$$
$$a_4 = V_{dcb} - R_g D_1 I_L$$
$$b_1 = R_b C_b C_{dcb} L_g L$$
$$b_2 = R_b R_g C_b C_{dcb} L + C_{dcb} L_g L + R_b R_L C_b C_{dcb} L_g$$
$$b_3 = R_b C_b L_g D_1^2 + R_b C_{dcb} L_g + R_b C_b L + R_g C_{dcb} L + R_b R_L R_g C_b C_{dcb} + R_L C_{dcb} L_g$$
$$b_4 = R_b R_g C_b D_1^2 + L_g D_1^2 + R_b R_g C_{dcb} + L + R_b R_L C_b + R_L R_g C_{dcb}$$
$$b_5 = R_g D_1^2 + R_L + R_b$$

B.2 Battery Voltage controller

$$c_1 = R_b C_b L L_g I_L$$
$$c_2 = R_b R_L C_b L_g I_L + L_g L I_L + R_b C_b L_g V_{dcb} D_1 + R_b R_g C_b L I_L$$
$$c_3 = R_L L_g I_L + L_g V_{dcb} D_1 + R_b L_g I_L + R_b R_L R_g C_b I_L + R_g L I_L + R_b R_g C_b V_{dcb} D_1$$
$$c_4 = R_L R_g I_L + R_g V_{dcb} D_1 + R_b R_g I_L$$

B.3 DC Bus Voltage controller

$$d_1 = R_b C_b L_I dcb$$
$$d_2 = R_b R_L C_b I_{dcb} + R_b C_b D_1^2 V_{dcb} + L I_{dcb}$$
$$d_3 = D_1^2 V_{dcb} + R_L I_{dcb} + R_b I_{dcb}$$
$$e_1 = R_b C_b D_1$$
$$e_2 = D_1$$

B.4 q-axis Current Controller (W_{cq})

$$a_0 = sign\left(v_{desti}\right) k_{pq} L_d$$
$$a_1 = sign\left(v_{desti}\right)\left(R_s k_{pq} + \frac{v_q^o}{v_d^o}\omega_{eo} L_d k_{pq} + L_d k_{iq}\right)$$
$$a_2 = sign\left(v_{desti}\right)\left(R_s k_{iq} + \frac{v_q^o}{v_d^o}\omega_{eo} L_d k_{iq}\right)$$
$$b_0 = L_q L_d$$
$$b_1 = R_s\left(L_d + L_q\right) + sign k_{pq} L_d$$
$$b_2 = R_s^2 + \omega_{eo}^2 L_d L_q + sign\left(v_{desti}\right)\left(R_s k_{pq} + \frac{v_q^o}{v_d^o}\omega_{eo} L_d k_{pq} + L_d k_{iq}\right)$$
$$b_3 = sign\left(v_{desti}\right)\left(R_s k_{iq} + \frac{v_q^o}{v_d^o}\omega_{eo} L_d k_{iq}\right)$$

B.5 Optimal Droop Gains for Constant Power Load Case

$$\begin{aligned} b =& (R_{c1} + R_{es1}) 4 R_{c1}^2 (R_{ci} + R_{esi}) (\frac{P_{CPL}}{n})^2 + 8 R_{c1} R_{d1-opt} (R_{ci} + R_{esi}) (\frac{P_{CPL}}{n})^2 \\ &+ 4 (R_{ci} + R_{esi}) R_{d1-opt}^2 (\frac{P_{CPL}}{n})^2 + 4 R_{c1} (\frac{P_{CPL}}{n}) (R_{ci} + R_{esi}) (V_o - I_1 (R_{d1-opt} + R_{c1}))^2 \\ &+ 4 R_{d1-opt} (\frac{P_{CPL}}{n}) (R_{ci} + R_{esi}) (V_o - I_1 (R_{d1-opt} + R_{c1}))^2 \\ &+ (R_{c1} + R_{es1}) (V_o - I_1 (R_{d1-opt} + R_{c1}))^4 \end{aligned}$$

Appendix C

Experimental setup

In this Section, the experimental rigs developed for the verification tests will be described. Two scaled different rigs are used to validate the finding in Chapter 4 and Chapter 6. The scaled model will allow for more extended tests including advanced concepts and future ideas that are deemed too risky to be performed on the actual S/G system and optimal power-sharing techniques.

C.1 Experimental setup for S/G system

The experimental rig's block diagram is shown in Fig. C.1. In comparison to the investigated S/G power system, an IM takes the place of the aircraft engine. The IM is equipped with a dedicated AC drive that regulates the machine's speed and torque. Depending on the starter or generator operation, the IM can be employed to apply load torque or drive the PMM. A PMM powered by two level converter represents the S/G and it is controlled by an AC drive controller. To apply the intended control scheme and control the PMM, a Digital Signal Processor (DSP) is used. Current and voltage sensors are used to measure i_{abc}, E_{dc}, and i_{dc} and provide these data to a Field Programmable Gate Array (FPGA). An encoder interface board is used to provide information about the PMM rotor position. The FPGA sends the output switching signals to the AFE converter. A HPI capture card is used to sends the measured and calculated variables to a computer. This card allows for bidirectional communication, and extra commands from the computer can be delivered through Matlab ®. The overall prototype setup is shown

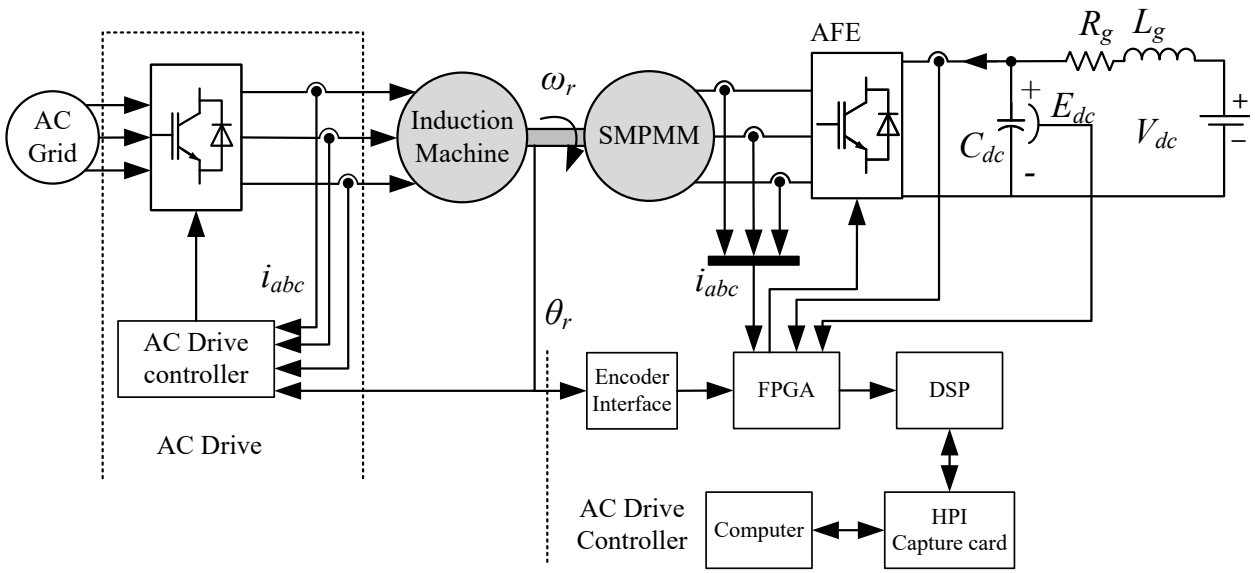

Fig. C.1: Layout diagram for the experimental rig of S/G system.

in Fig. 4.16 in the Aerospace Technology Centre at the University of Nottingham. The rig consists of two subsystems connected mechanically through the shared shaft. The first subsystem is the AC drive and involves the PMM, the two-level AFE, and the associated control equipment. While the other subsystem is an IM drive system, which comprises of an IM machine and its drive. Although the information on the shared shaft speed is shared, both of these subsystems are operated individually. A detailed descriptions of each prototype subsystem will be discuss in the following subsections.

C.1.1 AC Drive System (PMM Side)

The AC drive system, which emulates the S/G system, is the most important component of the test bench. The AC drive controller is used to apply the designed control schemes to this drive system. Fig. C.2 depicts the surface-mounted permanent magnet synchronous AC servomotor that was used in this study. It was manufactured by Parker (S/N ME14525155192I64A12 [164]). Table C.1 contains the required machine parameters. It's a eight-pole (four-pole pair) machine with a maximum speed of 4.5 krpm and a rated speed of 2.5 krpm (262 rad/sec). The nominal power output is 3.17 kW, with a rated torque of 13.6 N.m (from 12.5 A rated current). The machine contains a built-in encoder OIH 48 series (S/N TS5212N2508) for measuring rotor angle and a hall

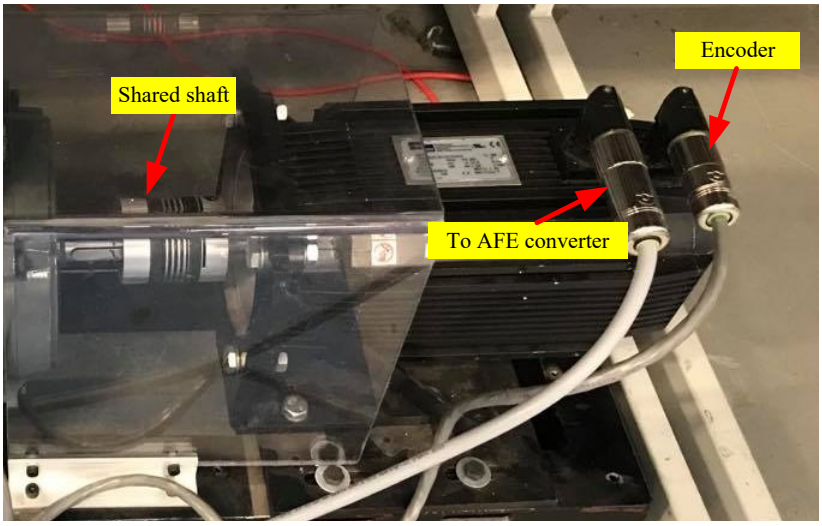

Fig. C.2: Parker ME series PMM.

effect sensor for machine start-up if needed. A SEMIKUBE power stack is used in the system [152]. It combines the circuits for sensing current via external current sensors, heat sink temperature via an external temperature sensor, and DC-link voltage via an external voltage sensor. The driver board also includes protection against overcurrent and overheating. Fig. C.3 depicts the IGBT power stack (SEMIKUBE), the entire bridge IGBT module (SKM400GB12E4) and the IGBT driver board. The interface board is used to make the connection between the SEMIKUBE and the control platform as shown in Fig. C.4. This receives the sensor signal from the SEMIKUBE, sends the corresponding

Table C.1: Experimental rig PMM parameters

Parameter	Value
Rated line voltage	230 $Vrms$
Machine stator resistance, R_s	0.30 Ω
Machine d-axis inductance, L_d	7.5 mH
Machine d-axis inductance, L_q	7.5 mH
Machine mutual flux, ϕ_m	0.158 Vs
Combined AC and DC machine inertia, J	0.0016 kgm^2
Viscous damping, B	0.00024 Nms
Mechanical friction, f_c	0.453 Nm

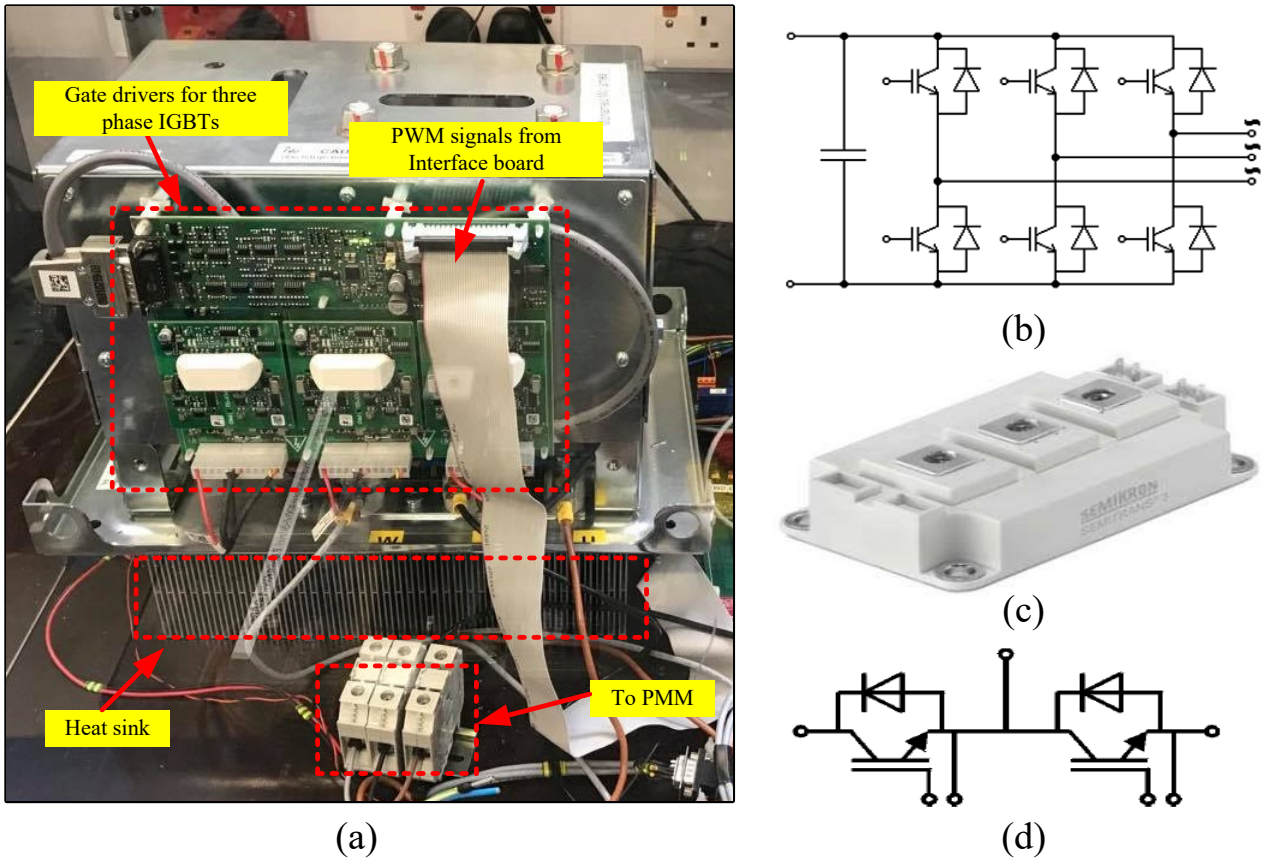

Fig. C.3: SEMIKUBE power stack. (a) Prototype. (b) Schematic. (c) IGBT modules prototype. (d) IGBT modules schematic.

conditioning sensor signals to the DSP/FPGA, and then delivers the PWM signals from the DSP/FPGA to the converter. The control platform comprises of a TIDSK 6713 board, an Actel FPGA ProAsic3 A3P400 board, and an HPI daughter card, as shown in Fig. C.5. Texas Instruments' C6713 DSK (DSP Starter Kit) is a development board based on the TMS320C6713 floating-point DSP. The FPGA board is equipped with ten 12-bit A/D channels, a 50 MHz clock, and ten fibre optic outputs. The DSK board and the FPGA card communicate via the DSK 80-pin EMIF connectors, which provide access to the DSP data and address buses, power supply, reading/writing control signals, timers, clocks, and interrupts to a daughter card. The three phase current and DC bus voltage, as well as the DC link current, are measured using the sensor board illustrated in Fig. C.6. The voltage and current measurements are made with the voltage transducer LEM LV 25-P [165] and the current transducer LA 55-P [166]. The voltage transducer LV25-P has a measurement

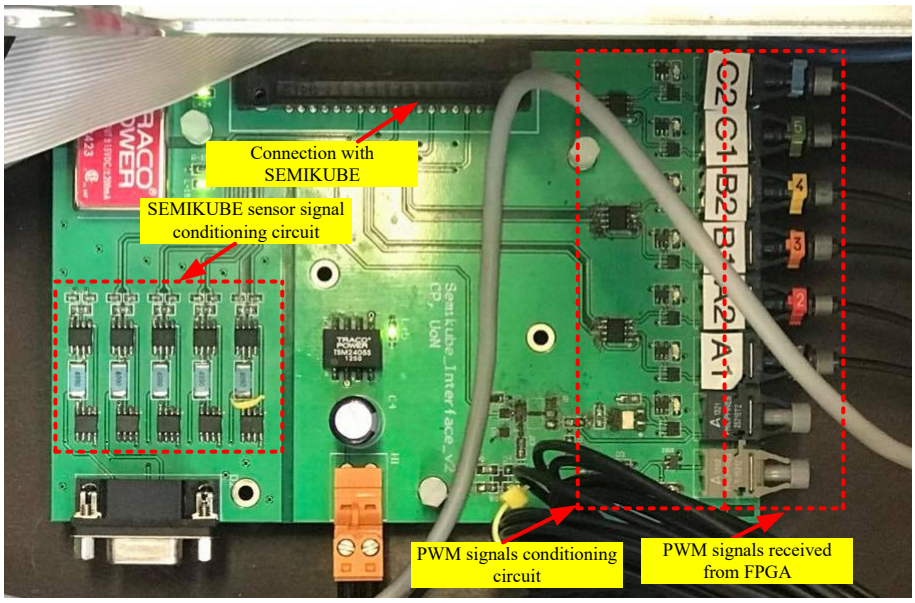

Fig. C.4: The interface board.

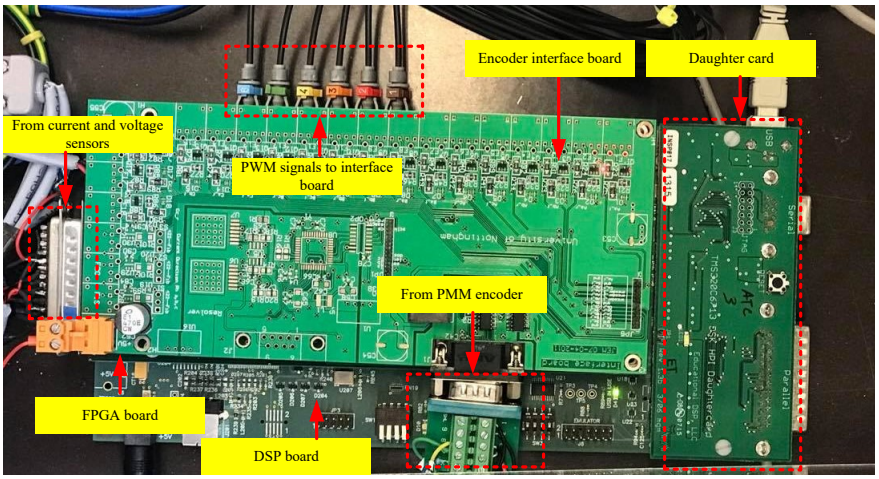

Fig. C.5: Control platform.

range of 10V to 500V, while the current transducer LA 55-P has a measurement range of -70A to 70A.

C.1.2 AC Drive System (IM Side)

The AC drive system's primary role in starter mode is to supply a load torque to the PMM. In generator mode, the PMM must be driven at a constant speed by the AC drive. As shown in Fig. C.7, a VASCAT induction machine (MOTOR MAC R 112.140) is chosen for this task. It's a four-pole machine with a maximum speed of 5 krpm [167] and a 4

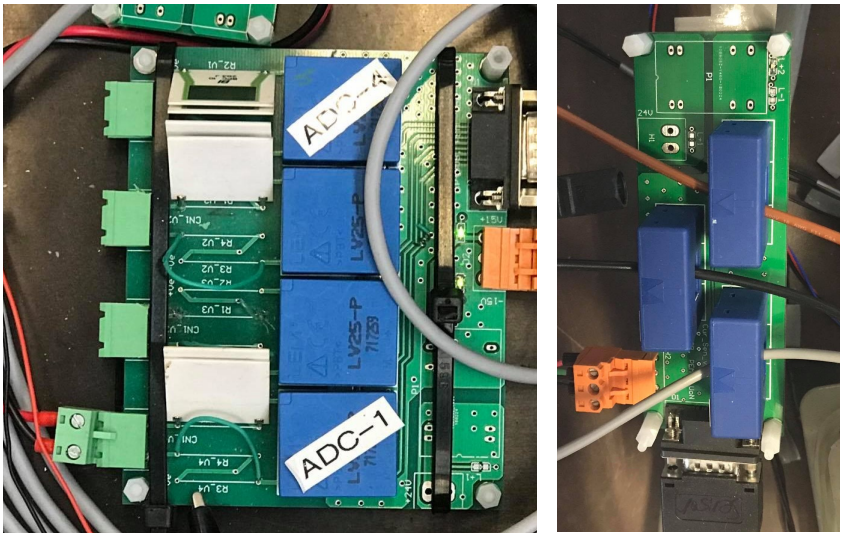

(a) (b)

Fig. C.6: Sensor board. (a) Voltage sensor. (b) Current sensor

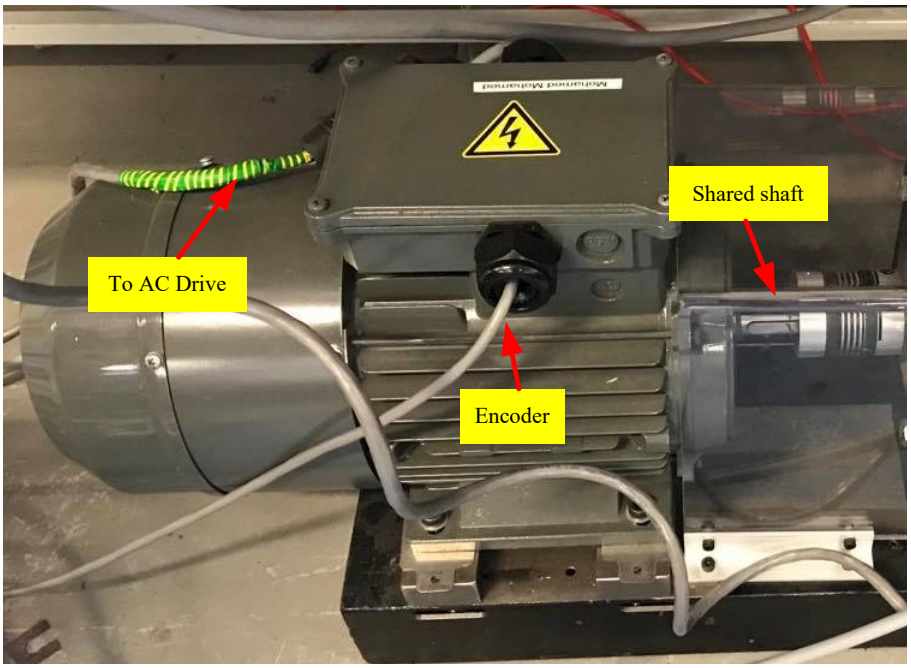

Fig. C.7: VASCAT induction machine

kW rating. Table C.2 contains more information regarding the induction machine. The induction machine was chosen with these specifications in order to drive the PMM up to and beyond its nominal speed (2500 rpm) and power (3.17kW) ratings. The induction machine has a built in incremental encoder to detect the rotor position and send it to the drive [168]. The AC drive (Mitsubishi-Regenerative-FR-A741 [169]) is chosen to

Table C.2: Induction machine parameters

	Service S1						Service S6-40%						
Connection	Nm	A	kW	rpm	Hz	Constant power speed (rpm)	Nm	A	kW	rpm	Hz	Constant power speed (rpm)	No load current
Y	5.0	1.8	0.76	1450	50	2820	7.3	2.3	1.11	1450	51	2120	1.1
D	5.0	3.1	1.35	2560	87	4990	7.3	4	1.95	2560	88	3760	2

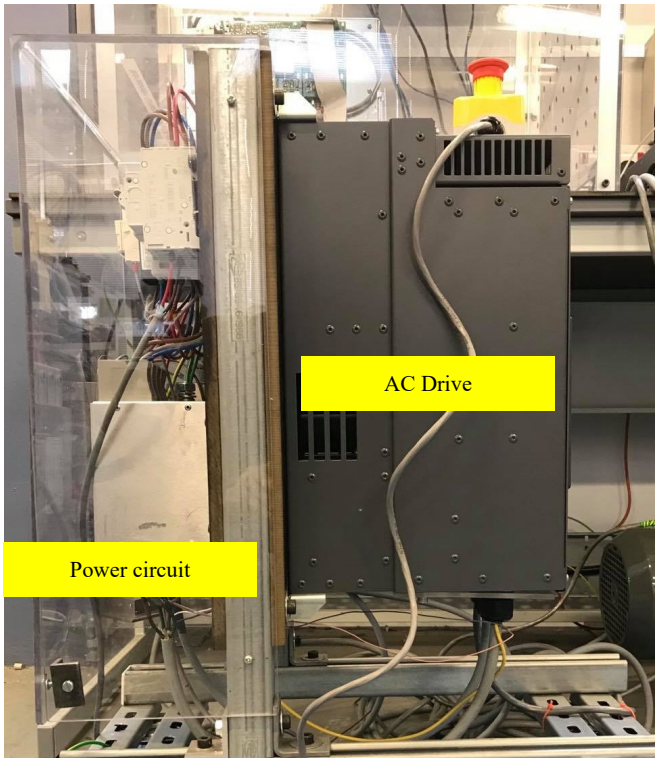

Fig. C.8: Mitsubishi AC drive with protection circuit

control the IM, as shown in Fig. C.8. It can operates in sensorless vector control or full closed-loop flux vector control (with optional encoder feedback card). Data for feedback control is provided via built-in sensors. The controller can be modified using the AC drive's built-in LCD interface. The AC drive can also be linked to a computer and the controller accessed via a software interface. The AC drive is protected from current surges and voltage spikes using fuses and contactors. The protective circuit is based on the drive's suggested schematic. The induction machine's speed control can be used to set the required speed reference value for motoring and generator modes.

C.2 Experimental setup for optimal droop gains design

Fig. C.9 depicts a block diagram of the lab prototype that was used to facilitate the investigation and verification of the important findings of Chapter 6. To simulate the first source, an autotransformer with the primary side connected to the utility grid is employed. As a result, the source 1 voltage frequency is the same as the utility grid's voltage frequency, which is 50Hz. To simulate the second source, a Chroma QuadTech 31120 programmable AC source with three phase inductors is utilised, with a voltage frequency of 50Hz. The digital control platform is the TMDSCNCD28379D control card as shown in Fig. C.10 [170]. The DC bus is coupled to a resistive load bank and an APM electronic load (E-load), which serve as CIL and CPL, respectively. Table C.3 lists some more system parameters. The voltage and current sensors used in this rig are the same sensors used in S/G lab prototype as shown in Fig. C.6. The converters (SEMIKUBE) and their corresponding interface boards are discussed in section B.1.1. Fig. C.11 shows the Chroma Quad Tech AC 31120 model which has a maximum power output of 12KVA,

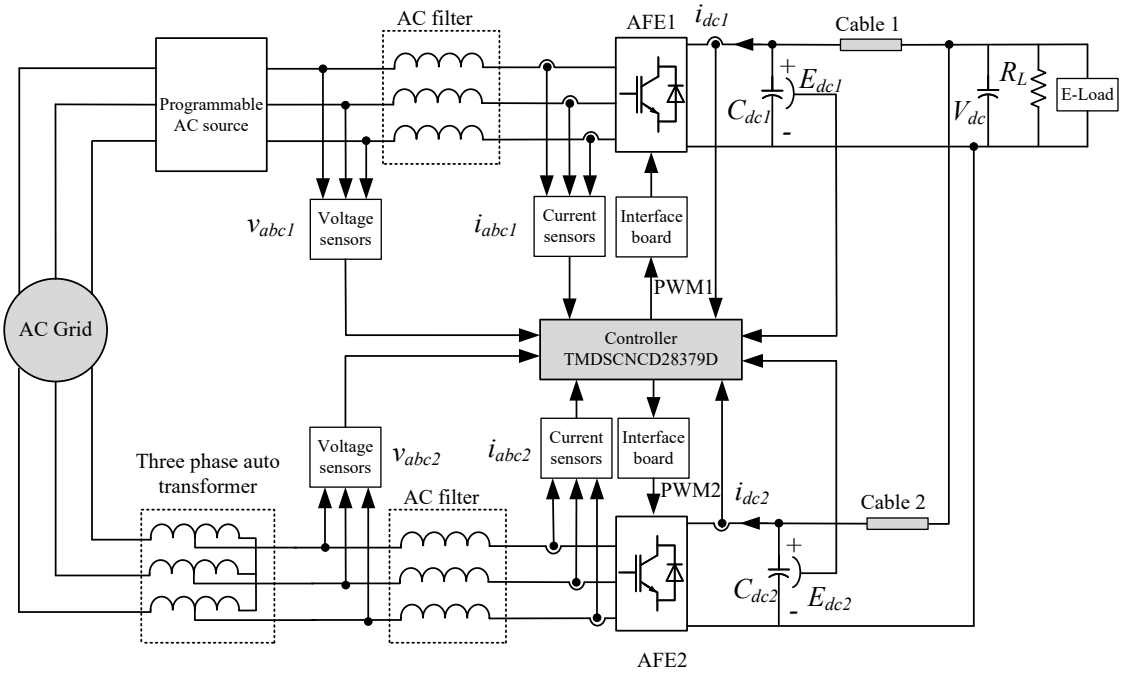

Fig. C.9: Layout diagram for the experimental rig of parallel operation of two sources

Table C.3: Parameters of the lap prototype

Parameter	Value
Rated DC bus voltage	270
Inductance of the AC filter	2.5 mH
DC bus capacitor	1.6 mF
Switching frequency	5 kHz
Current and voltage loops bandwidth	5 kHz/1 kHz

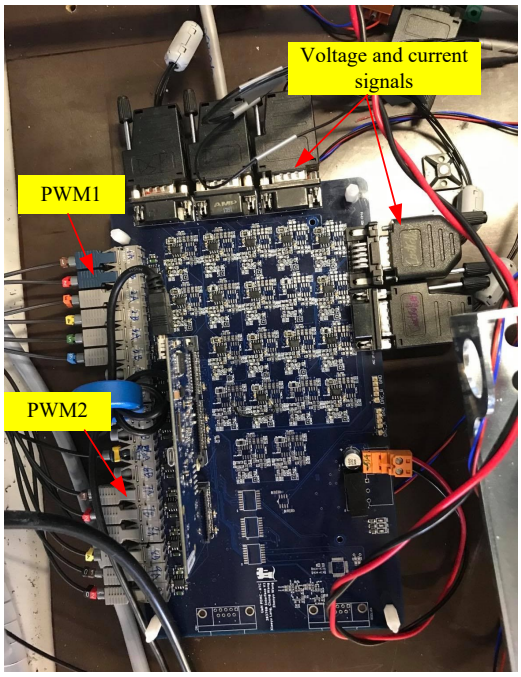

Fig. C.10: Control platform

a voltage range of 150VAC, and a frequency range of 15Hz to 1500Hz. When compared to the maximum rated current (32A), they can deliver up to four times the peak current. At 50/60Hz, it produces a clean sine waveform with typical distortion of less than 0.5 percent. It also offers precision measurements like RMS voltage, RMS current, real power, power factor, current crest factor, and so on. The front LCD panel and keyboard, as well as the remote control through Rs 232, USB, and ethernet interface, make this model simple to use [171]. Fig. C.12 presents the high power density programmable DC electronic load, it has a power output of 19.80 kW, a voltage output of 600 volts, and a current output of 1440 amps [172]. It supports the four fundamental operating modes of CV, CC, CR, and CP, as well as the three complex operating modes of CV+CC, CV+CR, and CR+CC.

Fig. C.11: Programmable AC source

OCP, OPP, OVP, OTP, and reverse alarm are all included in the protection package. The 0 to 10V input or output signal represents 0 to full range voltage or current, and it can be used for external control and monitoring. RS232, RS485 and USB communication ports are built-in.

Fig. C.12: Electronic load

Appendix D

Simulation Models

Simulation analysis was primarily done with Matlab/Simulink. The following were the models created in Simulink to support this study.

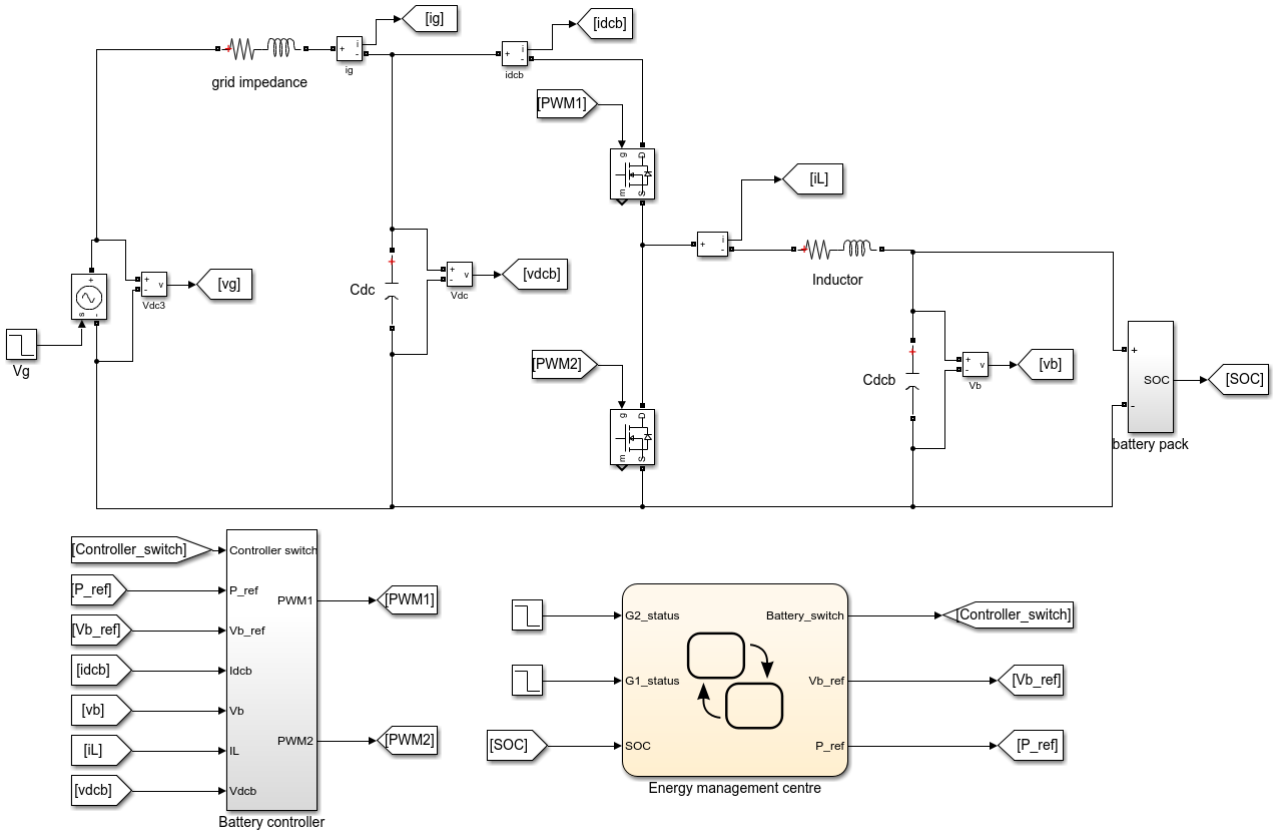

Fig. D.1: Battery multifunction controller consisting of battery pack, bidirectional DC-DC converter, DC bus, battery controller and energy management.

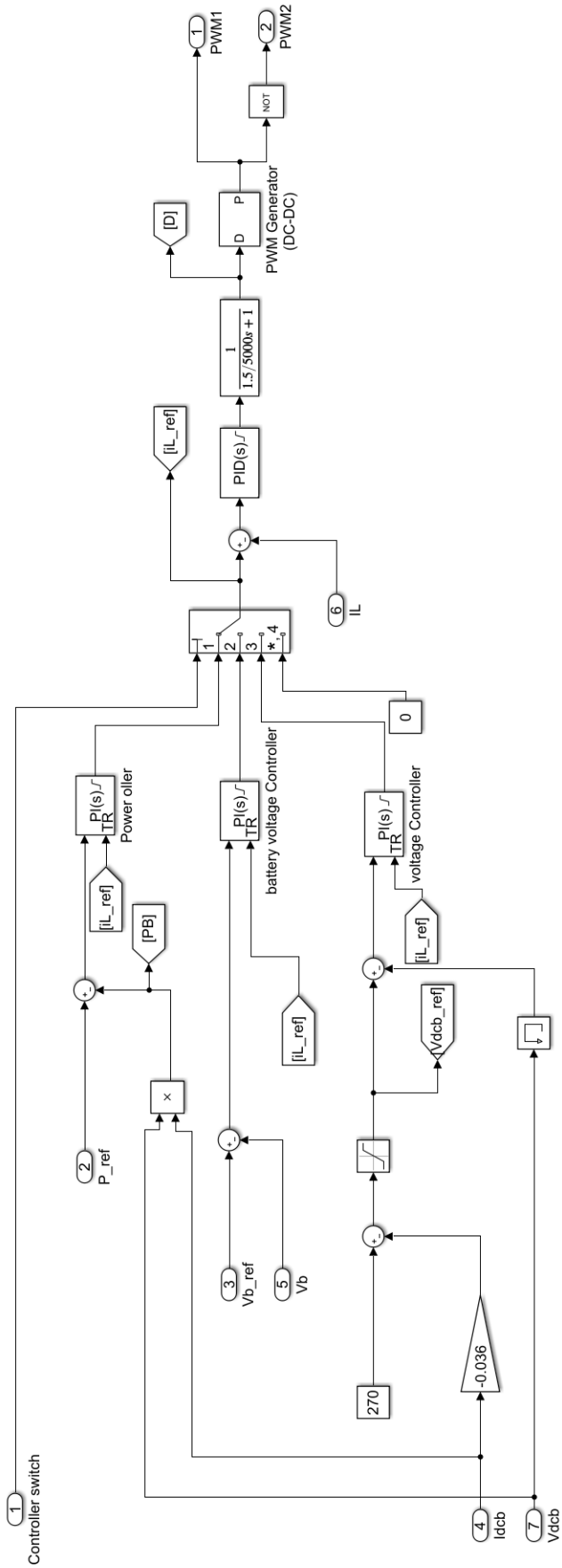

Fig. D.2: Battery controller.

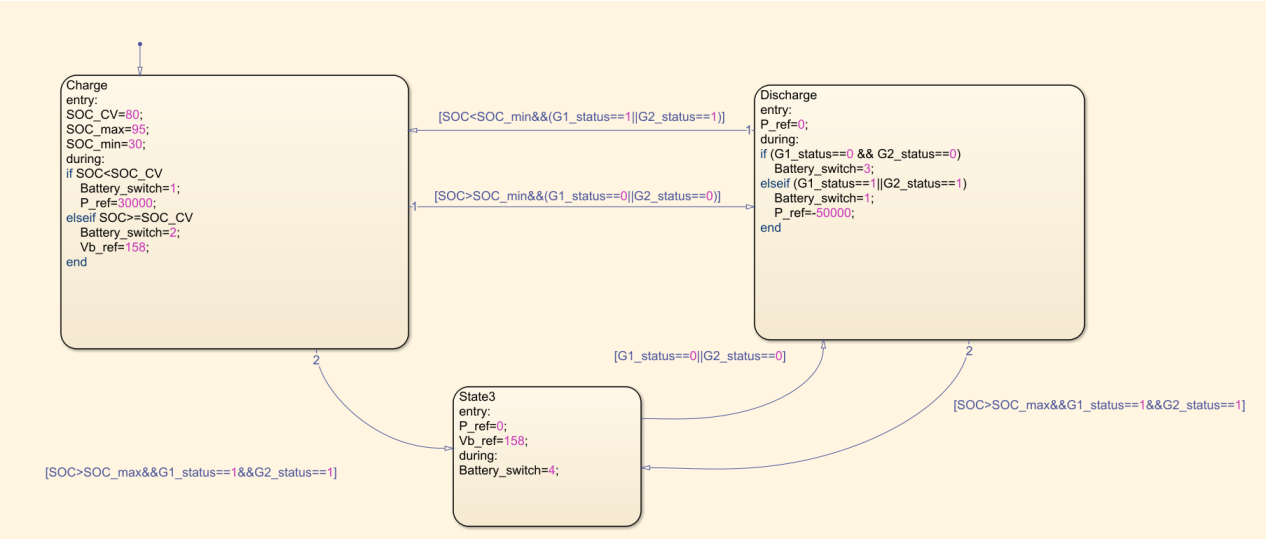

Fig. D.3: Energy management.

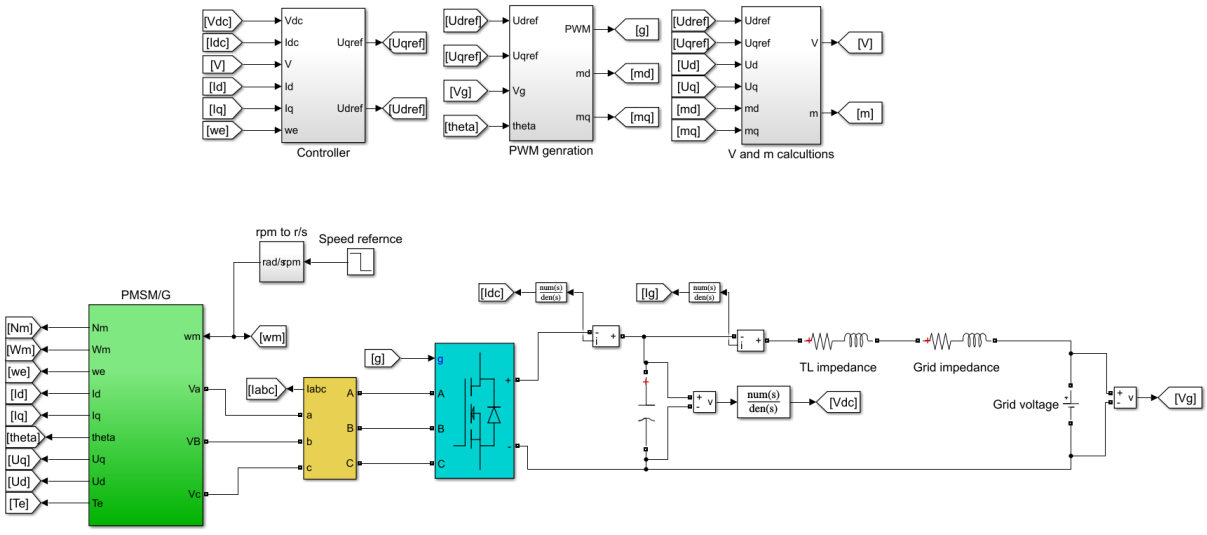

Fig. D.4: S/G power system consisting of PMM, AFE, DC bus,Transmission line and DC grid (for generation mode only).

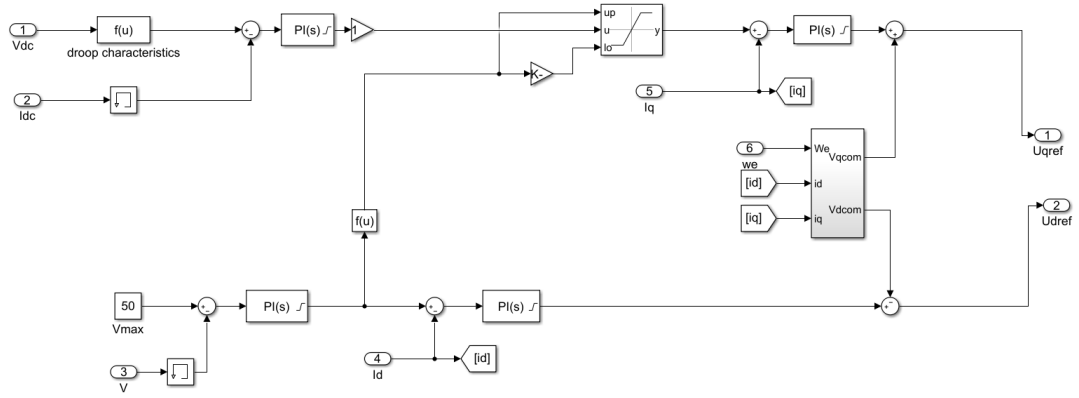

Fig. D.5: Controller.

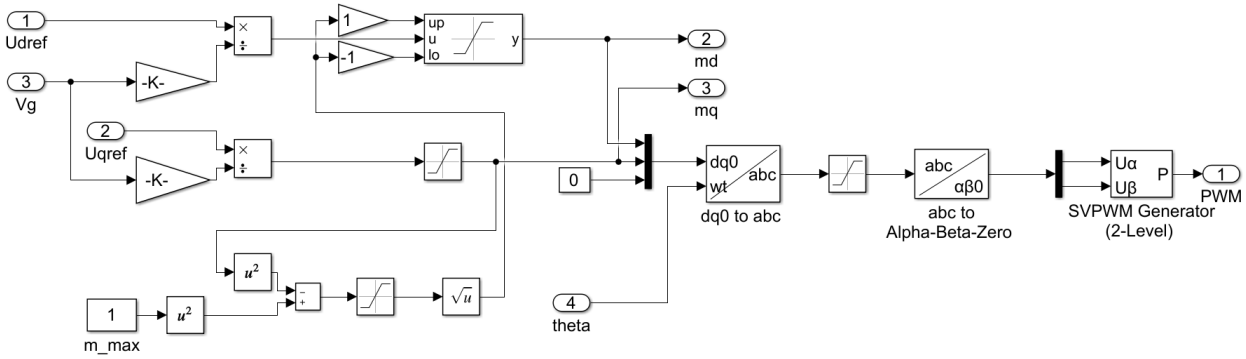

Fig. D.6: PWM genration.

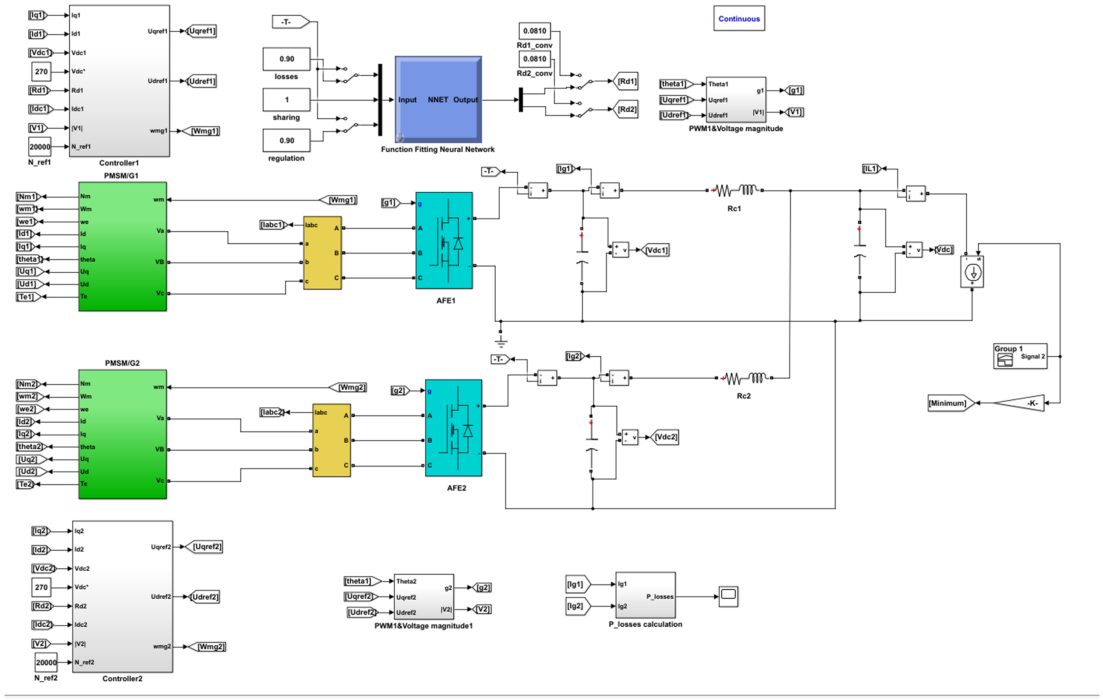

Fig. D.7: Optimal droop gain design using ANN.

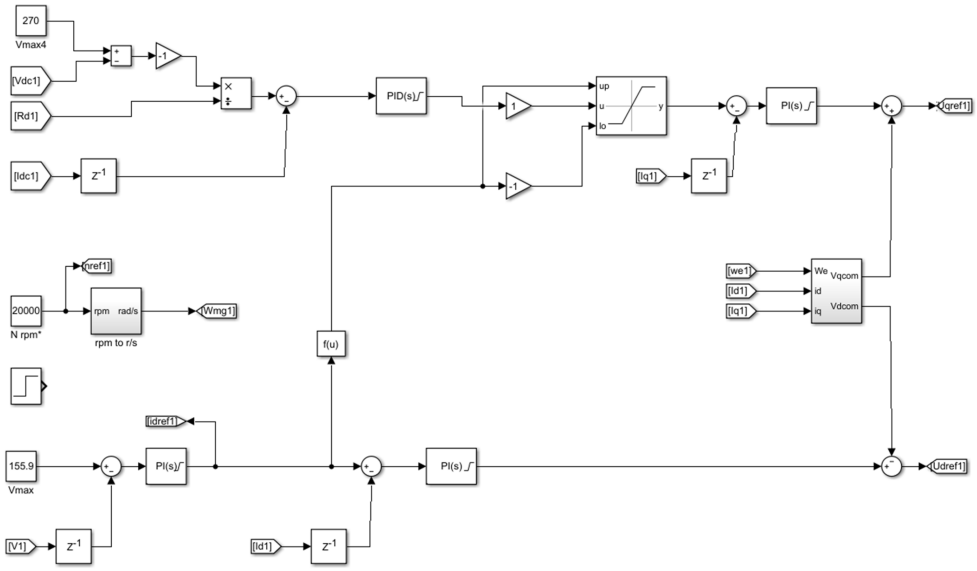

Fig. D.8: Controller for AFE converter.

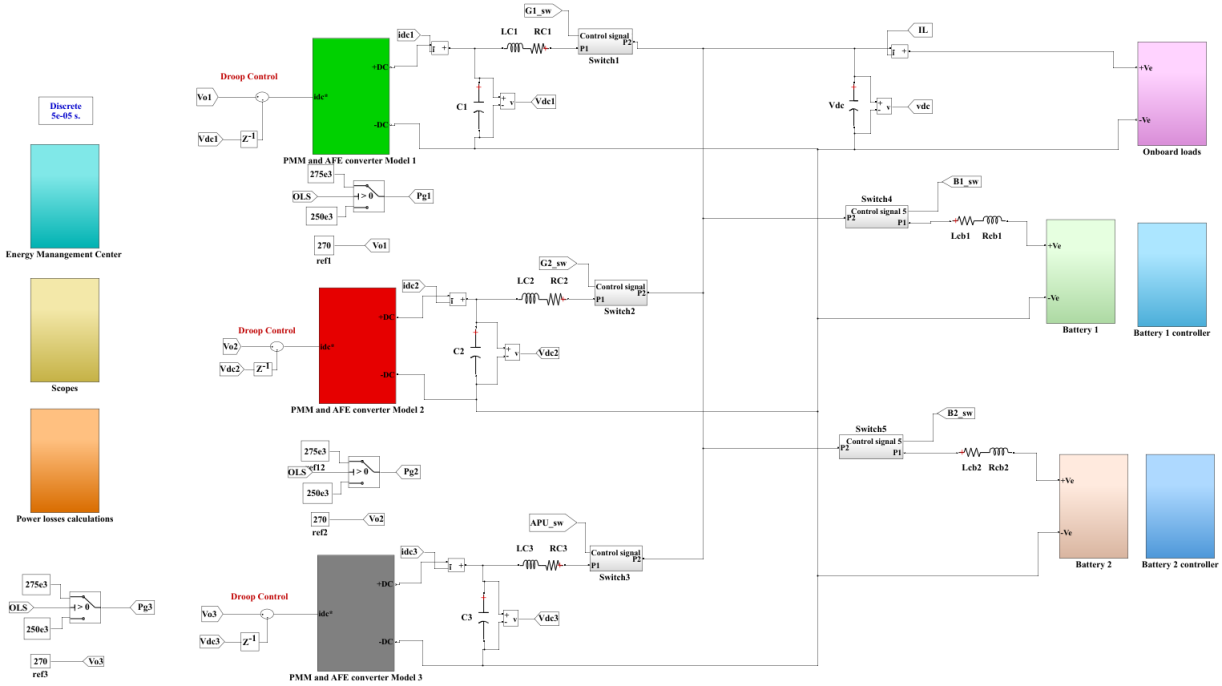

Fig. D.9: Overall EM strategy Simulink model.

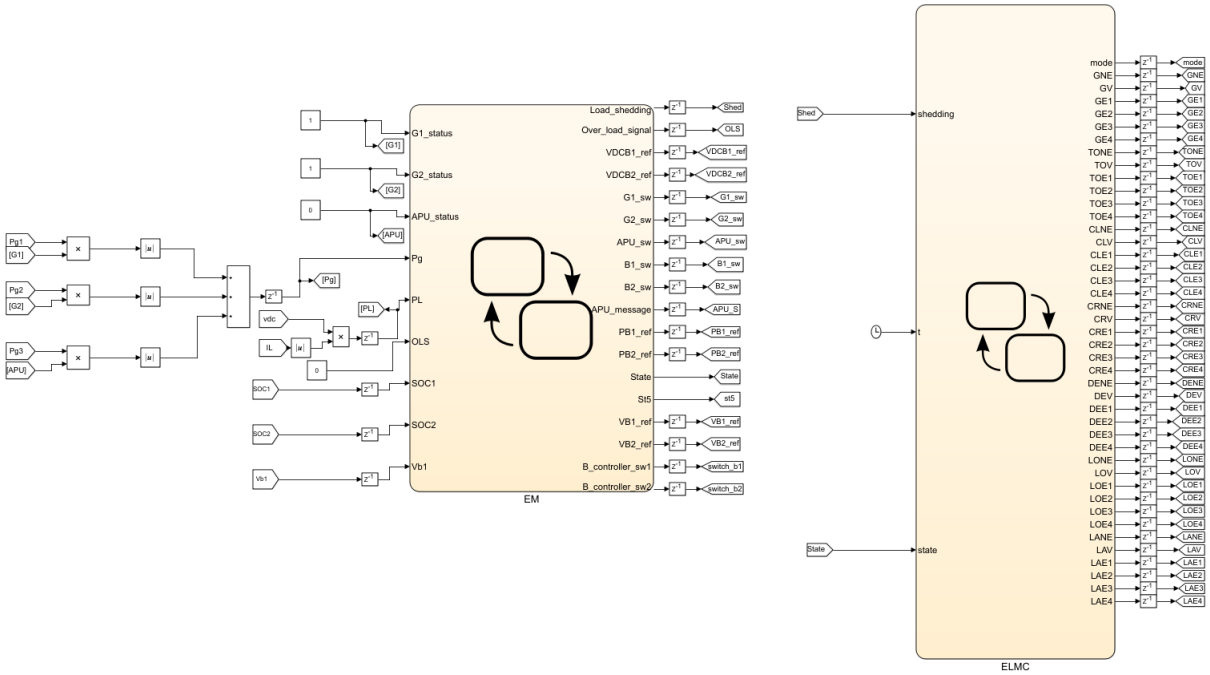

Fig. D.10: EM strategy.

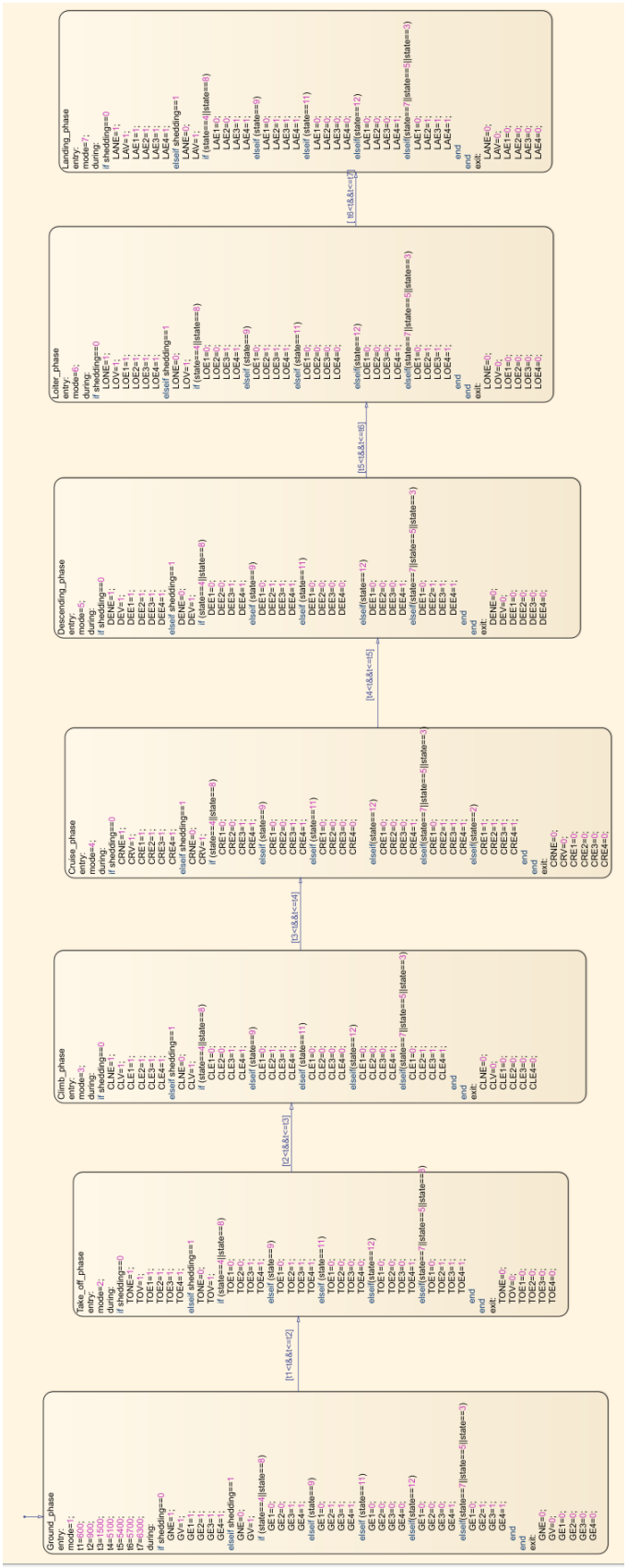

Fig. D.11: Energy load management centres.

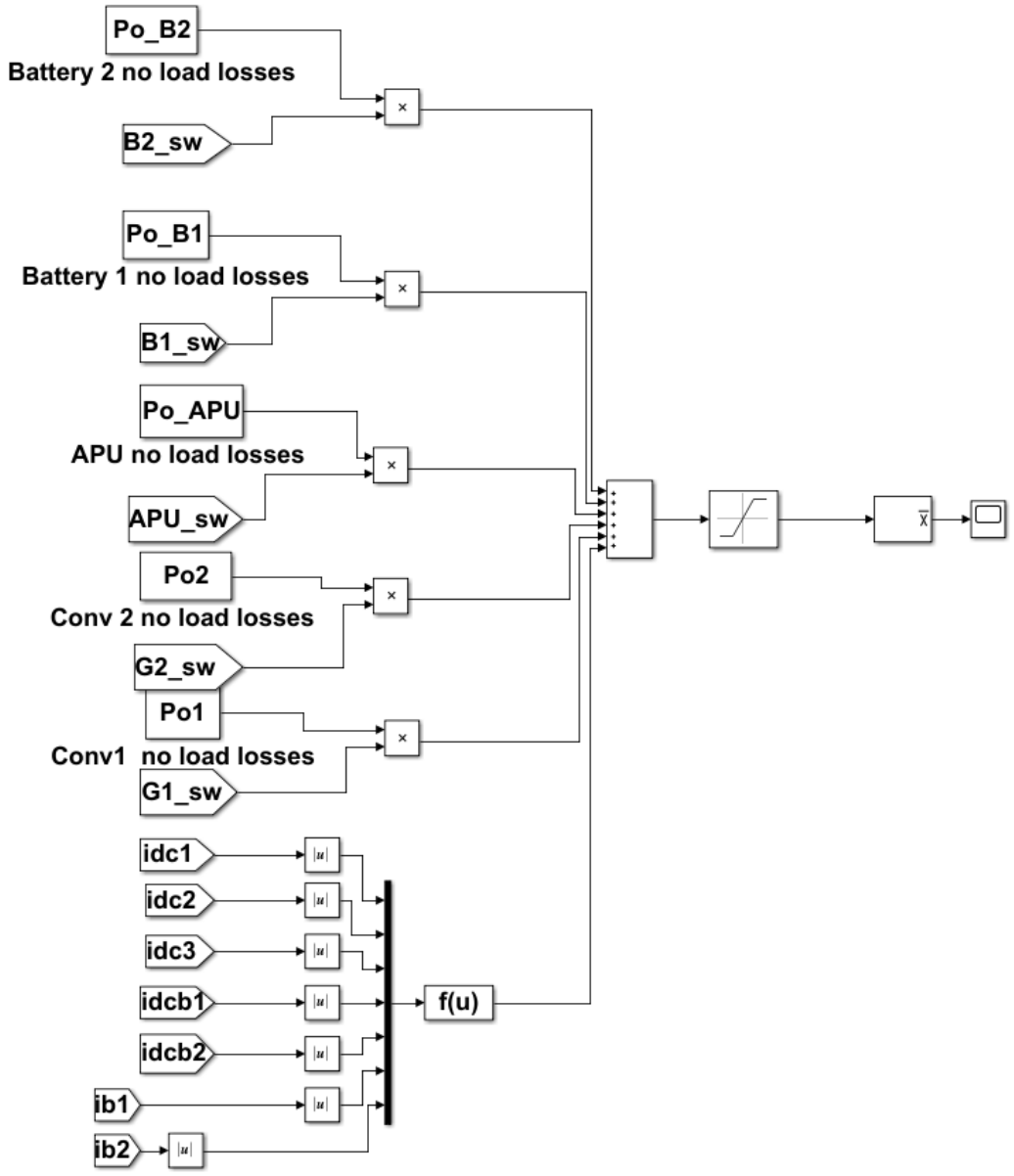

Fig. D.12: System losses calculation.

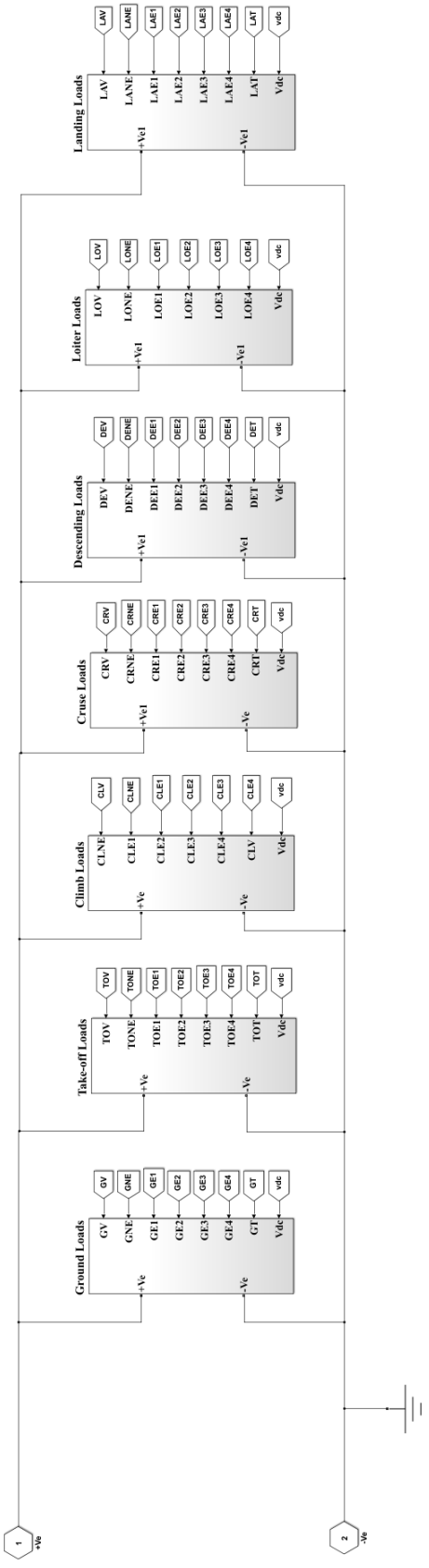

Fig. D.13: Onboard loads.

Modified Newton-Raphson code for PI design:

$clearall$

clc

$Wbw = 1000 * 2 * pi;$

$Ph = -45;$

$i = 0;$

$Kpo = 1e-2;$

$Kio = 10;$

$T13 = tf([1], [1.575e-30.24]);$

$fori = 0 : inf$

$PITF = tf([KpoKio], [10]);$

$OLTF_G = PI_TF * T13 * LPF;$

$G = feedback(OLTFG, 1);$

$magTF, phaseTF = bode(G, Wbw);$

$r1 = magTF - (1/sqrt(2))$

$r2 = phaseTF - Ph$

$deltaKp = 0.00001;$

$deltaKi = 0.00001;$

$Kp = Kpo + deltaKp;$

$Ki = Kio + deltaKi;$

$PITF = tf([KpKio], [10]);$

$OLTFG = PITF * T13 * LPF;$

$G = feedback(OLTFG, 1);$

$magTF, phaseTF = bode(G, Wbw);$

$r11 = magTF - (1/sqrt(2));$

$r21 = phaseTF - Ph;$

$PITF = tf([KpoKi], [10]);$

$OLTFG = PITF * T13 * LPF;$

$G = feedback(OLTFG, 1);$

$magTF, phaseTF = bode(G, Wbw);$

$r12 = magTF - (1/sqrt(2));$

$r22 = phaseTF - Ph;$

$J11 = (r11 - r1)/deltaKp;$

$J12 = (r12 - r1)/deltaKi;$

$J21 = (r21 - r2)/deltaKp;$

$J22 = (r22 - r2)/deltaKi;$

$J = [J11J12; J21J22];$

$ifabs(r1) < 0.001$

$break;$

$else$

$i = i + 1;$

$ifi == 10000$

$break$

end

$r = [r1; r2];$

$B1 = [Kpo; Kio];$

$C = inv(J);$

$B = B1 - (C * r) * 0.001;$

$Kp = B(1);$

$Ki = B(2);$

end

$Kpo = Kp;$

$Kio = Ki;$

$i;$

end

$PITF = tf([KpoKio], [10]);$

$OLTFG = PITF * T13 * LPF;$

$G = feedback(OLTFG, 1);$

$magTF, phaseTF = bode(G, Wbw);$

$bandwidth(G)$

$bandwidth(G)/(2 * pi)$

$f1 = figure;$

$bode(G), grid$

$f2 = figure;$

$step(G, 0 : 1e-6 : 0.1)$

The code to generates the training data can be given as follows :

$clearall$

clc

$Rc1 = 0.0081;$

$Rc2 = 0.0081;$

$Rd1 = 0.0810;$

$Rd2 = 0.0810;$

$RL = 1.35;$

$Vo1 = 270;$

$Vo2 = 270;$

$Po1 = 138;$

$Po2 = 282;$

$Rconv1 = 0.0281;$

$Rconv2 = 0.0574;$

$I1max = 170;$

$I2max = 170;$

$deltaV = 0.05 * 270;$

$Rd1conv = deltaV/I1max;$

$Rd2conv = deltaV/I2max;$

$IL = 300\%1 * (I1max + I2max)$

$j = 0;$

$Rd1step = 0.001;$

$Rd2step = 0.001;$

$Rd1percentage = 0.15;$

$Rd2percentage = 0.15;$

$\%conventional$

$I1conv = IL * (Rd2conv + Rc2)/(Rc1 + Rc2 + Rd1conv + Rd2conv);$

$I2conv = IL * (Rd1conv + Rc1)/(Rc1 + Rc2 + Rd1conv + Rd2conv); Vdcconv =$

$Vo1 - I1conv * Rd1conv - I1conv * (Rc1); deltavdcconv = 100 * abs(Vdcconv - Vo1)/Vo1; Plossconv = Po1 + Po2 + I1conv * I1conv * (Rc1 + Rconv1) + I2conv * I2conv * (Rc2 + Rconv2);$

$sharingconv = (I2conv/I2max)/(I1conv/I1max);$

$\%for$

$i = (Rd1 - Rd1percentage * Rd1) : Rd1step : (Rd1 + Rd1percentage * Rd1)$

$j = j + 1;$

$rd1 = i;$

$k = 0;$

for

$o = (Rd2 - Rd2percentage * Rd2) : Rd2step : (Rd2 + Rd2percentage * Rd2)$

$k = k + 1;$

$rd2 = o;$

$RRd1(j, k) = i;$

$RRd2(j, k) = o;$

$x(j, k) = 1;$

$I1(j, k) = IL * (rd2 + Rc2)/(Rc1 + Rc2 + rd1 + rd2);$

$\%if I1(j, k) > I1max$

$I1(j, k) = I1max;$

$I2(j, k) = IL - I1max;$

$else$

$I2(j, k) = IL * (rd1 + Rc1)/(Rc1 + Rc2 + rd1 + rd2);$

end

$\%Vdc(j, k) = Vo1 - I1(j, k) * rd1 - I1(j, k) * (Rc1);$

$deltavdc(j, k) = (100 * abs(Vdc(j, k) - Vo1)/Vo1)/5;$

$Ploss(j, k) = (Po1 + Po2 + I1(j, k) * I1(j, k) * (Rc1 + Rconv1) + I2(j, k) * I2(j, k) * (Rc2 + Rconv2))/Plossconv;$

$sharing(j, k) = ((I2(j, k)/I2max)/(I1(j, k)/I1max));$

end

end

$\%transfer\ matrix\ to\ vector$

$Rd1vec = RRd1';$

$Rd1vec1 = reshape(Rd1vec, 1, []);$

$Rd1column = Rd1vec1.';$

$\%Rd2vec = RRd2';$

$Rd2vec1 = reshape(Rd2vec, 1, []);$

$Rd2column = Rd2vec1.';$

$\%Plossvec = Ploss';$

$Plossvec1 = reshape(Plossvec, 1, []);$

$Plosscolumn = Plossvec1.';$

$\%sharingvec = sharing';$

$sharingvec1 = reshape(sharingvec, 1, []);$

$sharingcolumn = sharingvec1.';$

$\%deltavdcvec = deltavdc';$

$deltavdcvec1 = reshape(deltavdcvec, 1, []);$

$deltavdccolumn = deltavdcvec1.';$

Appendix E

Publication List

The research related to this thesis has been published in five international conferences and one journal paper. Also, one journal papers were submitted and are currently under review. Moreover, 2 journal are under editing and will be submitted in prestigious journals.

E.1 Conference Papers

1. M. A. A. Mohamed, Q. Guan and M. Rashed, "Control of DC-DC Converter for Interfacing Supercapcitors Energy storage to DC Micro Grids," 2018 IEEE International Conference on Electrical Systems for Aircraft, Railway, Ship Propulsion and Road Vehicles & International Transportation Electrification Conference (ESARS-ITEC), 2018, pp. 1-8.

2. M A. A. Mohamed, M. Rashed, S. Bozhko, "Enhanced Flux Weakening Control of PMM-Based Starter-Generator System in More Electric Aircraft,", The 10th International Conference on Power Electronics, Machines and Drives (PEMD), 2020, p. 249-254.

3. Mohamed A.A. Mohamed, Jason Atkin, Seang Yeoh, Mohsen Khalaf, Serhiy Bozhko,"Analysis and Design of Battery Controller for More Electric Aircraft," 2021 IEEE International Power and Renewable Energy Conference (IPRECON), 2021.

4. Mohamed A.A. Mohamed, Habibu Hussaini, Jason Atkin, Seang Yeoh, Serhiy Bozhko, "Optimal Droop Gain Design for MEA DC Microgrid based-on Artificial Neural Network," MEA 2021 conference, 2021.

5. H. Hussaini, T. Yang, Y. Gao, C. Wang, M. A. A. Mohamed and S. Bozhko, "Artificial Neural Network Aided Cable Resistance Estimation in Droop-Controlled Islanded DC Microgrids," IECON 2021 – 47th Annual Conference of the IEEE Industrial Electronics Society, 2021, pp. 1-7.

E.2 Journal Papers

1. Mohamed A.A. Mohamed, Mohamed Rashed, Xiaoyu Lang, Jason Atkin, Seang Yeoh, Serhiy Bozhko, "Droop control design to minimize losses in DC microgrid for more electric aircraft," Electric Power Systems Research, Volume 199, 2021.

E.3 Journal Papers under Review

1. Mohamed A.A. Mohamed, Seang Yeoh, Jason Atkin , Serhiy Bozhko, "Efficiency Focused Energy Management Strategy Based-on Optimal Droop Gain Design for More Electric Aircraft, " IEEE Transaction on Transportation Electrification Journal, Special Issue on Electrified Aircraft Technologies.

References

[1] F. Gao, "Decentralised control and stabilityanalysis of a multi-generatorbased electrical power system formore electric aircraft," PhD thesis, University of Nottingham, August 2016.

[2] Y. Liu, J. Deng, C. Liu, and S. Li, "Energy optimization analysis of the more electric aircraft," *IOP Conference Series: Earth and Environmental Science*, vol. 113, p. 012 152, 2018. DOI: 10.1088/1755-1315/113/1/012152.

[3] P. W. Wheeler, J. C. Clare, A. Trentin, and S. Bozhko, "An overview of the more electrical aircraft," *Proceedings of the Institution of Mechanical Engineers, Part G: Journal of Aerospace Engineering*, vol. 227, no. 4, pp. 578–585, 2013.

[4] K. Emadi and M. Ehsani, "Aircraft power systems: Technology, state of the art, and future trends," *IEEE Aerospace and Electronic Systems Magazine*, vol. 15, no. 1, pp. 28–32, 2000.

[5] A. S. Ian Moir, *Aircraft Systems: Machanical,electrical and avoionics subsystems integeration*. Willey, 2008.

[6] V. Madonna, P. Giangrande, and M. Galea, "Electrical power generation in aircraft: Review, challenges, and opportunities," *IEEE Transactions on Transportation Electrification*, vol. 4, no. 3, pp. 646–659, 2018.

[7] M. Sinnett, "787 no-bleed systems: Saving fuel and enhancing operational efficiencies," *Boeing Aero Mag*, vol. 4, pp. 6–11, 2007.

[8] X. Roboam, B. Sareni, and A. D. Andrade, "More electricity in the air: Toward optimized electrical networks embedded in more-electrical aircraft," *IEEE Industrial Electronics Magazine*, vol. 6, no. 4, pp. 6–17, 2012.

[9] M. Briere, "Gan based power devices: Cost-effective revolutionary performance," *Power Electronics Europe*, vol. 7, pp. 29–31, Jan. 2008.

[10] A. Y. Arabul, E. Kurt, F. K. Arabul, İbrahim Senol, M. Schrötter, R. Bréda, and D. Megyesi, "Perspectives and development of electrical systems in more electric aircraft," *International Journal of Aerospace Engineering*, 2021.

[11] B. H. Nya, J. Brombach, and D. Schulz, "Benefits of higher voltage levels in aircraft electrical power systems," in *2012 Electrical Systems for Aircraft, Railway and Ship Propulsion*, 2012, pp. 1–5.

[12] J. Brombach, A. Lücken, B. Nya, M. Johannsen, and D. Schulz, "Comparison of different electrical hvdc-architectures for aircraft application," in *2012 Electrical Systems for Aircraft, Railway and Ship Propulsion*, 2012, pp. 1–6.

[13] H. Wang, A. M. Khambadkone, and X. Yu, "Control of parallel connected power converters for low voltage microgrid—part ii: Dynamic electrothermal modeling," *IEEE Transactions on Power Electronics*, vol. 25, no. 12, pp. 2971–2980, 2010.

[14] Z. Fan, B. Fan, J. Peng, and W. Liu, "Operation loss minimization targeted distributed optimal control of dc microgrids," *IEEE Systems Journal*, pp. 1–11, 2020.

[15] M. Moahmed, "Droop control design to minimize losses in dc microgrid for mea," *Power system research*, 2020.

[16] S. Iqbal, M. Nasir, M. F. Zia, K. Riaz, H. Sajjad, and H. A. Khan, "A novel approach for system loss minimization in a peer-to-peer energy sharing community dc microgrid," *International Journal of Electrical Power and Energy Systems*, vol. 129, 2021.

[17] M. K. AL-Nussairi, R. Bayindir, S. Padmanaban, L. Mihet-Popa, and P. Siano, "Constant Power Loads (CPL) with Microgrids: Problem Definition, Stability Analysis and Compensation Techniques," *Energies*, vol. 10, no. 10, 2017.

[18] A. Griffo and J. Wang, "Large Signal Stability Analysis of 'More Electric' Aircraft Power Systems with Constant Power Loads," *IEEE Transactions on Aerospace and Electronic Systems*, vol. 48, no. 1, pp. 477–489, 2012.

[19] *MIL-STD-704F Aircraft Electrical Power Characteristics*, Department of Defence Interface Standard, 2004.

[20] A. Bakhshi, M. Bigdeli, M. Moradlou, and H. M. CheshmehBeigi, "More electric aircraft fault current protection: A review," in *2021 12th Power Electronics, Drive Systems, and Technologies Conference (PEDSTC)*, 2021, pp. 1–7.

[21] M.-C. Flynn, M. Sztykiel, C. E. Jones, P. J. Norman, G. M. Burt, P. Miller, and M. Husband, "Protection and fault management strategy maps for future electrical propulsion aircraft," *IEEE Transactions on Transportation Electrification*, vol. 5, no. 4, pp. 1458–1469, 2019.

[22] P. Cairoli, L. Qi, C. Tschida, V. R. Ramanan, L. Raciti, and A. Antoniazzi, "High current solid state circuit breaker for dc shipboard power systems," in *2019 IEEE Electric Ship Technologies Symposium (ESTS)*, 2019, pp. 468–476.

[23] A. D. Anderson, N. J. Renner, Y. Wang, S. Agrawal, S. Sirimanna, D. Lee, A. Banerjee, K. Haran, M. J. Starr, and J. L. Felder, "System weight comparison of electric machine topologies for electric aircraft propulsion," in *2018 AIAA/IEEE Electric Aircraft Technologies Symposium (EATS)*, 2018, pp. 1–16.

[24] J. A. Swanke, D. Bobba, T. M. Jahns, and B. Sarlioglu, "Design of high-speed permanent magnet machine for aerospace propulsion," in *2019 AIAA/IEEE Electric Aircraft Technologies Symposium (EATS)*, 2019, pp. 1–12.

[25] M. Abdul Sathar Eqbal, N. Fernando, M. Marino, and G. Wild, "Hybrid propulsion systems for remotely piloted aircraft systems," *Aerospace*, vol. 5, no. 2, 2018, ISSN: 2226-4310.

[26] K. Ni, Y. Liu, Z. Mei, T. Wu, Y. Hu, H. Wen, and Y. Wang, "Electrical and electronic technologies in more-electric aircraft: A review," *IEEE Access*, vol. 7, pp. 76 145–76 166, 2019.

[27] T. Finken, M. Felden, and K. Hameyer, "Comparison and design of different electrical machine types regarding their applicability in hybrid electrical vehicles," in *2008 18th International Conference on Electrical Machines*, 2008, pp. 1–5.

[28] N. Schofield and S. Long, "Generator operation of a switched reluctance starter/generator at extended speeds," *IEEE Transactions on Vehicular Technology*, vol. 58, no. 1, pp. 48–56, 2009.

[29] S. Jones and B. Drager, "Sensorless switched reluctance starter/generator performance," *IEEE Industry Applications Magazine*, vol. 3, no. 6, pp. 33–38, 1997.

[30] M. Elbuluk and M. Kankam, "Potential starter/generator technologies for future aerospace applications," *IEEE Aerospace and Electronic Systems Magazine*, vol. 12, no. 5, pp. 24–31, 1997.

[31] I. Alan and T. Lipo, "Starter/generator employing resonant-converter-fed induction machine. i. analysis," *IEEE Transactions on Aerospace and Electronic Systems*, vol. 36, no. 4, pp. 1309–1328, 2000.

[32] I. Alan and T. Lipo, "Starter/generator employing resonant-converter-fed induction machine. ii. hardware prototype," *IEEE Transactions on Aerospace and Electronic Systems*, vol. 36, no. 4, pp. 1319–1329, 2000.

[33] R. Anbarasu, R. Gupta, N. Sharma, G. Gauthaman, A. Wankhede, P. Chavda, J. Nataraj, and B. Bhattacharjee, "Design and experimental investigation of high speed squirrel cage induction motor," in *Proceedings of International Conference on Power Electronics, Drives and Energy Systems for Industrial Growth*, vol. 2, 1996, 920–926 vol.2.

[34] A. A. AbdElhafez and A. J. Forsyth, "A review of more electric aircraft," Aerpspace Science and Aviation Technology (ASAT), 2009.

[35] S. S. Yeoh, "Control strategies for the more electric aircraft starter-generator electrical power system.," PhD thesis, Electrical and Electronic Enginnering, 2016.

[36] R. R. Secunde, R. P. Macosko, and D. S. Repas, "Integrated engine generator concept for aircraft electric secondary power," NASA, Washington, DC, USA, Tech. Rep., 1972.

[37] S. B. Stephen, "Constant speed drive and generator," pat. 3576143 A, Apr. 1971.

[38] S.B.Barnhardt, "Cooling arrangement for an integrated drive-generatorsystem," pat. 4284913A, Aug. 1981.

[39] X. Roboam, "New trends and challenges of electrical networks embedded in "more electrical aircraft"," in *2011 IEEE International Symposium on Industrial Electronics*, 2011, pp. 26–31.

[40] R. Quigley, "More electric aircraft," in *Proceedings Eighth Annual Applied Power Electronics Conference and Exposition,*, 1993, pp. 906–911.

[41] M.J.Cronin, "Aircraft providing variable and constant electric power," pat. 4587436A, May 1986.

[42] A. Eid, H. El-Kishky, M. Abdel-Salam, and M. T. El-Mohandes, "On power quality of variable-speed constant-frequency aircraft electric power systems," *IEEE Transactions on Power Delivery*, vol. 25, no. 1, pp. 55–65, 2010.

[43] R. Abdel-Fadil, A. Eid, and M. Abdel-Salam, "Electrical distribution power systems of modern civil aircrafts," 2013.

[44] M. Olaiya and N. Buchan, "High power variable frequency generator for large civil aircraft," in *IEE Colloquium on Electrical Machines and Systems for the More Electric Aircraft (Ref. No. 1999/180)*, 1999, pp. 3/1–3/4.

[45] M. Tariq, A. I. Maswood, C. J. Gajanayake, and A. K. Gupta, "Modeling and integration of a lithium-ion battery energy storage system with the more electric aircraft 270 v dc power distribution architecture," *IEEE Access*, vol. 6, pp. 41 785–41 802, 2018.

[46] A. Recalde, M. Lukic, A. Hebala, P. Giangrande, C. Klumpner, S. Nuzzo, P. H. Connor, J. Atkin, S. Bozhko, and M. Galea, "Energy storage system selection for optimal fuel consumption of aircraft hybrid electric taxiing systems," *IEEE Transactions on Transportation Electrification*, pp. 1–1, 2020.

[47] A. Damiano, M. Porru, A. Salimbeni, A. Serpi, V. Castiglia, A. O. Di Tommaso, R. Miceli, and G. Schettino, "Batteries for aerospace: A brief review," in *2018 AEIT International Annual Conference*, 2018, pp. 1–6.

[48] D. A. Rand and P. T. Moseley, "Chapter 13 energy storage with lead–acid batteries," in *Electrochemical Energy Storage for Renewable Sources and Grid Balancing*, P. T. Moseley and J. Garche, Eds., Elsevier, 2015, pp. 201 –222.

[49] P. Bernard and M. Lippert, "Chapter 14 - nickel–cadmium and nickel–metal hydride battery energy storage," in *Electrochemical Energy Storage for Renewable Sources and Grid Balancing*, P. T. Moseley and J. Garche, Eds., Elsevier, 2015, pp. 223 –251.

[50] M. Tariq, A. I. Maswood, C. J. Gajanayake, and A. K. Gupta, "Aircraft batteries: Current trend towards more electric aircraft," *IET Electrical Systems in Transportation*, vol. 7, no. 2, pp. 93–103, 2017.

[51] A. Abdel-Hafez, "Power generation and distribution system for amore electric aircraft - a review," in, R. K. Agarwal, Ed. Feb. 2012, ch. 13, pp. 289–308.

[52] T. Wu, S. Bozhko, and G. Asher, "High speed modeling approach of aircraft electrical power systems under both normal and abnormal scenarios," in *2010 IEEE International Symposium on Industrial Electronics*, 2010, pp. 870–877.

[53] G. Buticchi, S. Bozhko, M. Liserre, P. Wheeler, and K. Al-Haddad, "On-board microgrids for the more electric aircraft—technology review," *IEEE Transactions on Industrial Electronics*, vol. 66, no. 7, pp. 5588–5599, 2019.

[54] P. Wheeler and S. Bozhko, "The more electric aircraft: Technology and challenges.," *IEEE Electrification Magazine*, vol. 2, no. 4, pp. 6–12, 2014.

[55] H. Yu, J. Deng, and Y. Li, "A diagnosis method of semiconductor power switch open-circuit fault in the pmsm drive system with the mpcc method," *IEEE Access*, vol. 9, pp. 109 822–109 832, 2021.

[56] S. Kouro, M. Malinowski, K. Gopakumar, J. Pou, L. G. Franquelo, B. Wu, J. Rodriguez, M. A. Pérez, and J. I. Leon, "Recent advances and industrial applications of multilevel converters," *IEEE Transactions on Industrial Electronics*, vol. 57, no. 8, pp. 2553–2580, 2010.

[57] S. Aurtenechea, M. A. Rodriguez, E. Oyarbide, and J. R. Torrealday, "Predictive direct power control of mv-grid-connected two-level and, three-level npc converters: Experimental results," in *2007 European Conference on Power Electronics and Applications*, 2007, pp. 1–10.

[58] A. I. M. Shukran, C. L. Toh, and C. W. Tan, "Modelling and analysis of 18-pulse rectification system for dc traction power substation," in *2021 IEEE Conference on Energy Conversion (CENCON)*, 2021, pp. 174–179.

[59] S. S. Yeoh, T. Yang, L. Tarisciotti, C. I. Hill, S. Bozhko, and P. Zanchetta, "Permanent-magnet machine-based starter–generator system with modulated model predictive control," *IEEE Transactions on Transportation Electrification*, vol. 3, no. 4, pp. 878–890, 2017.

[60] T. Friedli, J. W. Kolar, J. Rodriguez, and P. W. Wheeler, "Comparative evaluation of three-phase ac–ac matrix converter and voltage dc-link back-to-back converter systems," *IEEE Transactions on Industrial Electronics*, vol. 59, no. 12, pp. 4487–4510, 2012.

[61] P. Wheeler, J. Clare, L. Empringham, M. Apap, and M. Bland, "Matrix converters," *Power Engineering Journal*, vol. 16, no. 6, pp. 273–282, 2002.

[62] H.-N. Nguyen and H.-H. Lee, "A dsvm method for matrix converters to suppress common-mode voltage with reduced switching losses," *IEEE Transactions on Power Electronics*, vol. 31, no. 6, pp. 4020–4030, 2016.

[63] Y. Sun, X. Li, M. Su, H. Wang, H. Dan, and W. Xiong, "Indirect matrix converter-based topology and modulation schemes for enhancing input reactive power capability," *IEEE Transactions on Power Electronics*, vol. 30, no. 9, pp. 4669–4681, 2015.

[64] I. Munuswamy and P. W. Wheeler, "Third method for regenerative braking in matrix converter drive: More electric aircraft," in *2017 Innovations in Power and Advanced Computing Technologies (i-PACT)*, 2017, pp. 1–6.

[65] M. Aten, G. Towers, C. Whitley, P. Wheeler, J. Clare, and K. Bradley, "Reliability comparison of matrix and other converter topologies," *IEEE Transactions on Aerospace and Electronic Systems*, vol. 42, no. 3, pp. 867–875, 2006.

[66] F. Mumtaz, N. Zaihar Yahaya, S. Tanzim Meraj, B. Singh, R. Kannan, and O. Ibrahim, "Review on non-isolated dc-dc converters and their control techniques for renewable energy applications," *Ain Shams Engineering Journal*, 2021, ISSN:

2090-4479. DOI: https://doi.org/10.1016/j.asej.2021.03.022. [Online]. Available: https://www.sciencedirect.com/science/article/pii/S2090447921001933.

[67] W. Li and X. He, "Review of nonisolated high-step-up dc/dc converters in photovoltaic grid-connected applications," *IEEE Transactions on Industrial Electronics*, vol. 58, no. 4, pp. 1239–1250, 2011.

[68] L. B. Buss, ""electric airplane" environmental control systems energy requirements," *IEEE Transactions on Aerospace and Electronic Systems*, vol. AES-20, no. 3, pp. 250–256, 1984.

[69] T. Dragičević, X. Lu, J. C. Vasquez, and J. M. Guerrero, "Dc microgrids—part i: A review of control strategies and stabilization techniques," *IEEE Transactions on Power Electronics*, vol. 31, no. 7, pp. 4876–4891, 2016.

[70] F. Valenciaga and P. Puleston, "Supervisor control for a stand-alone hybrid generation system using wind and photovoltaic energy," *IEEE Transactions on Energy Conversion*, vol. 20, no. 2, pp. 398–405, 2005.

[71] F. Valenciaga and P. F. Puleston, "High-order sliding control for a wind energy conversion system based on a permanent magnet synchronous generator," *IEEE Transactions on Energy Conversion*, vol. 23, no. 3, pp. 860–867, 2008.

[72] S. K. Mazumder, M. Tahir, and K. Acharya, "Master–slave current-sharing control of a parallel dc–dc converter system over an rf communication interface," *IEEE Transactions on Industrial Electronics*, vol. 55, no. 1, pp. 59–66, 2008.

[73] J. M. Guerrero, J. C. Vasquez, J. Matas, L. G. de Vicuna, and M. Castilla, "Hierarchical control of droop-controlled ac and dc microgrids—a general approach toward standardization," *IEEE Transactions on Industrial Electronics*, vol. 58, no. 1, pp. 158–172, 2011.

[74] D. Salomonsson, L. Soder, and A. Sannino, "An adaptive control system for a dc microgrid for data centers," *IEEE Transactions on Industry Applications*, vol. 44, no. 6, pp. 1910–1917, 2008.

[75] L. Che and M. Shahidehpour, "Dc microgrids: Economic operation and enhancement of resilience by hierarchical control," *IEEE Transactions on Smart Grid*, vol. 5, no. 5, pp. 2517–2526, 2014.

[76] R. Olfati-Saber, J. A. Fax, and R. M. Murray, "Consensus and cooperation in networked multi-agent systems," *Proceedings of the IEEE*, vol. 95, no. 1, pp. 215–233, 2007.

[77] R. Olfati-Saber and R. Murray, "Consensus problems in networks of agents with switching topology and time-delays," *IEEE Transactions on Automatic Control*, vol. 49, no. 9, pp. 1520–1533, 2004.

[78] V. Nasirian, S. Moayedi, A. Davoudi, and F. L. Lewis, "Distributed cooperative control of dc microgrids," *IEEE Transactions on Power Electronics*, vol. 30, no. 4, pp. 2288–2303, 2015.

[79] L. Meng, T. Dragicevic, J. M. Guerrero, and J. C. Vasquez, "Dynamic consensus algorithm based distributed global efficiency optimization of a droop controlled dc microgrid," in *2014 IEEE International Energy Conference (ENERGYCON)*, 2014, pp. 1276–1283.

[80] X. Lu, J. M. Guerrero, K. Sun, and J. C. Vasquez, "An Improved Droop Control Method for DC Microgrids Based on Low Bandwidth Communication With DC Bus Voltage Restoration and Enhanced Current Sharing Accuracy," *IEEE Transactions on Power Electronics*, vol. 29, no. 4, pp. 1800–1812, 2014.

[81] J. Schonbergerschonberger, R. Duke, and S. Round, "Dc-bus signaling: A distributed control strategy for a hybrid renewable nanogrid," *IEEE Transactions on Industrial Electronics*, vol. 53, no. 5, pp. 1453–1460, 2006.

[82] K. Sun, L. Zhang, Y. Xing, and J. M. Guerrero, "A distributed control strategy based on dc bus signaling for modular photovoltaic generation systems with battery energy storage," *IEEE Transactions on Power Electronics*, vol. 26, no. 10, pp. 3032–3045, 2011.

[83] J. N. H. C. Ferreira L. Lampe and T. G. Swart, *Power Line Communications: Theory and Appl. for Narrowband and Broadband Communications over Power Lines*. John Wiley and Sons, 2010.

[84] T. Dragičević, J. M. Guerrero, J. C. Vasquez, and D. Škrlec, "Supervisory control of an adaptive-droop regulated dc microgrid with battery management capability," *IEEE Transactions on Power Electronics*, vol. 29, no. 2, pp. 695–706, 2014.

[85] X. Lu, K. Sun, J. M. Guerrero, J. C. Vasquez, and L. Huang, "Double-quadrant state-of-charge-based droop control method for distributed energy storage systems in autonomous dc microgrids," *IEEE Transactions on Smart Grid*, vol. 6, no. 1, pp. 147–157, 2015.

[86] X. Lu, K. Sun, J. M. Guerrero, J. C. Vasquez, and L. Huang, "State-of-charge balance using adaptive droop control for distributed energy storage systems in dc microgrid applications," *IEEE Transactions on Industrial Electronics*, vol. 61, no. 6, pp. 2804–2815, 2014.

[87] P. Saenger, K. Deschinkel, N. Devillers, and M. Pera, "An optimal sizing of electrical energy storage system for an accurate energy management in an aircraft," in *2015 IEEE Vehicle Power and Propulsion Conference (VPPC)*, 2015, pp. 1–6.

[88] C. Spagnolo, S. Sumsurooah, C. I. Hill, and S. Bozhko, "Smart controller design for safety operation of the mea electrical distribution system," in *IECON 2018 - 44th Annual Conference of the IEEE Industrial Electronics Society*, 2018, pp. 5778–5785.

[89] X. Giraud, H. Piquet, M. Budinger, X. Roboam, M. Sartor, and S. Vial, "Knowledge-based system for aircraft electrical power system reconfiguration," in *2012 Electrical Systems for Aircraft, Railway and Ship Propulsion*, 2012, pp. 1–6.

[90] B. Tang, S. Yang, L. Wang, and H. Zhang, "Power priority algorithm in application to aircraft distribution network reconfiguration," in *2016 International Conference on Electrical Systems for Aircraft, Railway, Ship Propulsion and Road Vehicles International Transportation Electrification Conference (ESARS-ITEC)*, 2016, pp. 1–5.

[91] C. Spagnolo, S. Sumsurooah, C. I. Hill, and S. Bozhko, "Finite state machine control for aircraft electrical distribution system," *The Journal of Engineering*, vol. 2018, no. 13, pp. 506–511, 2018.

[92] H. Xu, "Design, specification, and synthesis of aircraft electric power systems control logic," PhD thesis, Electrical Engineering California Institute of Technology Pasadena, California, May 2013.

[93] G. Riley, *Clips refernce manual, basic programming guide*, 30 Nov 2017.

[94] Xuesen Lin, "Multi-behaviors finite state machine," in *2009 IEEE Youth Conference on Information, Computing and Telecommunication*, 2009, pp. 201–203.

[95] D. Schlabe and J. Lienig, "Energy management of aircraft electrical systems - state of the art and further directions," in *2012 Electrical Systems for Aircraft, Railway and Ship Propulsion*, 2012, pp. 1–6.

[96] X. Lang, T. Yang, Z. Huang, C. Wang, Z. Wang, S. Bozhko, and P. Wheeler, "Stability improvement of onboard hvdc grid and engine using an advanced power generation center for the more-electric aircraft," *IEEE Transactions on Transportation Electrification*, pp. 1–1, 2021.

[97] J. CHEN, "Study of 270vdc system application," Master's thesis, School of Engineering, Aircraft Design Programme, Cranfield University, 2009-2010.

[98] D. Izquierdo, R. Azcona, F. J. L. d. Cerro, C. Fernández, and B. Delicado, "Electrical power distribution system (hv270dc), for application in more electric aircraft," in *2010 Twenty-Fifth Annual IEEE Applied Power Electronics Conference and Exposition (APEC)*, 2010, pp. 1300–1305.

[99] A. Batteries, "Nanophosphate lithium iron phosphate battery," Tech. Rep. [Online]. Available: `https://a123batteries.com/anr26650m1-b-lithiumwerks-nanophosphate-3-3v-2-5ah-lithium-iron-phosphate-battery/`.

[100] S. S. Yeoh, M. Rashed, M. Sanders, and S. Bozhko, "Variable-voltage bus concept for aircraft electrical power system," *IEEE Transactions on Industrial Electronics*, vol. 66, no. 7, pp. 5634–5643, 2019.

[101] S. Bozhko, M. Rashed, C. I. Hill, S. S. Yeoh, and T. Yang, "Flux-weakening control of electric starter–generator based on permanent-magnet machine," *IEEE Transactions on Transportation Electrification*, vol. 3, no. 4, pp. 864–877, 2017.

[102] S. Morimoto, Y. Takeda, T. Hirasa, and K. Taniguchi, "Expansion of operating limits for permanent magnet motor by current vector control considering inverter capacity," *IEEE Transactions on Industry Applications*, vol. 26, no. 5, pp. 866–871, 1990.

[103] S. Morimoto, M. Sanada, and Y. Takeda, "Wide-speed operation of interior permanent magnet synchronous motors with high-performance current regulator," *IEEE Transactions on Industry Applications*, vol. 30, no. 4, pp. 920–926, 1994.

[104] Z. Zhang, J. Huang, Y. Jiang, W. Geng, and Y. Xu, "Overview and analysis of pm starter/generator for aircraft electrical power systems," *CES Transactions on Electrical Machines and Systems*, vol. 1, no. 2, pp. 117–131, 2017.

[105] Z. Zhang, C. Wang, M. Zhou, and X. You, "Flux-weakening in pmsm drives: Analysis of voltage angle control and the single current controller design," *IEEE Journal of Emerging and Selected Topics in Power Electronics*, vol. 7, no. 1, pp. 437–445, 2019.

[106] D. Stojan, D. Drevensek, Plantic, B. Grcar, and G. Stumberger, "Novel field-weakening control scheme for permanent-magnet synchronous machines based on voltage angle control," *IEEE Transactions on Industry Applications*, vol. 48, no. 6, pp. 2390–2401, 2012.

[107] T. Kwon, G. Choi, M. Kwak, and S. Sul, "Novel flux-weakening control of an ipmsm for quasi-six-step operation," *IEEE Transactions on Industry Applications*, vol. 44, no. 6, pp. 1722–1731, 2008.

[108] J. Shi, T. Liu, and S. Yang, "Nonlinear-controller design for an interior-permanent-magnet synchronous motor including field-weakening operation," *IET Electric Power Applications*, vol. 1, no. 1, pp. 119–126, 2007.

[109] M. A. Rahman, D. M. Vilathgamuwa, M. N. Uddin, and King-Jet Tseng, "Nonlinear control of interior permanent-magnet synchronous motor," *IEEE Transactions on Industry Applications*, vol. 39, no. 2, pp. 408–416, 2003.

[110] A. M. Diab, S. Bozhko, M. Galea, and C. Gerada, "Stable and robust design of active disturbance-rejection current controller for permanent magnet machines in transportation systems," *IEEE Transactions on Transportation Electrification*, vol. 6, no. 4, pp. 1421–1433, 2020.

[111] TOSHIBA. (2021). Basics of lithium-ion batteries, [Online]. Available: `https://www.global.toshiba/ww/products-solutions/battery/scib/product/module/sip/download/batteryschool/episode1.html` (visited on 10/24/2021).

[112] K. Q. C. Liu KailongLi, "A brief review on key technologies in the battery management system of electric vehicles," *Frontiers of Mechanical Engineering*, vol. 14, no. 1, pp. 47–64, 2019.

[113] E. Banguero, A. Correcher, n. Pérez-Navarro, F. Morant, and A. Aristizabal, "A review on battery charging and discharging control strategies: Application to renewable energy systems," *Energies*, no. 4, 2018.

[114] "Lithium-ion battery fast charging: A review," *eTransportation*, vol. 1, p. 100 011, 2019.

[115] D. Berndt, *Maintenance-free batteries : lead-acid, nickel/cadmium, nickel/metal hydride : a handbook of battery technology*. Taunton : Research studies Press ; New York : Wiley, 1997.

[116] A. C. Hua and B. Z. Syue, "Charge and discharge characteristics of lead-acid battery and lifepo4 battery," in *The 2010 International Power Electronics Conference - ECCE ASIA -*, 2010, pp. 1478–1483.

[117] P. Notten, J. op het Veld, and J. van Beek, "Boostcharging li-ion batteries: A challenging new charging concept," *Journal of Power Sources*, vol. 145, no. 1, pp. 89–94, Jul. 2005.

[118] T.-H. Kim, J.-S. Park, S. K. Chang, S. Choi, J. H. Ryu, and H.-K. Song, "The current move of lithium ion batteries towards the next phase," *Advanced Energy Materials*, vol. 2, no. 7, pp. 860–872, 2012.

[119] D. Pavković, M. ć, M. Hrgetić, A. Komljenović, and V. Smetko, "Battery current and voltage control system design with charging application," in *2014 IEEE Conference on Control Applications (CCA)*, 2014, pp. 1133–1138.

[120] A. Al-Haj Hussein and I. Batarseh, "A review of charging algorithms for nickel and lithium battery chargers," *IEEE Transactions on Vehicular Technology*, vol. 60, no. 3, pp. 830–838, 2011.

[121] S. O. Yong and N. A. Rahim, "Development of on-off duty cycle control with zero computational algorithm for cc-cv li ion battery charger," in *2013 IEEE Conference on Clean Energy and Technology (CEAT)*, 2013, pp. 422–426.

[122] "Optimal battery charging, part i: Minimizing time-to-charge, energy loss, and temperature rise for ocv-resistance battery model," *Journal of Power Sources*, vol. 303, pp. 388 –398, 2016.

[123] Guan-Chyun Hsieh, Liang-Rui Chen, and Kuo-Shun Huang, "Fuzzy-controlled li-ion battery charge system with active state-of-charge controller," *IEEE Transactions on Industrial Electronics*, vol. 48, no. 3, pp. 585–593, 2001.

[124] R. Salas-Puente, S. Marzal, R. Gonzalez-Medina, E. Figueres, and G. Garcera, "Practical analysis and design of a battery management system for a grid-connected dc microgrid for the reduction of the tariff cost and battery life maximization," *Energies*, vol. 11, no. 7, 2018, ISSN: 1996-1073.

[125] N. Rigogiannis, D. Voglitsis, T. Jappe, and N. Papanikolaou, "Voltage transients mitigation in the dc distribution network of more/all electric aircrafts," *Energies*, vol. 13, no. 16, 2020, ISSN: 1996-1073.

[126] Q. L. Yu Zhang Ziguang Lu and S. Wei, "The research on bus voltage stabilization control of off-grid photovoltaic dc microgrid under impact load," *Mathematical Problems in Engineering*, p. 14, 2019.

[127] L. Saw, K. Somasundaram, Y. Ye, and A. Tay, "Electro-thermal analysis of lithium iron phosphate battery for electric vehicles," *Journal of Power Sources*, vol. 249, pp. 231 –238, 2014.

[128] J. Meng, G. Luo, M. Ricco, M. Swierczynski, D.-I. Stroe, and R. Teodorescu, "Overview of lithium-ion battery modeling methods for state-of-charge estimation in electrical vehicles," *Applied Sciences*, vol. 8, no. 5, 2018.

[129] M. Dubarry, G. Baure, C. Pastor-Fernández, T. F. Yu, W. D. Widanage, and J. Marco, "Battery energy storage system modeling: A combined comprehensive approach," *Journal of Energy Storage*, vol. 21, pp. 172 –185, 2019.

[130] O. Tremblay, L. Dessaint, and A. Dekkiche, "A generic battery model for the dynamic simulation of hybrid electric vehicles," in *2007 IEEE Vehicle Power and Propulsion Conference*, 2007, pp. 284–289.

[131] Y. Han, X. Ning, P. Yang, and L. Xu, "Review of Power Sharing, Voltage Restoration and Stabilization Techniques in Hierarchical Controlled DC Microgrids," *IEEE Access*, vol. 7, pp. 149 202–149 223, 2019.

[132] L. He, Y. Li, J. M. Guerrero, and Y. Cao, "A comprehensive inertial control strategy for hybrid ac/dc microgrid with distributed generations," *IEEE Transactions on Smart Grid*, vol. 11, no. 2, pp. 1737–1747, 2020.

[133] F. Chen, R. Burgos, D. Boroyevich, J. C. Vasquez, and J. M. Guerrero, "Investigation of Nonlinear Droop Control in DC Power Distribution Systems: Load Sharing, Voltage Regulation, Efficiency, and Stability," *IEEE Transactions on Power Electronics*, vol. 34, no. 10, pp. 9404–9421, 2019.

[134] F. Gao, S. Bozhko, A. Costabeber, C. Patel, P. Wheeler, C. I. Hill, and G. Asher, "Comparative Stability Analysis of Droop Control Approaches in Voltage-Source-Converter-Based DC Microgrids," *IEEE Transactions on Power Electronics*, vol. 32, no. 3, pp. 2395–2415, 2017.

[135] M. Nasir, Z. Jin, H. A. Khan, N. A. Zaffar, J. C. Vasquez, and J. M. Guerrero, "A Decentralized Control Architecture Applied to DC Nanogrid Clusters for Rural Electrification in Developing Regions," *IEEE Transactions on Power Electronics*, vol. 34, no. 2, pp. 1773–1785, 2019.

[136] F. Gao, S. Bozhko, G. Asher, P. Wheeler, and C. Patel, "An Improved Voltage Compensation Approach in a Droop-Controlled DC Power System for the More Electric Aircraft," *IEEE Transactions on Power Electronics*, vol. 31, no. 10, pp. 7369–7383, 2016.

[137] Y. Fu, Z. Zhang, Y. Mi, Z. Li, and F. Li, "Droop Control for DC Multi-Microgrids Based on Local Adaptive Fuzzy Approach and Global Power Allocation Correction," *IEEE Transactions on Smart Grid*, vol. 10, no. 5, pp. 5468–5478, 2019.

[138] J. Mohammadi and F. Badrkhani Ajaei, "Improved Mode-Adaptive Droop Control Strategy for the DC Microgrid," *IEEE Access*, vol. 7, pp. 86 421–86 435, 2019.

[139] L. Meng, Q. Shafiee, G. F. Trecate, H. Karimi, D. Fulwani, X. Lu, and J. M. Guerrero, "Review on Control of DC Microgrids and Multiple Microgrid Clusters," *IEEE Journal of Emerging and Selected Topics in Power Electronics*, vol. 5, no. 3, pp. 928–948, 2017.

[140] B. Ko, G. Lee, K. Choi, and R. Kim, "A Coordinated Droop Control Method Using a Virtual Voltage Axis for Power Management and Voltage Restoration of DC Microgrids," *IEEE Transactions on Industrial Electronics*, vol. 66, no. 11, pp. 9076–9085, 2019.

[141] Y. Liu, T. C. Green, J. Wu, K. Rouzbehi, A. Raza, and D. Xu, "A New Droop Coefficient Design Method for Accurate Power-Sharing in VSC-MTDC Systems," *IEEE Access*, vol. 7, pp. 47 605–47 614, 2019.

[142] G. Xu, D. Sha, and X. Liao, "Decentralized Inverse-Droop Control for Input-Series–Output-Parallel DC–DC Converters," *IEEE Transactions on Power Electronics*, vol. 30, no. 9, pp. 4621–4625, 2015.

[143] A. Khorsandi, M. Ashourloo, and H. Mokhtari, "An Adaptive Droop Control Method for Low Voltage DC Microgrids," in *The 5th Annual International Power Electronics, Drive Systems and Technologies Conference (PEDSTC 2014)*, 2014.

[144] Shivam and D. Ratna, "Voltage Regulation and Enhance Load Sharing in DC Microgrid Based on Particle Swarm Optimization in Marine Applications," *Indian Journal of Geo-Marine Sciences*, vol. 46, no. 10, pp. 2105–2113, 2017.

[145] G. Niyitegeka, J. Choi, and Y. Ok, "Improved Droop Control for Effective Load Sharing and Voltage Regulation in DC Microgrids," in *2016 Electric Power Quality and Supply Reliability (PQ)*, 2016.

[146] L. Meng, T. Dragicevic, J. M. Guerrero, and J. C. Vásquez, "Optimization with System Damping Restoration for Droop Controlled DC-DC Converters," in *2013 IEEE Energy Conversion Congress and Exposition*, 2013.

[147] A. M. Dissanayake and N. C. Ekneligoda, "Multiobjective Optimization of Droop-Controlled Distributed Generators in DC Microgrids," *IEEE Transactions on Industrial Informatics*, vol. 16, no. 4, pp. 2423–2435, 2020.

[148] A. A. Hadi, X. Fu, and R. Challoo, "IGBT Module Loss Calculation and Thermal Resistance Estimation for a Grid-Connected Multilevel Converter," in *Wide Bandgap Power and Energy Devices and Applications III*, International Society for Optics and Photonics, vol. 10754, SPIE, 2018.

[149] ABB. (May 2017). PRO-33.0-TL-OUTD. ABB, Ed., [Online]. Available: `https://new.abb.com/power-converters-inverters/solar/legacy/pro-33-0kw`.

[150] D. Auroux. (Fall 2007). Multivariable Calculus. MIT, Ed., [Online]. Available: `https://ocw.mit.edu/courses/mathematics/18-02-multivariable-calculus-fall-2007/index.htm`.

[151] S. A. Boctor, *Electric Circuit Analysis (2nd Ed.)* USA: Prentice-Hall, Inc., 1992, ISBN: 013251141X.

[152] S. INNOVATION+SERVICE. (2021). Igd-1-424-p1n4-dl-fa stacks, [Online]. Available: `https://www.semikron.com/products/product-classes/stacks/detail/igd-1-424-p1n4-dl-fa-08800445.html` (visited on 08/30/2021).

[153] S. Zhao, F. Blaabjerg, and H. Wang, "An overview of artificial intelligence applications for power electronics," *IEEE Transactions on Power Electronics*, vol. 36, no. 4, pp. 4633–4658, 2021.

[154] R. A.F.L.H.B.L.S.F.d.R. A. Ivan Nun da Silva Danilo Hernane Spatti, *Artificial Neural Networks: A Practical Course*. Springer, 2017.

[155] C. Vidal, P. Malysz, P. Kollmeyer, and A. Emadi, "Machine learning applied to electrified vehicle battery state of charge and state of health estimation: State-of-the-art," *IEEE Access*, vol. 8, pp. 52 796–52 814, 2020.

[156] Y.-M. Chiang, L.-C. Chang, and F.-J. Chang, "Comparison of static-feedforward and dynamic-feedback neural networks for rainfall–runoff modeling," *Journal of Hydrology*, vol. 290, no. 3, pp. 297–311, 2004, ISSN: 0022-1694. DOI: https://doi.org/10.1016/j.jhydrol.2003.12.033. [Online]. Available: https://www.sciencedirect.com/science/article/pii/S0022169403005043.

[157] T. Dragičević and M. Novak, "Weighting factor design in model predictive control of power electronic converters: An artificial neural network approach," *IEEE Transactions on Industrial Electronics*, vol. 66, no. 11, pp. 8870–8880, 2019.

[158] B. K. Bose, "Neural network applications in power electronics and motor drives—an introduction and perspective," *IEEE Transactions on Industrial Electronics*, vol. 54, no. 1, pp. 14–33, 2007.

[159] J. Arif, N. Ray Chaudhuri, S. Ray, and B. Chaudhuri, "Online levenberg-marquardt algorithm for neural network based estimation and control of power systems," in *2009 International Joint Conference on Neural Networks*, 2009, pp. 199–206.

[160] Y. Yang and Z. Gao, "Power management problem for civil aircraft under more electric environment," *International Journal of Aerospace Engineering Journal*, vol. 2020, 2020.

[161] A. Barzegar, R. Su, C. Wen, L. Rajabpour, Y. Zhang, A. Gupta, C. Gajanayake, and M. Y. Lee, "Intelligent power allocation and load management of more electric

aircraft," in *2015 IEEE 11th International Conference on Power Electronics and Drive Systems*, 2015, pp. 533–538.

[162] P. Nuzzo, H. Xu, N. Ozay, J. B. Finn, A. L. Sangiovanni-Vincentelli, R. M. Murray, A. Donzé, and S. A. Seshia, "A contract-based methodology for aircraft electric power system design," *IEEE Access*, vol. 2, pp. 1–25, 2014.

[163] M. A. A. Mohamed, S. Yeoh, J. Atkin, M. Khalaf, and S. Bozhko, "Analysis and design of battery controller for more electric aircraft application," in *2021 IEEE International Power and Renewable Energy Conference (IPRECON)*, 2021, pp. 1–6.

[164] Parker. (2021). Brushless servo motors, [Online]. Available: `https://www.micromech.co.uk/uploads/assets/pdf/parker/servo_motors/192_061013_smb_smh_sme_catalogue.pdf` (visited on 08/30/2021).

[165] LEM. (2021). Voltage transducer lv 25-p, [Online]. Available: `https://www.lem.com/sites/default/files/products_datasheets/lv_25-p.pdf` (visited on 08/30/2021).

[166] LEM. (2021). Current transducer la 25-p, [Online]. Available: `https://www.lem.com/sites/default/files/products_datasheets/la_25-p.pdf` (visited on 08/30/2021).

[167] VASCAT. (2021). Motor mac r 112.140, [Online]. Available: `https://vascat.es/wp-content/uploads/2021/05/Technical_datasheet_MAC-R.pdf` (visited on 08/30/2021).

[168] HEIDENHAIN. (2021). Ern 400 series, [Online]. Available: `https://www.heidenhain.de/produkte/drehgeber/anbau/ern-400#` (visited on 08/30/2021).

[169] Mitsubishi. (2021). Frequency inverter, fr -a741, [Online]. Available: `https://inverterdrive.com/file/Mitsubishi-Regenerative-FR-A741-Technical-Manual` (visited on 08/30/2021).

[170] T. Instruments. (2021). Tmdscncd28379d control card, [Online]. Available: `https://www.ti.com/lit/ug/sprui76a/sprui76a.pdf` (visited on 08/30/2021).

[171] Q. Tech. (2021). Ac 31120 model, [Online]. Available: https://www.yumpu.com/en/document/read/46070096/models-31120-31120a-31180-31180a-programmable-ac-power- (visited on 08/30/2021).

[172] A. Technologies. (2021). El600vdc19800w-a model, [Online]. Available: https://www.batterfly.com/PDF/Amp/apm-dc-electronic-load-data-sheet-all.pdf (visited on 08/30/2021).